Oxygen Reduction Reaction with Molybdenum-Containing Oxysulfide Nanoparticles : from Colloidal Synthesis to Surface Activity

Thi Kim-Chi Lê

Sorbonne Université

Ecole doctorale 397 : Physique et Chimie des Matériaux

Laboratoire de Chimie de la Matière Condensée de Paris (LCMCP)

Oxygen Reduction Reaction with Molybdenum-Containing Oxysulfide Nanoparticles: from Colloidal Synthesis to Surface Activity

Par Thi Kim-Chi LÊ

Thèse de doctorat de Sorbonne Université

Dirigée par Pr. Clément Sanchez et Dr. Sophie Carenco

Présentée et soutenue publiquement le 07 octobre 2020

Devant un jury composé de :

M. Pavel Afanasiev	Directeur de recherche CNRS – IRCELYON	Rapporteur
Mme Catherine Amiens	Professeur – LCC Toulouse	Rapporteuse
Mme Jennifer Peron	Maître de conférences – Université de Paris	Examinatrice
M. Clément Guibert	Maître de conférences – SU	Examinateur
M. Clément Sanchez	Professeur – SU et Collège de France	Directeur de thèse
Mme Sophie Carenco	Chargée de recherche CNRS – SU	Co-directrice de thèse

La réduction de l’oxygène et les nanoparticules contenant de l’oxysulfure de molybdène : de la synthèse colloïdale à la réactivité de surface

Acknowledgements

First of all, I would like to thank Prof. Clément Sanchez and Dr. Sophie Carenco to be my thesis director and thesis directrice. Especially for all that I learnt from Dr. Carenco, I can never thank her enough. Being my main supervisor who is always very supportive during these four years, she has taught me not only science but also the working method, to be a professional researcher.

I would like to thank also Prof. Florence Babonneau, former directrice, and Prof. Christian Bonhomme, director of LCMCP for their welcome in the laboratory during my project.

Next, I am thankful for the advice and discussions with Dr. Christel Laberty-Robert and Dr. David Portehault on the electrochemical parts. I appreciate very much Dr. Capucine Sassoye, Dr. Alex Lemarchand et M. Mohamed Selmane for their work on PDF, not only for the data treatment but also for the measurements, especially during the confinement. I would like to thank Ms. Isabelle Genois and Mr. Patrick Le Griel for their help on microscopies and elemental analysis. Also, I am grateful to the contribution of Dr. Alexy P. Freitas on the data treatment of XAS and XPS.

I am very grateful for the collaborations with other scientists, Dr. Andrea Zitolo, Dr. Benedikt Lassalle-Kaiser and Dr. Jean-Jacques Gallet, from SOLEIL Synchrotron for their work on XAS and XPS measurements; Dr. Asma Tougerti from Unité de Catalyse et Chimie du Solide, UCCS, Université de Lille I for her contributions on XAS data treatment; Dr. Mounib Bahri and Dr. Ovidiu Ersen from Institut de Physique et Chimie des Matériaux de Strasbourg, IPCMS for their work on HRTEM-EDS. Also, I would like to thank Dr. Victor Mougel and his colleagues for providing us the Mo(+III) precursor.

Following, I would like to thank all other members and former members of our research group in particular, of all LCMCP in general, as well as my other friends and especially my families for their support, their help in the lab and for all the discussions and ideas we shared.

Finally, I appreciate very much the ANR for funding the project OxySUN, without this, none of my scientific activities would be possible.

Table of Contents

Chapter I

Energy problems and propositions towards solutions

Tables of contents

1. Recent energy problems and fuel cells - some up-to-date achievements

1.1. Energy crisis for traditional fossil energy and alternative energy sources

Fire is present all along the human history as the symbol of the energy and the force of human evolution: it made our dawn of mankind. Since the first industrial revolution from mid-18th century, fossil energy started to be widely used to fulfill the increasing need of textiles, steel and machines of the industry. At the end of the first revolution, the process of coal oil distillation was invented by Abraham Gesner (Canadian physicist, 1797 – 1864) in 1849.[1] This was essential for the wide exploitation of oil during the 20th century,[2] even for the electricity production. Based on that new resource, we have developed modern technology, industry, new geopolitical game and societies that we are now living. However, petroleum as an energy source cannot assure the future of mankind: the undesirable effects of petroleum utilization on the climate were even predicted hundreds years ago. Currently, we are encountering many kinds of pollutions due to the petroleum utilization: first, toxic and non-toxic wastes from the extraction, the production, the transportation and then from the combustion, not to mention oil spills, etc. Although, humanity still depends very much on fossil fuel, even for developed European countries.[3] In this situation, according to some new estimations, the depletion of fossil fuel could come in around one century, for oil it's even closer: in about fifty years,[4,5] taking into account advancement in technology we can achieve each year. Moreover, the fossil reserves are not distributed homogenously all over the Earth with a large variety of compositions: only about 42 countries can produce oil while all about 220 nations around the world use it[2] (Figure 1). For oil, the proved reserves are mostly found in Middle East and the Americas (more than 80 % world proved reserves in 2018) while the production and consumption are not at all proportional (Figure 1B), e.g. in 2018 the Middle East produces roughly three times more than consuming while the Europe consumes roughly five times more than producing.[6] As the need of energy is always high, the need of petroleum reserves possession can be a serious reason for a war (or price wars[7]).

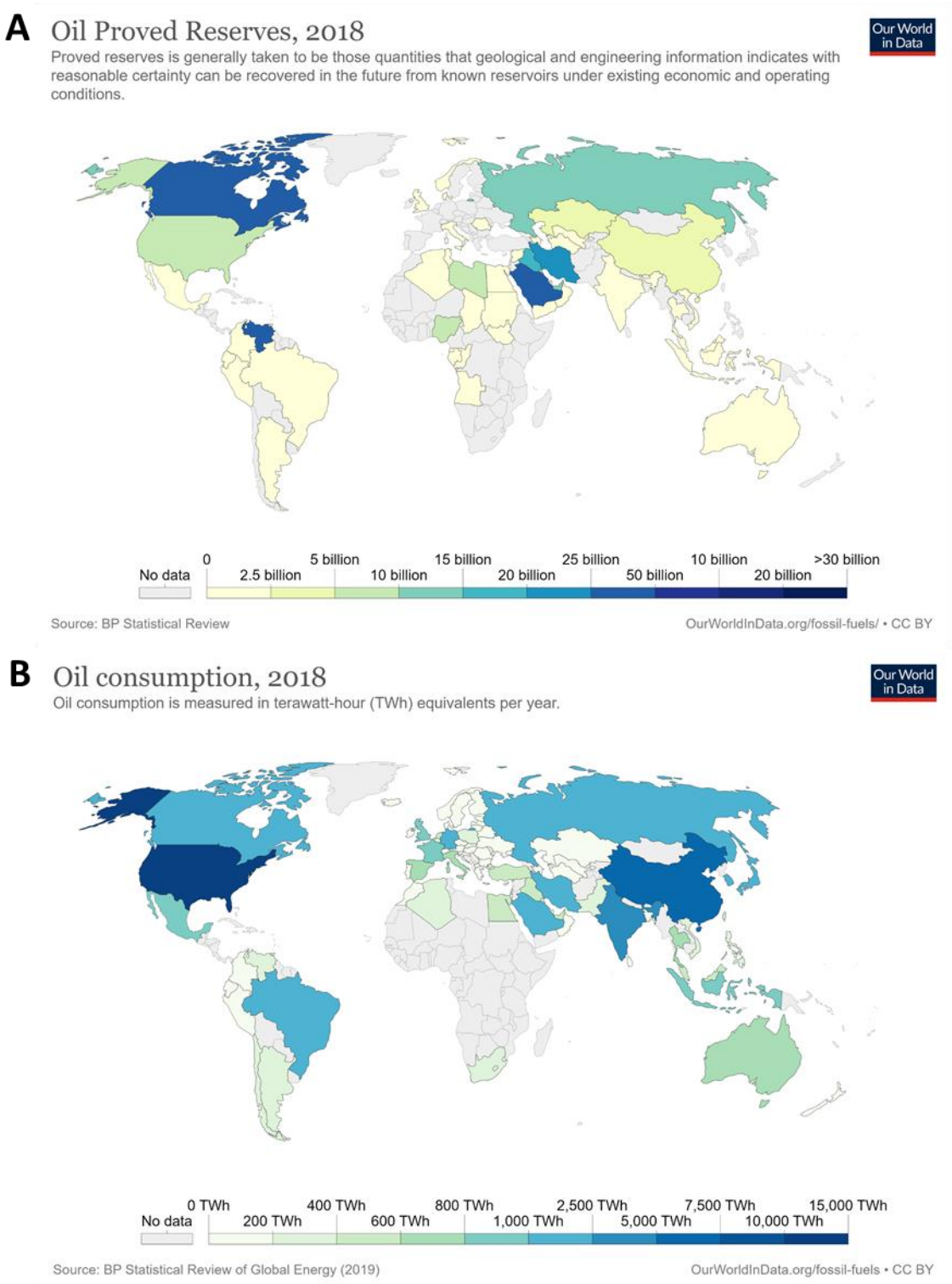

Figure 1 (A) Map of the oil proved reserves around the world. (B) Map of oil consumption around the world in 2019.[6] All figures are taken from the website ourworldindata.org with the references from BP Statistical Reviews.

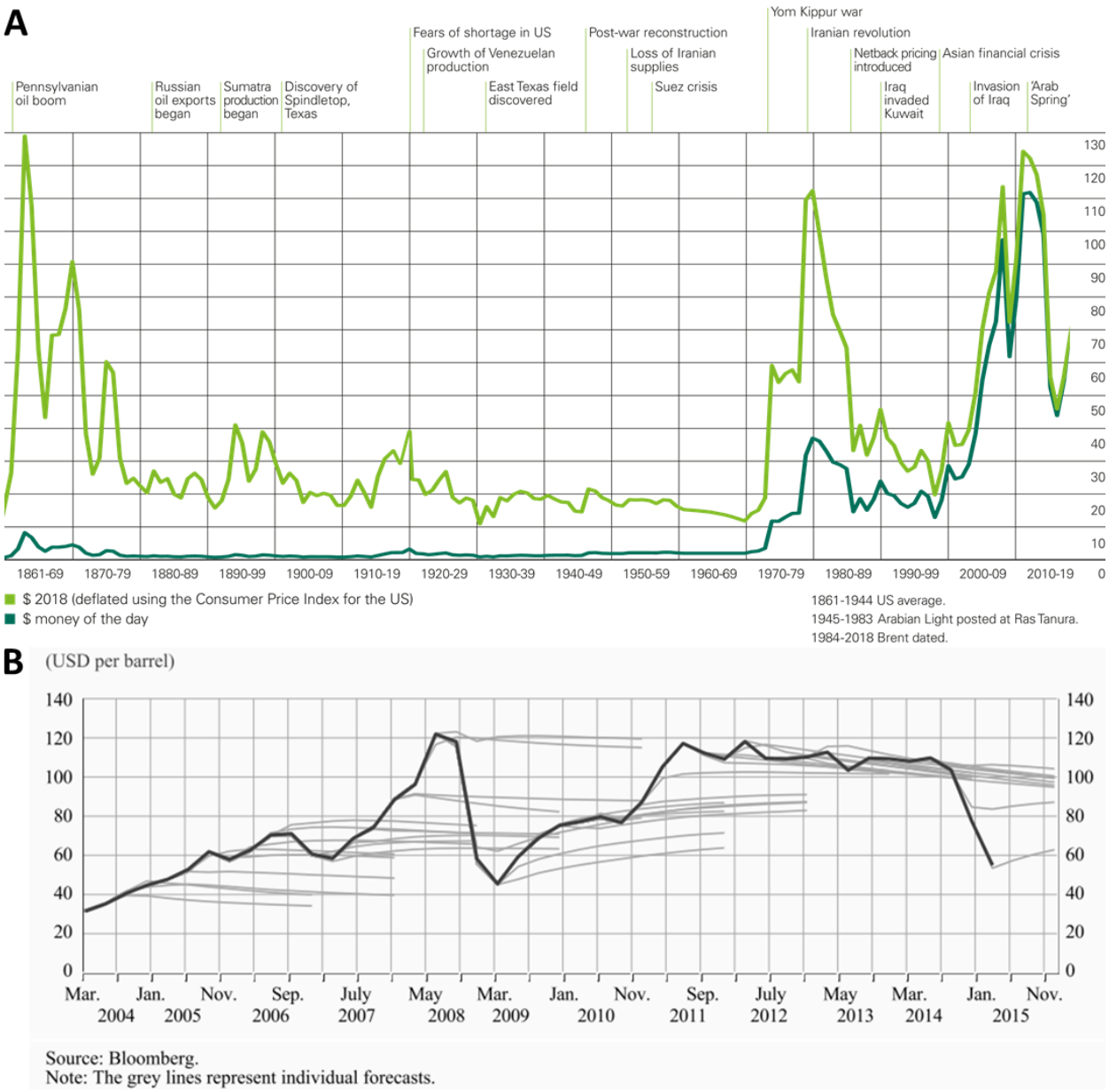

Figure 2 (A) Crude oil prices 1861 – 2018 with key events.[6] (B) Brent crude oil prices 2004 – 2015 and prices forecasts.[8] All figures are taken from the references.

Another inconvenience of using petroleum as the main energy source is that its price fluctuates in the function of political events[9] and the prediction of the price evolution trend is extremely hard[8] (Figure 2). For example, during the last 50 years, many events have resulted in dramatic and an immediate disruption of world crude oil production, hence, its price: the Iranian revolution in the fall of 1978, Iraq's invasion of Iran in September 1980, Iraq's invasion of Kuwait in August 1990, the global financial crisis in 2007-08,[6,9] the Arab spring in 2010s, and the most current one: COVID-19 pandemic in 2020. On April 20th 2020, the price of West

Texas Intermediate (WTI) Crude Oil (American benchmark) was down under US$0 (-US$37) per barrel, this is never ever preceded in the history.

For all these main reasons, lately, besides reducing carbon emission by education of high-carbon power consumption attitude and by technology development, we are also developing technologies for electricity production from low-carbon power sources such as the sun, the wind, the biomass, etc. The quest to the new "fire" is still in progress and one of the promising choices is to use hydrogen in fuel cell (one type of batteries which convert the chemical energy stored in chemical bonds into electrical energy) for clean electricity production.

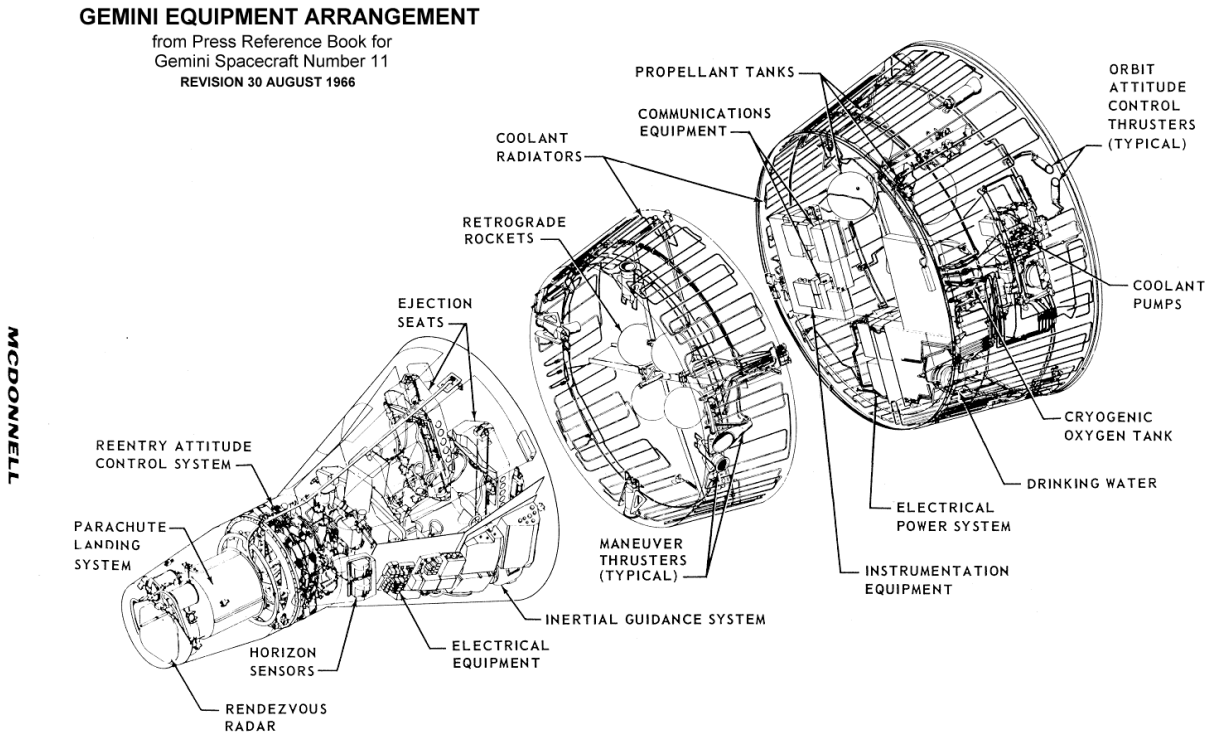

Figure 3 Equipment arrangement in Gemini spacecraft number 11 which successfully used an alkaline fuel cell system. Image source: nssdc.gsfc.nasa.gov

The fuel cell concept was demonstrated for the first time in 1801 by Humphry Davy (1778 – 1829, Cornish chemist and inventor) but it was only 38 years later that the first fuel cell, designed by William Grove (1811 – 1896, Welsh judge and physicist), appeared in the world. From this very first fuel cell to the first application of alkaline fuel cells in the Gemini earth-orbiting mission (1962 – 1966) (Figure 3), as the preparation period of the Apollo Project (1961 – 1975), about 125 more years were spent.[10] Since then, the end of Apollo Project, the fast growing technology led to the first fuel cell cars for public buyers. Nowadays, the researchers have developed several types of fuel cells. Among them, those using hydrogen as

a source energy are becoming an interesting choice for wide individual or collective usages. These are anion/proton exchange membranes fuel cells a.k.a AEMFCs and PEMFCs (Figure 4). In these fuel cells, in anode, there is an oxidation of hydrogen (fuel), a.k.a. Hydrogen Oxidation Reaction (HOR); and in cathode, there is a reduction of oxygen, a.k.a. Oxygen Reduction Reaction (ORR). The kinetics of both reactions are too slow that catalysts are essential to make them occurring much faster, hence, efficient enough for applications. Between these two, ORR is a more difficult process as it involves 4 electrons (direct mechanism by Volmer) instead of 2 electrons in HOR. This is also the reason why there are more electrocatalysts available for HOR than for ORR.

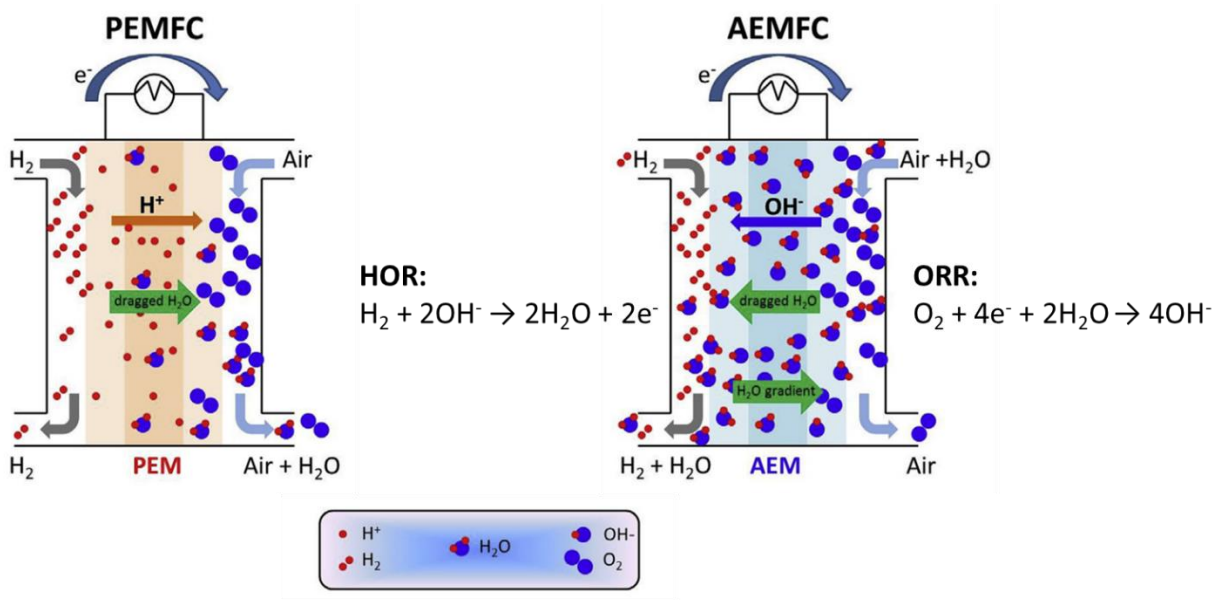

Figure 4 Principles of Proton Exchange Membrane Fuel Cell (PEMFCs) and Anion Exchange Membrane Fuel Cell (AEMFCs) with two reactions by Volmer in basic condition at anode (HOR) and at cathode (ORR). Schema reconstructed from a review by D. R. Dekel in 2018.[11]

The applications of hydrogen fuel cells started in 2008 with the Honda FCX Clarity, the first commercial hydrogen fuel cell automobile on sale. However, the application of hydrogen fuel cell in stationary started already in 1990s, tested in large vehicles as submarines since late 1970s (by US Navy). The fuel cell electrical vehicles (FCEVs) in general carry a hydrogen tank supplying a fuel cell to create electricity.

An advantage of the fuel cells is that there is no stored electrical energy like in batteries, rather, the energy is stored in a chemical form, in the hydrogen fuel. Hence, this application in vehicles demands a certain development of technology to assure the security and the cell efficacy. To spread the use of FCEVs, there are two main difficulties to resolve: the “fuel” and the “cell”.

For the fuel, as the catalysts for electrolysis became more efficient, the price of hydrogen produced by electrolysis was reduced from US$8 in 2006 to US$6 in 2011,[12] but stays quite stable until this day.[13] According to the recent report of Hydrogen Council published in January 2020,[13] the world industry targets to divide the retailing price per kg by two in 10 years and by three in 30 years, not mentioning that for industrial powering, the price can be even much lower. This aims to increase the access to greener energy sources for everyone and being more friendly to the environment. Along with developing the hydrogen production, the storage of hydrogen is also being improved to be lighter, larger and safer for all uses in FCEVs.[14] In 2019, the Guinness record for the longest multi-rotor flight time was achieved by South Korean company MetaVista (CSACSM) using Intelligent Energy's 800W fuel cell power.[15] The quadcopter drone flew for 12 hours, 7 minutes and 5 seconds using liquid hydrogen to fuel the module. The previous record stood at 2 hours, 6 minutes and 7 seconds. This country is planning to plant 86 hydrogen stations this year in addition to 28 current stations in 2019 and even reach 310 stations in 2022.[13,16] Europe, Japan, the US, etc. are also following this trend.

In terms of the cell, i.e. the design and the functioning of the device that generate electricity from the chemical fuel, the researchers have also gone a long way since the first commercial hydrogen fuel cell cars over 10 years ago. For the moment, the price of a hydrogen fuel cell car starts from €60 000, in the same price range as a Tesla, so, not quite affordable for the public. However, in addition to the same efficiency and the same advantages of these two types of vehicles (low engine noise and zero-emission during utilization), fuel cell vehicles require much shorter time of refueling and can be lighter than electrical vehicles as they do not contain heavy and hazardous batteries.[17] That is why the need of reducing the total price of a fuel cell car is increasing to fulfill the public demand. The main reason of the too high price is the catalyst for ORR and HOR in the cell.[18] For the moment, only noble metals are used although they are rare and expensive. The question of finding alternative non-noble metals catalysts is still a hot topic.

1.2. Catalyst problems of fuel cells and our idea

1.2.1. Commercial noble metals based hydrogen fuel cells catalysts

Currently, all catalysts used in fuel cells on sale are heterogeneous and are precious metals based (Pt, Pd, Ir, Ru, Rh),[19–21] the commercial devices should be also based on these catalysts even if detailed information on commercial system designs is not publicized. However, these highly efficient electrocatalysts are rare and expensive and are one of the reasons why the hydrogen transportation industry has never gained any real traction.

Considering ORR at the cathode, until this day, Pt and Pt-base (alloys, supported catalysts) are no doubt the best catalysts of the kind.[22] In 2018, A. Kulkarni *et al.* reviewed on Chemical Reviews that density functional theory (DFT) calculations have shown that the energetics of key reaction intermediates are linked by linear scaling relationships that have been indispensable for rationalizing trends in ORR catalytic activity across different materials.[22] These analyses often result in a "volcano relation" between catalytic activity and key adsorption energies, which, for instance, explains why Pt and Pd and their alloys are the best catalysts for ORR,[22] Figure 5 shows the ORR activity in function of $O_{intermediate}$ binding energy for each metal.[23] Hence, for performing ORR at low temperature (close to ambient temperature), Pt is still considered as a benchmark,[24] not to mention its remarkable stability compared to almost other materials being tested. As it is rare and expensive, the utilization should be maximized or even avoided to preserve Pt source.[25] The only way is to reduce the size of the particles as much as possible and/or to find a way to stabilize the catalysts. Pt can be coupled with other metals (noble or non-noble) in alloys or core-shell nanoparticles, or coupled with non-metals such as graphene as a supported catalyst.[26–28] These researches are for finding a way to reduce the Pt loading quantity in catalysts while keeping or increasing their efficacy and stability.

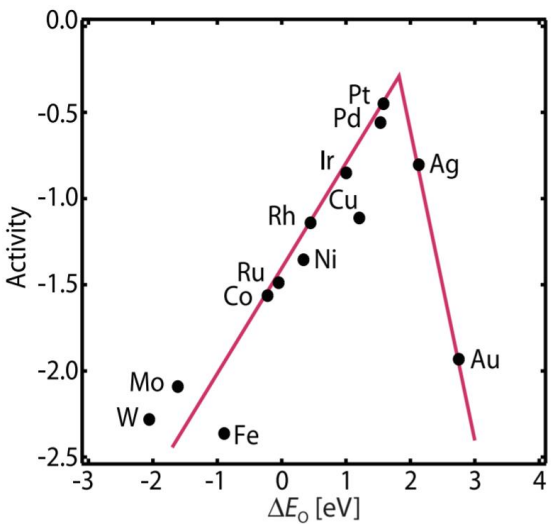

Figure 5 Volcano plot showing the ORR activity of a metal in function of the O (of an intermediate) binding energy.[23]

During 15 years from 2002 to 2017, researchers found the way to reduce significantly the Pt loading per vehicle from 80 g in 2002 to 10 g in 2017 (Figure 6).[18] Based on an approximation of Bryan Pivovar on Nature Catalysis in 2019, the total cost of a FCEV is near US$45 kW^{-1} at large volume, it has to be targeted to near US$30 kW^{-1} to reach full parity with internal

combustion vehicles, not mentioning a strong cost of Pt components.[18] However, in this field, researchers have gone a long way to improve the commercial viability. Many research programs are ongoing on the way to increase the catalytic activity. A current work between German and Czechs researchers shows the optimal nanoparticles size is 1.1 nm.[29] They confirmed this theoretical prediction by practical tests where Pt nanoparticles were doped on MOF-template. By reducing the nanoparticles size to ca. 1 nm, the ORR activity observed was doubled compared to a commercial Pt/C.[29] According to them, this is the best performance ever reported for Pt-pure catalysts for ORR, of similar sizes.

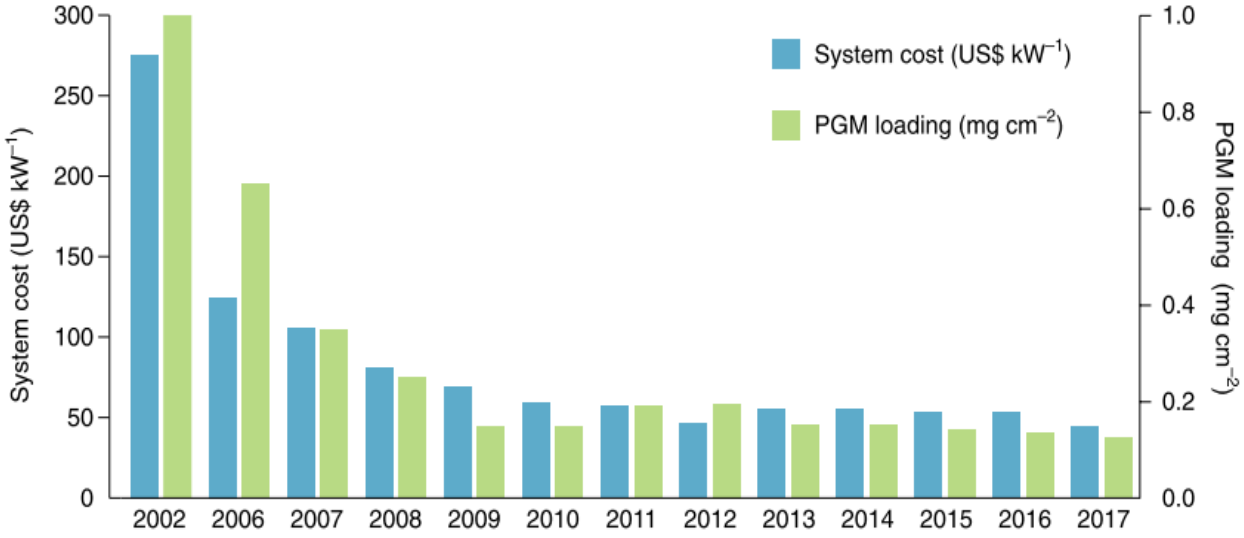

Figure 6 Evolution of the system cost and the Platinum Group Metals (PGM) loading 2002 – 2017.[18]

This is very interesting and seems to be promising but to be honest, a FCEV's final price would not be reduced significantly when the noble metals are still in use.[18,25] This is a huge struggle for the transport company to stay with this utilization: from 2009 to 2017, the system cost and platinum group metals loading stayed mostly stable, compared to the price drop from 2002 to 2009.[18] Even a large company, Mercedes-Benz, announced late April 2020 that it stops chasing the dream of individual car with fuel cell because of costly research and lack of market interest. The struggle of making fuel cell viable for individual utilization is inspiring researchers around the world to find new non-noble metal catalysts in parallel with other technology development. The further advances to reach the activity level and stability level of Pt-based catalysts are still very important but going towards non-noble metal based systems may reduce the vehicle price, hence, create market interests and finally cause much less environmental impact.

1.2.2. Alternative non-noble metal based ORR catalysts: some current researches

Talking about ORR activity, lately there are many researches on Co showing that it may be a good candidate. For example, it can be in the metallic or oxide (Co_3O_4) nanoparticles (≈ 20 nm) supported on graphitic nanofiber.[30] In this article, the catalyst and commercial Pt/C show not only comparable reactivity but also comparable stability over time even in the presence of methanol. Its remarkable stability for ORR catalysis in basic medium is even higher than commercial Pt/C. Another interesting catalyst is Mn-containing perovskites such as the layered perovskite $La_{0.5}Sr_{1.5}MnO_4$ (l-LSMO) and of the pseudo-cubic perovskite $La_{0.7}Sr_{0.3}MnO_3$ (pc-LSMO).[31] For decades, Mn-based oxides were shown to be promising for ORR in alkaline condition. These two perovskites have high ORR selectivity for 4-electron ORR and show the best stability ever reported for all perovskites in ORR.

As mentioned above, Pt can be coupled with non-metal materials to form supported catalysts. Among the light elements currently being studied, carbon based materials are good choice as they are inexpensive and easy to mass-produce.[26]

Also, as the graphene is more fashionable than ever, in some works graphene is doped with single metallic atoms, not only Pt but also non-noble metals (light elements in groups IIIA, IVA, VA, VIA and VIIA, or heavy metals like Co, Mo).[32–35] The heteroatom doping on graphene makes the transportation of electrons better in the material, the metallic atoms doping creates active sites on graphene. Altogether, they make a much higher activity for the new material than initial graphene. A recent paper shows interesting results with a doping of N, Co and Mo at the same time by chemical vapor deposition (CVD).[32] Although the measured overpotential[i] is higher for synthesized materials than commercial Pt/C while the maximum current[ii] is practically the same for both, this case is still worth a look compared to other cases as the fabrication of graphene is much simpler and much more inexpensive than Pt/C. The graphene is also a very light material which can be very interesting for wide application in vehicles to reduce the total weight. However, the doping method by CVD is only interesting for fine research aims, as it requires a CVD furnace, for instance, not available for large-scaled industrial production.

[i] The overpotential is the difference between the measured half-wave potential and the theoretical one (at ideal conditions). The lower it is, the sooner the reaction occurs, hence, the more active the catalyst is.
[ii] The higher the maximum current is, the more active sites are in function, hence, the better the catalyst's performance is.

1.2.3. Mo compounds as a new research direction for ORR catalysis

Coming back to our case, we chose to work with molybdenum, a transition metal which is relatively more abundant, inexpensive and accessible than noble metals. Mo has the electronic configuration of $[Kr]4d^5 5s^1$, which means it can have many oxidation states from 0 to +VI. In organometallic compounds with π-acceptor ligands like carbonyl, Mo can be in reduced states: -I in $Na_2[Mo_2(CO)_{10}]$[36] or -II in $Na_2[Mo(CO)]$ which needs to be kept at lower than -30 °C as it is extremely unstable.[37] Depending on the compounds, it is reported that Mo can have various coordinations from 4 to 8 and a varied stereochemistry.[38] According to Sebenik *et al.* in Ullmann's Encyclopedia of Industrial Chemistry, Mo can form compounds with inorganic and organic ligands and has a preference for oxygen, sulfur, fluorine and chlorine donor atoms. It can form also bi- and polynuclear compounds containing O-bridges, Cl ligand-bridges and/or Mo-Mo bonds.[38]

When it comes to a catalyst, a center atom should be able to form unstable intermediate complexes easily with reactants. As Mo can tolerate many coordinations and oxidation states, also a high ability to bind to any kind of ligand, it should easily form intermediates during the catalytic process. In practice, Mo compounds have been used for catalysis in industry for a very wide range of reactions: from hydrogenation, selective oxidation, isomerization, etc. in either homogenous or heterogeneous forms, alone or associated with other elements (Co, Ni, V, C, S, Al_2O_3).[38] In industry, the utilization of MoS_2 and MoO_3 in heterogeneous catalysis in petrochemistry has been reported more than 30 years ago.[39]

About the abundance in the Earth's crust, molybdenum is not one of the most abundant elements but definitely not a rare one either: it is from 1000 to 100 000 times more frequently found in the earth's crust than the best known ORR catalysts (Pt, Pd, Ir) (Figure 7). Molybdenum is considered as one of the major industrial metals as its major application is to manufacture sustainable stainless steel: according to International Molybdenum Association (IMOA), 72 % of Mo in total 265 000 tons produced in 2018 are in steel, of which mostly two thirds are in engineering steel. In 2019, it was even reported at about 80 %.[40] It means that the fabrication of Mo is always maintained stable by the industrial world. In the opinion of the US Geological Survey (USGS), "…resources of molybdenum are adequate to supply world needs for the foreseeable future".[40] Some loose coherence between the oil price and the molybdenum ore price has been noticed[41] but lately, the molybdenum price was predicted not to rally.[42] During 2019, the molybdenum oxide daily global spot price was ranging from US$18.22/kg to US$27.94/kg in the world market and dropped to US$19.80/kg in the end of April 2020 because

of the COVID-19 pandemic.[43] In the report of the full year 2019 published on 4th May 2020, General Moly Inc. shared their vision on the constrained molybdenum price even with the difficulties during the pandemic.[43] This is a big economical advantage for molybdenum utilization compared to rare metals: in January 2006, the London p.m. fixing was already US$1049.50/troz (27.83 €/g) for Pt and US$287/troz (7.61 €/g) for Pd.[44]

In short, for the researches on new electro-catalysts for the use in fuel cell or on catalysis in general, molybdenum is an interesting choice, both in the aspect of potential activity and in the economical point of view.

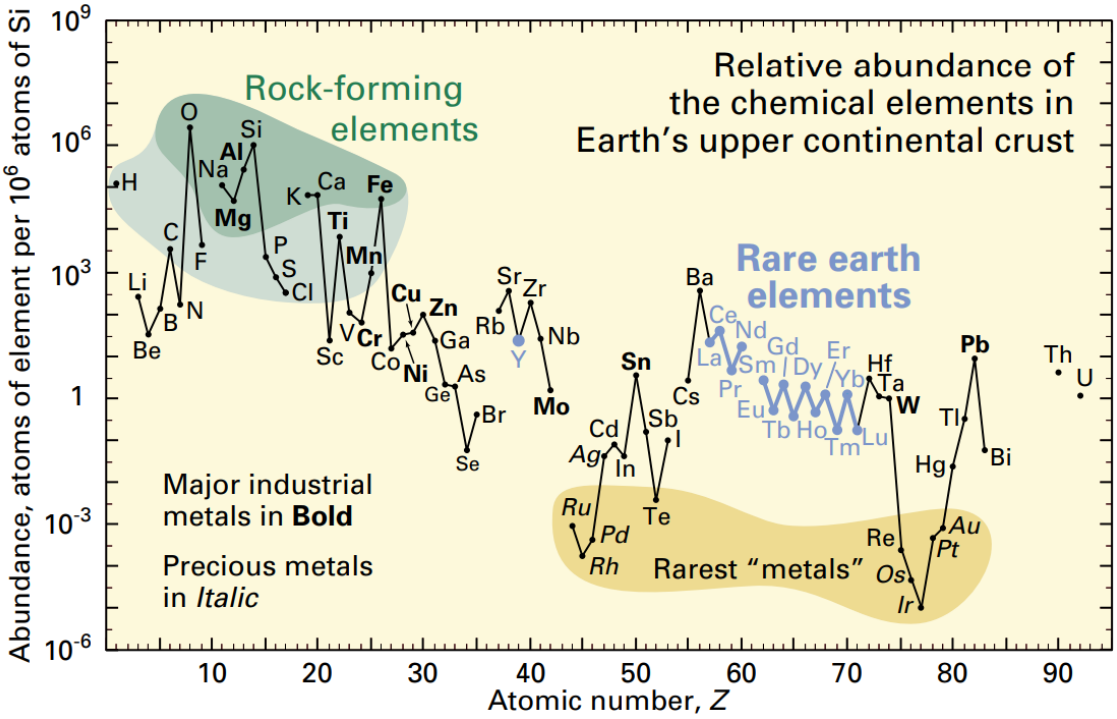

Figure 7 Figure from a fact sheet by USGS in 2002.[45] Abundance (atom fraction to 10^6 atoms of Si) of the chemical elements in Earth's upper continental crust as a function of atomic number. Many of the elements are classified into (partially overlapping) categories: (1) rock-forming elements (major elements in green field and minor elements in light green field); (2) rare earth elements (lanthanides, La–Lu, and Y; labeled in blue); (3) major industrial metals (global production > ~ 3×10^7 kg/year; labeled in bold); (4) precious metals (italic); and (5) the nine rarest "metals"—the six platinum group elements plus Au, Re, and Te (a metalloid).

1.2.3.1. Common molybdenum compounds

Considering the important compounds of Mo, the first one to be mentioned is MoS_2, a semi-conductor with the indirect band gap measured at 1.2 V. It is found on Earth in molybdenite mineral. Since its discovery in 1781 by Peter Jacob Hjlem (1746 – 1813, Swedish chemist and

mineralogist), it is widely used in industry as a lubricant as it has a lamellar and inert structure like graphite (Figure 8A). In terms of catalysis, it is used as Hydrodesulfurization (HDS) catalyst in the Co-doped or Ni-doped forms.[46] For electrochemical devices, it can serve as a material for cathode of Li-ion batteries, just like graphite.[47] The reason is not only that the lamellar structure facilitates the electron transport but also because Mo can change its form from trigonal prismatic to octahedral during the insertion of one Li atom per MoS_2 in the lattice by applying a voltage, in this case, some new phases Li_xMoS_2 are formed.[47,48] For applications in fuel cells, MoS_2 can perform to a certain extent as an ORR catalyst, not only in basic conditions[49–53] but also in acid conditions.[54,55] The ORR activity of MoS_2 is quite low compared to Pt/C, even when the particles size was reduced to ca. 2 nm.[49]

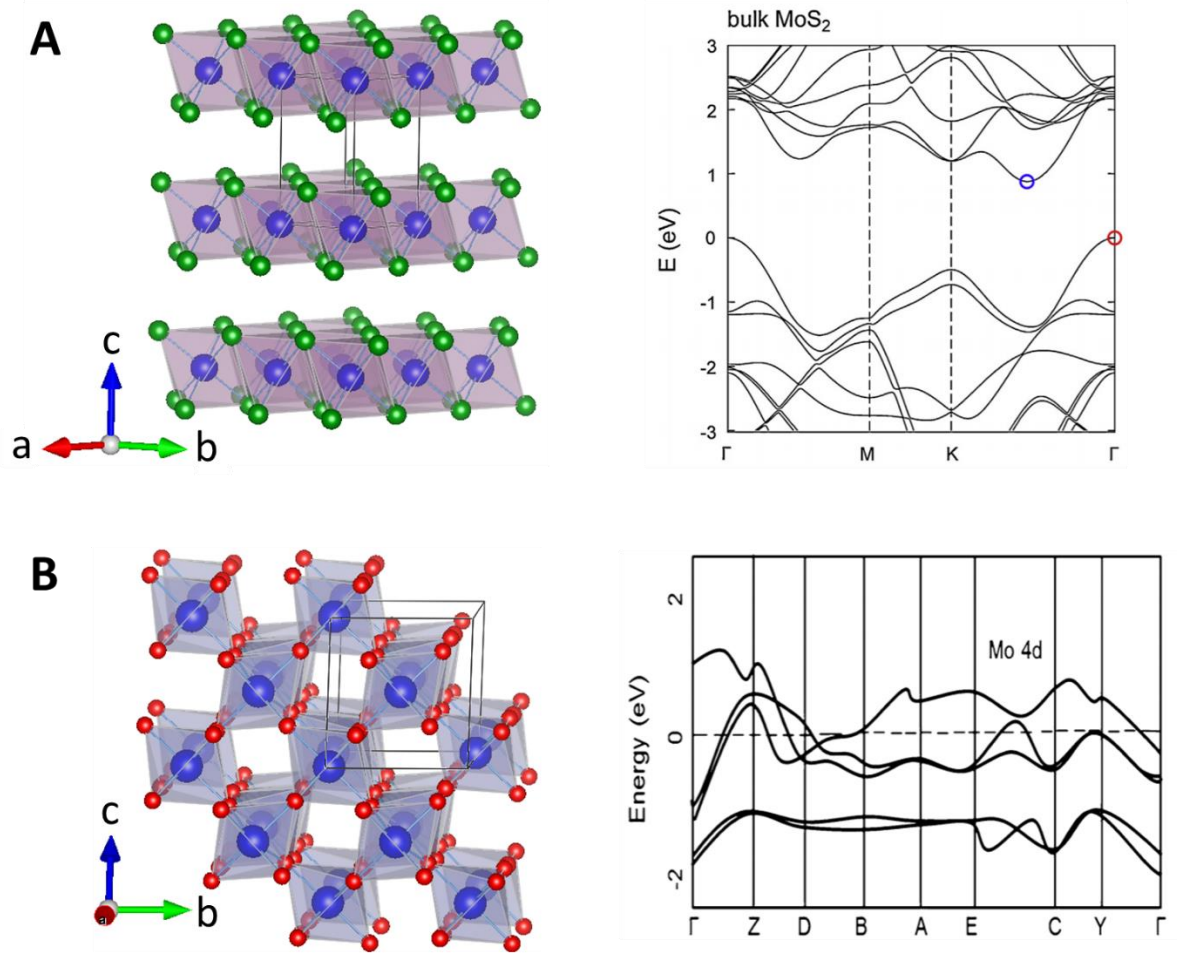

Figure 8 (A)Crystalline structure hexagonal and calculated band structure by DFT[56] of MoS_2. (B) Crystalline structure monoclinic and calculated band structure by DFT[57] of MoO_2.

Another interesting compound of Mo is MoO_2. It is remarkably stable chemically; it is soluble in neither acid nor base. Unlike MoS_2 which is a semi-conductor, MoO_2 is an especially good conductor even comparable to metals. In a recently published paper, F. Kaiser *et al.* showed

thermoelectric measurements on molybdenum oxides. They found that MoO_2 has its electrical conductivity σ of 5×10^5 S.m^{-1} at 298 K.[58] This value is very low compared to a good conductive metal like copper ($\sigma = 6 \times 10^7$ S.m^{-1})[59] but comparable to some metallic alloys such as Nichrome ($\sigma = 9 \times 10^5$ S.m^{-1}).[60] The DFT calculations of Eyert et al. established that the hybridization between Mo 4d and O 2p orbitals, the interactions between Mo 4d orbitals and their contribution to the band structure.[57] Figure 8B shows the monoclinic structure of MoO_2 and its band structure from the reference.[57] In this band structure, the Mo 4d orbitals (t_{2g} states) are degenerate with the Fermi level, which make it a conductor as a semi-metal. This is also reported by C. Zhang et al. in 2018.[61] Grace to this conductivity, it can be used as an anode in Li-ion batteries or in a solid oxide fuel cell (SOFC).[62] Also, for ORR, some researches showed that MoO_2 can perform a certain activity[61] or be a conducting template for cobalt active sites inserted at doping concentration.[63]

1.2.3.2. Molybdenum oxysulfides

1.2.3.2.1. State of the art

Now imagine that we can combine both MoS_2 and MoO_2 into an uncommon compound: oxysulfide MoO_xS_y. In these compounds, there are only Mo-O and Mo-S bonds, and no bond between O and S. Imagine that we can combine also the characteristics of both sulfides and oxides in this family of compounds: having ORR active sites like both MoS_2 (edges S-50 % and S-100 %)[64] and MoO_2 (under-coordinated Mo on surface)[61] with a conductivity like MoO_2. In fact, this family of compounds does not have a very long history compared to other common Mo compounds such as MoO_2 and MoS_2 mentioned earlier in this chapter.

The molybdenum oxysulfide was firstly known in application as an inorganic complex for lubricant: molybdenum oxysulfide dithiocarbamates. The compound and its preparation process were patented in 1967.[65] However, some chemical methods which could lead to isolable non-molecular phases MoO_xS_y were reported even earlier.[66–68]

1. Reaction of MoO_2Cl_2 with Na_2S in ethanol as given by ter Meulen in 1925:[66]

$$MoO_2Cl_2 + Na_2S \rightarrow MoO_2S + 2\ NaCl$$

2. Reaction of MoS_2 and H_2O as described by Cannon in 1961:[67]

$$MoS_2 + H_2O_{(g)} \rightarrow MoOS_2 + H_2$$

3. Thermal decomposition of $(NH_4)_2MoO_2S_2$ as proposed by Spengler and Weber in 1959[68] although the thiomolybdate was already reported in 1884 by G. Krüss *et al.*[69] This method requires a heating up to 800 to 1000 °C.

$(NH_4)_2MoO_2S_2 \rightarrow MoOS_2 + 2\ NH_3 + H_2O$

In 1978, G. Tsigdinos *et al.* attempted to reproduce these three reactions without any positive results.[66] The first method led to a mixture of unidentifiable products while the second one gave neither H_2 nor H_2S. For the last method, they believed that the amorphous product $MoOS_{1.93}$ obtained was not a mixture of MoS_3 and MoO_3 but a true transient oxysulfide.[66] This method then became one of the most popular synthesis for amorphous molybdenum oxysulfide in late 1980s and early 1990s.[70–73] In 1989, K. M. Abraham *et al.* discovered that molybdenum oxysulfide could be useful for cathode material in Li-ion batteries[70] and one year later they patented it as a material for active cathode and the preparation process based on the thermal decomposition of ammonium mono- and di-thiomolybdate.[74] They probably saw a future for molybdenum oxysulfide in energy industry! During the next few years, they pursued the research on the structure and the behavior of material in Li-ion batteries. The results of structural analysis and on the mechanism of thermal decomposition by Fourier Transform Infrared Spectroscopy (FTIR) were showed in 1993.[72] They described molybdenum oxysulfides as a 2D polymer with the structure of monomer changed in function of decomposition temperature (Figure 9A). Each monomer in any case contained two Mo atoms linking to each other by O-bridging, the S atoms could link to one or two Mo atoms as a bridge. They claimed that the higher the decomposition temperature is, the closer the obtained composition is to $MoOS_2$. Hence, the formation of oxysulfide phases was considered at the temperature as high as 300 °C via a condensation-polymerization reaction involving the molybdate and thiomolybdate in solid state (Figure 9A).[72]

The compositions of resulting oxysulfides at different decomposition temperatures were found to be different, hence, the capacities of Li insertion were different too. The highest capacity was found to be for the product of the decomposition at 300 °C.[71] For instance, all the works based on the thermal decomposition of thiomolybdate found are quite brief on structural analysis and principally on the application in Li-ion batteries. With the promising results in applications, they stated that the further studies on the structure and properties of molybdenum oxysulfides should be pursued.

From mid 1990s, another new method was introduced: Radio Frequency magnetron sputtering (physical vapor deposition – PVD). To our knowledge, this method was first reported by E. Schmidt *et al.* in 1994[75] to find a new material for solid-state Li-ion microbatteries.[73] They also investigated the thin films' physical properties and their local structure by X-ray absorption spectroscopy (XAS), X-ray photoelectron spectroscopy (XPS) and IR analysis.[76] By PVD, the oxysulfides formed were amorphous, homogeneous and had a semi-conducting behavior similar to MoS_2, this led to their assumption of crystalline structure similarity between molybdenum oxysulfide and molybdenum disulfide.[73] In terms of local structure, the results suggested three different local environment of Mo, i.e. sulfur-like as in the 2H-MoS_2, oxygen-like as in MoO_2 or MoO_3 and mixed environment of oxygen and sulfur (S^{2-} and S_2^{2-}).[76] However, this did not lead yet to a structural model proposition. By the same method, molybdenum oxysulfide on thin films for Li-ion batteries was fabricated and analyzed later by different groups.[77–83] Still, no structural model was proposed after all.

In 2000s, a "softer" way was tested to synthesize molybdenum oxysulfide: in solution, without heating. P. Afanasiev *et al.* reported the synthesis of molybdenum oxysulfide by precipitation from water-acetone solutions for the first time in 2003.[84] The results showed vesicle-like and tubular morphologies of the particles due to the micelle effect. This kind of morphology clearly increases the specific surface of the material, which increases also the contact with other substance around, i.e. a good characteristic for a catalyst in general.[84] The local structure was also analyzed by XAS, XPS and IR. The results of Extended X-ray Absorption Fine Structure (EXAFS) analysis at Mo K-edge showed that in the first shell of Mo atom, there are 1 O atom and 4 S atoms. Combining with the results of other methods, they proposed a structure of oligomer for molybdenum oxysulfide, where each Mo atom linked to the O atom by a double bond and all S atoms were bridges (Figure 9B).[84] Later, D. Genuit continued this work with the same structure proposition (Figure 9C) and proposed a way to make a hydrotreating catalyst from molybdenum oxysulfide.[85] Since then, no other paper was found concerning the same or other synthesis in solution.

Table 1 Summary of molybdenum oxysulfides syntheses in literature.

Year	Authors	Synthesis conditions	Oxysulfide confirmed?	Ref.
1925	ter Meulen	$MoO_2Cl_2 + Na_2S \rightarrow MoO_2S + 2\ NaCl$ In absolute ethanol	Rejected by G. Tsigdinos *et al.* in 1978	66, 68
1959	Spengler and Weber	$(NH_4)_2MoO_2S_2 \rightarrow MoOS_2 + 2\ NH_3 + H_2O$ Heating up to 800 to 1000 °C	Product confirmed as $MoOS_{1.93}$ by G. Tsigdinos *et al.* in 1978	66, 68, 69
1961	Cannon	$MoS_2 + H_2O_{(g)} \rightarrow MoOS_2 + H_2$ Heating up to 500 °C	Rejected by G. Tsigdinos *et al.* in 1978	66 – 68
1989 to 1993	K. M. Abraham *et al.*	$(NH_4)_2MoO_2S_2 \rightarrow MoOS_2 + 2\ NH_3 + H_2O$ $(NH_4)_2MoO_3S \rightarrow MoO_2S + 2\ NH_3 + H_2O$ Heating up to 300 °C	$MoO_{1.2}S_{1.7}$ $MoO_{1.7}S_{0.95}$ Amorphous, no proof of structure Patented in 1990	70, 74
		$(NH_4)_2MoO_2S_2 \rightarrow MoOS_2 + 2\ NH_3 + H_2O$ Heating up to 380 °C	Structure studied by FTIR Mechanism proposed Oxysulfide formed from 300 °C	71, 72
1994 to 1995	E. Schmidt *et al.*	Radio Frequency magnetron sputtering (physical vapor deposition – PVD) Target made of pressed MoS_2 powder. O_2 is introduced in the chamber (pressure before deposition of 10^{-5} Pa) by a leak-valve.	Thin films Structure studied by FTIR, XPS and EXAFS	73, 75, 76

		Sputtering conditions: a power density of 2.3 $W.cm^{-2}$ at a frequency of 13.56 MHz, 1 Pa of argon at rt. and a target-substrate distance of approximately 70 mm. The average sputtering rate was about 130 $A.min^{-1}$.		
2003	P. Afanasiev *et al.*	Precursors: $(NH_4)_2Mo_2S_{12}$ or $(NH_4)_6Mo_7O_{24}{\cdot}4H_2O + (NH_4)_2S$ Precipitation in water-acetone solution (colloidal) in presence of HCl	Amorphous Structure studied by EXAFS, XPS, IR, UV-Vis, SEM Structure proposed as oligomers	84 – 85

In terms of hydrotreating catalysis, as mentioned above, MoS_2 was widely used in petrol industry for HDS reaction for years. One of the ways to prepare the catalyst is the reduction of MoO_3 by H_2S. In 1935, Gaelle and Michelitsch stated that during this process, molybdenum oxysulfides were formed, which led to a catalyst not well defined.[86] In 1949, in a paper, E. Badger *et al.* declined this statement and claimed that the final product was a mixture of MoO_2 and MoS_2, together in an amorphous solid.[86] This hypothesis turned out untrue when other research groups confirmed the oxysulfide intermediates during sulfidation of MoO_3 by the same or different method.[87–89] T. Weber *et al.* studied the sulfidation of MoO_3 by H_2S with a proposed mechanism, confirming the formation of molybdenum oxysulfide as intermediates during the reaction at around 150 – 200 °C by XPS and IR analyses (Figure 9D).[87] Although, the formation of molybdenum oxysulfide in this case was far from the thermodynamic equilibrium. The molybdenum oxysulfide layer on the surface of some catalysts during some reactions were even considered as the active sites and the reason for a better catalytic activity for different organic reactions.[90–92]

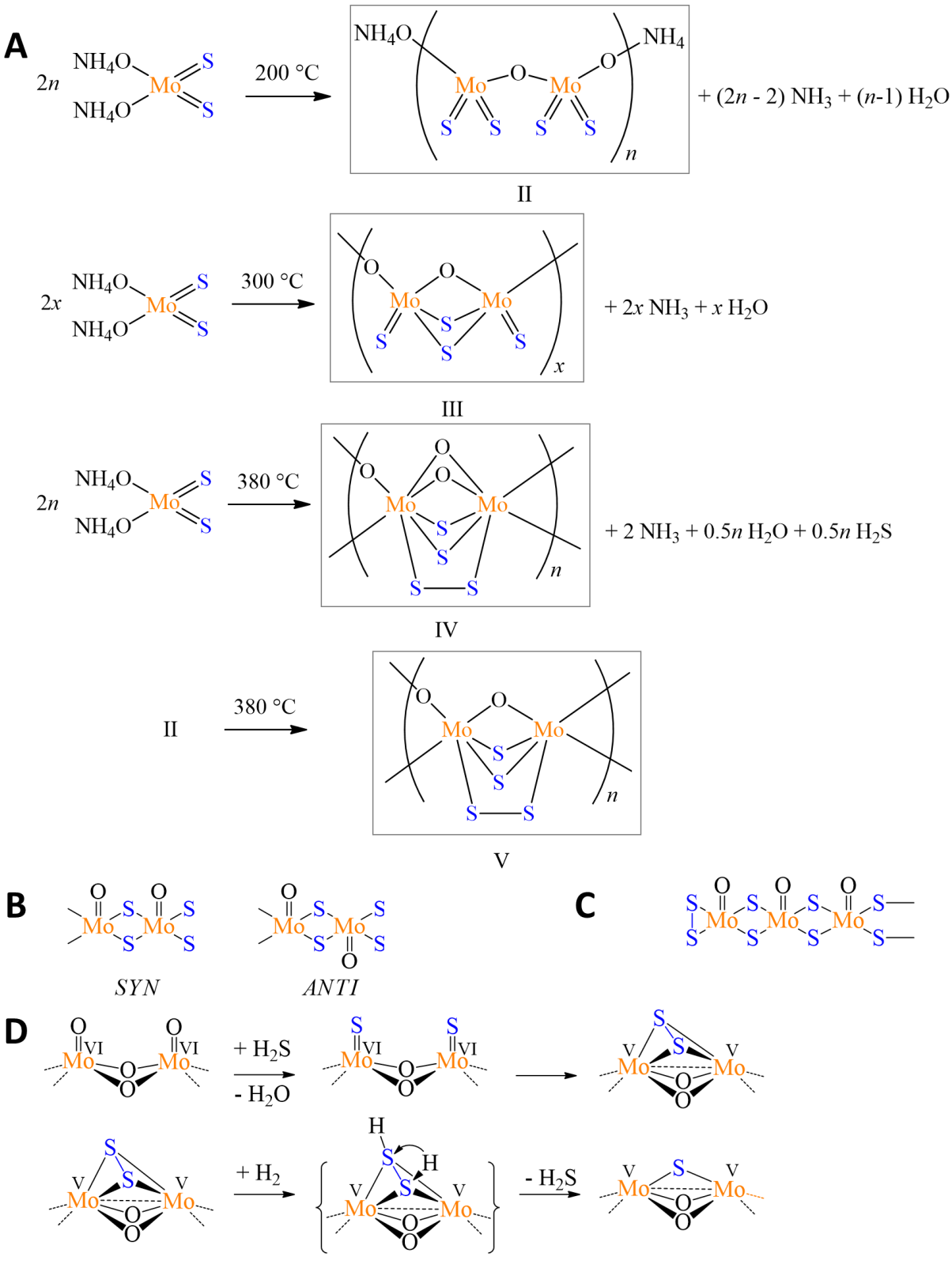

Figure 9 (A) Mechanism of thermal decomposition and structure propositions from K. M. Abraham et al.[72] (B) Structure proposition from P. Afanasiev et al.[84] (C) Structure proposition from D. Genuit et al.[85] (D) Mechanism of sulfidation of MoO_3 to obtain MoS_2 structure propositions for oxysulfide intermediates from T. Weber et al.[87] All reactions are exactly

reconstructed from the references. Molybdenum atoms are highlighted in orange and sulfur atoms are highlighted in blue.

A recent work of A. Rochet *et al.* on HDS Mo-based catalysts using Quick-XAS at Synchrotron SOLEIL observed the intermediates of oxysulfides during the catalysts preparation.[93] In this article, they proposed an extraction of components from the catalysts' EXAFS spectra. One of the four components during the preparation of Mo/Al_2O_3 catalyst was confirmed by EXAFS calculations that it contained Mo–Mo distances (at ~2.85 Å) characterizing the oxysulfide. However, because of the lack of complementary information on the chemical nature of sulfur ligands forming the oxysulfide species, they could not propose any structural model yet.[93] Nevertheless, this complete work demonstrated a very powerful tool to investigate catalysts under realistic conditions, which we can apply to our own work (in collaboration with beamline scientists).

For other electrochemical reactions like Hydrogen Evolution Reaction (HER), molybdenum oxysulfide sites are also claimed to be intermediates during the reduction process of protons.[94] Lately, another work stated that $Mo_xS_yO^-$ clusters formed on the surface of MoS_2 during the electrochemical reaction (HER) might favor the H_2 insertion.[95]

Independently, in the Handbook of Inorganic Substances edition 2017, two other molybdenum oxysulfides $MoS_{0.12}S_{1.88}$ and $Mo_4S_{0.42}O_{10.56}$ were listed.[96] $MoS_{0.12}S_{1.88}$ was reported to be reddish and has the prototype of VO_2/Pearson symbol mP12 (monoclinic)/Space group 14. $Mo_4S_{0.42}O_{10.56}$ was reported to be bluish dark and has the prototype of Mo_4O_{11}/ Pearson symbol oP60 (orthorhombic)/Space group 33. However, to the best of our knowledge, synthesis and structural features tend to be discussed in separated works: the literature on this topic is difficult to grasp.

1.2.3.2.2. Oxysulfides synthesis from our viewpoint

Though molybdenum oxysulfides are uncommon, it does not mean that other metal oxysulfides were not seen elsewhere. Synthesis of lanthanide oxysulfides nanoparticles is very well described and even already in applications in many domains.[97] In a recent review on metal oxysulfides, C. Larquet et S. Carenco detailed numerous synthesis methods of Ln_2O_2S, from solid state to molten salt and in solution (both in water and in organic solvents). To favor the nanoscaled materials, soft conditions should be considered, here, in solution.[97] Under soft conditions, mild temperatures and small grain size can unlock metastable structures. Also, diffusion processes are much faster over nanometric distances and lead to efficient substitution

reactions with nanoscaled materials.[97] Hence, energy input by heating needs to be limited to prevent the excessive growth and sintering, i.e. to keep the particles at nanoscale.

In our group, we have been working on $Gd_{2(1-y)}Ce_{2y}O_2S$ ($0 \leq y \leq 1$) for five years. The synthesis is carried out **in colloidal solution** with organic solvent (1-octadecene) and organic long-chained stabilizers (oleic acid). This method requires a much lower heating temperature (310 °C) than thermal decomposition (usually 600 – 1300 °C)[97] and the organic long-chained stabilizers in the solution stabilize the surface of nanoparticles to keep them totally at nanoscale. This synthesis protocol is well-described and well-controlled to make lanthanide oxysulfide nanoparticles not only by our groups but also others,[98] it will be explained more in detailed in the next part of this chapter. Hence, this is a good starting point for our new research direction, even if the chemistry of d-block metals is fairly different.

Unlike for lanthanide oxysulfides, the synthesis of transition metal oxysulfides is very challenging due to the large radius difference between O(-II) (1.26 Å) and S(-II) (1.70 Å) associated with different affinities to metals. For molybdenum in particular, as mentioned above, there are not yet many researches. The synthesis methods, considering only the chemical ones, produced only unwell-identified amorphous molybdenum oxysulfide, despite interesting porous structure and promising possible applications. As we have a good background knowledge on other well-known Gd_2O_2S-based oxysulfides,[99–104] it is very encouraging for us to apply the same method to make molybdenum oxysulfides at nanoscale which are electrochemically active. By using molecular precursors, heating at low temperature, adding organic ligands, we expect to have nanoparticles of molybdenum oxysulfides that have never been preceded.

2. Research initiatives and practical conditions

2.1. Research initiatives

To our knowledge until this moment, there is no other study on molybdenum oxysulfide based on the same synthesis as Gd_2O_2S in organic solution, which will be detailed in the next part of this chapter.[99]

Scheme 1 shows our project initiatives. To start the project, the study of synthesis and the characterizations on Mo-containing Gd_2O_2S-based nanoparticles was conducted. As there is no preceding work on molybdenum oxysulfide nanoparticles made in colloidal organic solution

and the chemistry of d-block metals is way different from that of lanthanide, the synthesis based on Gd_2O_2S needed to be adapted and optimized to control the structure of Mo-containing products. Along with the practical work on the synthesis, different analysis methods were used to understand the structure of Mo-containing products and also to evaluate the modification of initial synthesis, such as Energy Dispersive Spectroscopy (EDS) for the compositions, X-ray Diffraction (XRD) for the crystalline structures and Transmission Electron Microscopy (TEM) for the morphologies.

The introduction of Mo in the Gd_2O_2S system can be done by two ways in one pot: in a one-step protocol where all precursors are added at the same time (similar to $(Gd_{1-y}Ce_y)_2O_2S$ $(0 \leq y \leq 1)$ synthesis[99]) or in a two-step protocol where Mo precursor is added to freshly prepared and unwashed Gd_2O_2S nanoparticles. The products obtained by these two methods were totally different (based on EDS, XRD and TEM results), as will be exposed in the following chapters. The first question that we need to answer is whether the products are still nanoscaled as Gd_2O_2S nanoparticles and the structure of products made by each method. As the Mo-containing materials have not been described before, the routine characterization methods are not enough to fully understand the structure of the products of the syntheses. For this reason, further analysis (e.g. XAS, XPS) was performed through collaborations. A further study can be carried on with the same synthesis method without any Gd precursor added. This is new and would be interesting as the results are unpredictable due to the difference of chemistry between transition metals and lanthanides.

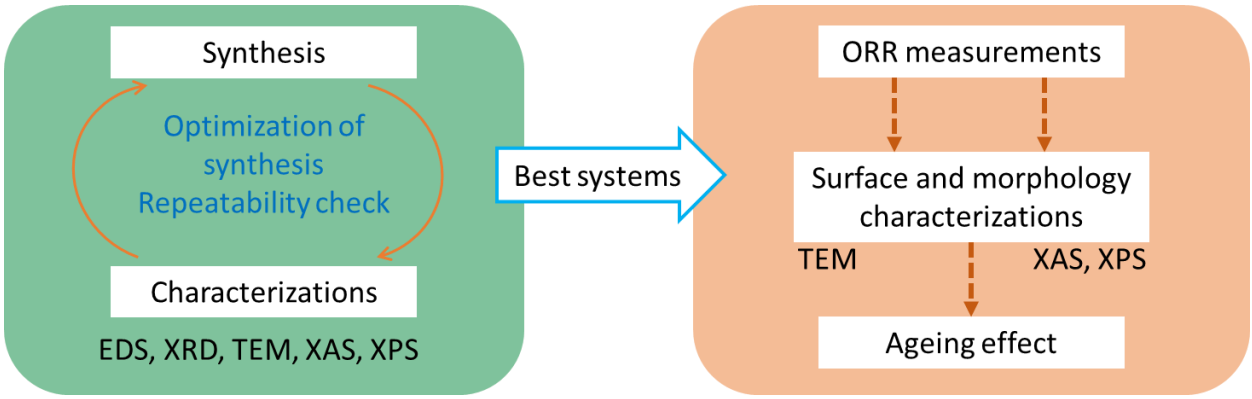

Scheme 1 Our project initiatives.

We consider the system that we understand the most and we control the best as the most valuable one. The samples with this system will be tested for Oxygen Reduction Reaction (ORR) to investigate their activity. Before measuring the performance in electrocatalysis, their stability, etc., the activity is investigated *ex situ* in our laboratory. Then, further analysis will

be done to understand more about the structure and also the mechanism of the electrochemical reaction in presence of the materials using *operando* measurements. Finally, the study of ink's ageing effect on the structure and morphology of nanoparticles will be considered. At this stage, the second question to answer is whether the Mo-containing nanoparticles have activity towards O_2 and what is the relation between the structure (crystalline and local) of these nanoparticles and the activity if there is any.

To answer these two questions is to propose a structural model of molybdenum oxysulfide as nanoparticles.

2.2. Preliminary results and discussion on the synthesis initiatives

2.2.1. Gd_2O_2S-based system: substitution of Gd by Ce in the structure

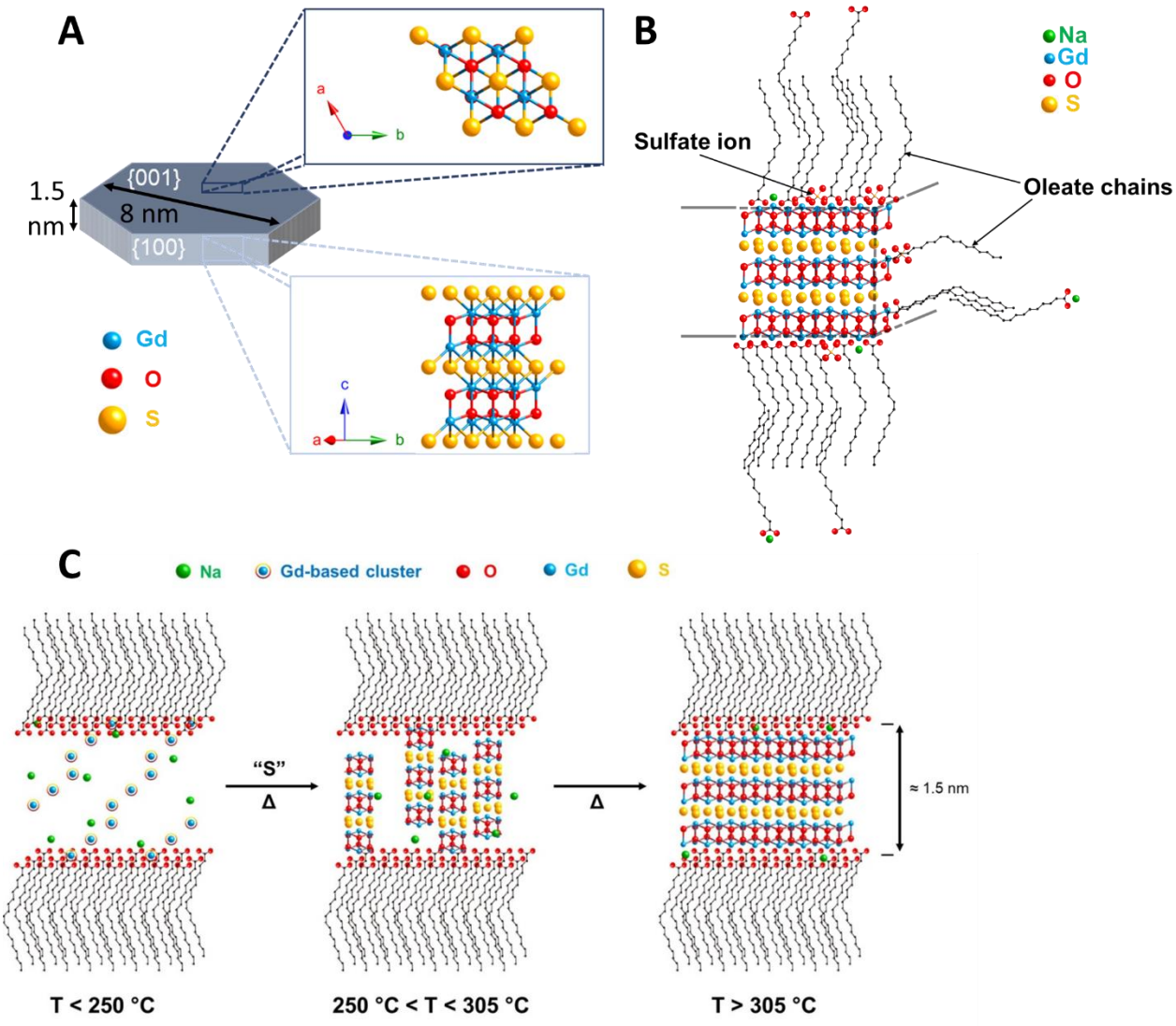

Figure 10 (A) Nanoplate morphology of Gd_2O_2S with the average sizes and illustrated crystalline structure, figure from C. Larquet's thesis.[101] *(B) Illustration of organic ligands and*

how they structure on the surface of nanoparticles, figure from C. Larquet's thesis.[101] *(C) Proposed formation mechanism of* Gd_2O_2S.[104]

As we start from the base of Gd_2O_2S, we need to understand as much as possible its structure and characteristics. Since more than five years, in our group, the nanoparticles of Gd_2O_2S with or without Ce were studied on all aspects: the formation, the structure, the morphology and the toxicology for applications, etc. In terms of morphology, the nanoparticles are in the shape of hexagonal nanoplatelets of about 8 nm wide and about 1.5 nm thick. They have the lamellar structure with Gd in coordination 7: each Gd links with 4 O and 3 S (Figure 10A).[99] This structure is quite common for lanthanide oxysulfides due to the similar crystal radii (ranging from $r_{La(+III)} = 1.24$ Å to $r_{Lu(+III)} = 1.00$ Å) and the similar oxidation states available.[98] Also, we understand the formation mechanism of Gd_2O_2S[104] which conducts to nanoparticles with a significant organic ligands amount on their surface (Figure 10B). This quantity was measured as about 30 wt% to the total mass of the sample.[103] This plays a major role on the dispersion of nanoparticles in different types of solvent, hence, in the ink making for electrochemical tests in our own work. The proposed formation mechanism **in colloidal solution** can be explained simply as: (1) the formation of a mesophase from sodium oleate chains, which "shapes" the particles later, (2) the clusters are formed between 250 °C and 305 °C, (3) the nanoparticles are finished between 305 °C and 310 °C.[104] This understanding gives an advantage to understand the structure and how the nanoparticles are formed when Mo precursors are added.

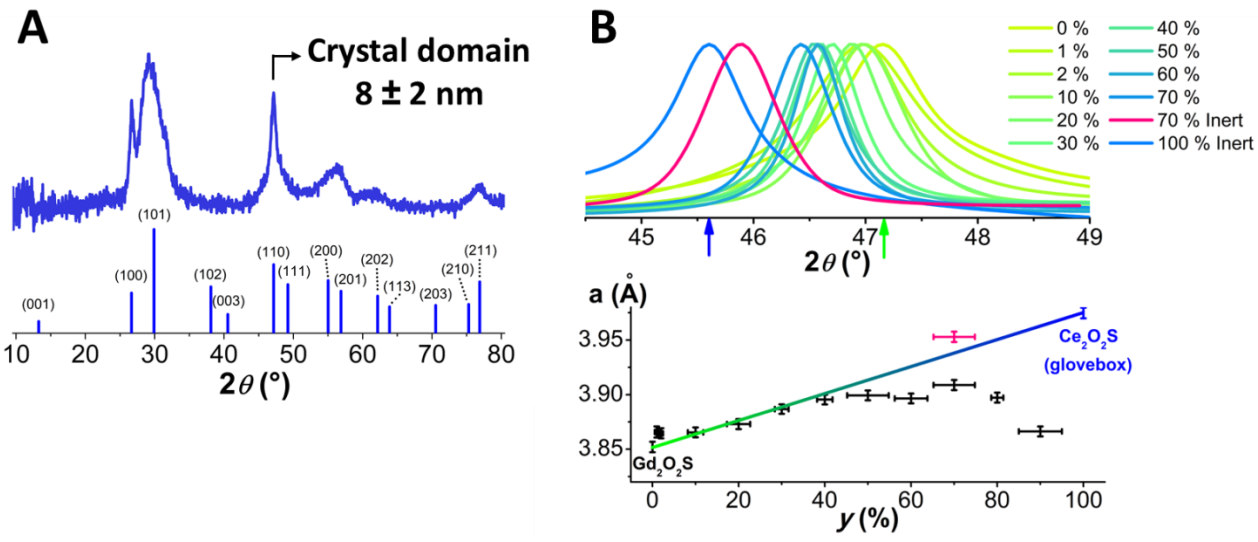

Figure 11 (A) Diffractograms of Gd_2O_2S *with theoretical peak positions. (B) Fit of peaks (110) and the application of Vegard's law on the data set.*[99] *y is the percentage of Ce introduced as well as the percentage of Gd substituted by Ce from initial* Gd_2O_2S *phase.*

In terms of multimetallic nanoparticles where random Gd sites in Gd_2O_2S are substituted by another cation, the team studied in detail the substitution Gd by Ce for the magnetic characteristics of $(Gd_{1-y}Ce_y)_2O_2S$ $(0 \leq y \leq 1)$.[100] This substitution can be made easily as the difference of crystal ionic radii between Gd(+III) and Ce(+III) with the same coordination 7 is only 6 % of $r_{Gd(+III)}$ ($r_{Gd(+III)}$ = 1.14 Å; $r_{Ce(+III)}$ = 1.21 Å, data in Table 2). This substitution can be detected and confirmed by XRD and interpreted with the Vegard's law. This law explains the linear relation between the lattice constant and the ratio of substitution. In the case of Gd-Ce, the peak (110) was used for this analysis, not only because it gives access to the lattice parameter *a*, but also because it is the thinnest peak in the diffractograms of Gd_2O_2S-based phases (Figure 11A). Figure 11B shows the positions of peak (110) of samples series $(Gd_{1-y}Ce_y)_2O_2S$ $(0 \leq y \leq 1)$ (converted to % in the figure), and the value of lattice constant *a* (Å) in function of *y* (%). The linear relation is only satisfied for $y \leq 40$; for higher *y* the Vegard's law is not followed anymore. The reason was found to be the change of oxidation state of Ce from +III to +IV which leads to the change of the crystalline structure. In the case where Ce_2O_2S was kept in the glovebox, under inert atmosphere, the Vegard's law was verified.[99]

2.2.2. Possibility of Mo insertion in Gd_2O_2S structure

Back to our project where we want to introduce Mo in the Gd_2O_2S structure in the same way as the introduction of Ce in this structure, there are several differences that complicate the situation. Firstly, molybdenum is a transition metal, logically its characteristics are far from the lanthanides because of different kinds of valence electrons. Next, the large difference of atomic number causes also a large difference of crystal radius. Considering the same oxidation state of +III for both metals, the crystal radius difference is 0.31 Å ($r_{Gd(+III)}$ = 1.14 Å; $r_{Mo(+III)}$ = 0.83 Å, data in Table 2). There are two possibilities: possible substitution Gd-Mo or no substitution at all. The second case is much more likely as the difference is too large, the crystal could shrink too much if some Gd sites are substituted by Mo. Considering the same coordination 7 for both metals, only Mo(+VI) is possible. The crystal radius difference is now slightly smaller ($r_{Gd(+III)}$ = 1.14 Å; $r_{Mo(+VI)}$ = 0.87 Å, data in Table 2) but the difference of charge is now much more difficult to overcome. It may be even harder in this case to have a Gd-Mo substitution. In any case, the utilization of Vegard's law can reveal which possibility is true.

Table 2 Radius of concerning ions with comparable coordination number.[105]

Ions	Coordination number	Ionic radius in crystal (Å)
Gd(+III)	VII	1.14
Ce(+III)	VII	1.21
Mo(+VI)	VII	0.87
Mo(+III)	VI	0.83

In short, a structure with Gd_2O_2S base where a number of random Gd sites are substituted by Mo appears to be very difficult to obtain. In the literature, we did not find any bimetallic Mo-Gd oxysulfide. As theoretically, a substitution Gd-Mo in Gd_2O_2S appears to be unlikely, we headed towards Mo-containing Gd_2O_2S-like nanoparticles by doping the surface of nanoparticles with Mo. In order to favor the formation of this kind of materials, we developed two protocols in one step or two steps, always based on the initial synthesis of Gd_2O_2S. In the one-step protocol (Scheme 2A), all the precursors are added at the same time before heating. In the two-step protocol (Scheme 2B), Gd_2O_2S is formed in the first step, then Mo precursor is added to these freshly formed, unwashed nanoparticles and reheated for the second step.

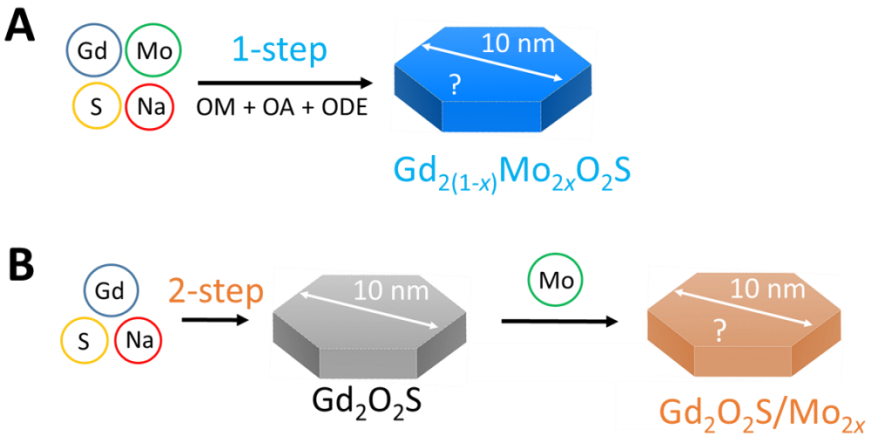

Scheme 2 Two ways toward Mo-containing nanoparticles synthesis, based on Gd_2O_2S synthesis: (A) protocol in one step and (B) protocol in two steps.

To understand the products, characterizations will be done for crystalline structure, elemental compositions and morphology directly in our laboratory. In terms of local structure, we now

have for the possibility to measure XRD on a wide angular range and use the Pair Distribution Function analysis (PDF) to exploit also the X-ray diffusion in plus, thanks to the expertise of Capucine Sassoye and Mohamed Selmane at Laboratoire de la Chimie de la Matière Condensée de Paris (LCMCP). Moreover, we have the possibility to measure the products by spectroscopies at SOLEIL Synchrotron: this will give us not only supplementary information on local structure but also the information of oxidation state of Mo. Regarding spectroscopy of Mo, there are many articles since 100 years on oxidation states in different compounds of Mo which can serve as reference to the actual analysis.

Even though this project is considered as very hard as we are linking two very different chemistries (d-block metals and lanthanide structure), it is still very interesting to discover new materials and maybe find a useful application with them. With our knowledge on the basic system of Gd_2O_2S and with all the possible collaborations, we will surely get to have sweet fruits at the end of the project.

3. References

(1) Totten, G. E. In Context a Time of Highlights from the Histories of ASTM Committee D02 and the Petroleum Industry. *Stand. News* **2004**, *32* (6).

(2) Hall, C.; Tharakan, P.; Hallock, J.; Cleveland, C.; Jefferson, M. Hydrocarbons and the Evolution of Human Culture. *Nature* **2003**, *426* (6964), 318–322. https://doi.org/10.1038/nature02130.

(3) Martins, F.; Felgueiras, C.; Smitkova, M.; Caetano, N. Analysis of Fossil Fuel Energy Consumption and Environmental Impacts in European Countries. *Energies* **2019**, *12* (6), 1–11. https://doi.org/10.3390/en12060964.

(4) Stephens, E.; Ross, I. L.; Mussgnug, J. H.; Wagner, L. D.; Borowitzka, M. A.; Posten, C.; Kruse, O.; Hankamer, B. Future Prospects of Microalgal Biofuel Production Systems. *Trends Plant Sci.* **2010**, *15* (10), 554–564. https://doi.org/10.1016/j.tplants.2010.06.003.

(5) Ritchie, H. How long before we run out of fossil fuels? https://ourworldindata.org/how-long-before-we-run-out-of-fossil-fuels (accessed May 11, 2020).

(6) *BP Statistical Review of World Energy 2019*; 2019.

(7) Watkins, S. Why Saudi Arabia Will Lose The Next Oil Price War https://oilprice.com/Energy/Energy-General/Why-Saudi-Arabia-Will-Lose-The-Next-Oil-Price-War.html (accessed Jun 11, 2020).

(8) Central Bank, E. *Economic Bulletin Article: Forecasting the Price of Oil*; 2015.

(9) Hamilton, J. D. *Causes and Consequences of the Oil Shock of 2007-08*; 2009.

(10) Warshay, M.; Prokopius, P. R. The Fuel Cell in Space: Yesterday, Today and Tomorrow. *J. Power Sources* **1990**, *29* (1–2), 193–200. https://doi.org/10.1016/0378-7753(90)80019-A.

(11) Dekel, D. R. Review of Cell Performance in Anion Exchange Membrane Fuel Cells. *J. Power Sources* **2018**, *375*, 158–169. https://doi.org/10.1016/j.jpowsour.2017.07.117.

(12) *2011 Fuel Cell Technologies*; 2012.

(13) Hydrogen Council. *Path to Hydrogen Competitiveness A Cost Perspective*; 2020.

(14) Chen, Z.; Li, P.; Anderson, R.; Wang, X.; Zhang, X.; Robison, L.; Redfern, L. R.; Moribe, S.; Islamoglu, T.; Gómez-Gualdrón, D. A.; et al. Balancing Volumetric and Gravimetric Uptake in Highly Porous Materials for Clean Energy. *Science (80-.).* **2020**, *368* (6488), 297–303. https://doi.org/10.1126/science.aaz8881.

(15) Longest remote-controlled (RC) model multicopter flight (duration) https://www.guinnessworldrecords.com/world-records/longest-rc-model-multicopter-flight-(duration) (accessed May 11, 2020).

(16) Yoon-seung, K. S. Korea to install hydrogen charging stations without delay https://en.yna.co.kr/view/AEN20191021006900320 (accessed May 11, 2020).

(17) Thomas, C. E. Fuel Cell and Battery Electric Vehicles Compared. *Int. J. Hydrogen Energy* **2009**, *34* (15), 6005–6020. https://doi.org/10.1016/j.ijhydene.2009.06.003.

(18) Pivovar, B. Catalysts for Fuel Cell Transportation and Hydrogen Related Uses. *Nat. Catal.* **2019**, *2* (7), 562–565. https://doi.org/10.1038/s41929-019-0320-9.

(19) Banham, D.; Ye, S. Current Status and Future Development of Catalyst Materials and Catalyst Layers for Proton Exchange Membrane Fuel Cells: An Industrial Perspective. *ACS Energy Lett.* **2017**, *2* (3), 629–638. https://doi.org/10.1021/acsenergylett.6b00644.

(20) Fuelcellstore - Catalyst https://www.fuelcellstore.com/fuel-cell-components/catalyst (accessed May 12, 2020).

(21) Umicore - Products https://pmc.umicore.com/en/products?tax_application[]=Fuel+Cells (accessed May 12, 2020).

(22) Kulkarni, A.; Siahrostami, S.; Patel, A.; Nørskov, J. K. Understanding Catalytic Activity Trends in the Oxygen Reduction Reaction. *Chem. Rev.* **2018**, *118* (5), 2302–2312. https://doi.org/10.1021/acs.chemrev.7b00488.

(23) Seh, Z. W.; Kibsgaard, J.; Dickens, C. F.; Chorkendorff, I.; Nørskov, J. K.; Jaramillo, T. F. Combining Theory and Experiment in Electrocatalysis: Insights into Materials Design. *Science (80-.).* **2017**, *355* (6321), eaad4998. https://doi.org/10.1126/science.aad4998.

(24) Wei, C.; Rao, R. R.; Peng, J.; Huang, B.; Stephens, I. E. L.; Risch, M.; Xu, Z. J.; Shao-Horn, Y. Recommended Practices and Benchmark Activity for Hydrogen and Oxygen Electrocatalysis in Water Splitting and Fuel Cells. *Adv. Mater.* **2019**, *31* (31), 1–24. https://doi.org/10.1002/adma.201806296.

(25) Sealy, C. The Problem with Platinum. *Mater. Today* **2008**, *11* (12), 65–68. https://doi.org/10.1016/S1369-7021(08)70254-2.

(26) Ren, X.; Lv, Q.; Liu, L.; Liu, B.; Wang, Y.; Liu, A.; Wu, G. Current Progress of Pt and Pt-Based Electrocatalysts Used for Fuel Cells. *Sustain. Energy Fuels* **2019**, *4* (1), 15–30. https://doi.org/10.1039/c9se00460b.

(27) Wang, X. X.; Swihart, M. T.; Wu, G. Achievements, Challenges and Perspectives on Cathode Catalysts in Proton Exchange Membrane Fuel Cells for Transportation. *Nat. Catal.* **2019**, *2* (7), 578–589. https://doi.org/10.1038/s41929-019-0304-9.

(28) Tian, X.; Zhao, X.; Su, Y. Q.; Wang, L.; Wang, H.; Dang, D.; Chi, B.; Liu, H.; Hensen, E. J. M.; Lou, X. W.; et al. Engineering Bunched Pt-Ni Alloy Nanocages for Efficient Oxygen Reduction in Practical Fuel Cells. *Science (80-.).* **2019**, *366* (6467), 850–856. https://doi.org/10.1126/science.aaw7493.

(29) Garlyyev, B.; Kratzl, K.; Rück, M.; Michalička, J.; Fichtner, J.; Macak, J. M.; Kratky, T.; Günther, S.; Cokoja, M.; Bandarenka, A. S.; et al. Optimizing the Size of Platinum Nanoparticles for Enhanced Mass Activity in the Electrochemical Oxygen Reduction Reaction. *Angew. Chemie - Int. Ed.* **2019**, *58* (28), 9596–9600. https://doi.org/10.1002/anie.201904492.

(30) Tang, H.; Chen, W.; Wang, J.; Dugger, T.; Cruz, L.; Kisailus, D. Electrocatalytic N-Doped Graphitic Nanofiber – Metal/Metal Oxide Nanoparticle Composites. *Small* **2018**, *14* (11), 1–9. https://doi.org/10.1002/smll.201703459.

(31) Gonell, F.; Sanchez-Sanchez, C. M.; Vivier, V.; Méthivier, C.; Laberty-Robert, C.; Portehault, D. Structure-Activity Relationship in Manganese Perovskite Oxide Nanocrystals from Molten Salts for Efficient Oxygen Reduction Reaction Electrocatalysis. *Chem. Mater.* **2020**, acs.chemmater.0c00681. https://doi.org/10.1021/acs.chemmater.0c00681.

(32) Tavakkoli, M.; Flahaut, E.; Peljo, P.; Sainio, J.; Davodi, F.; Lobiak, E. V.; Mustonen, K.; Kauppinen, E. I. Mesoporous Single-Atom-Doped Graphene-Carbon Nanotube Hybrid: Synthesis and Tunable Electrocatalytic Activity for Oxygen Evolution and Reduction Reactions. *ACS Catal.* **2020**, 4647–4658. https://doi.org/10.1021/acscatal.0c00352.

(33) Zhang, X.; Xia, Z.; Li, H.; Yu, S.; Wang, S.; Sun, G. The Mechanism and Activity of Oxygen Reduction Reaction on Single Atom Doped Graphene: A DFT Method. *RSC Adv.* **2019**, *9* (13), 7086–7093. https://doi.org/10.1039/c9ra00167k.

(34) Yang, L.; Cheng, D.; Xu, H.; Zeng, X.; Wan, X.; Shui, J.; Xiang, Z.; Cao, D. Unveiling the High-Activity Origin of Single-Atom Iron Catalysts for Oxygen Reduction Reaction. *Proc. Natl. Acad. Sci. U. S. A.* **2018**, *115* (26), 6626–6631. https://doi.org/10.1073/pnas.1800771115.

(35) Liu, J.; Jiao, M.; Lu, L.; Barkholtz, H. M.; Li, Y.; Jiang, L.; Wu, Z.; Liu, D. J.; Zhuang, L.; Ma, C.; et al. High Performance Platinum Single Atom Electrocatalyst for Oxygen Reduction Reaction. *Nat. Commun.* **2017**, *8* (May), 1–9. https://doi.org/10.1038/ncomms15938.

(36) Didier Astruc. *Organometallic Chemistry and Catalysis*; Springer Berlin Heidelberg: Berlin, Heidelberg,

2007. https://doi.org/10.1007/978-3-540-46129-6.

(37) Ellis, J. E. Metal Carbonyl Anions: From [Fe(CO)4]2- to [Hf(CO)6]2- and Beyond. *Organometallics* **2003**, *22* (17), 3322–3338. https://doi.org/10.1021/om030105l.

(38) Sebenik, R. F.; Burkin, A. R.; Dorfler, R. R.; Laferty, J. M.; Leichtfried, G.; Meyer-Grünow, H.; Mitchell, P. C. H.; Vukasovich, M. S.; Church, D. A.; Van Riper, G. G.; et al. Molybdenum and Molybdenum Compounds. In *Ullmann's Encyclopedia of Industrial Chemistry*; Wiley-VCH Verlag GmbH & Co. KGaA: Weinheim, Germany, 2000; pp 413–454. https://doi.org/10.1002/14356007.a16_655.

(39) HABER, J. Molybdenum Compounds in Heterogeneous Catalysis. In *Studies in Inorganic Chemistry*; Elsevier B.V., 1994; Vol. 19, pp 477–617. https://doi.org/10.1016/B978-0-444-88198-4.50015-2.

(40) Outteridge, T.; Kinsman, N.; Ronchi, G.; Mohrbacher, H. Editorial: Industrial Relevance of Molybdenum in China. *Adv. Manuf.* **2020**, *8* (1), 35–39. https://doi.org/10.1007/s40436-019-00270-5.

(41) General Moly Inc. Molybdenum Market Factors – A New Paradigm Emerging. 2017.

(42) Pratima Desai; K. Sathya Narayanan; David Evans. Plentiful supplies to hamper molybdenum's price rally https://www.reuters.com/article/us-molybdenum-stainless/plentiful-supplies-to-hamper-molybdenums-price-rally-idUSKBN1Y11B6 (accessed Jun 8, 2020).

(43) General Moly Inc. *Reports Full Year 2019 Results*; 2020.

(44) Hagelüken, C. Markets for the Catalyst Metals Platinum, Palladium and Rhodium. *Metall* **2006**, *60* (1–2), 31–42.

(45) U.S. Geological Survey. *Rare Earth Elements — Critical Resources for High Technology*; 2002.

(46) Kumar, N.; Seminario, J. M. Computational Chemistry Analysis of Hydrodesulfurization Reactions Catalyzed by Molybdenum Disulfide Nanoparticles. *J. Phys. Chem. C* **2015**, *119* (52), 29157–29170. https://doi.org/10.1021/acs.jpcc.5b09712.

(47) Whittingham, M. S. Lithium Batteries and Cathode Materials. *Chem. Rev.* **2004**, *104* (10), 4271–4301. https://doi.org/10.1021/cr020731c.

(48) Rudolph R. Haering, James A. R. Stiles, K. B. Lithium Molybdenum Disulfide Battery Cathode. 4,224,390, 1980.

(49) Wang, T.; Gao, D.; Zhuo, J.; Zhu, Z.; Papakonstantinou, P.; Li, Y.; Li, M. Size-Dependent Enhancement of Electrocatalytic Oxygen-Reduction and Hydrogen-Evolution Performance of MoS2 Particles. *Chem. - A Eur. J.* **2013**, *19* (36), 11939–11948. https://doi.org/10.1002/chem.201301406.

(50) Huang, H.; Feng, X.; Du, C.; Wu, S.; Song, W. Incorporated Oxygen in MoS_2 Ultrathin Nanosheets for Efficient ORR Catalysis. *J. Mater. Chem. A* **2015**, *3* (31), 16050–16056. https://doi.org/10.1039/C5TA01600B.

(51) Chua, X. J.; Pumera, M. The Effect of Varying Solvents for MoS_2 Treatment on Its Catalytic Efficiencies for HER and ORR. *Phys. Chem. Chem. Phys.* **2017**, *19* (9), 6610–6619. https://doi.org/10.1039/C6CP08205J.

(52) Arunchander, A.; Peera, S. G.; Sahu, A. K. Synthesis of Flower-like Molybdenum Sulfide/Graphene Hybrid as an Efficient Oxygen Reduction Electrocatalyst for Anion Exchange Membrane Fuel Cells. *J. Power Sources* **2017**, *353*, 104–114. https://doi.org/10.1016/j.jpowsour.2017.03.149.

(53) Zuo, L. X.; Jiang, L. P.; Zhu, J. J. A Facile Sonochemical Route for the Synthesis of MoS2/Pd Composites for Highly Efficient Oxygen Reduction Reaction. *Ultrason. Sonochem.* **2017**, *35*, 681–688. https://doi.org/10.1016/j.ultsonch.2016.02.006.

(54) Rowley-Neale, S. J.; Fearn, J. M.; Brownson, D. A. C.; Smith, G. C.; Ji, X.; Banks, C. E. 2D Molybdenum Disulphide (2D-MoS_2) Modified Electrodes Explored towards the Oxygen Reduction Reaction. *Nanoscale* **2016**, *8* (31), 14767–14777. https://doi.org/10.1039/C6NR04073J.

(55) Rowley-Neale, S. J.; Smith, G. C.; Banks, C. E. Mass-Producible 2D-MoS 2 -Impregnated Screen-Printed Electrodes That Demonstrate Efficient Electrocatalysis toward the Oxygen Reduction Reaction. *ACS Appl. Mater. Interfaces* **2017**, *9* (27), 22539–22548. https://doi.org/10.1021/acsami.7b05104.

(56) Yazyev, O. V.; Kis, A. MoS2 and Semiconductors in the Flatland. *Mater. Today* **2015**, *18* (1), 20–30. https://doi.org/10.1016/j.mattod.2014.07.005.

(57) Harrison, K. W.; Corolewski, C. D.; McCluskey, M. D.; Lindemuth, J.; Ha, S.; Norton, M. G. Electronic Transport in Molybdenum Dioxide Thin Films. *J. Mater. Sci. Mater. Electron.* **2015**, *26* (12), 9717–9720. https://doi.org/10.1007/s10854-015-3639-2.

(58) Kaiser, F.; Schmidt, M.; Grin, Y.; Veremchuk, I. Molybdenum Oxides MoO x: Spark-Plasma Synthesis and Thermoelectric Properties at Elevated Temperature. *Chem. Mater.* **2020**, *32* (5), 2025–2035. https://doi.org/10.1021/acs.chemmater.9b05075.

(59) National Bureau of Standards, U. S. *Copper Wire Tables*; Washington Govt. Print. Off. 1914, 1914; Vol. 31.

(60) Helmenstine, A. M. Table of Electrical Resistivity and Conductivity https://www.thoughtco.com/table-of-electrical-resistivity-conductivity-608499 (accessed May 13, 2020).

(61) Zhang, C.; Zou, X.; Du, Z.; Gu, J.; Li, S.; Li, B.; Yang, S. Atomic Layers of MoO_2 with Exposed High-Energy (010) Facets for Efficient Oxygen Reduction. *Small* **2018**, *1703960* (Ldmd), 1703960. https://doi.org/10.1002/smll.201703960.

(62) Ellefson, C. A.; Marin-Flores, O.; Ha, S.; Norton, M. G. Synthesis and Applications of Molybdenum (IV) Oxide. *J. Mater. Sci.* **2012**, *47* (5), 2057–2071. https://doi.org/10.1007/s10853-011-5918-5.

(63) Yang, L.; Yu, J.; Wei, Z.; Li, G.; Cao, L.; Zhou, W.; Chen, S. Co-N-Doped MoO2nanowires as Efficient Electrocatalysts for the Oxygen Reduction Reaction and Hydrogen Evolution Reaction. *Nano Energy* **2017**, *41* (January), 772–779. https://doi.org/10.1016/j.nanoen.2017.03.032.

(64) Hao, Y.; Gong, P.; Xu, L.; Pu, J.; Wang, L.; Huang, L. Contrasting Oxygen Reduction Reactions on Zero- and One-Dimensional Defects of MoS 2 for Versatile Applications. *ACS Appl. Mater. Interfaces* **2019**, *11* (49), 46327–46336. https://doi.org/10.1021/acsami.9b14502.

(65) Farmer, H. H.; Rowan, E. V. US 3356702 - Molybdenum Oxysulfide Dithiocarbamates and Processes for

Their Preparation, 1967.

(66) Tsigdinos, G. A. Inorganic Sulfur Compounds of Molybdenum and Tungsten. In *Topics in Current Chemistry*; 1978; Vol. 76, pp 65–105. https://doi.org/10.1007/BFb0047027.

(67) CANNON, P.; NORTON, F. J. Reaction between Molybdenum Disulphide and Water. *Nature* **1964**, *203* (4946), 750–751. https://doi.org/10.1038/203750a0.

(68) Spengler, G.; Weber, A. Über Die Schmierfähigkeit Organischer Molybdänverbindungen. *Chem. Ber.* **1959**, *92* (9), 2163–2171. https://doi.org/10.1002/cber.19590920931.

(69) Krüss, G. Ueber Die Schwefelverbindungen Des Molybdäns; *Justus Liebigs Ann. Chem.* **1884**, *225* (1), 1–57. https://doi.org/10.1002/jlac.18842250102.

(70) Abraham, K. M. Lithium/Molybdenum Oxysulfide Secondary Batteries. *J. Electrochem. Soc.* **1989**, *136* (2), 576. https://doi.org/10.1149/1.2096686.

(71) Pasquariello, D. M.; Dunn, W. J.; Abraham, K. M. Rechargeable Lithium-Molybdenum Oxysulfide Batteries. In *Proceedings of the 34th International Power Sources Symposium*; IEEE, 1990; pp 94–97. https://doi.org/10.1109/IPSS.1990.145800.

(72) Abraham, K. M.; Pasquariello, D. M. Synthesis, Characterization, and Lithium Battery Applications of Molybdenum Oxysulfides. *Chem. Mater.* **1993**, *5* (9), 1233–1241. https://doi.org/10.1021/cm00033a009.

(73) Levasseur, A.; Schmidt, E.; Meunier, G.; Gonbeau, D.; Benoist, L.; Pfister-Guillouzo, G. New Amorphous Molybdenum Oxysulfide Thin Films Their Characterization and Their Electrochemical Properties. *J. Power Sources* **1995**, *54* (2), 352–355. https://doi.org/10.1016/0378-7753(94)02100-H.

(74) Abraham, K. M.; Needham, M.; Pasquariello, D. M.; Pawtucket, R. I. US4934922 - Cathode-Active Materials for Secondary Batteries, 1990.

(75) Schmidt, E.; Weill, F.; Meunier, G.; Levasseur, A. New Amorphous Molybdenum Oxysulfides Obtained in the Form of Thin Films and Their Characterization by TEM. *Thin Solid Films* **1994**, *245* (1–2), 34–39. https://doi.org/10.1016/0040-6090(94)90873-7.

(76) Schmidt, E.; Sourisseau, C.; Meunier, G.; Levasseur, A. Amorphous Molybdenum Oxysulfide Thin Films and Their Physical Characterization. *Thin Solid Films* **1995**, *260* (1), 21–25. https://doi.org/10.1016/0040-6090(94)06463-6.

(77) Benoist, L.; Gonbeau, D.; Pfister-Guillouzo, G.; Schmidt, E.; Meunier, G.; Levasseur, A. XPS Analysis of Oxido-Reduction Mechanisms during Lithium Intercalation in Amorphous Molybdenum Oxysulfide Thin Films. *Solid State Ionics* **1995**, *76* (1–2), 81–89. https://doi.org/10.1016/0167-2738(94)00226-I.

(78) Dupin, J. C.; Gonbeau, D.; Martin-Litas, I.; Vinatier, P.; Levasseur, A. Amorphous Oxysulfide Thin Films MOySz (M = W, Mo, Ti) XPS Characterization: Structural and Electronic Pecularities. *Appl. Surf. Sci.* **2001**, *173* (1–2), 140–150. https://doi.org/10.1016/S0169-4332(00)00893-X.

(79) Yufit, V.; Nathan, M.; Golodnitsky, D.; Peled, E. Thin-Film Lithium and Lithium-Ion Batteries with Electrochemically Deposited Molybdenum Oxysulfide Cathodes. *J. Power Sources* **2003**, *122* (2), 169–

173. https://doi.org/10.1016/S0378-7753(03)00401-4.

(80) Golodnitsky, D.; Yufit, V.; Nathan, M.; Shechtman, I.; Ripenbein, T.; Strauss, E.; Menkin, S.; Peled, E. Advanced Materials for the 3D Microbattery. *J. Power Sources* **2006**, *153* (2), 281–287. https://doi.org/10.1016/j.jpowsour.2005.05.029.

(81) Martinez, H.; Benayad, A.; Gonbeau, D.; Vinatier, P.; Pecquenard, B.; Levasseur, A. Influence of the Cation Nature of High Sulfur Content Oxysulfide Thin Films MOySz(M = W, Ti) Studied by XPS. *Appl. Surf. Sci.* **2004**, *236* (1), 377–386. https://doi.org/10.1016/j.apsusc.2004.05.010.

(82) Golodnitsky, D.; Nathan, M.; Yufit, V.; Strauss, E.; Freedman, K.; Burstein, L.; Gladkich, A.; Peled, E. Progress in Three-Dimensional (3D) Li-Ion Microbatteries. *Solid State Ionics* **2006**, *177* (26-32 SPEC. ISS.), 2811–2819. https://doi.org/10.1016/j.ssi.2006.02.048.

(83) Shembel, E.; Apostolova, R.; Nagirny, V.; Kirsanova, I.; Chivikov, S. Thin Layer Electrolytic Molybdenum Oxysulfides for Lithium Secondary Batteries with Liquid and Polymer Electrolytes. In *5th Advanced Batteries and Accumulators – ABA-2004*; 2004; pp 6–9.

(84) Afanasiev, P.; Bezverkhy, I. Genesis of Vesicle-like and Tubular Morphologies in Inorganic Precipitates: Amorphous Mo Oxysulfides. *J. Phys. Chem. B* **2003**, *107* (12), 2678–2683. https://doi.org/10.1021/jp021655k.

(85) Genuit, D.; Bezverkhyy, I.; Afanasiev, P. Solution Preparation of the Amorphous Molybdenum Oxysulfide MoOS 2 and Its Use for Catalysis. *J. Solid State Chem.* **2005**, *178* (9), 2759–2765. https://doi.org/10.1016/j.jssc.2005.06.016.

(86) Badger, E. H. M.; Griffith, R. H.; Newling, W. B. S. The Catalytic Decomposition of Simple Heterocyclic Compounds - I. Preparation and Properties of Molybdenum Sulphide and Nickel Sulphide Catalysts. *Proc. R. Soc. London. Ser. A. Math. Phys. Sci.* **1949**, *197* (1049), 184–193. https://doi.org/10.1098/rspa.1949.0057.

(87) Weber, T.; J. C. Muijsers; J. H. M. C. van Wolput; Verhagen, C. P. J.; Niemantsverdriet, J. W. Basic Reaction Steps in the Sulfidation of Crystalline MoO3 to MoS2, As Studied by X-Ray Photoelectron and Infrared Emission Spectroscopy. *J. Phys. Chem.* **1996**, *100* (33), 14144–14150. https://doi.org/10.1021/JP961204Y.

(88) Muijsers, J. C.; Weber, T.; Vanhardeveld, R. M.; Zandbergen, H. W.; Niemantsverdriet, J. W. Sulfidation Study of Molybdenum Oxide Using MoO3/SiO2/Si(100) Model Catalysts and Mo-IV3-Sulfur Cluster Compounds. *J. Catal.* **1995**, *157* (2), 698–705. https://doi.org/10.1006/jcat.1995.1335.

(89) Senthilkumar, V.; Tam, L. C.; Kim, Y. S.; Sim, Y.; Seong, M. J.; Jang, J. I. Direct Vapor Phase Growth Process and Robust Photoluminescence Properties of Large Area MoS2 Layers. *Nano Res.* **2014**, *7* (12), 1759–1768. https://doi.org/10.1007/s12274-014-0535-7.

(90) Massoth, F. E. Studies of Molybdena-Alumina Catalysts. IV. Rates and Stoichiometry of Sulfidation. *J. Catal.* **1975**, *36* (2), 164–184. https://doi.org/10.1016/0021-9517(75)90022-6.

(91) Scholz, G. A.; Morrison, S. R. Methanation on Exfoliated and Supported MoS 2. *Can. J. Chem.* **1989**, *67*

(5), 862–866.

(92) Hao, Y.; Zhang, Y.; Chen, A.; Fang, W.; Yang, Y. Study on Methanethiol Synthesis from H2S-Rich Syngas over K 2MoO4 Catalyst Supported on Electrolessly Ni-Plated SiO2. *Catal. Letters* **2009**, *129* (3–4), 486–492. https://doi.org/10.1007/s10562-008-9827-4.

(93) Rochet, A.; Baubet, B.; Moizan, V.; Devers, E.; Hugon, A.; Pichon, C.; Payen, E.; Briois, V. Intermediate Species Revealed during Sulfidation of Bimetallic Hydrotreating Catalyst: A Multivariate Analysis of Combined Time-Resolved Spectroscopies. *J. Phys. Chem. C* **2017**, *121* (34), 18544–18556. https://doi.org/10.1021/acs.jpcc.7b03735.

(94) Tran, P. D.; Tran, T. V.; Orio, M.; Torelli, S.; Truong, Q. D.; Nayuki, K.; Sasaki, Y.; Chiam, S. Y.; Yi, R.; Honma, I.; et al. Coordination Polymer Structure and Revisited Hydrogen Evolution Catalytic Mechanism for Amorphous Molybdenum Sulfide. *Nat. Mater.* **2016**, *15* (6), 640–646. https://doi.org/10.1038/nmat4588.

(95) Gupta, A. K.; Topolski, J. E.; Nickson, K. A.; Jarrold, C. C.; Raghavachari, K. Mo Insertion into the H2 Bond in MoxSy- + H2 Reactions. *J. Phys. Chem. A* **2019**, *123* (33), 7261–7269. https://doi.org/10.1021/acs.jpca.9b04079.

(96) Villars, P.; Cenzual, K.; Gladyshevskii, R. *Handbook of Inorganic Substances 2017*; 2017.

(97) Larquet, C.; Carenco, S. Metal Oxysulfides: From Bulk Compounds to Nanomaterials. *Front. Chem.* **2020**, *8* (March). https://doi.org/10.3389/fchem.2020.00179.

(98) Ding, Y.; Gu, J.; Ke, J.; Zhang, Y. W.; Yan, C. H. Sodium Doping Controlled Synthesis of Monodisperse Lanthanide Oxysulfide Ultrathin Nanoplates Guided by Density Functional Calculations. *Angew. Chemie - Int. Ed.* **2011**, *50* (51), 12330–12334. https://doi.org/10.1002/anie.201105025.

(99) Larquet, C.; Nguyen, A.-M.; Ávila-Gutiérrez, M.; Tinat, L.; Lassalle-Kaiser, B.; Gallet, J.-J.; Bournel, F.; Gauzzi, A.; Sanchez, C.; Carenco, S. Synthesis of Ce 2 O 2 S and Gd 2(1– y) Ce 2 y O 2 S Nanoparticles and Reactivity from in Situ X-Ray Absorption Spectroscopy and X-Ray Photoelectron Spectroscopy. *Inorg. Chem.* **2017**, *56* (22), 14227–14236. https://doi.org/10.1021/acs.inorgchem.7b02336.

(100) Larquet, C.; Klein, Y.; Hrabovsky, D.; Gauzzi, A.; Sanchez, C.; Carenco, S. Tunable Magnetic Properties of (Gd,Ce) 2 O 2 S Oxysulfide Nanoparticles. *Eur. J. Inorg. Chem.* **2019**, *2019* (6), 762–765. https://doi.org/10.1002/ejic.201801466.

(101) Larquet, C. Nanoparticles of Lanthanide and Transition Metal Oxysulfides: From Colloidal Synthesis to Structure, Surface, Optical and Magnetic Properties, 2018.

(102) C. Larquet, A.-M. Nguyen, T. K.-C. Le, M. Avila-Gutierrez, S. C. Les Oxysulfures de Lanthanides Un Terrain de Jeu Pour La Nanochimie. *Actual. Chim.* **2019**, *436*, 28–31.

(103) Larquet, C.; Hourlier, D.; Nguyen, A.; Torres-Pardo, A.; Gauzzi, A.; Sanchez, C.; Carenco, S. Thermal Stability of Oleate-Stabilized Gd 2 O 2 S Nanoplates in Inert and Oxidizing Atmospheres. *ChemNanoMat* **2019**, *5* (4), 539–546. https://doi.org/10.1002/cnma.201800578.

(104) Larquet, C.; Carriere, D.; Nguyen, A.-M.; Le, T. K.-C.; Frogneux-Plé, X.; Génois, I.; Le Griel, P.; Gauzzi,

A.; Sanchez, C.; Carenco, S. Unraveling the Role of Alkali Cations in the Growth Mechanism of Gd 2 O 2 S Nanoparticles. *Chem. Mater.* **2020**, *32* (3), 1131–1139. https://doi.org/10.1021/acs.chemmater.9b04059.

(105) Shannon, R. D. Revised Effective Ionic Radii and Systematic Studies of Interatomic Distances in Halides and Chalcogenides. *Acta Crystallogr. Sect. A* **1976**, *32* (5), 751–767. https://doi.org/10.1107/S0567739476001551.

Chapter II

Synthesis and characterization of Gd_2O_2S/Mo_{2x} by a two-step protocol

Tables of contents

1. Why a two-step protocol for Mo-containing Gd_2O_2S-based nanoparticles?

In this project, we are interested in making molybdenum oxysulfide nanoparticles but for the moment there is no report on a precise synthesis giving a well-defined crystalline compound within morphology-controlled nanoparticles. Moreover, all the existing methods are at high temperature or use physical techniques. To the best of our knowledge, almost no research is done on a colloidal synthesis of molybdenum-based oxysulfide nanoparticles in organic solvent, although it may provide better defined nanoparticles at lower energetic cost. In contrast, the colloidal synthesis of Gd_2O_2S nanoplatelets is well-known with the product structure well-described (Figure 1A-C).[1,2] Our idea is to put a layer of Mo on the Gd_2O_2S nanoparticles freshly formed to make core-shell nanoparticles (Figure 1E). As Mo has a high affinity for S, it could bind with sulfides in Gd_2O_2S and the rest of sulfur in the medium after the formation of Gd_2O_2S to form a shell of molybdenum sulfide, or even an oxysulfide with Mo-S sites similar to these of MoS_2. As it is known that the Mo-S edge sites in MoS_2 (Figure 1D) is the active site for reactions such as in heterogeneous catalysis for hydrodesulfurization (HDS),[3,4] and in electrocatalysis, oxygen reduction reaction (ORR),[5] by this method, we may have an interesting catalyst for ORR.

The synthesis should contain two steps: firstly, Gd_2O_2S nanoplatelets are classically made without being isolated from the reaction medium. Then, a molybdenum precursor is added and the mixture is heated to form the shell. We expect to have a shell of molybdenum oxysulfide on the surface of Gd_2O_2S nanoplatelets in the final product.

In the following chapter, a sample will be identified by the number of molar equiv. of Mo *vs.* Gd as follow, where *x* is molar ratio Mo/Gd. The molar quantity of Gd in each sample is constant of 0.5 mmol. The number *x* will be known as the name of considering sample and also the introduced ratio value between Mo and Gd. The first sample of the series with $x = 0$ is noted as Gd_2O_2S/Mo_0 which was made from Gd_2O_2S annealed directly in the reaction medium after the reaction. All the synthesis protocols will be detailed in part 2.

Gd_2O_2S/Mo_{2x} $\quad x = \frac{n_{Mo\ introduced}}{0.5}$

0.5 = introduced molar quantity of Gd precursor

x = molar ratio $\frac{Mo}{Gd}$

= name of sample

$2x$ = theoretical notation index

Example: for a sample of 0.18: $x = \frac{n_{Mo\ introduced}}{0.5} = 0.18$, the sample is noted $Gd_2O_2S/Mo_{0.36}$.

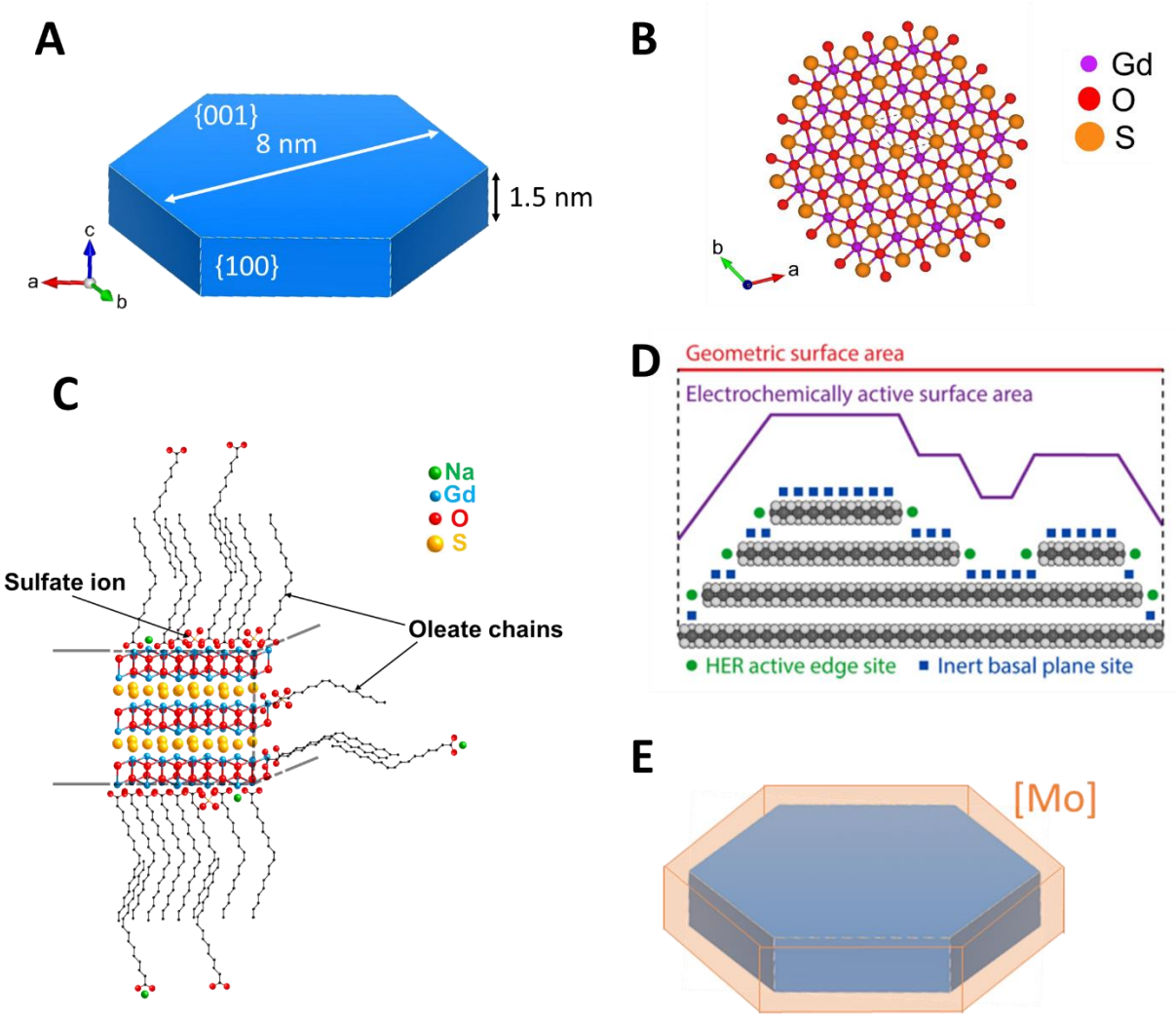

Figure 1 (A-C) Structure of Gd_2O_2S nanoplatelets: (A) shape and average size of nanoparticles; (B) crystalline structure along the plane normal to the c axis and (C) nanoplatelets with oleate ligands on their surface, figure from Clément Larquet's thesis.[6] *(D) Active site in MoS_2: Mo-S edge sites, figure by Benck, J. D. et al.*[7] *(E) Core-shell nanoparticles Gd_2O_2S/Mo_{2x} expected from this initiative.*

2. Synthesis protocol

2.1. How to choose the precursor?

Summary equation of the synthesis:

$$1^{st}\text{ step: } Gd(acac)_3 + \frac{1}{16}S_8 + Na(oleate) \xrightarrow{310\ °C} \frac{1}{2}Gd_2O_2S_{1-2\varepsilon} + \varepsilon\, S_{excess}$$

$$2^{nd}\text{ step: } Gd_2O_2S + 2x\,[Mo^{+X}] \xrightarrow{310\ °C} Gd_2O_2S/Mo_{2x},\ 0 < x < 2.03$$

The detailed synthesis protocols are described in the Experimental Section. For reference, a sample with $x = 0$ was done (Gd_2O_2S/Mo_0). For Mo-containing samples, there are 3 Mo molecular precursors used: $Cp_2Mo_2^{(+I)}(CO)_6$, $Mo^{(+III)}(acac)_3$ and $Mo^{(+VI)}O_2(acac)_2$. They were selected based on their limited toxicity, solubility in organic solvents (in oleylamine, oleic acid and 1-octadecene in this case). $Cp_2Mo_2^{(+I)}(CO)_6$ and $Mo^{(+VI)}O_2(acac)_2$ are commercial. $Mo^{(+III)}(acac)_3$ is not yet commercial: it was provided to our group by V. Mougel and colleagues from Collège de France. The Mo(+VI) precursor can be stored easily in a cabinet with a film on the cap to avoid the humidity. The others are stored in the freezer of the glovebox at -40 °C.

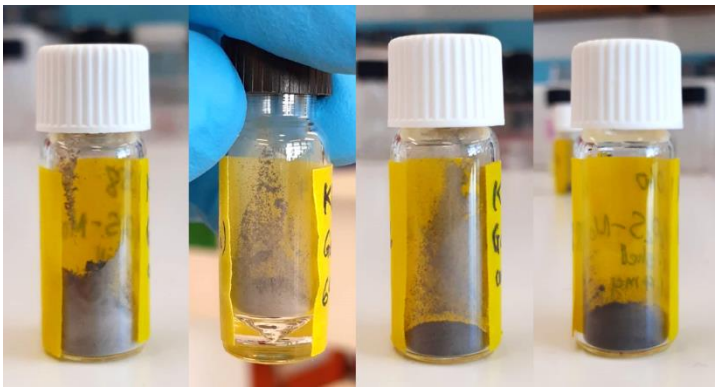

Figure 2 Samples made with Mo(+VI) precursor, from left to right: x = 0.05, 0.18, 0.25 and 0.43. Their colors go darker from left to right, from brown to very dark brown, close to black.

Our research started with the Mo(+VI) precursor because it is the safest and the most inexpensive soluble compound. Few Mo-containing samples Gd_2O_2S/Mo_{2x} were made with this precursor with a gradient of Mo, x from 0.05 to 0.43. The yield of the synthesis was estimated with the formula Gd_2O_2S/Mo_{2x} varying between about 70 % and 140 % (Table 1, in orange), which suggests that other phase(s) are formed, which may contain Mo. The majority of concerning elements (Gd, Mo and S) are found in final powder than lost in the washing supernatants. The quantity of organic ligand was not subtracted for yield calculation, and

contributed to the uncertainty on the calculated yield. The color of obtained powder varies between brown to very dark brown (nearly black) (Figure 2).

Table 1 Yields of Gd_2O_2S/Mo_{2x} syntheses with 3 kinds of Mo precursors: Mo(+I) (in white), Mo(+III) (in blue) and Mo(+VI) (in orange).

x	**0.02**	**0.05**	**0.11**	**0.18**		**0.22**	**0.25**	**0.35**	**0.43**	**1.00**	**2.03**
yield (%)	97	92	89	97	86	70	68	69	162	46	35
		109	97	63	91	76	71	123	137	54	
		106	106	103	135	89	80			111	
		111	108	120			121				
				88							

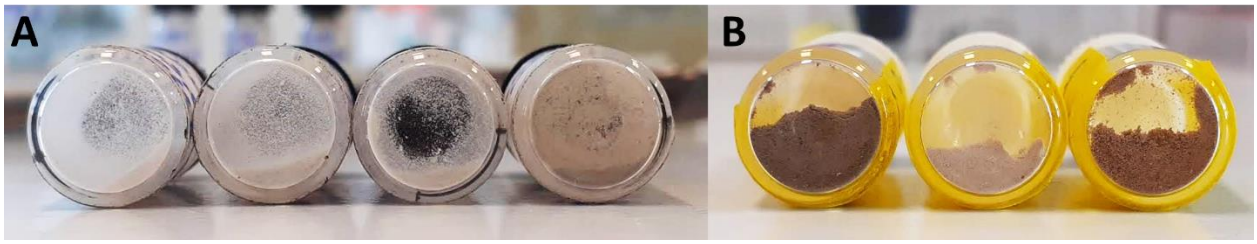

Figure 3 Samples made with Mo(+I) precursor: (A) x from left to right: 0.05, 0.11, 0.18, 0.25. The sample color becomes darker when x increase from 0.05 to 0.30, from off-white to light brown. (B) x from left to right: 0.43, 1, 2.03. The color does not go darker from left to right: from brown to light brown then brown but it is coherent with the elemental analysis result which will be discussed later in this chapter.

$Cp_2Mo_2(CO)_6$ is not as stable as $MoO_2(acac)_2$. The formal oxidation state of Mo here is +I and the precursor has a Mo-Mo bond. Because of this lower oxidation state, we expect this precursor to be more reactive than Mo(+VI) which is known to be the most thermodynamically stable oxidation state of Mo.[8] $Mo(acac)_3$ is an uncommon precursor which is not yet commercial, but we tested it because it has similar ligands than $Gd(acac)_3$. Only few samples with *x* equals to 0.05 and 0.18 were done to compare with other precursors. For both precursors Mo(+VI) and Mo(+I), the yield varies between about 50 % to about 140 % (except for sample $x = 2.03$) (Table 1, in white and blue). The color is much lighter for samples with Mo(+I) precursor than ones with Mo(+VI) precursor, meanwhile ones with Mo(+III) are quite darker (Figure 3 and Figure 4).

For a simple synthesis, no sulfur was added in the 2nd step and the reaction temperature was not modified for the 2nd step, a family of powders was made with a gradient of introduced Mo

molar quantity, *x* from 0.02 to 2.03. For these series, the color of samples changes much more than for the case of Mo(+VI) precursor: from off-white at low percentage to brown at the highest percentage. It means much lighter than in the case of Mo(+VI). It is clear that there is an effect of precursor on the final powder (Figure 3).

Figure 4 Samples made with Mo(+III) precursor: x from left to right: 0.05, 0.18. Their colors are much darker than powders made with 2 other precursors: very dark brown for sample x = 0.05 and black for sample x = 0.18.

2.2. First optimization of synthesis protocol

We consider a classical synthesis with the molybdenum precursor introduced after the formation of Gd_2O_2S, expecting to form Gd_2O_2S nanoplatelets with Mo on their surface. After the formation of Gd_2O_2S nanoparticles, Mo molecular precursor is added. During the second step, the solution is also heated during 30 min under a nitrogen flux. The product is isolated only after the second step to obtain the final powder.

A series of samples are made with *x* from 0.05 to 2.03 with the Mo(+I) precursor (which will be commented in the next section) with the products' diffractograms clearly different from these of Gd_2O_2S. The brief optimization using Mo(+I) precursor would make any change be more visible than other precursors.

Previous researches from Ding *et al.* and from our research group show that Gd_2O_2S nanoparticles contain only 0.2 molar equiv. of S *vs.* Gd, instead of 0.5 as introduced.[1,2] It means that after the formation of Gd_2O_2S nanoparticles, there is still an excess of sulfur in the reaction medium but its form is not yet determined.

There are two points that we wanted to clarify in this part: firstly, should the temperature be set lower than 310 °C for the 2nd step (250 °C in this test) to prevent the modification of Gd_2O_2S nanoparticles as they start to grow from 280 °C?[9] Secondly, is an addition of S_8 necessary, on top of the 0.5 equiv. already introduced? There can be an addition at the beginning of the 1st step ($a \neq 0$) or before the 2nd step ($b \neq 0$).

$$1^{st}\ \text{step:}\quad Gd(acac)_3 + \left(\frac{1}{16} + a\right) S_8 + Na(oleate) \xrightarrow{310\ °C} \frac{1}{2} Gd_2O_2S_{1-2\varepsilon} + \varepsilon\, S_{excess}$$

$$2^{nd}\ \text{step:}\quad Gd_2O_2S + 2x\ [Mo^{+X}] + b\ S_8 \xrightarrow{250\ °C} Gd_2O_2S/Mo_{2x},\ 0 < x < 2.03$$

Figure 5A shows a comparison between diffractograms of two samples with x = 0.11 (a = b = 0): the first one was with the 2nd step done at 310 °C and the latter one was with the 2nd step done at 250 °C. are similar. Compared to Gd_2O_2S/Mo_0 reference (in black), the blue and red diffractograms show slight differences. Although all the peaks are at the same positions, their relative intensities are slightly different. As in the case of the reference, the peak (101) is split into two peaks, respectively at 28.9 ° and 31 °. This feature in the diffractograms, related to crystalline structure changes *vs.* the classical Gd_2O_2S made by the one-step protocol (see Chapter III), are not caused by Mo addition but the reheating in the 2nd step. Also, the two Mo-containing powders show little difference with this reference sample. Moreover, the EDS results presented on Figure 5A (with automatic data fitting from the built-in software) show that for the same introduced quantity of Mo, the 2nd step at 310 °C seems to lead to a powder containing more Mo than the other one (observed Mo/Gd = 0.07 *vs.* 0.01) with the same S quantity (lower than Gd_2O_2S). Then, it is practically easier to stay with the method of the first synthesis than changing the temperature of the 2nd step: both steps are heated at 310 °C.

Figure 5B shows the difference of crystalline structures of powders $Gd_2O_2S/Mo_{0.22}$ (x = 0.11) with more sulfur added at the beginning of the synthesis ($a = \frac{1}{16}$ and $a = \frac{19}{16}$). The more sulfur is added in the synthesis, the more sulfur is obtained in the final phase and the less the splitting of peak (101) is. In fact, with 20 times more sulfur than original protocol ($a = \frac{19}{16}$, curve d), peak (101) is no more split, the maximum is located at 29.7 °, i.e. to the left of the classical Gd_2O_2S for which the corresponding (101) peak is located at 29.4 °, the same position as the first maximum for Gd_2O_2S/Mo_0 (dash line). For all cases, the concerning maxima are to the left of theoretical peak (110) of Gd_2O_2S which is located at 29.9 ° (JCPDS file 00-026-1422, experimental-based). Also, additional unidentified phases are obtained: a peak at 21.3 ° and a shoulder at around 32.8 ° appear in this diffractogram. This suggests that with more sulfur added at the beginning of the synthesis, more secondary phases are formed, while the global structure of nanoparticles does not change. Similar to this case, with twice the quantity of sulfur (a = 1/16, curve c), there is no clear difference compared to the diffractograms of samples with a = 0 (curve b) and x = 0 (curve a): all peaks in a) and b) are found in c) at the same positions.

EDS results show that when adding a double quantity of S_8 (a = 1/16), observed S/Gd ratio is higher than in original synthesis (0.19 *vs.* 0.11) while observed Mo/Gd is lower (0.01 *vs.* 0.07).

Figure 5C shows the difference of crystalline structures of powders made with 1.00 equiv. (x = 1.00) and 2.03 equiv. (x = 2.03) of Mo with sulfur added after the first step of the synthesis (b = 1/16 and b = 1/32). Supposing that secondary phase(s) are made from reaction(s) between Mo, S_{excess} and other species in the reaction medium, and the reactions are maintained for all values of x, the introduction of more Mo may enhance these reactions and make the detection of the corresponding products easier. So, we chose to test with x = 1.00 and x = 2.03. In both cases, the additional sulfur increases significantly the quantity of both Mo and S (result by EDS, curve b *vs.* curve c and curve d *vs.* curve e). At the same time, there are more Bragg peaks appearing compared to the same synthesis without additional S (curves c and e, blue dash lines). They are the same in both diffractograms c and e (blue dash line). Some Bragg peaks found in sample x = 2.03, with or without additional S, are also found in "MoS_2" sample (curve f, red dash line, this sample is made in the same method without $Gd(acac)_3$, 2 equiv of S to Mo, see Chapter IV). This suggests that these peaks belong to phases which contain surely Mo, S and maybe O (perhaps of MoO_xS_y kind). The formation of these crystalline phases (whose presence is unsure in other samples with lower x) are separated from the formation of the other Gd_2O_2S-based ones. The final powders are more complicated in this case and the additional sulfur does not facilitate the analysis of final powders.

To summarize, reheating the reaction medium during the 2nd step is the cause of diffractogram modification, this does not have any relation with the addition of Mo. The temperature of heating in the 2nd step does not have any effect to the final structure. So, heating at 310 °C for the 2nd step is practically better than heating it at lower temperature, it even gives more Mo in final powders. The additional sulfur, at any time of the synthesis, does not help understanding the compositions/structures of final products as it creates additional phases which cannot be identified for the moment. Therefore, the original protocol is finally the best condition we can have for now, it is maintained without any modification.

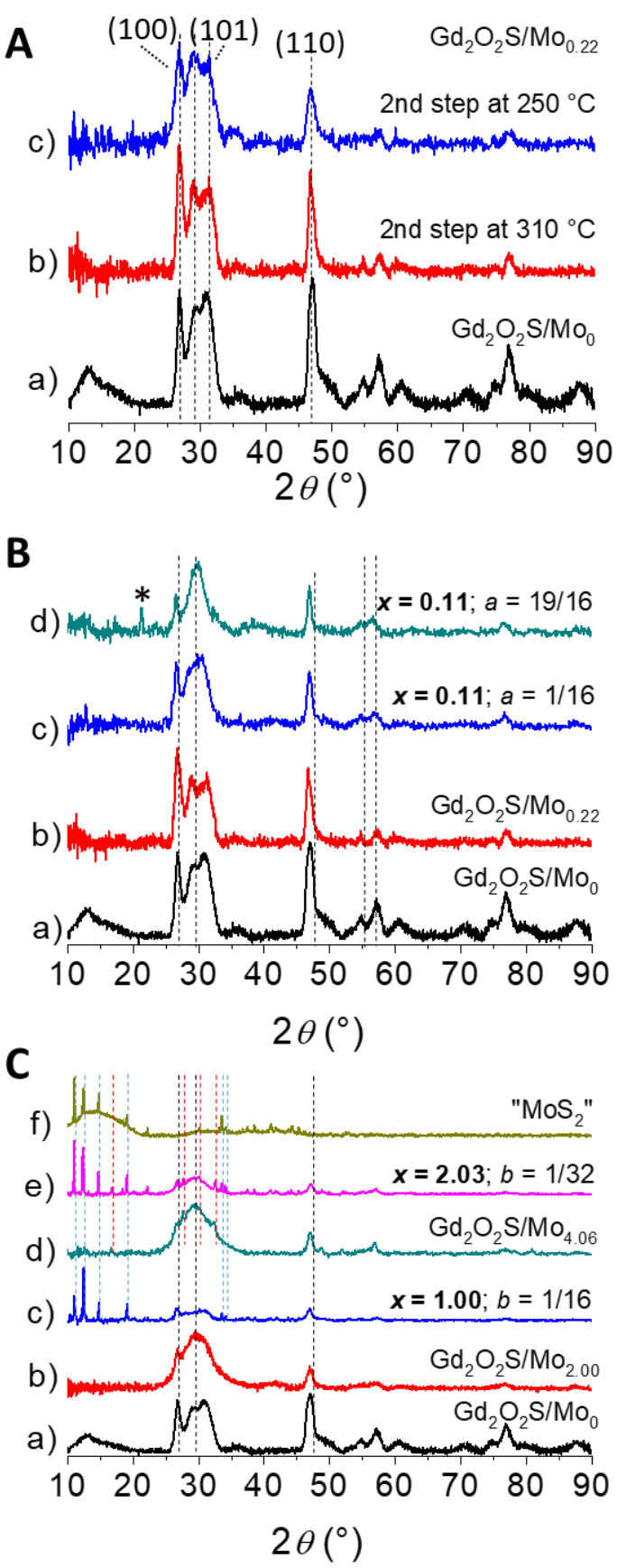

	Observed Mo/Gd	Observed S/Gd
c)	0.01	0.11
b)	0.07	0.11
a)		0.14
d)	0.21	1.35
c)	0.01	0.19
b)	0.07	0.11
a)		0.14
f)	-	-
e)	0.60	0.31
d)	0.45	0.19
c)	0.47	0.45
b)	0.13	0.13
a)		0.14

Figure 5 (A) Comparison of crystalline structure and of observed ratio Mo/Gd and S/Gd between 2-step sample without Mo and others with Mo, 2nd step at 250 °C instead of 310 °C,

test with x = 0.11. (B) Comparison of crystalline structure and of observed ratio Mo/Gd and S/Gd an annealed Gd_2O_2S sample (Gd_2O_2S/Mo_0) and others with Mo (x = 0.11), S is added at the beginning of the protocol, reference sample with x = 0.11 and Gd_2O_2S/Mo_0. (C) Comparison of crystalline structure and of observed ratio Mo/Gd and S/Gd between 2-step sample without Mo and others with Mo, S is added after the 1st step, reference sample x = 2.03 and Gd_2O_2S/Mo_0. The columns on the right, labeled as "Observed Mo/Gd" and "Observed S/Gd", indicated the molar ratio measured by EDS on the final powders.

2.3. Secondary phase(s) in final products: analysis on samples with $x = 0.18$

From the diffractograms of the very first samples $Gd_2O_2S/Mo_{0.36}$ (x = 0.18) made at 310 °C, we observe obvious changes compared to classical Gd_2O_2S nanoparticles which may come from secondary phase(s) (Figure 6B). To find out what they could be, first of all, an analysis by Scanning Transmission Electron Microscopy - Energy-dispersive X-ray spectroscopy (STEM-EDS) was done on a sample to see if the distributions of concerning elements (Gd, Mo, S) were even at nanoscale. This analysis was performed by Mounib Bahri and Ovidiu Ersen (Institut de Physique et Chimie des Matériaux de Strasbourg, IPCMS). Figure 6A shows an image of a group of nanoparticles where all Gd, Mo and S are distributed homogenously in the sample at this scale. This suggests that at nanoscale, the material is *possibly* a homogenous mix of different phases.

From the ICDD PLU2019 database, one phase of gadolinium molybdenum oxide sulfide $GdMoO_4S_{0.5}$ (JCPDS file 00-057-0084) that was claimed to be indexed but no such phase or others which contain all four elements were found in ICSD database. About the gadolinium molybdenum oxide, there are several phases found from the ICDD PLU2019 database of all quality levels but there are only six of them can be matched with the diffractograms of samples: Gd_2MoO_6 (monoclinic, JCPDS file 00-024-0423, indexed only), $Gd_4Mo_4O_{11}$ (orthorhombic, JCPDS file 04-011-0366), Gd_3MoO_7 (orthorhombic, JCPDS file 04-017-0037), $Gd_2(MoO_4)_3$ (monoclinic, JCPDS file 00-067-0152), Gd_6MoO_{12} (cubic, JCPDS file 00-024-1085) and $Gd_2Mo_3O_9$ (tetragonal, JCPDS file 00-033-0548, indexed). These seven structures have Bragg peaks possibly corresponding to a part of sample's diffractogram (Figure 6B). Among these phases, the structures of $Gd_2Mo_3O_9$ and Gd_6MoO_{12} cannot be found on ICSD. Gd_2MoO_6, Gd_3MoO_7 and $Gd_2(MoO_4)_3$ are different kinds of molybdate. All found structures are redrawn in Figure 6C-F, the atomic radii are symbolic only.

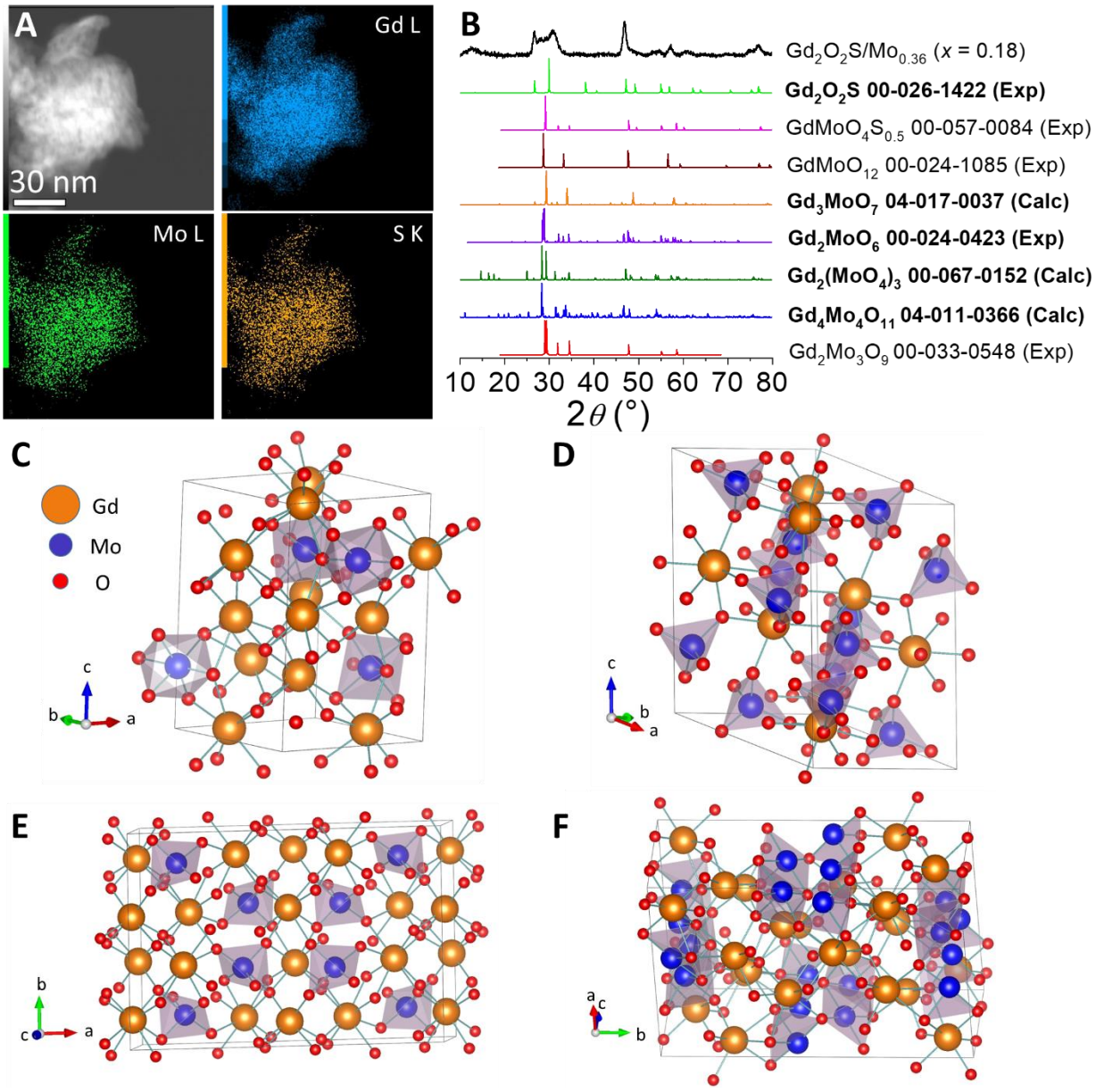

Figure 6 (A) Images of STEM-EDS cartography done one a $Gd_2O_2S/Mo_{0.36}$ (x = 0.18) sample, made with Mo(+I) precursor. The measurements were realized by Mounib Bahri and Ovidiu Ersen (Institut de Physique et Chimie des Matériaux de Strasbourg, IPCMS). The scale bar is the same for all images. (B) XRD pattern of $Gd_2O_2S/Mo_{0.36}$ made at 310 °C with 7 possible secondary phases based on peak positions: $GdMoO_4S_{0.5}$ (JCPDS file 00-057-0084), $Gd_4Mo_4O_{11}$ (orthorhombic, JCPDS file 04-011-0366), $Gd_2(MoO_4)_3$ (monoclinic, JCPDS file 00-067-0152), Gd_2MoO_6 (monoclinic, JCPDS file 00-024-0423, indexed only), Gd_3MoO_7 (orthorhombic, JCPDS file 04-017-0037), Gd_6MoO_{12} (cubic, JCPDS file 00-024-1085) and $Gd_2Mo_3O_9$ (tetragonal, JCPDS file 00-033-0548, indexed). In bold: structures found in ICSD

database and redrawn. (C) Orthorhombic Gd_3MoO_7, Space group: $P2_12_12_1$, a = 7.4459 Å, b = 7.4840 Å, c = 10.5620 Å.[10] ***The color code is common for (C-F).*** *(D) Monoclinic α-$Gd_2(MoO_4)_3$, Space group: C2/c, a = 7.54873 Å, b = 11.43897 Å, c = 11.46897 Å, α = γ = 90 °, β = 109.3176 °.*[11] *(E) Monoclinic Gd_2MoO_6, Space group: C2/c, a = 16.527 Å, b = 11.184 Å, c = 5.420 Å, α = γ = 90 °, β = 108.438 °.*[12,13] *(F) Orthorhombic $Gd_4Mo_4O_{11}$, Space group: Pbam, a = 10.7940 Å, b = 15.9876 Å, c = 5.6942 Å.*[14]

In three structures of molybdate (Figure 6C-E), the oxidation state of Mo is +VI and all Mo centers are equivalent. In Gd_2MoO_6 and $Gd_2(MoO_4)_3$, Mo centers are tetrahedral[11–13] while in Gd_3MoO_7 it is octahedral.[10] In contrast, the structure of $Gd_4Mo_4O_{11}$ is much more complicated than these molybdates. There are 3 types of Mo (apixal Mo1, Mo2 and Mo3) depending on their position in the space, with the oxidation state estimated for Mo_4 groups of +X ($14e^-$ per Mo_4 group).[15] Each Mo1 links to 5 others Mo and 5 O and each Mo2/Mo3 links to 7 others Mo and 4 O.[15]

For the moment, we keep in mind these possibilities of principal secondary phases. As they have many differences in Mo's oxidation state and Mo's geometrical environment, the local structure analysis methods will be helpful to understand the final powders. This will be discussed further this chapter.

3. Characterization of the powders

3.1. Trends observed in the samples series as a function of *x*

3.1.1. Trends in composition by EDS

As mentioned at the beginning of the chapter, three kinds of precursors were used for the synthesis of Gd_2O_2S/Mo_{2x}. Here, we show the detailed analysis for samples with $a = b = 0$, with a second step at 310 °C, corresponding to our optimized protocol. Figure 7 shows the global results of analysis on their composition by EDS. For this analysis, the detector can only detect elements heavier than Fluorine. It means that the amount of oxygen in the powder is only a proposed value (based on the Gd_2O_2S structure, without counting organic ligands) as we cannot quantify it. The other concerned elements (Gd, Mo, S and Na) are quantified by automatic calculation by the software INCA.

The difficulty in data treatment of this method is that the peaks S K-edge and Mo L-edge which allow the elemental quantification are located mostly at the same position (Figure 7E). Hence,

the reconstruction of the curve (elemental quantification) done automatically by the software INCA may cause some errors on the final amount of Mo and S. For this reason, the calculation below is only an assumption for the moment. It is also the reason why a re-calculation by deconvolution is necessary to confirm the showed results.

Figure 7A and B show the relation between observed molar ratio Mo/Gd and S/Gd and *x* for all samples, calculated from EDS measurements with the supposition that no Gd is lost during the second step of synthesis. Each point on the graph represents an average value of 5 zones of measurement and the error bars represent the standard deviation for these 5 zones. The samples made with **Mo(+I)** precursor are represented in black, the samples made with **Mo(+VI)** are in red and in green are the samples with **Mo(+III)**. Figure 7A shows also the possible behaviors of observed ratio Mo/Gd when *x* increases: (1) very small amount of Mo is lost after 2nd step (hard orange line) or (2) the sample can tolerate a maximum ratio Mo/Gd around only 0.05 (dash line). The hard orange line is $\boldsymbol{y = 0.8956\ x - 0.0194}$. It passes on most of points corresponding to samples made with the Mo(+I) precursor. However, two out of three points corresponding to $x = 1.0$ and one corresponding to $x = 2.03$ are situated way too much lower than expected (marked with red fleshes) and for samples with $x < 0.5$, the points rather make a cloud than follow the bisector. The dash line corresponds to the average value of observed ratio Mo/Gd of samples with *x* from 0.05 to 0.18, made with Mo(+I) precursor.

Figure 7B shows the expected ratio S/Gd of 0.13 with a dash line: it is the observed value in Gd_2O_2S/Mo_0 reference, lower than that in Gd_2O_2S nanoparticles (0.18 ± 0.02, calculated average from 6 samples, verified by our group and another group[1,2]). Regardless of the trend for the observed Mo/Gd ratio, the observed S/Gd ratio does not increase above 0.2 (for average values, Figure 7D). It even decreases as soon as Mo is added in the synthesis from about 0.2 down to about 0.1 at $x \approx 0.1$ then increases back up to 0.2 at $x = 0.25$. The lower bound for observed S/Gd ratio is similar to what is found in Gd_2O_2S/Mo_0 reference. For $x > 0.25$, the observed S/Gd ratio tends not to change anymore. Even when $x = 1.0$, there is no additional S found in the final powder. These results suggest that the introduction of molybdenum precursor (regardless of its oxidation state and of the observed crystalline phases) does not result in the incorporation of more sulfur in the final power.

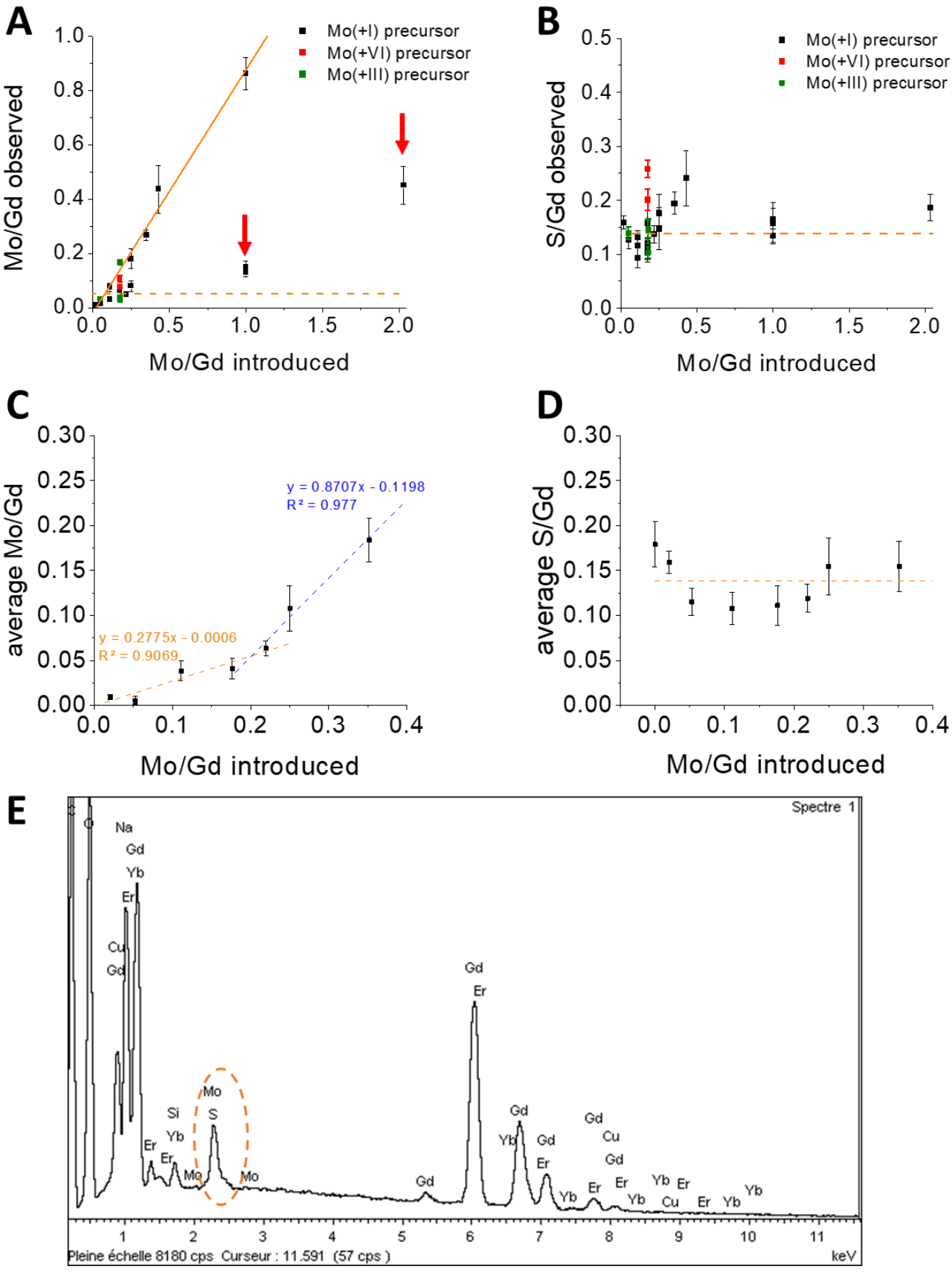

Figure 7 Composition analysis by EDS of all samples. (A) Observed molar ratio Mo/Gd vs. introduced ratio: samples made with Mo(+I) precursor (black), Mo(+VI) precursor (red) and

Mo(+III) precursor (green). (B) Observed molar ratio S/Gd vs. introduced molar ratio Mo/Gd: samples made with Mo(+I) precursor (black), Mo(+VI) precursor (red) and Mo(+III) precursor (green). The dash line represents the ratio S/Gd in Gd_2O_2S/Mo_0 reference. (C) Average observed molar ratio Mo/Gd vs. introduced ratio for all samples made with Mo(+I) precursor up to x = 0.35, the dash line represents an estimation of possible trends. (D) Average observed molar ratio S/Gd vs. introduced Mo/Gd ratio for all samples made with Mo(+I) precursor up to x = 0.35, the dash line represents the average ratio S/Gd in Gd_2O_2S/Mo_0 reference. (E) Spectrum of a zone on a sample $Gd_2O_2S/Mo_{0.36}$ (x = 0.18). In circle: inseparable peaks S K-edge and Mo L-edge.

In order to provide a deeper analysis, we focalized on the samples prepared with up to 0.4 equiv. of the Mo(+I) precursor (Figure 7C and D). In each graph, the points are average values calculated from all samples having the same *x*. The error bars on these graphs represent the standard deviation between them. These reduced dataset is more consistent and easier to analyze. Two trends are observed in Figure 7C, indicated by two dash lines which are the regression in two subgroups of samples, above and below $x = 0.25$. Figure 7D indicates a possible decrease of S amount in the final powder when the Mo amount increases to this value. In the first regime, the slope of 0.3 suggests that not all the introduced Mo is present in the final powder. In the second regime, a higher slop of 0.8 is observed, suggested that another reaction (or set of reactions) allows to incorporate more Mo in the final powders. Because the observed S/Gd ratio mostly stays constant, such reaction might not involve the presence of separated molybdenum sulfide species. Structural analysis was then performed to gain further insights.

3.1.2. Trends from structural analysis

Figure 8 shows the diffractograms of three families of samples made with three different precursors in comparison with annealed Gd_2O_2S nanoparticles as reference. In most of the diffractograms, there is a broad signal around 13 ° which is the position of peak (001) of Gd_2O_2S. In the direction [001], the thickness of the Gd_2O_2S nanoparticles is only about 1.5 to 2 nm,[6] hence, it is comprehensible to observe a very large peak (001). Also, around this region, there can be some contribution of the organic ligands' organization on the nanoparticles' surface. In any case, present or absent, the broad peak does not affect the rest of the diffractograms. We exclude it from data analysis from now on.

For the samples made with Mo(+I) precursor, the value of *x* in the synthesis varies between 0.02 to 2.03. For the two other series with the two other precursors, less samples were prepared:

only three values of x for the Mo(+VI) precursor and two values for the Mo(+III) precursor. They are displayed to provide a comparison in terms of precursor reactivity. The diffractograms of classical Gd_2O_2S and Gd_2O_2S/Mo_0 references are showed in Figure 8A with the positions of Gd_2O_2S bulk phase's Bragg peaks (JCPDS file 00-026-1422, experiment-based). As mentioned previously, after reheating the medium to 310 °C for 30 min to make Gd_2O_2S/Mo_0, the crystalline structure of original Gd_2O_2S has already evolved: there is a clear splitting of the peak (101) and a small peak shift for peak (110) distance (dash line). The small peak shift can be observed better in the zooms. The dash lines in the four zooms are all aligned to the peak (110) of the JCPDS file 00-026-1422 to better visualize the peak shifts.

With an addition of Mo(+VI) precursor (Figure 8B), the final powders tend to have less differences in the zone of peak (101) compared to classical Gd_2O_2S than samples with other precursors, but more differences to Gd_2O_2S/Mo_0 reference. If we analyze specifically all the samples $x = 0.18$ with different Mo precursors, we observe that there is no obvious shift for peak (110) (marked with dash line) in the case of Mo(+VI) precursor while obvious for the two other ones. This is coherent with the shift on the peak (101) mentioned above.

For the series made with Mo(+I) (Figure 8C), there is clearly a splitting of peak (101) into 2 peaks with their intensities varying with x and an obvious shift of peak (110) to the left (longer distance). Also, from observation, we can initially divide these series into two subgroups: $x \leq 0.25$ where the splitting is visible and $x > 0.25$ where there is no more splitting. It means that the structures are similar to the reference $x = 0$. The value of $x = 0.25$ which divides the XRD data into two subgroups here is the same as the one which divided the EDS data into two subgroups. At very high introduced quantity of Mo ($x = 2.03$), the secondary peaks are identified as of Na_2MoO_4 (Figure 8C, zoom, JCPDS file 01-084-6509, calc).

For samples made with Mo(+III) precursor (Figure 8D), there exists also a splitting of peak (101), but the intensity varies more randomly than in function of x. Here, we observe an obvious shift of peak (110) to the longer distance too.

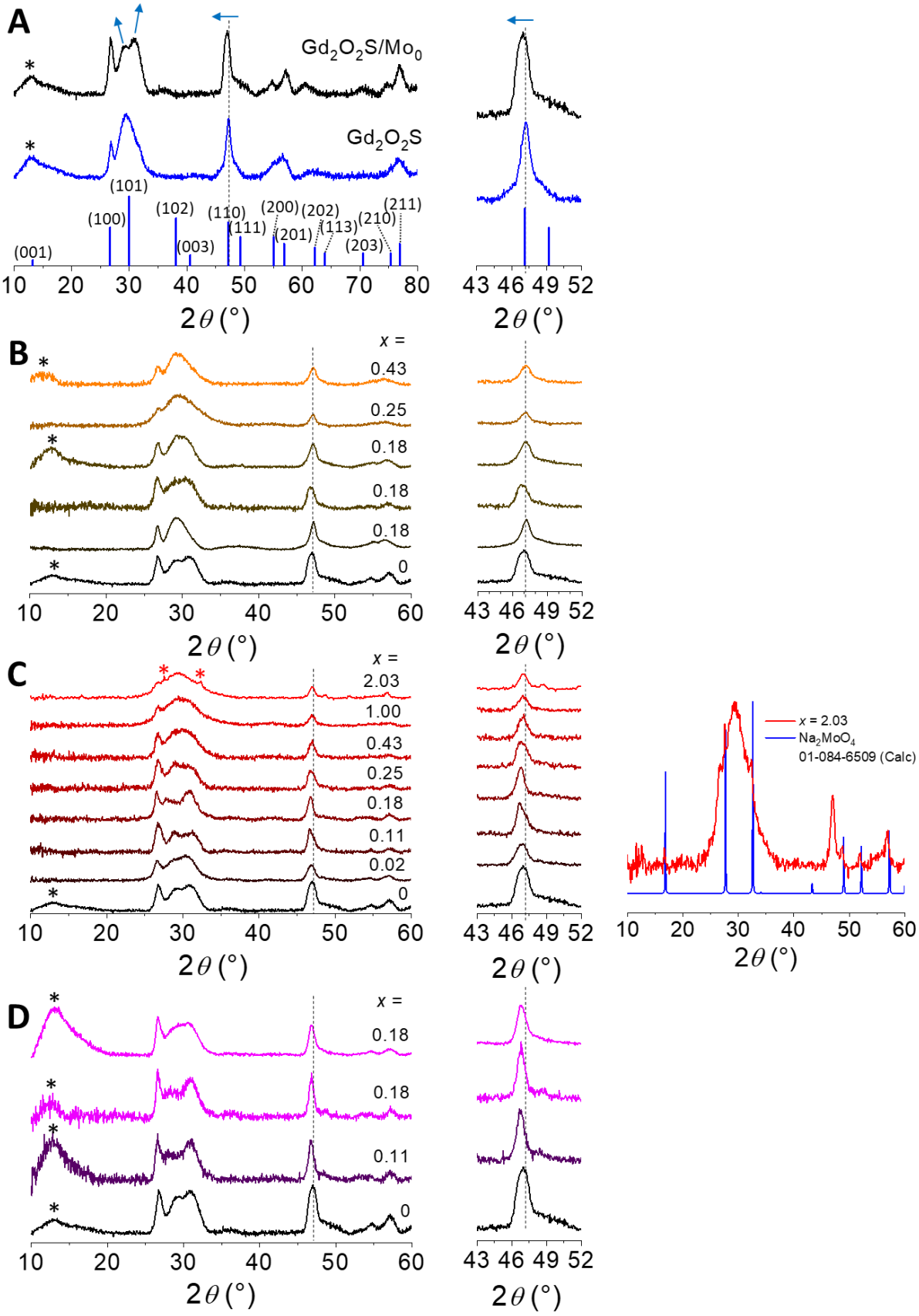

Figure 8 (A) XRD of classical Gd_2O_2S and Gd_2O_2S/Mo_0 reference with peaks positions from JCPDS file 00-026-1422, experiment-based, and a zoom on peaks (110) and (111). Dash line:

peak (110) used for structural analysis. Broad peaks marked with black star may be attributed to peak (001) and some organic ligands' organization, not yet well identified. (B) XRD of the samples series made with Mo(+VI) precursor x = 0.18; 0.25 and 0.43 with a zoom on peaks (110) and (111). (C) XRD of the full samples series made with Mo(+I) precursors x from 0.02 to 2.03 with a zoom on peaks (110) and (111) and a zoom on the sample x = 2.03 in comparison with Na_2MoO_4 (JCPDS file 01-084-6509, calculated). (D) XRD of samples made with Mo(+III) precursors with x = 0.05 and 0.18 with a zoom on peaks (110) and (111). peaks marked with red star: may belong to some secondary phase(s).

At this point, the observed structural evolution could not be assigned to the apparition of new phases or structural distortions of existing phases. Regarding this latter point, we have used in a previous study the (110) peak, the thinnest of the pattern, as a direct indication of modification of the lattice parameter *a* (as explained in chapter I).[2] In a further section, we tried to employ the same methodology, but first, we investigated the impact of the second step on the structure and the morphology of the initial nanoparticles (without Mo).

3.1.3. Consequence of the second heating step on the initial nanoparticles

First, we investigated the change in morphology of Mo-containing products to classical Gd_2O_2S and Gd_2O_2S/Mo_0 reference by Transmission Electron Microscopy (TEM) (Figure 9). We are able to observe these nanoparticles at high magnification (×350 000) on {001} face and {100} side (of Gd_2O_2S nanoparticles) with our equipment. Globally, the morphology of nanoplates is maintained in all samples made by the two-step protocol with or without Mo (Figure 9A and C). Unlike classical Gd_2O_2S (made by the one-step protocol), Gd_2O_2S/Mo_0 displays an interplanar distance of 8.0 Å (Figure 9B), too large to correspond to any interreticular distance. In fact, it is not observed by XRD even at small angles (see Annex 1), so, cannot correspond to any distance between two atomic planes. This distance is also observed in other samples with Mo, e.g. a $Gd_2O_2S/Mo_{0.36}$ sample in Figure 9D and a $Gd_2O_2S/Mo_{0.86}$ sample in Figure 9E. This distance is present in mostly all samples made with Mo(+I) precursor: 26/33 samples were analyzed by TEM, this distance was observed in all of them (in 4 samples, this distance was blurred). The strange thing about this distance is that it can be present or not just by changing very slightly the focus (Figure 14E, F) and totally absent on the diffractograms at small angles (Annex 1) and on the electron diffraction patterns. At the same time, another type of nanoparticles was observed (Figure 9F) for a sample with $x = 1.0$. They are much bigger than Gd_2O_2S (about 30 nm of diameter) with "holes" and the crystalline domains seem very large. This nanoparticles type is not frequently observed, perhaps the reason is that they are minority

in the sample even with high value of *x*, which is coherent with the diffractograms (no obvious thin peaks are present). Despite that their diffraction fringes are clear in more than one direction, this crystalline phase is not yet identified. The morphology of these big nanoparticles is similar to that of "$MoO_{(2.5+0.5a)}S_{0.5}/Na_a$" which will be discussed in Chapter IV.

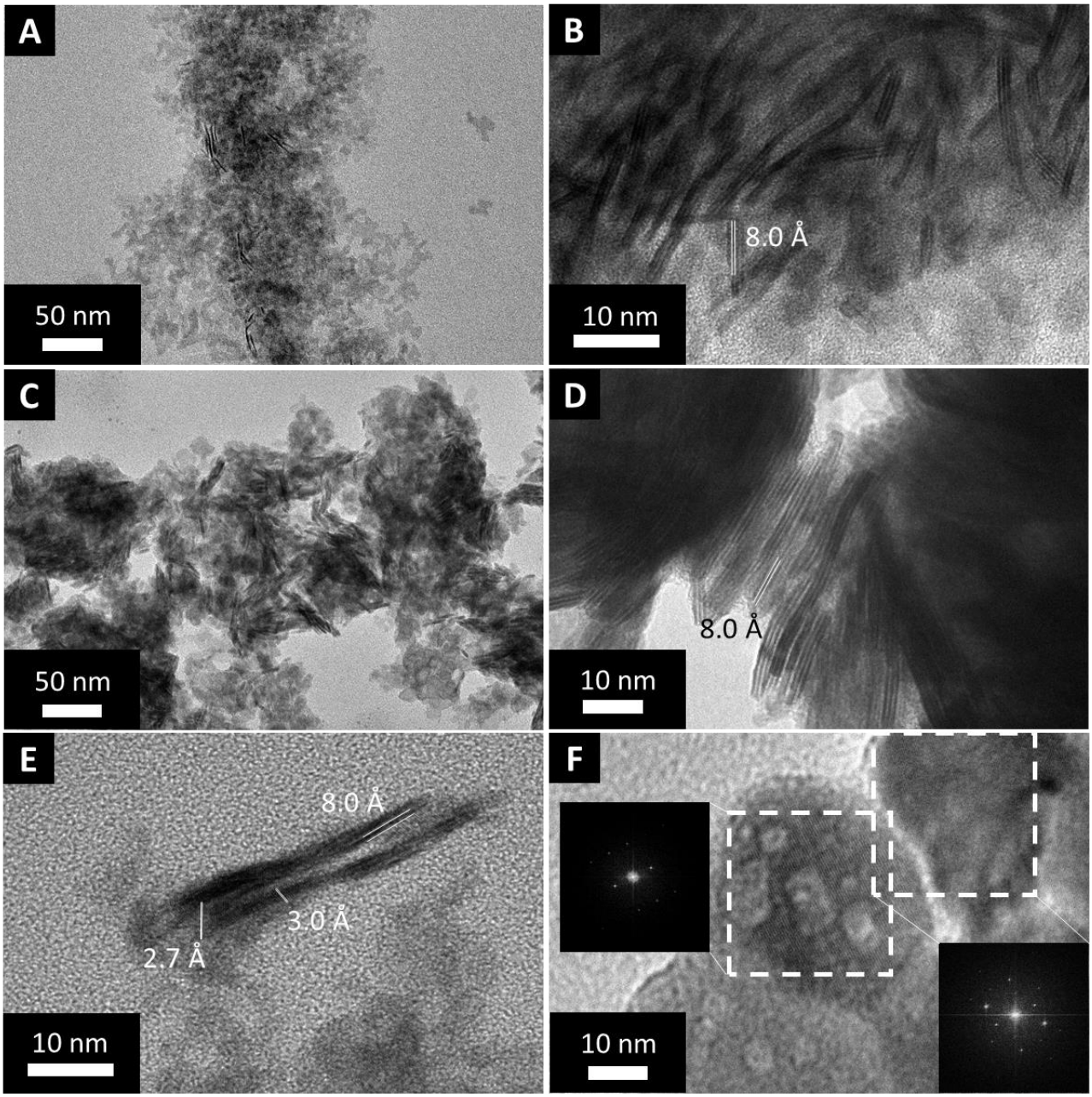

Figure 9 (A) TEM images of Gd_2O_2S nanoparticles showing nanoparticles by {001} face and {100} side: zoom at ×42 000. (B) TEM images of Gd_2O_2S/Mo_0 nanoparticles zoom at ×350 000. (C) Morphology of Mo-containing samples seen by TEM, with x up to 0.25, zoom at ×42 000. (D) Nanoplatelet-like Mo-containing nanoparticles morphology, with x up to 0.25, zoom at ×265 000. (E) Nanoparticles with x much higher than 0.25 (here x = 0.43), zoom at

×350 000. (F) Other crystalline nanoparticles with holes on the surface or inside them, observed in one Mo-containing sample with x = 1.0, not yet identified, zoom at ×265 000. The calculated FFT are shown for 2 nanoparticles.

The change in local structure of Gd_2O_2S after the 2nd step is investigated by Pair Function Distribution (PDF). The PDF analysis was done not only using LCMCP equipment but also in SOLEIL Synchrotron on beamline Crystal (measurements performed by Capucine Sassoye and Alex Lemarchand from our laboratory, see Experimental Section). The comparison between experimental patterns of the same sample measured by both instruments shows that the signal quality by our laboratory X-ray source and measurement setup is good enough for comparing the experimental data with the simulated ones (Annex 2). The comparison of two experimental curves (Figure 10A) shows that both samples (classical Gd_2O_2S in black and Gd_2O_2S/Mo_0 in orange) measured at LCMCP have the same contribution of peaks up to 100 Å. Globally, there are only differences in intensity and FWHM (full width at half maximum) but no difference in peak positions: the peaks of Gd_2O_2S/Mo_0 are slightly thinner and more intense than those of Gd_2O_2S. Knowing that the average size of nanoparticles from the synthesis in one step is about 6 nm, here we observe an attenuation of the signal (marked with dash line) around 6 nm which is coherent (Figure 10A). The high similarity between the two curves signifies that the shape and size of the nanoparticles after annealing do not change, i.e. the 2nd step does not have any effect on the shape and size of the nanoparticles. Knowing that the yield of Gd_2O_2S/Mo_0 is much higher than Gd_2O_2S (102 % *vs.* 80 % in average), there might be some additional surface ligands in annealed sample compared with the initial one, possibly because the ligands are better organized on the nanoparticles.

The surface ligands are analyzed by IR in ATR mode. The results and proposition of band attributions are shown in Figure 10B. For the measurements, the quantity difference between samples is neglectible, so, the difference in band intensity reflects only the structural difference between the samples. The comparison between two IR spectra shows several obvious difference between two samples without Mo. Firstly, peaks at 2921 cm^{-1} (asymmetric stretching ν_a), 2852 cm^{-1} (symmetric stretching ν_s) attributed to methyl and methylene groups (C-H) have higher intensities. Secondly, the wide bands between 1300-1600 cm^{-1} attributed to COO sketching are also more intense for the Gd_2O_2S/Mo_0 sample than classical Gd_2O_2S. These wide COO bands will be discussed more in detail below. In general, all the peaks of Gd_2O_2S/Mo_0 sample are not only more intense (visible peaks are principally from organic components) but also thinner, especially there are a large enhancement of the peaks at 1492 cm^{-}

[1] (medium), at 858 cm^{-1} (changes from weak to medium), and an apparition of a new thin peak at 1105 cm^{-1} (weak).

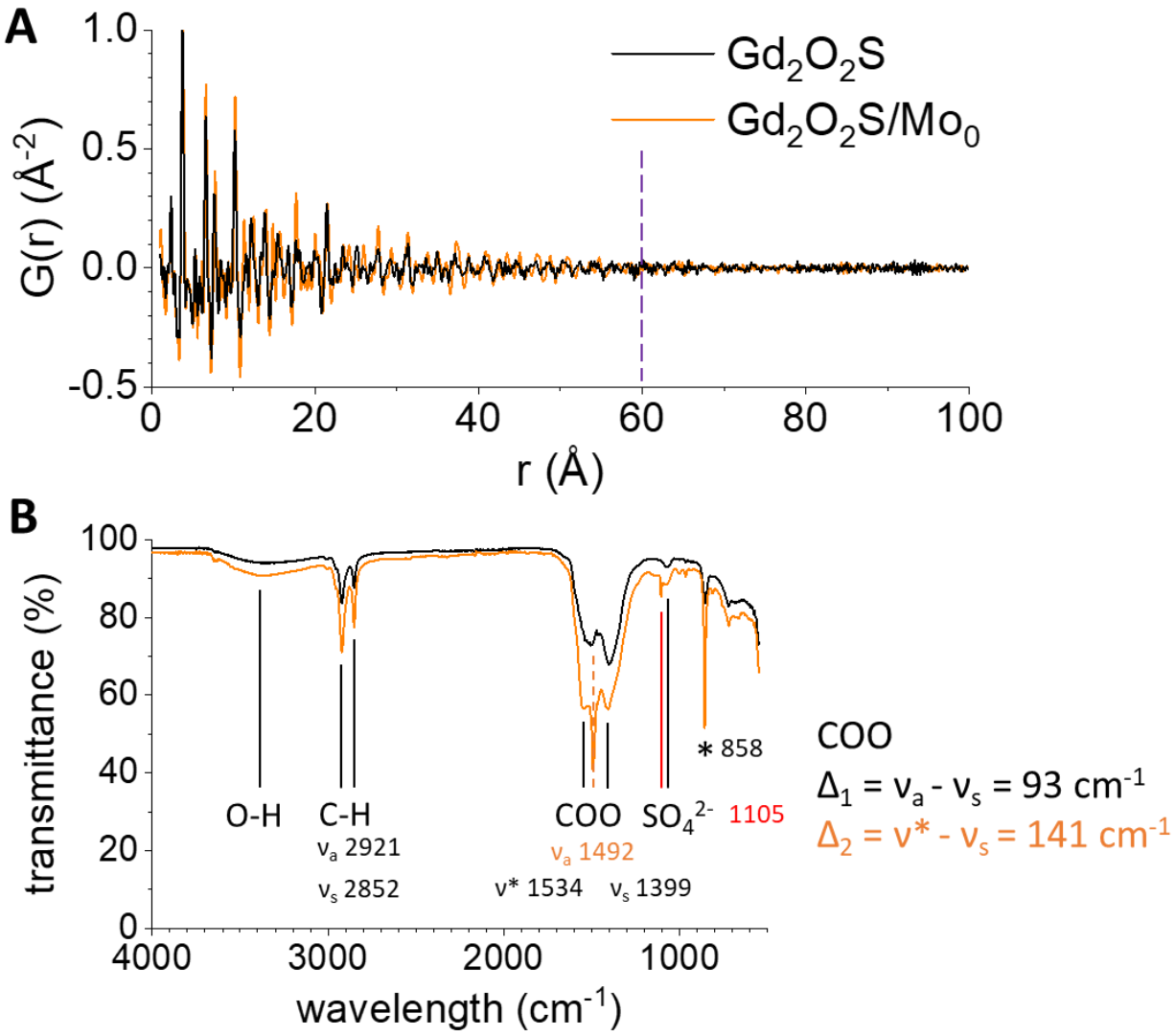

Figure 10 (A) Comparison of PDF patterns between Gd_2O_2S nanoparticles and Gd_2O_2S/Mo_0, both measured at LCMCP, patterns extracted up to 100 Å with Q_{max} = 15. (B) Comparison of IR spectra measured in ATR mode between Gd_2O_2S nanoparticles and Gd_2O_2S/Mo_0. The legend in (A) is common for both (A, B).

The changes are visible in particular in the carboxylate region, we propose here a hypothesis on band attribution and interpretation of these results. In general, thinner IR bands correspond to weaker intermolecular interaction around the concerning bond and more intense peaks correspond to more polarized bonds.[16] About the COO bands, for Gd_2O_2S/Mo_0 nanoparticles, the peak at 1492 cm^{-1} (asymmetric stretching ν_a) is not only enhanced but also much more intense than the peak at 1399 cm^{-1} (symmetric stretching ν_s). The bump at about 1534 cm^{-1} in

Gd_2O_2S becomes a separated peak at 1542 cm^{-1} in Gd_2O_2S/Mo_0 (named ν* as now it is not surely attributed yet). The splitting values for these peaks are $\Delta_1 = 93\ cm^{-1}$ ($\nu_a - \nu_s$) and $\Delta_2 = 143\ cm^{-1}$ ($\nu^* - \nu_s$). Based on a molecular model of $Ce_{19}O_{32}$,[17] the splitting Δ_1 could be attributed to chelating oleate chains and the splitting Δ_2 can be attributed to bridging ones, ν_s is the same for both of them.[18] This suggests that firstly, there are more ligands on the surface of the nanoparticles and are more ordered after annealing; secondly, the bonding type of ligands to the surface is probably different. This observation is quite coherent with other works on oleate chains as surface ligands on different types of nanoparticles (CeO_2, both peaks are thin, ν_s more intense;[19] ZrO_2 film on Al, thin peak ν_s, large peak ν_a, peak ν_s more intense;[20] PbS quantum dots, measured in absorbance, all peaks are large, ν_a and ν* more intense, ν_a more intense than ν*[18]).

The thin peak at 858 cm^{-1} is not yet attributed for the moment but it is possibly from the organic component as it follows the trend of the peaks corresponding to C-H and COO. In a work on ceria nanoparticles, a similar peak observed with the similar behavior as our case can be a point supporting to this hypothesis.[21]

The apparition of the thin peak at 1105 cm^{-1} is not yet understood. This is the zone of S-O bonding of sulfate's vibrations, the peak might correspond to another kind of linking between sulfate and the nanoparticles.

From these results, we can state that after annealing, there is no change in the inorganic phase of Gd_2O_2S (by PDF analysis). There are only changes in the way the surface ligands linking to the nanoparticles, which causes the changes in the diffractograms (as the nanoparticles are very thin, it is easy to be affected by surface ligands), the morphology and the IR spectra. Although some reference articles are found for IR analysis, there are still many different points between them and our spectra on the peak width and the ratio between two stretching modes of COO, a further work is essential to understand the organization of surface ligands in the annealed sample(s) (without and with Mo). We also confirm that the change in the morphology of nanoparticles observed by TEM is totally independent with the presence of Mo in the synthesis.

The quest on Mo-containing structure continues!

3.1.4. Trends in local structures by XAS for samples made with Mo(+I) precursor

In order to understand the structure and also the relation between it and the electroactivity later, we performed spectroscopy analysis on the samples series made with Mo(+I): X-ray

Absorption Spectroscopy (XAS) and X-ray Photoelectron Spectroscopy (XPS) at SOLEIL Synchrotron.

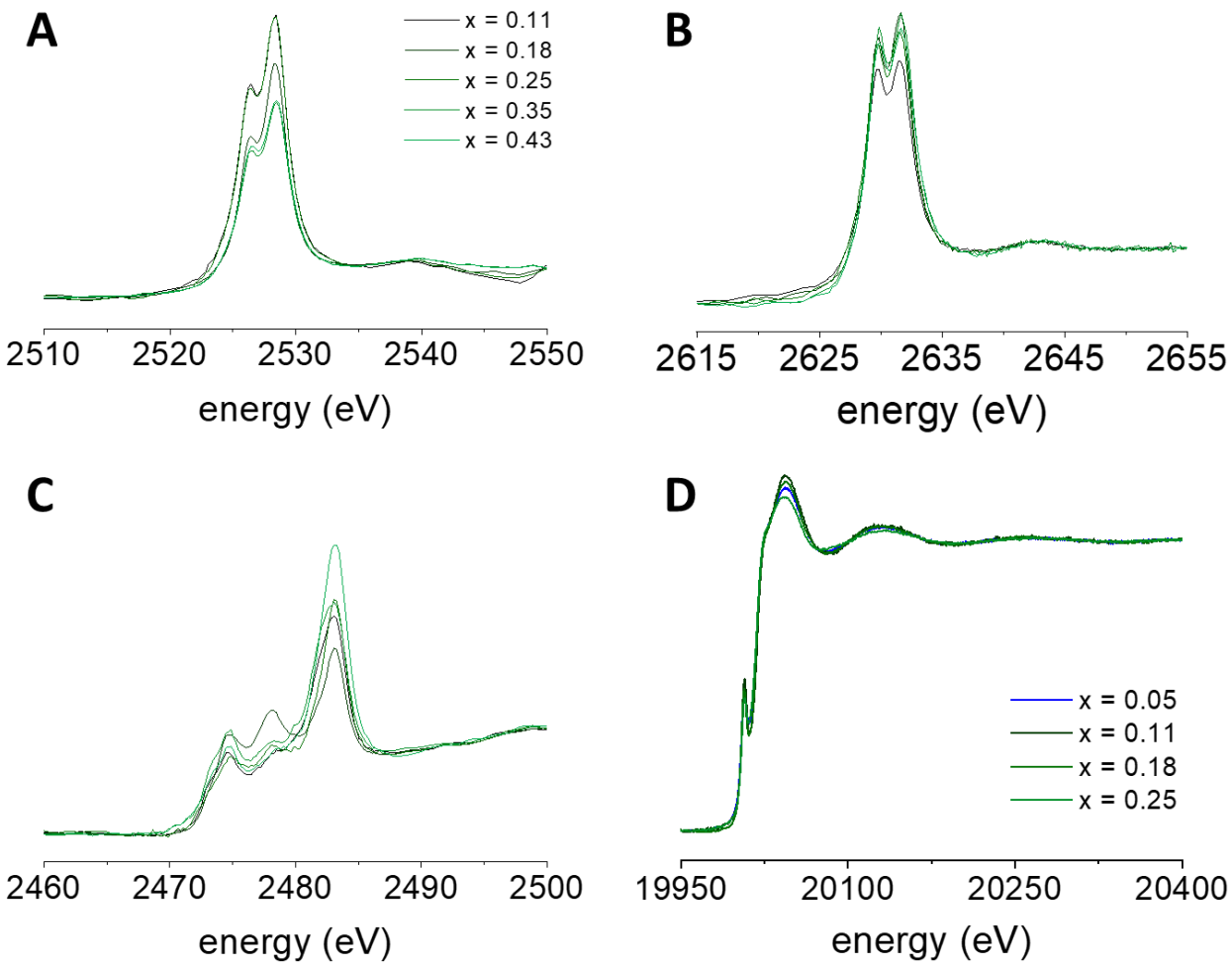

Figure 11 X-ray Absorption Spectroscopy (XAS) of samples made with Mo(+I) precursor at (A) Mo L_3-edge, (B) Mo L_2-edge, (C) S K-edge and (D) Mo K-edge. The legend in (A) is common for (A-C).

Figure 11 shows the spectra of these samples at K-edge, $L_{3,2}$-edges of Mo and K-edge of S. They are obtained with the samples diluted in pellets with graphite. At Mo L_3-edge, the edge of all samples are the same at 2523.8 eV based on the position of the signal's first derivative (Figure 11A). The splitting energy is 2 eV, identical for all samples. At L_2-edge, there are less effect of spin-orbit coupling, the similarity between samples becomes more visible (Figure 11B). The splitting energy here is 1.8 eV.

In terms of S K-edge, the spectra all contain 3 peaks at 2472.6 eV, 2476.4 eV and 2481.3 eV with their intensities varying randomly from one sample to the other (Figure 11C). The last peak at 2481.3 eV is always the most intense of the three. From our first observation, we can

state that the local structures of all Mo-containing samples in this series are similar, there is no threshold of *x* value for a division in subgroups as for XRD and EDS results.

Similarly to the Mo L_2-edge spectra, at Mo K-edge, we observe that all samples with $x \leq 0.25$ have the same edge (20 004 eV, first derivative), pre-edge (peak at 20 006 eV) and the shape of multiple-scattering zone (Figure 11D), which suggests a high similarity of local environment, geometry and oxidation state of Mo in all samples. The presence of quite intense pre-edge confirms the majority of tetrahedral Mo centers in the powders. However, the intensity of the white line does vary in function of increasing *x*, the order of decreasing white line intensity is: $x = 0.11 > x = 0.18 > x = 0.05 > x = 0.25$, i.e. no clear tendency for this variation.

We will discuss these results in the next part for the oxidation state of Mo in the synthetic samples, to understand the geometry and the local environment of Mo centers as well as the relation structure-electrochemical activity.

The oxidation state of Mo was evaluated by XPS performed on a lab instrument and on the beamline TEMPO-B at SOLEIL, and they were treated and interpreted by Alexy Freitas in our research team. The discussion below is written by the same author. It is issued from analysis data on the sample KL151 $Gd_2O_2S/Mo_{0.36}$ ($x = 0.18$).

One representative dataset of the Mo 3d – S 2s region is shown on Figure 12A. Due to spin-orbit coupling, the Mo 3d orbitals are splitted into Mo $3d_{3/2}$ and Mo $3d_{5/2}$. Thus, the expected XPS signal for Mo is a doublet, exhibiting a splitting of 3.15 eV and an intensity ratio of 2:3. In our case, an acceptable fitting of the signal for Mo 3d signal (at BE > 230 eV) can be achieved using two doublets, suggesting the presence of two redox states in the sample.

However, the attribution of these components is difficult because the positions of the doublets do not correspond to any known Mo species. According to NIST XPS database and to the literature, the binding energy of the $3d_{5/2}$ orbital for molybdenum is expected to range between 227.6 eV and 232.5 eV for Mo(0) and Mo(+VI), respectively. For the first component, the Mo $3d_{5/2}$ peak is located at 233.9 eV (and the Mo $3d_{3/2}$ is located at 237.05 eV), while the second component is located at 235.15 eV for Mo $3d_{5/2}$ (and 238.3 eV for the Mo $3d_{3/2}$), meaning that, in both components, the 3d electrons have binding energies higher than Mo(+VI). Because the 4d shell of Mo(+VI) is empty, is highly unlikely that we formed some "Mo(+VII)" or "Mo(+VIII)" compound. Instead, in collaboration with Asma Tougerti (Unité de Catalyse et Chimie du Solide, UCCS, Université de Lille I), we propose that Mo and Gd have a stabilizing

interaction which would stabilize the 3d orbitals of Mo. The supposed interaction could involve Mo 3d electrons and Gd 4p electrons, since their binding energies are close (around 270 – 285 eV for Gd 4p). To check this hypothesis, we are currently performing energy calculations of such exotic interaction. In the future, an XPS on the region Gd 4p would be very interesting to confirm this interaction between Mo 3d and Gd 4p.

On Figure 12A is also shown the XPS signal of the S 2s region. In good agreement with the signal of the S 2p region (Figure 12B), we needed three components to obtain a decent fit of the signal. These three components are located at 226.1, 227.8 and 228.9 eV and are attributed to S(-II), S(+IV) and S(+VI) respectively, according to NIST XPS database.

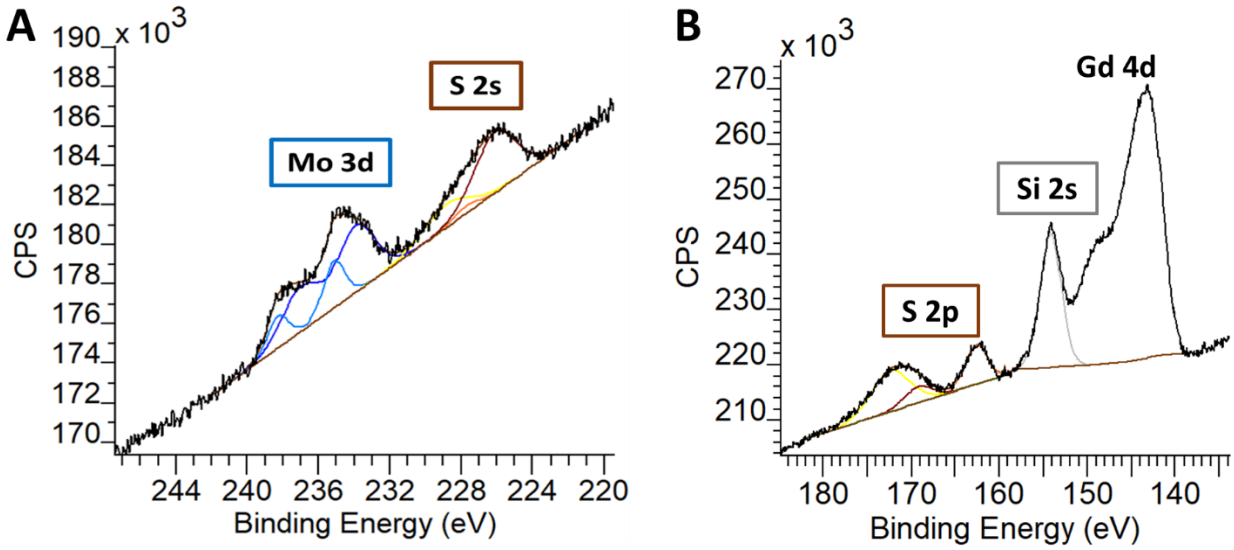

Figure 12 (A) XPS signal of the Mo 3d – S 2s region of the $Gd_2O_2S/Mo_{0.36}$ (x = 0.18) sample (KL151). In light blue, the most "oxidized" Mo-species, with the $3d_{5/2}$ peak at 235.15 eV, in dark blue the most "reduced" Mo-species, with the $3d_{5/2}$ peak at 233.9 eV. In brown, signal attributed to S(-II), in orange, signal attributed to S(+IV), and in yellow signal attributed to S(+VI). (B) XPS signal of the Gd 4d – S 2p region of the same sample. In brown, signal attributed to S(-II), in orange, signal attributed to S(+IV), and in yellow signal attributed to S(+VI).

For the same sample, we also analyzed the Gd 4d – S 2p region, shown on Figure 12B. First, we note the presence of silicon: the peak at 155 eV is attributed to Si 2s. There are two hypotheses for the presence of Si: it can come from either the Si wafer onto the sample was deposited, or it can be residual grease from the glassware, taken during the uptake or the washing steps. Second, the Gd 4d region is also straightforward to interpret: the signal can be attributed to only Gd(+III) species (complicated multiplet).[22] Regarding the S 2p region, three

doublets are necessary to correctly fit the data. These three signals are attributed to the presence of S(-II), S(+IV) and S(+VI) species. Here we observe an inversion of ratio between 2 components S(-II) and S(+VI) from the S 2s region (Figure 12A) to S 2p region (Figure 12B). The reason is that there is a signal massive by Gd 4d in the region of S 2p of S(+VI), which means the component S(+VI) in S 2p region is its sum with Gd 4d.[22]

3.1.5. Surface activity evaluation on spinning Glassy Carbon Electrode (GCE) in basic medium

Electrochemical tests of Oxygen Reduction Reaction (ORR) were performed to investigate the activity of selected samples. All measurements were done in a solution of KOH 0.1 M (pH 13) as electrolyte, renewed for each working day and saturated previously with O_2; in the working range 0 V to -0.6 V *vs.* Ag/AgCl in saturated KCl, i.e. 0.964 V to -0.364 V *vs.* Reverse Hydrogen Electrode (RHE) at pH 13, with a scan rate of 10 mV/s; and with a rotation rate of 1600 rpm of the working electrode during the runs.

For this work, the tests are only preliminary: the aim is to validate the working method, then to have first idea of the materials' ORR reactivity, the effect of introduced Mo on the observed reactivity and finally, the repeatability of the test. This is the reason why the further analysis on the performance and the mechanism (by calculating and commenting the Tafel plots) is not yet considered.

Figure 13 shows the measured curves normalized by the geometric surface area of electrode (0.196 cm^2). The tests for activity were done with inks having weight ratio C black/nanoparticles of 1:1 and 2:1 (ink type Cx1 and Cx2 respectively, see Experimental Section) and they were repeated at least once. To compare activity of different samples, we use the difference of half-wave potential ($E_{1/2}$) between sample/ink and naked electrode. This value is noted $\Delta E_{1/2}$. The higher $\Delta E_{1/2}$ is, the more active the sample/ink is (the reaction occurs sooner). In our case, the difference of potential measured at -1.0 mA/cm^2 (noted ΔE) is also used as supplementary information as $\Delta E_{1/2}$ is small. In general, the results of electrochemical tests depend as much on external conditions than on the activity of material itself: these are delicate measurements to carry out. Moreover, the obtained current in these tests are much lower than for reference catalyst (e.g. Pt on C black, etc.) and quite close to that of naked electrode; the data treatment is then delicate.

For reference, commercial MoS_2 (90 nm mesh) purchased from SIGMA was used as well as Gd_2O_2S/Mo_0. From the literature, we know that MoS_2 can be active for ORR due to the Mo-S

edges, it gets more active when the nanoparticle size is reduced:[7,5] a smaller size of nanoparticles can increase the ratio of active sites on the surface, hence, makes them potentially more accessible for the reactants. If we consider the obtained nanoparticles as supported catalysts where the support is Gd_2O_2S/Mo_0 nanoparticles, we needed to see if the support itself is active for ORR or not.

In comparing activity of Gd_2O_2S/Mo_0 with naked electrode, we see that the 2 cyclic voltammetry (CV) curves can be mostly superposed (Figure 13A). The maximum current is the same for naked electrode and Gd_2O_2S/Mo_0 in an ink Cx2). We can state that the Gd_2O_2S support is not active at all and any activity that we can observe in the next part has to come from the added Mo.

Considering a sample $Gd_2O_2S/Mo_{0.36}$ and commercial MoS_2 (90 nm), for the same kind of ink (weight ratio C black/nanoparticles 2:1), the two CV curves are close but cannot be totally superposed (Figure 13B). $\Delta E_{1/2}$ and ΔE are respectively 0.02 V and 0.02 V for commercial MoS_2, 0.04 V and 0.13V for the $Gd_2O_2S/Mo_{0.36}$ sample. Both values are higher for $Gd_2O_2S/Mo_{0.36}$ than commercial MoS_2 but for the reason mentioned above of the low current regime, we can only state that both solids have the same activity for ORR. The important point is that our Mo-containing sample is slightly active for ORR and this activity is linked strictly to the presence of Mo in the sample. The detailed calculation will be presented in the part 4.4 of this chapter.

To understand the stability of nanoparticles in the inks over time, we tested $Gd_2O_2S/Mo_{0.36}$ sample twice in two inks with Cx1 and Cx2 (see Experimental Section for the full description of the ink compositions). For the ink Cx1, the tests were done just after the ink preparation and after 6 days. For the other ink, the tests were done just after the preparation and after 1 day. The comparisons of observed activity are shown in Figure 13C and D. The CV curves of fresh ink and after 1 day can be totally superposed (Figure 13C), $\Delta E_{1/2}$ and ΔE are both 0.01 V. After 6 days, the activity is lost, $\Delta E_{1/2}$ and ΔE in this case are reduced from 0 V to -0.01 V and from 0.13 V to 0.04 V respectively, the maximum current is also reduced (Figure 13D).

The reason of activity loss was investigated by electrochemical tests with two inks made with a fresh nanoparticles suspensions and with a 2-month old one. Figure 13E shows the activity comparison of $Gd_2O_2S/Mo_{0.36}$ in these two inks with a reference of an ink Cx2. $\Delta E_{1/2}$ observed for the ink made with a new suspension (in blue), an old suspension (in red) and a reference (in green) are 0.04 V, 0.05 V and 0.03 V respectively. These values are very close but when we

consider the maximum current in plus, it becomes clearer that the 2-week old suspension gives an ink less active than a fresh suspension or an fresh ink Cx2. This suggests that there is an ageing of nanoparticles in the ink during the time that deactivates them (this point will be revisited in the next part). Or there may be a physical evolution of the nanoparticles (e.g. aggregation) in the inks which makes the number of electroactive component lowered after a time than in the fresh inks.

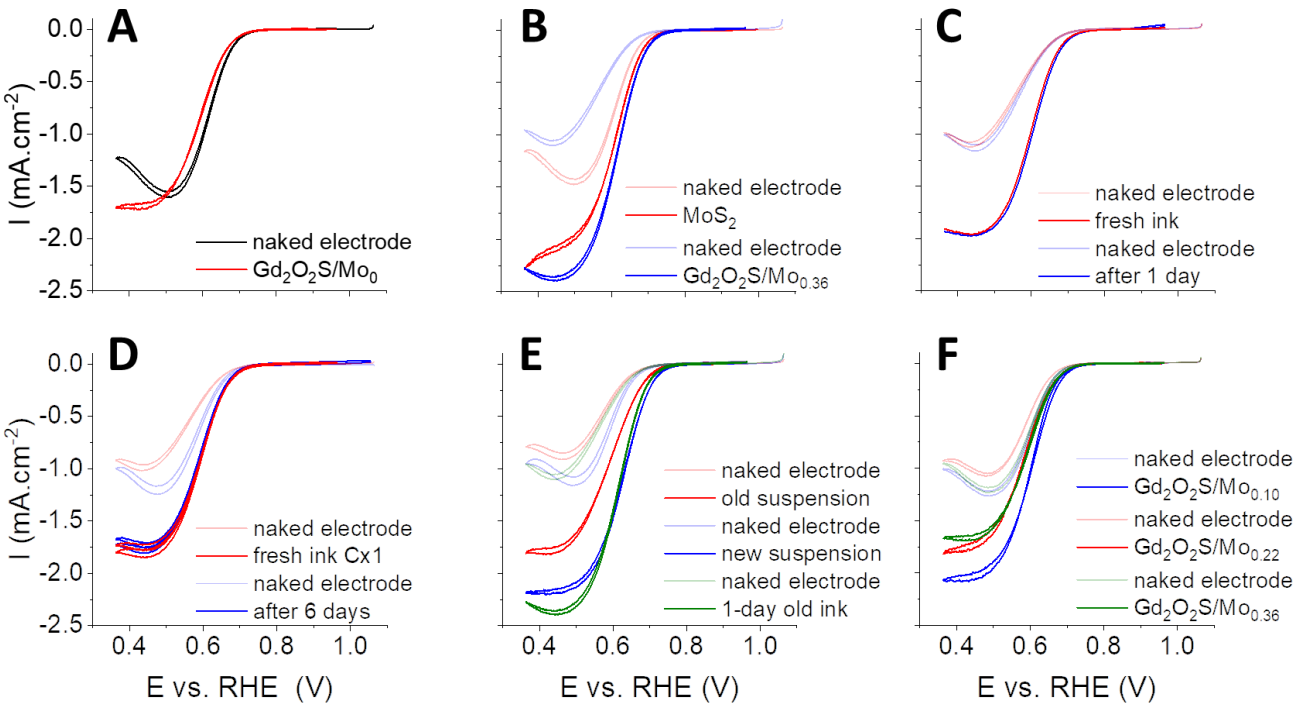

Figure 13 (A) Electrochemical tests of Gd_2O_2S/Mo_0 reference (ink Cx2). Comparison of activity between: (B) commercial MoS_2 (90 nm) and $Gd_2O_2S/Mo_{0.36}$; (C) the same ink: fresh and after 1 day; (D) the same ink: fresh and after 6 days; (E) an ink made from nanoparticles, an ink ma de from a fresh nanoparticle suspension and from an old suspension; (F) $Gd_2O_2S/Mo_{0.10}$, $Gd_2O_2S/Mo_{0.36}$ and $Gd_2O_2S/Mo_{0.36}$. All the tests are done with inks having weight ratio C black/nanoparticles of 2:1; except for the case of (D), it was 1:1. All the graphs have the same scale. Measurement conditions: electrolyte KOH 0.1 M (pH 13), rotation rate 1600 rpm, scan rate 10 mV/s.

The same tests were done on samples with $x = 0.05$ and 0.11 to see if there is any trend of activity as a function of x (Figure 13F). As they are all very slightly active, it is difficult to say if there is any trend but we can say that all three samples are active. It means that even a very small amount of Mo present in final powder can make it active for ORR.

We are at very beginning of the project, not everything about the structure is well described. The electrochemical tests are considered now only as a technique of characterization of surface's activity. No optimization of ink preparation was done and we do not discuss the performance of materials.

3.2. Characterization of $Gd_2O_2S/Mo_{0.36}$ samples

3.2.1. Morphology analysis

To understand the structure of material more in detail, we chose samples $x = 0.18$ for further structural analysis. The electrochemical tests shown previously were also done mainly with this sample.

Figure 14 shows the main observation of morphology in a final powder (A, B), in the ink before (C) and after (D) electrochemical reaction. The reference taken in this part is Gd_2O_2S/Mo_0 as the heating during the second step affected the final product's crystalline structure (Figure 8A), it can also effective for nanoparticles' morphology (Figure 9). Globally, obtained nanoparticles are nanoplatelets with stacking as in the case of classical Gd_2O_2S (Figure 14A). When the nanoparticles are observed closer, an interplanar distance of 8.0 Å is found by ImageJ analysis (Figure 14B). As mentioned previously, this distance does not correspond to any inter-reticular distance and cannot be seen by XRD at small angles, it can only be seen by adjusting the focus very slightly in TEM. This observation is typical for all samples made by the two-step protocol, with or without Mo (Figure 14E). Besides, others distances ranging between 2.9 Å and 3.3 Å are also found frequently in all samples, including the annealed sample without Mo (Figure 14B-F). These values correspond to interplanar distances in (110) and (101) directions of classical Gd_2O_2S. Here we cannot distinguish these two interplanar distances because the images are not from high resolution TEM (HRTEM), their quality is not good enough to have an accurate image treatment.

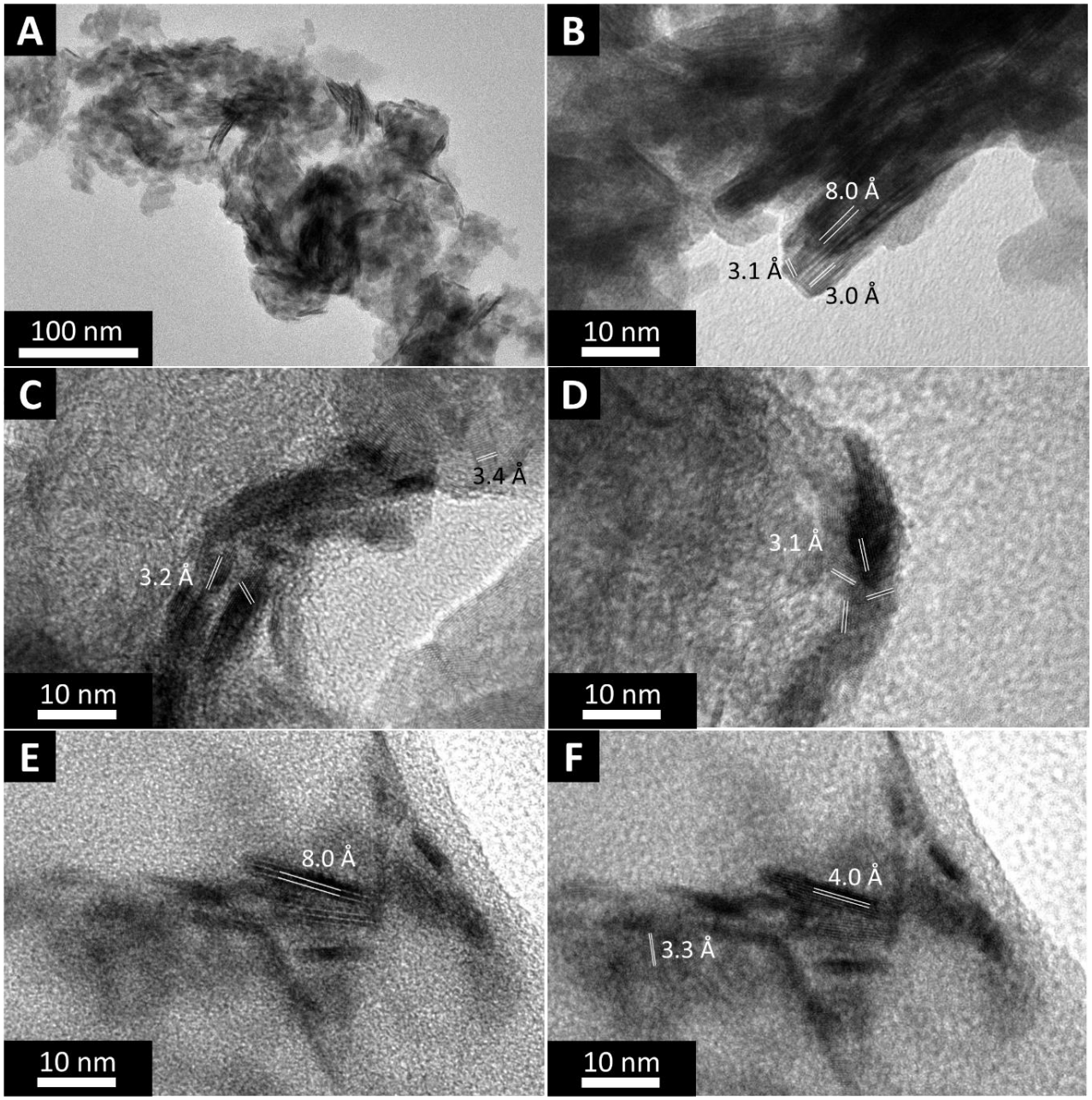

Figure 14 (A) A TEM image of a $Gd_2O_2S/Mo_{0.36}$ (x = 0.18) sample which is representative for the series' morphology. Morphology of samples with x = 0.18 (B) in the powder, (C) in a fresh ink, and (D) in the deposition after the electrochemical test. (E, F) Morphology of Gd_2O_2S/Mo_0 reference in powder with frequently observed interplanar distances. Images are taken at ×350 000.

3.2.2. Local structure analysis

As we have seen above, at Mo K-edge, all samples with $x \leq 0.25$ have the same edge and shape of spectrum. Here we compare the spectrum of sample $x = 0.18$ to some available references: Na_2MoO_4, MoS_2 and MoS_4^{2-} (Figure 15A). We observe that the sample's spectrum is different

from MoS_2 and MoS_4^{2-} (in purple and magenta) which do not have any pre-edge and the edges are located far to the lower energy. In contrast, its edge and pre-edge are very similar to molybdate (in orange). The only differences are the intensity of pre-edge peak and the shape of multiple-scattering zone which may be from the difference of crystal size. The perfect superposition of edge between commercial Na_2MoO_4 and the $x = 0.18$ sample suggests a similar oxidation state between the two: +VI in the synthetic samples with $x \leq 0.25$. This is coherent with other results:

+ analysis by XPS formerly: the oxidation state of Mo is +VI (Figure 12).
+ the splitting energy at Mo L_3-edge of 2 eV seen in Figure 11A, which, in plus, corresponds to the tetrahedral geometry of a cation nd^0 (Mo(+VI) $4d^0$), theoretically.[23]
+ the existence of 2 maxima at Mo L_3-edge in the same figure with a higher intensity for the 2nd one confirms again the tetrahedral geometry.[24,25]

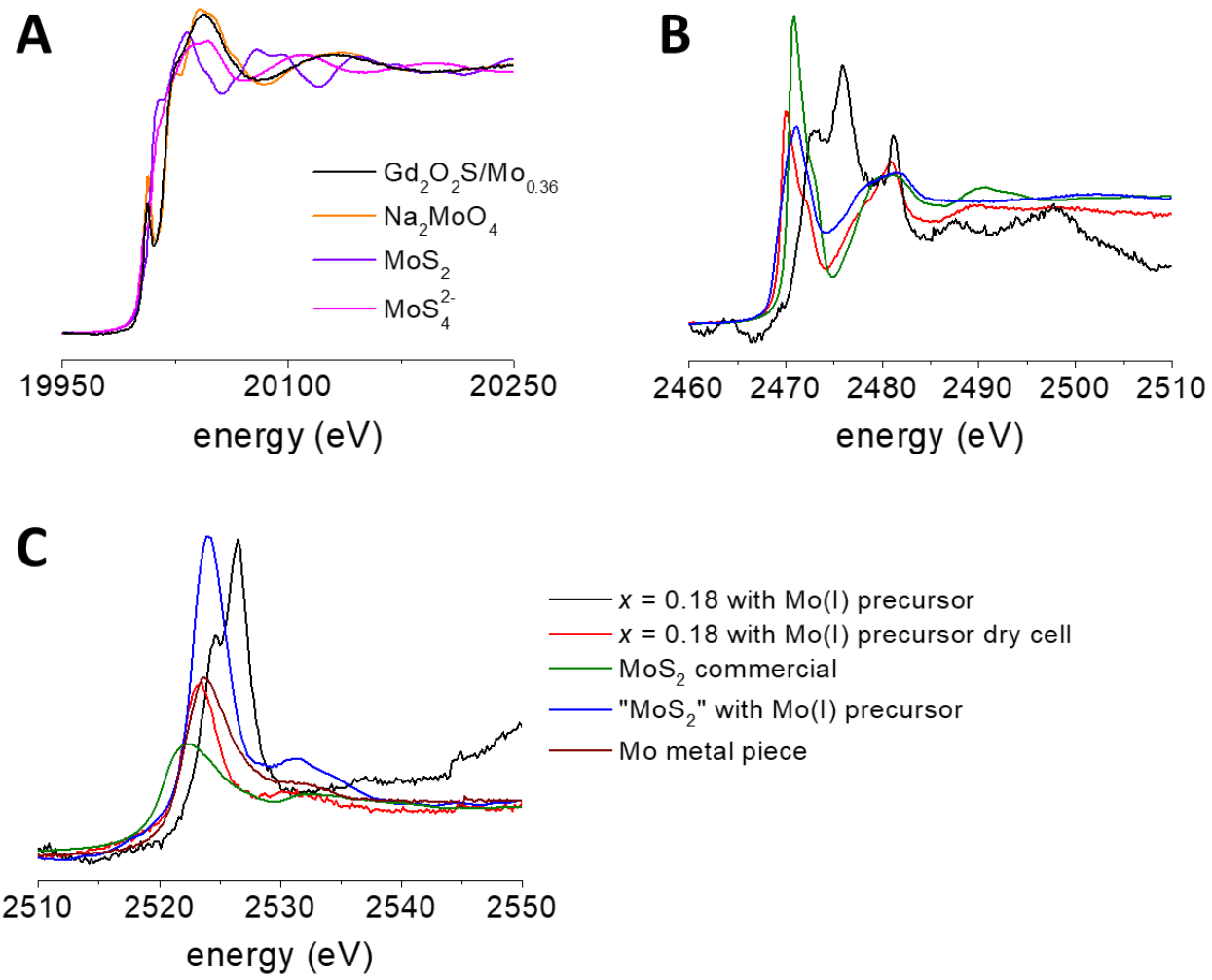

Figure 15 (A) Comparison between the spectrum of $Gd_2O_2S/Mo_{0.36}$ ($x = 0.18$) and some references: Na_2MoO_4, MoS_2 and MoS_4^{2-} commercial products. (B) Comparison of XAS at S K-

edge, a sample $Gd_2O_2S/Mo_{0.36}$ made with Mo(+I) precursor in pellet, itself deposed on a membrane coated with gold for in situ test, a sample "MoS_2" made with Mo(+I) precursor and MoS_2 commercial. (C) Comparison of XAS at Mo L_3-edge between a sample $Gd_2O_2S/Mo_{0.36}$ made with Mo(+I) precursor in pellet, itself deposed on a membrane coated with gold for in situ test, a sample "MoS_2" made with Mo(+I) precursor, commercial MoS_2 and a piece of metallic Mo.

This sample was used for *in situ* electrochemical tests, it was measured at Mo L_3-edge and S K-edge. Figure 15B shows the comparison at S K-edge of this sample measured in pellet and in electrochemical cell with commercial MoS_2 and another sample made without any Gd precursor (introduced S/Mo = 2, see Chapter IV). First of all, we see a total difference between the spectrum of sample in pellet and itself in a deposition in electrochemical cell (in black and red). The deposition was made from the sample freshly taken out of the glovebox then wetted with some drops of absolute ethanol. It was measured about 10 minutes after being made on the electrode. In the pellet, the sample was diluted with graphite, then pressed under a pressure of 2 tons, kept in air during about 1 day before being measured. The edge in this case is shifted largely to the right of the scale, which means sulfur in the pellet is more oxidized than in the deposition. The deposition has its spectrum quite similar to commercial MoS_2 (in red and green) and different from the sample "MoS_2" (see Chapter IV for more information on this sample) at the edge and also the position and intensity of peaks corresponding to oxidized sulfur around 2480 eV (in red and blue).

Figure 15C shows the comparison at Mo L_3-edge of the $Gd_2O_2S/Mo_{0.36}$ sample in pellet and in a fresh deposition with commercial MoS_2, a "MoS_2" sample also made with Mo(+I) precursor and a metallic Mo piece. Based on the position of the first derivative, the edges are found as 2523.8 eV, 2521.8 eV, 2521.9 eV, 2521.9 eV and 2520.3 eV, respectively.

Again, we observe a difference between the $Gd_2O_2S/Mo_{0.36}$ sample in the pellet and in the deposition as at S K-edge (in red and black). There is a similarity between the deposition and commercial MoS_2 (in red and green): same edge and shape of spectrum, they are obviously more oxidized than the Mo piece we used as reference. The sample "MoS_2" made with Mo(+I) precursor, however, has the same peak as the $Gd_2O_2S/Mo_{0.36}$ sample in the fresh deposition and commercial MoS_2 (in red, blue and green). Among these three, the $Gd_2O_2S/Mo_{0.36}$ sample's spectrum and the commercial MoS_2's spectrum are more comparable (from the edge to the multi-scattering region) than to the "MoS_2" sample's one. This may suggest a similar local environment of S atoms in the considering $Gd_2O_2S/Mo_{0.36}$ sample in the fresh deposition and

in the commercial MoS_2. This is very important to find out in the future which S atoms have the local environment changed in contact with ethanol, the mechanism of this process and if there is any relation with the reduction of Mo by ethanol.

From the XAS in pellets, we can see that the Mo centers in these series are tetrahedral and quite similar to the oxide (molybdate). The big question that we try to answer in the next part is that whether it is possible for Mo-O and Mo-S bonds co-exist in some sort of oxysulfide and the relation between Mo-containing species and Gd_2O_2S.

4. Discussion

There are three possibilities of product's nature made by this method:

- Formation of Mo-containing phase(s) in 2nd step destroys completely Gd_2O_2S. Only other phase(s) are collected after the 2nd step.
- Gd_2O_2S stays intact, and separated Mo-containing phase(s) is obtained.
- Gd_2O_2S partially changed and there is a formation of Mo-containing phase(s):
    + Some double layers $[Gd_2O_2]^{2+}$ are separated to S^{2-} layer, then they link to $Mo^{\delta+}$ by O terminated: Mo-O bonding is expected to observed by local structure analysis (EXAFS, PDF)
    + Some double layers $[Gd_2O_2]^{2+}$ are dissolved to expose S^{2-} layer. $Mo^{\delta+}$ then comes to link to this layer.
    + $Mo^{\delta+}$ links to S^{2-} on the side of Gd_2O_2S nanoparticles.
    + All of above.
    + Mo-containing phase(s) and Gd_2O_2S are independent.

    In each case, a typical bonding, i.e. Mo-O, Mo-S or both of them, is expected to be observed by local structure analysis including Pair Distribution Function (PDF) and/or Extended X-ray Absorption Fine Structure (EXAFS).

Mo(+I) precursor is the most interesting among the three precursors tested in this part because firstly, it is one of the two commercial precursors and it is easier to oxidize than reducing Mo(+VI) during the nanoparticles synthesis. Next, between Mo(+I) and Mo(+VI), the former makes products with visible differences to Gd_2O_2S (observed by XRD) while the latter does not (Figure 8). Mo(+III) precursor is kind of a homemade product, it arrived later in the project

and in a small amount, only some samples are made to have the idea of the precursor's role on the final product's structure.

Therefore, the discussion below is mainly based on the study with Mo(+I) precursor.

4.1. Composition analysis

Figure 7A shows the observed Mo/Gd ratio by EDS *vs*. introduced ratio Mo/Gd (x) in each sample in the whole series. There are 2 lines which may describe the variation trend of obtained Mo quantity in the products: it may increase linearly up to $x = 1$ (solid line) or it may stay still at about 0.05 molar equiv. Mo/Gd (dash line). Both of them does not fit to all samples. Moreover, there is limit x at 0.25 mentioned above for crystalline structure seen by XRD, it need to be taken into account for analysis. Looking at the compositions in average of low x samples, there might be 2 trend lines possible for 2 subgroups of samples: $x \leq 0.25$ and $x \geq 0.25$ (Figure 7C). R^2 of both regressions are higher than 0.90, this model is clearly better than the first proposed trend lines. This suggests that more Mo is lost when small quantity is introduced (slope of 0.277, in orange) while Mo stays mostly entirely when more Mo is added (slope of 0.871, in blue). Also, it is possible that the introduction of more Mo in the synthesis favorited some secondary reaction between Mo and other compounds in the medium. It means that with higher x (2^{nd} subgroup), the samples may contain more impurities than with lower x (1^{st} subgroup), which can be considered coherent with some large well defined crystalline nanoparticles seen in a $x = 1.0$ sample (Figure 9F). In any case, due to the most recent result, no increase of sulfur was observed in any sample made by the two-step protocol, comparing to Gd_2O_2S/Mo_0 reference and even slightly lower to that in classical Gd_2O_2S (Figure 7D). For these reasons, we focus only on samples with $x \leq 0.25$ for further analysis and activity tests. Moreover, we wanted to make a new catalyst, the aim is not to use a large quantity of metal but the minimum of it.

The distribution of concerned elements (Gd, S, Mo) is shown in Figure 6A. This method STEM-EDS helps to study a small number of nanoparticles as it has a high zooming capacity. In our case, as on the surface of nanoparticles there is a layer of organic ligand which is easily burned under X-ray beam, we could not go on one or some nanoparticles but a small group of them. These images show an even distribution for each element at nanoscale. This suggests

that Gd-containing phase and Mo-containing phase(s) (regardless separated or linked) are well mixed together at nanoscale (investigating scale).

4.2. A closer look at the crystalline structure of Gd_2O_2S/Mo_{2x} ($x \leq 0.25$)

To understand the crystalline structure of final powders, each powder is analyzed by XRD with adapted sample holders to avoid systematical errors of Bragg peaks' positions which certainly affects the precision of the analysis. For fitting curves, the diffractograms are collected between 20 ° and 60 ° with the best conditions (see Experimental Section) to have the best fit possible.

In general, a change in the crystalline structure, such as a defection, a substitution, an insertion etc. can be traced in a diffractogram via the position of peaks compared to a diffractogram reference. The reference can be the diffractogram of the bulk phase with well-defined thin peaks (experiment-based) or from calculations. Considering the case of $Gd_{2(1-y)}Ce_{2y}O_2S$ where Ce atoms substitute a certain number of Gd sites in the structure of Gd_2O_2S (analytically), this substitution can be traced as a peak shift produced in the diffractograms via the Vegard's law.[2] The average size of nanoparticles is about 6 nm large and 1.5 to 2 nm thick, which broadens the Bragg peaks as predicted by the Scherrer's relation. The best peak of the diffractogram to study the shift value is then (110), which is the sharpest of all. The value of this shift follows the Vegard's law, the shift should increase linearly with the increase of the inserted cation (here, Ce) in the structure of the initial compound (here, Gd_2O_2S).[2] In this case, as Mo is introduced in the synthesis of Gd_2O_2S before isolating the nanoparticles, at the beginning, we were expecting a substitution of Gd sites by Mo atoms but for the reason that it is technically impossible (see Chapter I), we wanted to find out which kind of relation between added Mo atoms and the initial structure Gd_2O_2S is. Hence, we applied the same analysis method for the Mo-containing samples. As we observed earlier in this Chapter, there is a small shift of peak (110) for all samples made by the two-step protocol, regardless the Mo quantity. Here this shift will be analyzed closer in order to understand if it is significant for a structural modification. To analyze precisely the diffractograms, firstly, the uncertainty of the method should be known. It is discussed below, based on the direct estimation on the $Mo@Gd_2O_2S$ nanoparticles system.

To fit the diffractograms, using FULLPROF software, there are 3 methods in ascending order of precision level: peak by peak < pattern-matching < refinement Rietveld. For pattern-matching method, the FWHM, the lattice parameters and the background are all included in the calculation. The Rietveld refinement contains the atom positions in addition (relative intensity of peaks). These 2 fitting methods permit a precise crystalline model but it requires a

diffractogram very well defined with sharp peaks. Fitting peak by peak cannot give a crystalline model with constraints of atom positions but it can give the peak position and its FWHM quite precisely. In our case, it is clear that the diffractograms contain too few and too broad peaks, the only way is to fit them peak by peak.

The uncertainty of peak position comes from the uncertainty of instrument, from the calculation of FULLPROF and the mechanical movements of sample holders. This uncertainty in ° leads to the uncertainty in Å of interplanar distance by Bragg's law calculation.

For the instrument, its uncertainty originates the uncertainty of diffractogram via Bragg's law. By calculation, the uncertainty on Bragg peaks is found.

Bragg's law : $\lambda = 2d \sin\theta$

où θ en rad

$$\Leftrightarrow \quad \ln\lambda = \ln 2 + \ln d + \ln\sin\theta$$

$$\Leftrightarrow \quad \frac{d\lambda}{\lambda} = 0 + \frac{dd}{d} + \frac{\cos\theta \; d\theta}{\sin\theta}$$

$$\Leftrightarrow \quad \frac{\Delta d}{d} = \frac{\Delta\lambda}{\lambda} + \frac{\cos\theta \; \Delta\theta}{\sin\theta}$$

Instrument uncertainty : $\frac{\Delta\lambda}{\lambda} = 0.0001$: X-ray source (notice Bruker D8)

$\Delta\theta = 0.01\,°$: detector (notice Bruker D8)

For peak (110) at around 47 °, it is found that Δd = 0.0005 Å.

The uncertainty caused by FULLPROF is given by the software after the fitting is finished. This value does not change significantly from a sample to the other. The taken value is $0.000358\,°$, from a 0.11 equiv. Mo sample made in only one step. This value needs to be multiply by 4 for the raison of underestimation of software (typical for FULLPROF). Δd is found of 0.001 Å.

The uncertainty caused by mechanical movements is obtained by an analysis on a series of Gd_2O_2S made by myself and C. Larquet, an older PhD candidate in our team. All the powders are made by the same synthesis and analyzed in the same manner. The position of peak (110) should be the same by good repeatability of the synthesis, the standard deviation of this peak should give the total uncertainty which contains the mechanical movement's uncertainty and also the manipulations between batches. With 6 samples, the average interplanar distance on

(110) direction is found at **1.931 ± 0.003 Å**. Hence, the total uncertainty is finally 0.003 Å (compared to 0.0015 Å uncertainty without taking into account the mechanical movements).

As a consequence, theoretically, a change in interplanar distance is significant if it is superior to 0.003 Å.

In practice, the uncertainty is set at 0.005 Å, which is already over-estimated compared to the calculation.

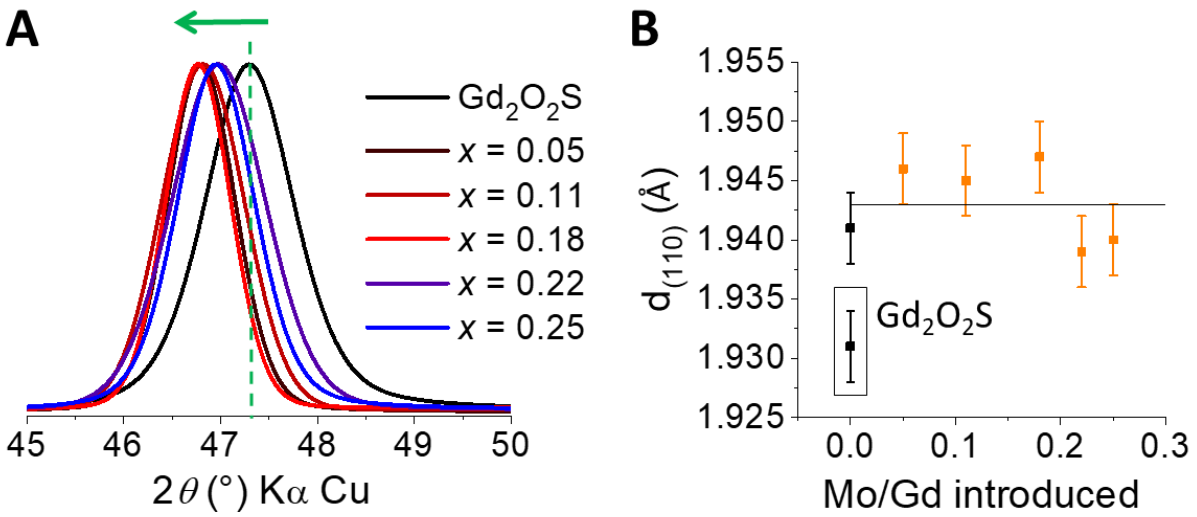

*Figure 16 (A) Fitted curves of peak (110) from diffractograms of samples with x from 0 to 0.25. This peak is fitted separately to the rest of each pattern. (B) The peak shift of **0.016 ± 0.003 Å** between samples with Mo, classical Gd_2O_2S (black, in cadre) and Gd_2O_2S/Mo_0 (black) reference on the graph.*

By applying this data treatment method, the fits of peaks (110) of powders with $x \leq 0.25$ were done (Figure 16A) and show an obvious mostly constant shift compared to classical Gd_2O_2S (Figure 16B). For 3 first Mo-containing samples, the average interplanar distance is 1.946 ± 0.004 Å, for 2 others it is 1.939 ± 0.001 Å, and for Gd_2O_2S/Mo_0, it is 1.943 ± 0.004 Å. The average interplanar distance for all 6 samples is **1.943 ± 0.004 Å**, hence, an average peak shift of is **0.012 ± 0.003 Å**. The difference in interplanar distance for the first 3 Mo-containing samples is 0.015 ± 0.004 Å, for the 2 others it is 0.008 ± 0.003 Å and for Gd_2O_2S/Mo_0, it is 0.012 ± 0.004 Å. Despite that the shifts are not exactly the same for these 3 cases, it is always significant. This peak displacement clearly does not follow the Vegard's law. It is more like a switching on-off effect: the shift occurs at the same value regardless the introduced Mo quantity, as soon as the powder is made by the two-step protocol.

Looking at the diffractograms, it is clear that the characteristic peaks of Gd_2O_2S (peaks (100), (101), (110)) are still visible in all the diffractograms despite the change in the position and the shape of peak (101) (Figure 8). From these XRD patterns and taking into consideration the argument in 3.1, the only possibility is that Gd_2O_2S nanoparticles evolves after the 2nd step but not either destroyed or modified drastically, during this time (an)other phase(s) containing Mo is made.

Taking into account the fact that the distribution of Gd, Mo and S is homogenous and that the S quantity does not increase with the Mo quantity increase despite the high affinity of Mo to S, and the shift occurs even with $x = 0$, we can state that:

+ Gd_2O_2S's structural evolution and morphology modification are due to the 2nd step and independent with the addition of Mo (mentioned briefly in part 3.1.2 and in detail in this part);
+ The sulfur-containing organic species after the 1st step of the synthesis may be not active anymore as sulfide-forming source;
+ Mo-containing phase(s) is evenly distributed amongst modified Gd_2O_2S nanoparticles.

However, the cause of morphology change and the relation between these different phases are not yet clear. We can still expect some kind of a core-shell or a composite, for instance. This may be coherent with the very first idea of this synthesis that Mo stays only on the surface of Gd_2O_2S nanoplatelets which allows an even distribution of Mo-containing phase(s) around Gd_2O_2S nanoparticles and at the same time, their unchanged structure. This may occur via links between Mo atoms and either only with the O terminated layer or several type of O to create a shell and not to increase S quantity in final product. These points will be revisited in the next part to combine with the results from other analysis methods.

4.3. A closer look on $Gd_2O_2S/Mo_{0.36}$ samples

For now, we have seen that there are no changes in crystalline structure and morphology of initial Gd_2O_2S nanoparticles depending on the Mo's presence in the powders. As the Mo atoms are surely present, we have to find out where they are and how they exist in these powders. What we have known on Mo centers from the previous discussions is that Mo's geometry is principally tetrahedral with the oxidation state of +VI in the powders and may have the local environment close to molybdate type.

Concerning the splitting of peak (101), as briefly described in part 2.3, there are 4 molybdate phases that can have the diffractograms matching those of synthetic samples with $x = 0.18$:

Gd_3MoO_7, $Gd_2(MoO_4)_3$, Gd_2MoO_6 and $Gd_4Mo_4O_{11}$ (Figure 6C-F). However, the Mo sites are not exactly the same in these structures:

- In $Gd_4Mo_4O_{11}$ model, the oxidation state of Mo is +2.5 ($14e^-$ for each Mo_4). There are 3 types of Mo in this structure: apical Mo1 links with 5 other Mo (1 Mo1, 2 Mo2 and 2 Mo3) and 5 O; each Mo2 or Mo3 links with 7 other Mo (4 Mo1, 2 Mo3 and 1 Mo2) and 4 O.[14] They are all not in centrosymmetric geometry but none of them is tetrahedral.
- In Gd_3MoO_7 model, the oxidation state of Mo is +VI but Mo atoms are in octahedral geometry.[10]
- In α-$Gd_2(MoO_4)_3$ model, the oxidation state of Mo is +VI. There is only 1 type of Mo in this structure: Mo links with 4 O in an environment of a simple kind of molybdate.[11]
- In Gd_2MoO_6 model, the oxidation state of Mo is +VI. There is only 1 type of Mo in this structure: Mo links with 4 O in an environment of a simple kind of molybdate.[12,13]

From here, $Gd_4Mo_4O_{11}$ and Gd_3MoO_7 can be already excluded as it either does not contain Mo at the right oxidation state or cannot create an intense pre-edge at Mo K-edge due to the centrosymmetric geometry. There are two possibilities of molybdate are α-$Gd_2(MoO_4)_3$ and Gd_2MoO_6 which are very similar: monoclinic, space group *C2/c*. To find out if the Mo-containing phases contain also Gd at the same time as one kind of molybdate as discussed, further local analyses (EXAFS, PDF) have to be done for find the possible Gd-Mo distances if there are any.

For the local environment and the center ion Mo, we will discuss the results from XAS (XANES and EXAFS) and PDF. As the nanoparticles are very thin and not very large, the analysis by PDF is very useful.

First of all, for the analysis of the oxidation state of metallic center ion, an energy shift of approximately 1.5 eV at L-edge, in general, can be considered for a formal transition of valence while it is about 2 eV for the edge and 0.6 eV for the pre-edge at K-edge.[26] It means that in all cases, even if the spectra of synthetic samples are not exactly the same, the differences are small enough to conclude the same oxidation state for all, i.e. the observation of Mo(+VI) in the previous parts is now considered as validated.

In Figure 15C, there is an energy shift of 2 eV between the edge of the $Gd_2O_2S/Mo_{0.36}$ sample in pellet and in a fresh deposition. This corresponds to a transition of valence of Mo centers from +VI to a lower state. The reason for the edge changes after the preparation of the deposition may be due to the reduction of Mo(+VI) in the oxide by ethanol (solvent) that has

been reported in other works.[27] As both the Mo L_3-edge and the S K-edge and in the fresh deposition are the same as commercial MoS_2 (Figure 15B-C), after the preparation of the deposition, Mo is reduced to Mo(+IV) as in MoS_2. The similarity of sulfur's local environment between the deposition and commercial MoS_2 gives the idea that maybe Mo is not only reduced in contact with ethanol but also is changed from oxide-like (molybdate) to sulfide-like by some mechanism. This process has to be reversible because after being in contact with air during a day, the spectrum of the dried deposition became identical to the one in pellet at Mo $L_{3,2}$-edges (data not shown). Also, the peak corresponding to sulfate at 2481.2 eV (attributed to sulfate), which is absent in the fresh deposition, became present in the old one. It suggests that the ink preparation for ex situ electrochemical tests might play a role on the observed activity and storing samples in glovebox is not necessary. This latter point can be confirmed by the similarity between the XAS of a two-month old $Gd_2O_2S/Mo_{0.36}$ sample and an one-year old $Gd_2O_2S/Mo_{0.22}$ sample, all in pellets (Figure 17A). This is possibly because +VI is the most stable state of Mo, thermodynamically.[8]

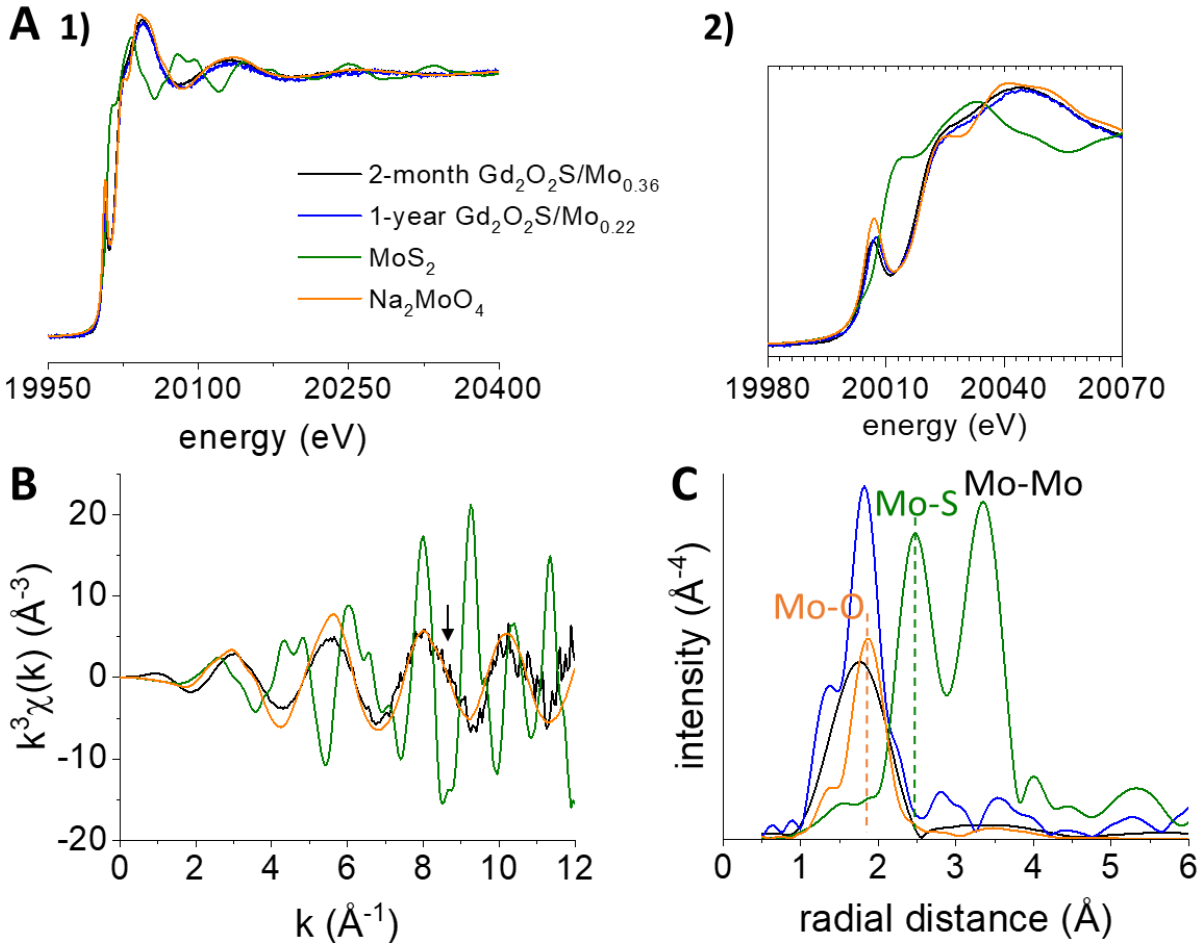

Figure 17 (A) (1) Comparison of XAS between a two-month old $Gd_2O_2S/Mo_{0.36}$ sample, an one-year old $Gd_2O_2S/Mo_{0.22}$ sample, commercial MoS_2 and commercial Na_2MoO_4 at Mo K-edge.

(2) A zoom on the XANES parts of samples in (A1) is provided. The legend is common for all figures. (B) Oscillations in function of k (Å^{-1}), calculated from the spectra in (A). (C) Distribution of radial distance (Å), calculated from the spectra in (A) and adjusted by +0.5 Å to visualize the veritable bond lengths. The intensity of two synthetic samples are multiplied by 1.5 for better data visualization.

Now, coming to the local structure of Mo in the $Gd_2O_2S/Mo_{0.36}$ sample, the difference of XANES part shown in Figure 17A signifies that Mo exists in the isolated molybdate tetrahedron, not in any kind of defined crystals. The oscillations extracted from the XAS in Figure 17A which have very much noise confirms this point. Considering only $k < 8$ Å^{-1} where the contributions of light elements are maximum, the oscillation of the $Gd_2O_2S/Mo_{0.36}$ sample is a highly similar to that of commercial Na_2MoO_4 up to $k = 8$ Å^{-1} (marked by an arrow, corresponding to the first sphere around a Mo atom). The distribution of pseudo-radial distances calculated from the same spectra (Figure 17C) confirms the isolated tetrahedral molybdate again: there are peaks corresponding to only Mo-O distance (as in Na_2MoO_4, bond length 1.9 Å) and an absence of peak corresponding to Mo-S distance (as in MoS_2, bond length 2.4 Å) in synthetic samples.

For the reason that the Mo-containing phase is amorphous, an analysis by PDF can be useful as it may reveal the relation between Mo and the support structure Gd_2O_2S. In the previous parts, we have seen that the inorganic phase Gd_2O_2S is not destroyed but evolved by the heating during the 2nd step of the synthesis (observation in part 3.1.3, confirmation in part 4.2) and there are possibly a rearrangement of surface ligands. Hence, before modelling the patterns, a simple comparison between the experimental curves can show already some ideas about the changes in local structure linking directly to the presence of Mo atoms. First of all, the PDF patterns of Gd_2O_2S from CRYSTAL Beamline and from LCMCP instrument are globally comparable but in detail, there are some differences between them: around short distance 4.5 Å, there are some variations that the cause is not yet clear, which make it impossible to compare the results from a dataset to the other (see Annex 2). For the Mo-containing samples, the intensity of signal decreases largely with the increase of Mo content (Annex 3). This may be due to a technical problem (too short wavelength at CRYSTAL Beamline), there are too much absorption of the beam by Mo-containing samples, which is probably the problem of strange peak intensity variations at the end. Hence, again, it is only meaningful for now to compare the patterns within the same dataset (for further information, see Annex 3).

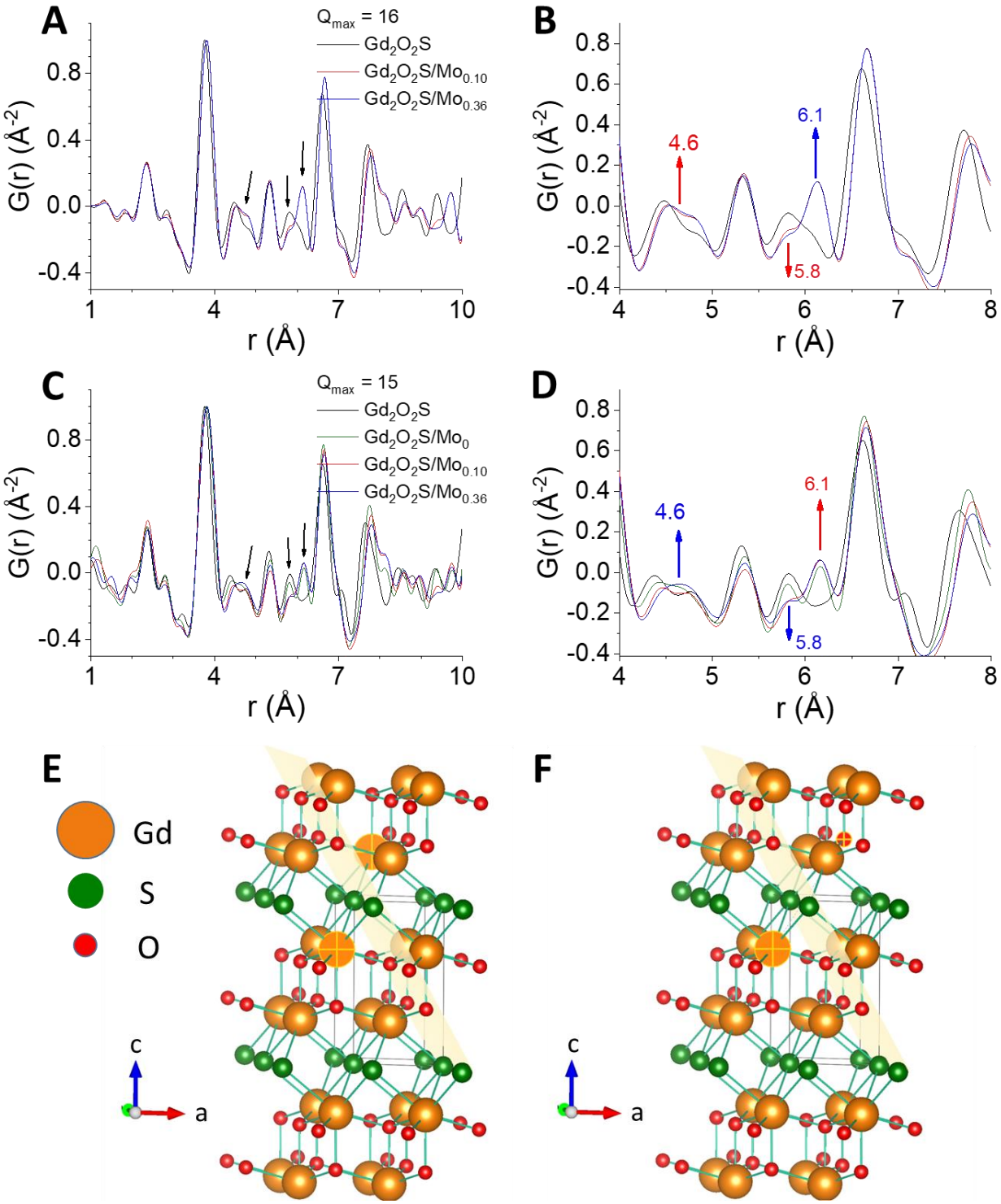

Figure 18 (A) Comparison of normalized PDF patterns acquired at SOLEIL between a sample Gd_2O_2S non annealed and two Mo-containing samples with different x: $Gd_2O_2S/Mo_{0.10}$ (x = 0.05) and $Gd_2O_2S/Mo_{0.36}$ (x = 0.18). The difference between samples with Mo and without Mo are marked by arrows. The legend is common for (A, B). (B) A zoom between 4 Å and 8 Å where the evolution is the most visible. Colored arrows and the numbers signify the direction of peak evolution and the distances corresponding. (C) Comparison of normalized PDF

patterns acquis at LCMCP between a sample Gd_2O_2S non annealed, an annealed sample Gd_2O_2S/Mo_0 and two Mo-containing samples with different x: $Gd_2O_2S/Mo_{0.10}$ (x = 0.05) and $Gd_2O_2S/Mo_{0.36}$ (x = 0.18). The difference between samples with Mo and without Mo are marked by arrows. The legend is common for (C, D). (D) A zoom between 4 Å and 8 Å where the evolution is the most visible. Colored arrows and the numbers signify the direction of peak evolution and the distances corresponding. (E, F) Distances Gd-Gd and Gd-O (concerning the atoms marked with a cross in each figure) to which the peak 5.8 Å can be attributed to with the plane {101}. Figure constructed from JCPDS file 04-008-6593 and measured in VESTA.

Figure 18 shows the comparison of normalized PDF patterns between samples with and without Mo in each dataset: (A, B) include data from SOLEIL, extracted with Q_{max} = 16 and (C, D) include data from LCMCP, extracted with Q_{max} = 15. For the technical reason, the annealed sample Gd_2O_2S/Mo_0 was not measured at CRYSTAL Beamline. Hence, only the dataset from LCMCP combines all the needed samples. However, the treatment for both dataset is necessary to solve the structure of synthesized nanoparticles.

Globally, in each dataset, the introduction of Mo in the samples does not change drastically the PDF patterns compared to Gd_2O_2S/Mo_0 or Gd_2O_2S (Figure 18A, C). At this point, we revisit the evolution from Gd_2O_2S to Gd_2O_2S/Mo_0 to better analyze the Mo-containing samples later. Figure 18B, D, there are two peak evolutions between these two samples: a decrease of peak 5.8 Å and an apparition of peak 6.1 Å. The distance 5.8 Å can be attributed to the distance extraplanar Gd-Gd and Gd-O (considering $[Gd_2O_2]^{2+}$ as a plane, the distance is considered "extraplanar" because of the S atom between them, Figure 18E, F) across the {101} plane for Gd_2O_2S. No intraplanar distance was found at these values. By annealing the sample to obtain Gd_2O_2S/Mo_0, the number of distance 5.8 Å decreases obviously while the apparition of the distance 6.1 Å is obvious with the intensity even higher than that of the peak 5.8 Å in Gd_2O_2S (Figure 18C, D, black curve *vs.* green curve). We can surely state that the evolutions of the structure linking to these two distances are totally independent to the presence of Mo. It means that for the model construction in the future, we need to consider one with the same planes $[Gd_2O_2]^{2+}$ as Gd_2O_2S with a probable modified interplanar local rearrangement. Coming back to Mo-containing samples, we observe also the evolutions for peaks 5.8 Å, 6.1 Å and for the peak 4.6 Å in addition. Otherwise, there is a small shift of all peaks to the longer distance not only for Mo-containing samples but also for the annealed sample without Mo. This may suggest a possible dilatation of unit cell and an introduction of disorder/surface ligands rearrangements with the presence of Mo.

Figure 18B, D illustrate the most visible intensity evolution in function of Mo introduced quantity of three peaks corresponding to the distances: 4.6 Å (increasing), 5.8 Å (continue to decrease) and 6.1 Å (continue to increase). The increase of the peak 4.6 Å can be seen in both datasets (Figure 18A-D) but seems to be a little more visible in the SOLEIL dataset than in the LCMCP dataset. The peak 5.8 Å decreases intensely compared to Gd_2O_2S/Mo_0 in both measurements. The peak 6.1 Å is already visible for annealed sample without Mo and increases with the Mo's presence. In short, only the evolution of the peak 4.6 Å is totally linked to the presence of Mo in the synthesis. The evolutions of the other two peaks 5.8 Å and 6.1 Å are caused surely by the 2nd step of the synthesis, the role of Mo on these two peaks is not yet sure if veritable.

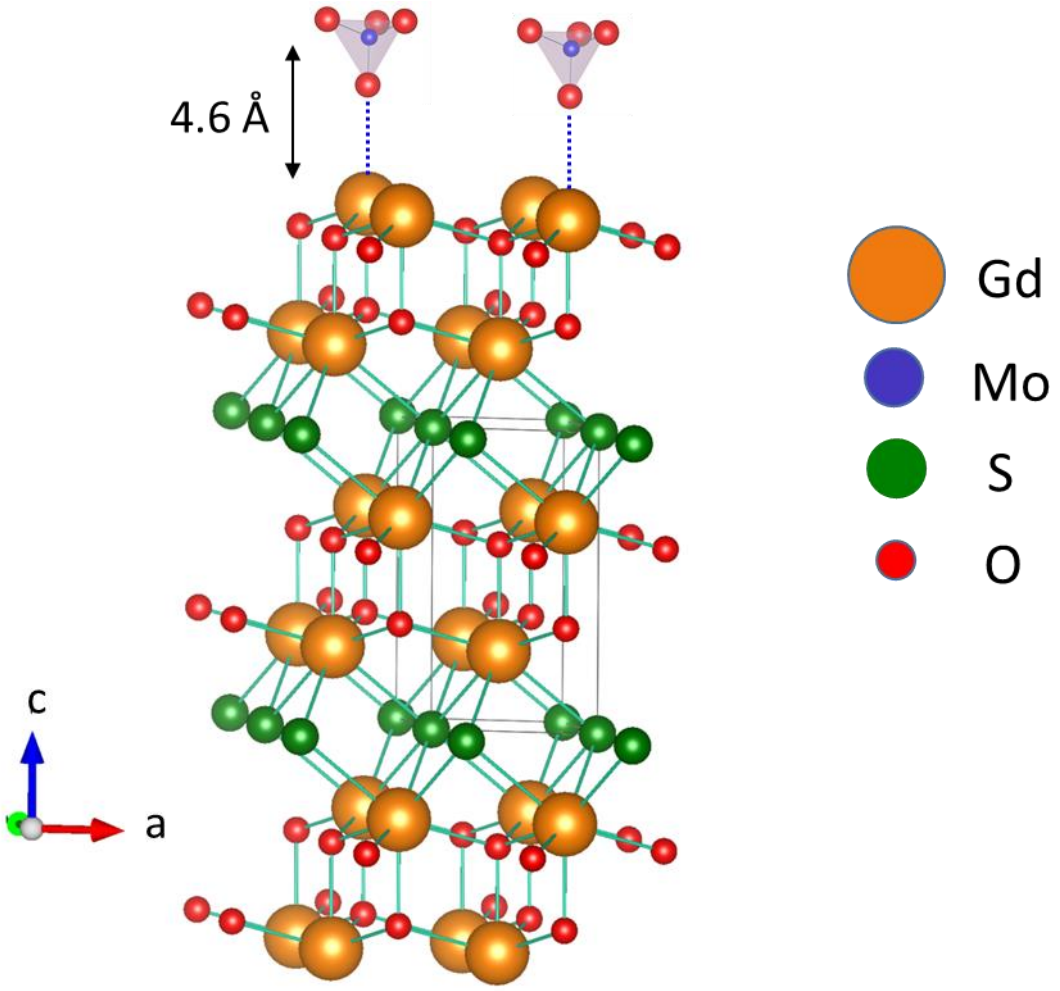

Figure 19 A proposition of molybdate-doped Gd_2O_2S structure made by the two-step protocol.

By different methods of spectroscopy, we now understand that Mo in the samples has the oxidation state of +VI, exists in isolated molybdate tetrahedron. Freshly, we saw a peak at 4.6 Å in the PDF patterns which is surely linked to the Mo's presence in the sample.

Unfortunately, it is difficult to observe and analyze the first sphere of Mo since the peaks possibly corresponding to Mo-O distance (at around 1.7 – 1.8 Å) can be hidden under the Gd-O peak (at 2.3 Å) and the quantity of Mo in the sample is very low compared to Gd. Figure 19 illustrates a proposed structure for the Mo-containing samples made by the two-step protocol, taking into account all the conditions above. In this model, the molybdate tetrahedrons link weakly to the surface of nanoparticles by Gd-O bonds. Assume that such distance Gd-Mo is 4.6 Å, the distance Gd-O should be around 2.8 Å, which is 0.5 Å longer than a normal Gd-O. It is sure that the number of this distance Gd-Mo is very low because of the low quantity of Mo but by the high diffusion factor of Mo and Gd, the peak Gd-Mo could become visible as in measured PDF patterns.

For now, we can state that Mo in the sample is in tetrahedral molybdate form with a hypothesis of molybdate tetrahedrons dispersed on the surface of Gd_2O_2S nanoparticles by weak interaction Gd-O along with the organic ligands. By continuing on PDF calculations and also on the other data treatments, we hope to confirm the proposed model (or another one, otherwise) for the structure of Mo-containing nanoparticles made by the two-step protocol.

4.4. Understanding the activity of synthesized samples by comparing to commercial MoS_2 nanoparticles using different methods of current normalization

4.4.1. Initiatives and calculations

4.4.1.1. Initiatives

To compare the activity of concerning materials and the reference, we have to normalize the measured activity to the same criterion. The easiest way is to normalize them to the geometric surface area of the electrode (0.196 cm^2) as shown in Figure 13. In this case, we observe that the activity of the $Gd_2O_2S/Mo_{0.36}$ sample is quite close to the reference MoS_2 90 nm (Figure 13B). However, this normalization is not precise because the size of nanoparticles in these two depositions are far different from one to the other. For this reason, other normalizations by the geometrical surface of nanoparticles or by the geometrical surface of only active sites were done. For all normalization methods, the calculations are done for one deposition of 5 µL of ink, i.e. 5 µg of material (ink concentration: 1 mg/mL). In the case of synthesized nanoparticles, the mass of organic ligands is approximately 30 % of total material mass.[6] It means that in each deposition, there is only 3.5 µg of synthesized nanoparticles instead of 5 µg as in the case of MoS_2.

4.4.1.2. Calculations

Notations: m_{d1} = MoS_2 mass in 1 deposition = 5 µg

m_{d2} = Mo-containing nanoparticles mass in 1 deposition = 3.5 µg

d = MoS_2 density at 25 °C = 5.06 g/mL

r = radius of 1 MoS_2 nanoparticle = 45 nm

r_{Mo} = crystal radius of Mo(+IV) in coordination 6 = 0.8 Å [28]

r_S = crystal radius of S(-II) in coordination 6 = 1.7 Å [28]

v_1 = volume of 1 MoS_2 nanoparticle

s_1 = geometrical surface of 1 MoS_2 nanoparticle

s_{Mo} = geometrical surface occupied by 1 exposing Mo atom on the surface

s_S = geometrical surface occupied by 1 exposing S atom on the surface

V_1 = volume of all MoS_2 nanoparticles in 1 deposition

N_1 = number of MoS_2 nanoparticles in 1 deposition

S_1 = geometrical surface of all MoS_2 nanoparticles in 1 deposition

S_{Mo}^1 = geometrical surface occupied by exposing Mo atoms on all the MoS_2 nanoparticles surface in 1 deposition

a = diameter of 1 $Gd_2O_2S/Mo_{0.36}$ nanoparticle = 8 nm

h = thickness of 1 $Gd_2O_2S/Mo_{0.36}$ nanoparticle = 1.5 nm

m_1 = mass of 1 $Gd_2O_2S_{0.60}$ nanoparticle according to the model of C. Larquet

s_2 = geometrical surface of 1 Gd_2O_2S nanoparticle with or without Mo

m_2^i = mass of 1 $Gd_2O_2S_{0.60}/Mo_{0.36}$ nanoparticle according to the model of C. Larquet if Mo/Gd = 0.18 (i for introduced Mo/Gd value)

N_2^i = number of $Gd_2O_2S/Mo_{0.36}$ nanoparticles in 1 deposition

S_2^i = geometrical surface of all $Gd_2O_2S/Mo_{0.36}$ nanoparticles in 1 deposition

S_{Mo}^{i} = geometrical surface occupied by exposing Mo atoms on $Gd_2O_2S/Mo_{0.36}$ nanoparticles surface in 1 deposition

m_2^e = mass of 1 $Gd_2O_2S_{0.60}/Mo_{0.36}$ nanoparticle according to the model of C. Larquet if Mo/Gd = 0.05 (e for EDS Mo/Gd value)

N_2^e = number of $Gd_2O_2S/Mo_{0.36}$ nanoparticles in 1 deposition

S_2^e = geometrical surface of all $Gd_2O_2S/Mo_{0.36}$ nanoparticles in 1 deposition

S_{Mo}^{e} = geometrical surface occupied by exposing Mo atoms on $Gd_2O_2S/Mo_{0.36}$ nanoparticles surface in 1 deposition

N_A = Avogadro number = 6.022 10^{23} $mole^{-1}$

According to the work of R. D. Shannon,[28] the crystal radius of Mo(+IV) and Mo(+VI) in coordination 6 are not very different (0.8 Å *vs.* 0.7 Å). The performed calculation is an approximation so the same value of Mo radius is taken for all cases.

For indexing in the figures below, all total geometrical surfaces are noted as S_{tot}, all geometrical surfaces of exposing Mo atoms are noted as S_{Mo}, all number densities of exposing Mo atoms are noted as N_{Mo1} and all area number densities of exposing Mo atoms are noted as N_{Mo2}. Ir in the figures stands for the measured current without calculations and N_{Mo} stands for the total number of exposing Mo atoms in each deposition.

- For MoS_2:

$$v_1 = \frac{4}{3}\pi r^3 = \frac{4}{3}\pi 45^3 \text{ nm}^3$$

$$V_1 = \frac{m_{d1}}{d} = \frac{5\ \mu g}{5.06 \frac{g}{mL}}$$

$$s_1 = 4\pi r^2 = 4\pi 45^2 \text{ nm}^2$$

$$s_{Mo} = 4\pi {r_{Mo}}^2 = 4\pi 0.08^2 \text{ nm}^2$$

$$s_S = 4\pi {r_S}^2 = 4\pi 0.17^2 \text{ nm}^2$$

$$N_1 = \frac{V_1}{v_1} = \frac{5\ \mu g}{5.06 \frac{g}{mL} \frac{4}{3}\pi 45^3 \text{ nm}^3} = 2.6\ 10^9$$

$$S_1 = s_1 . N_1 = 4\pi 45^2\ \text{nm}^2 \frac{5\ \mu\text{g}}{5.06 \frac{\text{g}}{\text{mL}} \frac{4}{3}\pi 45^3\ \text{nm}^3} = \mathbf{0.67\ cm^2}$$

Assuming that on the surface of each MoS_2 nanoparticle, the ratio between the number of Mo atoms and S atoms is also 0.5.

$$N^1_{Mo1} = \frac{s_1}{s_{Mo} + 2\, s_S} = \frac{4\pi 45^2\ \text{nm}^2}{4\pi 0.08^2\ \text{nm}^2 + 2\ 4\pi 0.17^2\ \text{nm}^2} = \mathbf{31,542}$$

$$S^1_{Mo} = s_{Mo} . N^1_{Mo1} . N_1 = \pi 0.08^2\ \text{nm}^2\ 31{,}542\ 2.6\ 10^9 = \mathbf{0.016\ cm^2}$$

- For $Gd_2O_2S/Mo_{0.36}$: taking the model of C. Larquet, in 1 nanoparticle, there are 1800 Gd atoms, 1800 O atoms and 542 S atoms.[6]

$$m = m_{Gd} + m_O + m_S = 1800 \frac{157\ \text{g/mole}}{N_A} + 1800 \frac{16\ \text{g/mole}}{N_A} + 542 \frac{32\ \text{g/mole}}{N_A}$$

$$= \frac{3.3\ 10^5\ \text{g/mole}}{N_A}$$

$$m_{d2} = m + m_{Mo} = 3.5\ \mu\text{g}$$

$$s_2 = \frac{3a^2\sqrt{3}}{2} + 6ah = \left(\frac{8^2\sqrt{3}}{2} + 6\frac{8}{\sqrt{3}}1.5\right)\text{nm}^2 = 9.7\ 10^1\ \text{nm}^2$$

If Mo/Gd = 0.18 as the introduced value:

$$N^i_{Mo1} = \mathbf{317}$$

$$m^i_2 = m + m_{Mo} = \frac{3.3\ 10^5\ \text{g/mole}}{N_A} + 317 \frac{96\ \text{g/mole}}{N_A} = \frac{3.6\ 10^5\ \text{g/mole}}{6.022\ 10^{23}\ \text{mole}^{-1}} = 6.1\ 10^{-19}\text{g}$$

$$N^i_2 = \frac{m_{d2}}{m^i_2} = \frac{3.5\ \mu\text{g}}{6.1\ 10^{-19}\text{g}} = 5.7\ 10^{12}$$

$$S^i_2 = s_2 . N^i_2 = 9.7\ 10^1\ \text{nm}^2\ 5.8\ 10^{12} = \mathbf{5.6\ cm^2}$$

$$S^i_{Mo} = s_{Mo} . N^i_{Mo1} . N^i_2 = \pi 0.08^2\ \text{nm}^2\ 317\ 5.8\ 10^{12} = \mathbf{0.37\ cm^2}$$

If Mo/Gd = 0.05 as the obtained value by EDS:

$$N^e_{Mo1} = \mathbf{95}$$

$$m^e_2 = m + m_{Mo} = \frac{3.3\ 10^5\ \text{g/mole}}{N_A} + 95 \frac{96\ \text{g/mole}}{N_A} = \frac{3.4\ 10^5\ \text{g/mole}}{6.022\ 10^{23}\ \text{mole}^{-1}} = 5.7\ 10^{-19}\text{g}$$

$$N_2^e = \frac{m_{d2}}{m_2^e} = \frac{3.5\ \mu g}{5.7\ 10^{-19} g} = 6.1\ 10^{12}$$

$$S_2^e = s_2 . N_2^e = \ 9.7\ 10^1\ nm^2\ 6.1\ 10^{12} = \mathbf{5.9\ cm^2}$$

$$S_{Mo}^e = s_{Mo} . N_{Mo1}^e . N_2^e = \pi 0.08^2\ nm^2\ 95\ 6.1\ 10^{12} = \mathbf{0.12\ cm^2}$$

If Mo/Gd = 0.11 as the introduced value:

$$N_{Mo1}^i = \mathbf{198}$$

$$m_2^i = m + m_{Mo} = \frac{3.3\ 10^5\ g/mole}{N_A} + 198\frac{96\ g/mole}{N_A} = \frac{3.5\ 10^5\ g/mole}{6.022\ 10^{23}\ mole^{-1}} = 5.8\ 10^{-19} g$$

$$N_2^i = \frac{m_{d2}}{m_2^i} = \frac{3.5\ \mu g}{5.8\ 10^{-19} g} = 6.0\ 10^{12}$$

$$S_2^i = s_2 . N_2^i = \ 9.7\ 10^1\ nm^2\ 6.0\ 10^{12} = \mathbf{5.9\ cm^2}$$

$$S_{Mo}^i = s_{Mo} . N_{Mo1}^i . N_2^i = \pi 0.08^2\ nm^2\ 198\ 6.0\ 10^{12} = \mathbf{0.24\ cm^2}$$

4.4.2. Discussions on results of different normalizations and the relation to the other structural analysis results

Before going further on the results of different normalization methods, we come back to the loss of ORR reactivity after 2 weeks that was mentioned previously. For each deposition, the old inks are sonicated during about 30 min formerly, hence, we assume that the nanoparticles aggregates are broken to well disperse in the suspension, i.e. the nanoparticles quantity in each deposition is practically identical. The loss of reactivity in this case, as a consequence, has to be caused by a change in the nature of active sites (structure, oxidation states, local environment) and/or in the number of active sites (progressive deactivation, left out aggregates) in ethanol during long time. Taking into account the XANES Mo L_3-edge and S K-edge (Figure 15) which shows a clear and quick reduction of Mo from +VI-like in the powder to +IV-like in contact with ethanol (only 5 to 10 min of deposition preparation), the evolution of nanoparticles here in the two-week old inks is inevitable. Also, with this hypothesis, the ink preparation could be seen as an activation process for the nanoparticles. For the moment, we do not have yet any spectroscopic results of the evolution of deposition (with the same ink compositions or simplified) before, during and after the electrochemical test. Some preliminary works were done on SAMBA and LUCIA Beamlines for validate the working method but for technical problems, we do not obtain yet any results on concerning samples.

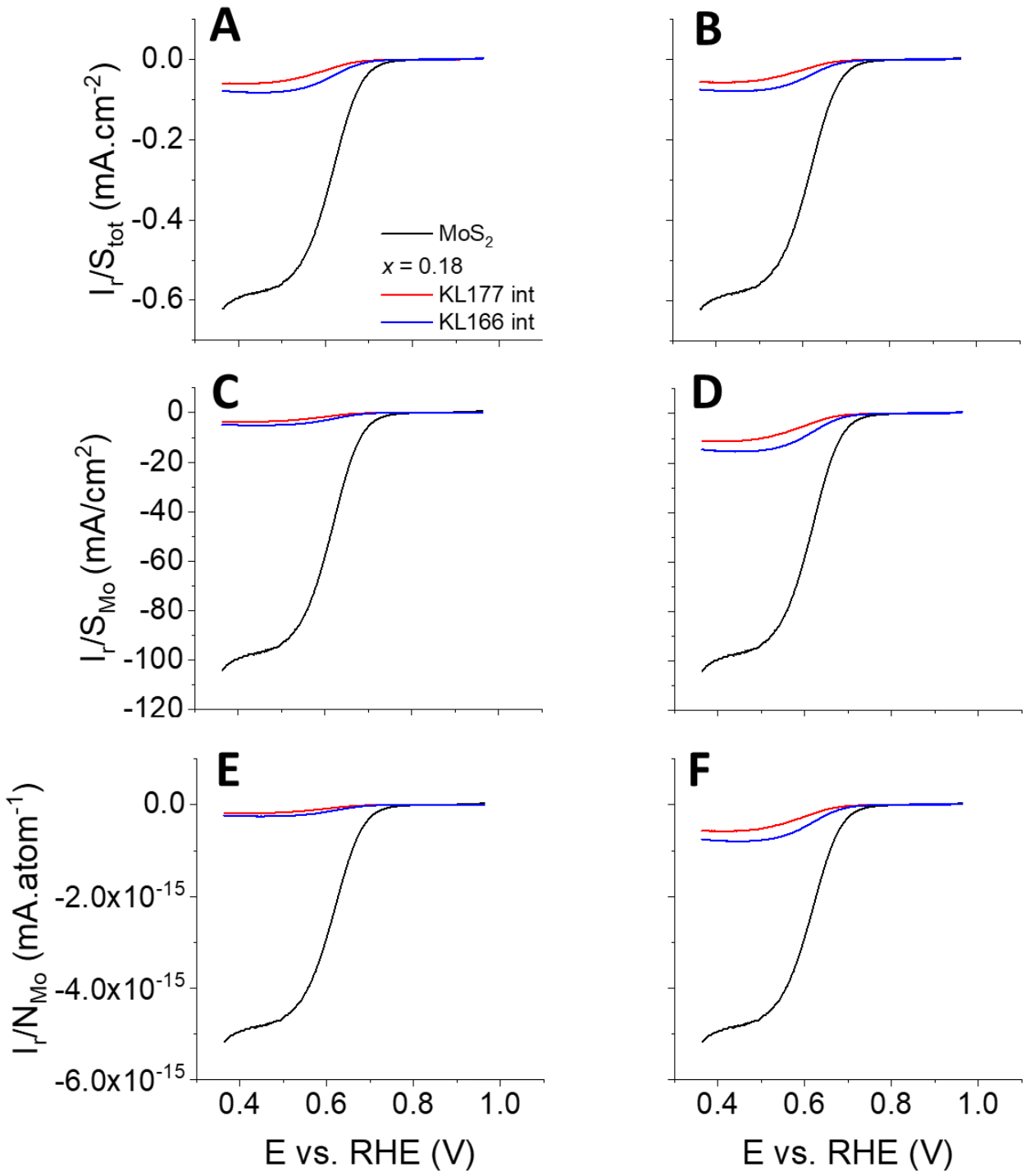

Figure 20 Comparison of LSV curves between MoS_2 reference (black) and 2 samples with the same x = 0.18 KL177 (red) and KL166 (blue): (A) current normalized by the total geometrical surface of all nanoparticles in the deposition, calculations for synthesized samples using introduced ratio Mo/Gd. The legend is common for all figures (A-F). (B) Current normalized by the total geometrical surface of all nanoparticles in the deposition, calculations for synthesized samples using ratio Mo/Gd obtained by EDS. (C) Current normalized by the total geometrical surface of only exposing Mo atoms in the deposition, calculations for synthesized

samples using introduced ratio Mo/Gd. (D) Current normalized by the total geometrical surface of only exposing Mo atoms in the deposition, calculations for synthesized samples using ratio Mo/Gd obtained by EDS. (F) Current normalized by the total number of exposing Mo atoms in the deposition, calculations for synthesized samples using introduced ratio Mo/Gd. (D) Current normalized by the total number of exposing Mo atoms in the deposition, calculations for synthesized samples using ratio Mo/Gd obtained by EDS.

In this part, the commercial nanoparticles MoS_2 will be considered to evaluate the ORR activity of synthetics nanoparticles. There will be also a comparison between two samples with $x = 0.18$ (same nature, different batch number) to evaluate the repeatability of both the synthesis and the electrochemical tests.

Figure 20A shows the comparisons of normalized by geometrical surface of all nanoparticles in the deposition between the reference and 2 different samples with the same $x = 0.18$ (KL177 and KL166). First, we observe that for synthesized samples, the kind of Mo/Gd ratio used in the calculation does not have much impact on the value of normalized current (red and blue curves). From the Figure 13, the activities of 3 samples are considered *similar*. In the surface calculation, we see that the total nanoparticles surface of MoS_2 deposition is mostly 8 times smaller than the surface of synthesized samples (0.67 cm^2 *vs.* 5.6 cm^2). Logically, the calculated current shown in this figure is about 8 times higher for MoS_2 than synthesized samples. This 8 times difference in ORR activity is based on a surface activity underestimation of every sample since by normalizing the current by the total surface, we assume already that all the nanoparticles' surface has the same activity meanwhile it is not the case: exposing Mo sites *vs.* exposing S sites of MoS_2 (Figure 1D), exposing Mo sites *vs.* exposing surface of Gd_2O_2S support which is totally inactive (Figure 13A, if we assume the structure of the materials as simple as the core-shell in Figure 1E).

Now, going further in this direction, we take into account the difference of activity between sites on the same nanoparticles' surface. The normalization here is done with the surface occupied by exposing Mo atoms on the surface of nanoparticles only (Figure 20C). In this case, the surface of exposing Mo atoms is about 20 times smaller for MoS_2 than for synthesized samples (0.004 cm^2 *vs.* 0.09 cm^2). It means that logically, the normalized current of reference is about 20 times higher than synthesized samples. The current difference of the same sample calculated with introduced Mo/Gd ratio and with EDS Mo/Gd ratio is now clearer but still not significant compared to the normalized current of MoS_2. This result is confirmed by the activity normalization for each exposing Mo atom in Figure 20E. The value in this graph can also be

seen as the activity unit in other graphs later in this part. The relation between the reference and synthesized samples is found again at about 20 times more active for the reference. In other words, this calculation method using the Mo/Gd ratio = x = 0.18 suggests that the active sites in MoS_2 are about 20 times more active than active sites in synthesized samples with x = 0.18.

The same reasoning can be applied for Figure 20B-D-F, they are obtained after calculations using the Mo/Gd ratio from EDS analysis of 0.05. The total geometrical surface of synthesized sample now is 5.9 cm^2, about 9 times larger than MoS_2 reference and the total surface of exposing Mo atoms is 0.03 cm^2, about 7 times larger than MoS_2 reference. As a consequence, the activity of one active site in MoS_2 is about 7 times higher than an active site in synthesized materials (Figure 20F).

Finally, between the red (KL177) and blue (KL166) curves in Figure 20, the difference seem to be large but in practice, this is not significant as we are analyzing very low current (comparing to naked electrode and benchmark Pt/C), any difference in the surroundings can cause a deviation of the current. For these two samples and also for other samples with different x values, the measured ORR activity is identical. This shows that not only the synthesis is repeatable but also the electrochemical tests.

About the relation between the structure and the reactivity, we propose three hypotheses from the current results:

1. For a heteroatom-doped material, the electron conductivity can be enhanced, hence, results a more rapid kinetics of the reaction and the doped material is more active than non-doped one, considering the same electrochemical reaction. This observation is applied widely for graphenes.[29,30] In our case, there may be the same phenomenon: if the modified Gd_2O_2S nanoparticles is the initial non-doped material and the Mo is linked to the surface of these nanoplates as a dopant, the increase of activity from non-doped to doped material can be seen as the increase of electron conductivity enhancement from non-doped to doped one. This hypothesis can be considered coherent with the hypothesis of the existence of gadolinium molybdate discussed previously: the molybdate is present in a very thin layer on the nanoparticles as a dopant. This can satisfy the conditions of: structure mostly amorphous, local environment as molybdate, Mo seen as a dopant which increases the activity of initial Gd_2O_2S. The difference between the activity of synthetic samples and commercial MoS_2 can be explained by the difference in Mo's local environment (sulfide-like *vs.*

oxide-like) which cause a difference in OH^- adsorption and transportation (we are not yet sure about the activivity issued of the reduction by ethanol). However, for this hypothesis, Gd_2O_2S itself has to have ORR reactivity also. This point is not yet studied but can be verified in the future by an electrochemical test without C black in the ink.

2. Unlike the first hypothesis, here, we assume that Gd_2O_2S nanoparticles do not perform any catalytic activity for ORR (which is more likely) and serve strictly a support for Mo-containing phases only. In this case, it is logical not to observe any ORR reactivity of Gd_2O_2S nanoparticles as shown previously. However, the same electrochemical test without C black in the ink is still necessary to verify their inactivity. The Mo now is present in separated phases which is mostly amorphous (invisible for XRD), in a local environment similar to molybdate. Assuming that the ethanol reduces (XANES results on Mo $L_{3,2}$-edges) and somehow sulfidizes (XANES results on S K-edge) partially these phases to activate them (electrochemical results), the measured ORR activity of the sample is comparable with that of MoS_2 as they all possess Mo-S edges. The activity difference between them can be explained that in the synthetic sample, even if the initial oxide-like phase is sulfidized partially, the difference in local environment (100 % Mo-S *vs.* Mo-S and Mo-O coexistence) or the number of active sites 100 % Mo-S (in the case of Mo-O and Mo-S are in separated phases) can still cause the difference in OH^- adsorption and transportation. The lower activity of synthetic samples compared to commercial MoS_2 nanoparticles is now understandable. For this hypothesis, we need to find a way to investigate if there are any Mo-S bonds after the ink preparation, in addition to the reactivity test for Gd_2O_2S without C black.
3. Taking into account the latest results on PDF analysis freshly discussed, the third hypothesis can be considered as a combination of the two previous: molybdate-doped Gd_2O_2S. If Gd_2O_2S itself is active for ORR, maybe there is an effect of molybdate on the electron conduction which enhance the reactivity. If Gd_2O_2S is totally inactive, it can still be a support for modified molybdate (by ethanol) as active sites.

In short, all results from different normalization methods describe the activity of the synthesized materials in the same way without any contradiction between them. According to these results and the CV comparisons between samples and reference, the EDS results can be considered now as more accurate than the introduced ratio when it comes to the materials' compositions as the calculated activity is more or less identical for all samples. Compared to

MoS_2 reference, our synthesized materials are about 7 times less active (in case of taking the composition by EDS). We proposed two hypotheses on the relation structure-reactitvity of the synthetic samples. The main difference between these two is the activity of initial modified Gd_2O_2S. The result of electrochemical test on this sample without C black in the ink will answer which hypothesis is more appropriate.

5. Conclusion

In this chapter, we treated the study on the synthesis in two steps and the characterization of Mo-containing samples resulting from these syntheses. For instance, we understand many interesting things about not only the synthesis method but also the structures, both crystalline and local, of the final products. The 2nd step of the synthesis plays probably a big role on the introduction of disorder and the rearrangement of surface ligands to the nanoparticles which causes the change in crystalline structure, interpreted by XRD and PDF patterns, and the change in morphology, observed by TEM. These modifications are independent from the addition of Mo atoms into the initial system of Gd_2O_2S which is confirmed by all used structural analysis techniques (XRD, TEM, EXAFS and PDF). It has been found also by XAS and PDF that the Mo-containing phases are not massive and that they are well mixed with the Gd-containing phase. The peak at 4.6 Å in PDF patterns is a significant feature from these Mo-containing particles.

By combining the results of different spectroscopy methods and of PDF data treatment, we propose a structural model where Mo exists in isolated tetrahedrons, linking to the Gd_2O_2S nanoparticles by weak interaction between Gd and O. By this way, the final products can be seen as a supported catalyst as the samples with low Mo doping and they showed already an ORR activity in basic medium, even if it is still far from the activity benchmark Pt/C for the moment. Based on all the analysis results on both the structure and the ORR reactivity, we start to have some statements on the relation between the structure and the performed reactivity.

The PDF analysis plays a very big role on the identification of the final product because it is very well adapted for amorphous/dispersed materials like in our case. By continuing the PDF calculations, we will arrive to a more detailed and better described proposition of structure. Also, the further electrochemical analysis *in situ* coupled with XAS will give the essential information not only on the relation structure-reactivity but also the mechanism of the ORR. Furthermore, the DFT calculations can provide the information on the OH^- adsorption on the

nanoparticles (exposed surface of active Mo sites), which will help explaining the reaction mechanism along with the calculations with Tafel plots.

For sure, there are still many points to understand on these series of samples, which is complicated and also very interesting. We finish by now with a very first interesting model for Mo-containing nanoparticles made by the two-step protocol. Once a more detailed description of the series is achieved, the subject on the ORR activity and its mechanism will be back on the table.

6. References

(1) Ding, Y.; Gu, J.; Ke, J.; Zhang, Y. W.; Yan, C. H. Sodium Doping Controlled Synthesis of Monodisperse Lanthanide Oxysulfide Ultrathin Nanoplates Guided by Density Functional Calculations. *Angew. Chemie - Int. Ed.* **2011**, *50* (51), 12330–12334. https://doi.org/10.1002/anie.201105025.

(2) Larquet, C.; Nguyen, A.-M.; Ávila-Gutiérrez, M.; Tinat, L.; Lassalle-Kaiser, B.; Gallet, J.-J.; Bournel, F.; Gauzzi, A.; Sanchez, C.; Carenco, S. Synthesis of Ce 2 O 2 S and Gd 2(1– y) Ce 2 y O 2 S Nanoparticles and Reactivity from in Situ X-Ray Absorption Spectroscopy and X-Ray Photoelectron Spectroscopy. *Inorg. Chem.* **2017**, *56* (22), 14227–14236. https://doi.org/10.1021/acs.inorgchem.7b02336.

(3) Sebenik, R. F.; Burkin, A. R.; Dorfler, R. R.; Laferty, J. M.; Leichtfried, G.; Meyer-Grünow, H.; Mitchell, P. C. H.; Vukasovich, M. S.; Church, D. A.; Van Riper, G. G.; et al. Molybdenum and Molybdenum Compounds. In *Ullmann's Encyclopedia of Industrial Chemistry*; Wiley-VCH Verlag GmbH & Co. KGaA: Weinheim, Germany, 2000; pp 413–454. https://doi.org/10.1002/14356007.a16_655.

(4) Kumar, N.; Seminario, J. M. Computational Chemistry Analysis of Hydrodesulfurization Reactions Catalyzed by Molybdenum Disulfide Nanoparticles. *J. Phys. Chem. C* **2015**, *119* (52), 29157–29170. https://doi.org/10.1021/acs.jpcc.5b09712.

(5) Wang, T.; Gao, D.; Zhuo, J.; Zhu, Z.; Papakonstantinou, P.; Li, Y.; Li, M. Size-Dependent Enhancement of Electrocatalytic Oxygen-Reduction and Hydrogen-Evolution Performance of MoS2 Particles. *Chem. - A Eur. J.* **2013**, *19* (36), 11939–11948. https://doi.org/10.1002/chem.201301406.

(6) Larquet, C. Nanoparticles of Lanthanide and Transition Metal Oxysulfides: From Colloidal Synthesis to Structure, Surface, Optical and Magnetic Properties, 2018.

(7) Benck, J. D.; Hellstern, T. R.; Kibsgaard, J.; Chakthranont, P.; Jaramillo, T. F. Catalyzing the Hydrogen Evolution Reaction (HER) with Molybdenum Sulfide Nanomaterials. *ACS Catal.* **2014**, *4* (11), 3957–3971. https://doi.org/10.1021/cs500923c.

(8) Schieder, M.; Bojer, C.; vom Stein, J.; Koch, S.; Martin, T.; Schmalz, H.; Breu, J.; Lunkenbein, T. Template Removal via Boudouard Equilibrium Allows for Synthesis of Mesostructured Molybdenum Compounds. *Angew. Chemie - Int. Ed.* **2017**, *56* (45), 13968–13972.

https://doi.org/10.1002/anie.201610786.

(9) Gutiérrez, M. A. A. Master Thesis, 2015.

(10) Wakeshima, M.; Hinatsu, Y. Magnetic Properties and Structural Transitions of Orthorhombic Fluorite-Related Compounds Ln3MO7 (Ln=rare Earths, M=transition Metals). *J. Solid State Chem.* **2010**, *183* (11), 2681–2688. https://doi.org/10.1016/j.jssc.2010.09.005.

(11) Morozov, V. A.; Raskina, M. V.; Lazoryak, B. I.; Meert, K. W.; Korthout, K.; Smet, P. F.; Poelman, D.; Gauquelin, N.; Verbeeck, J.; Abakumov, A. M.; et al. Crystal Structure and Luminescent Properties of R2- XEux(MoO4)3 (R = Gd, Sm) Red Phosphors. *Chem. Mater.* **2014**, *26* (24), 7124–7136. https://doi.org/10.1021/cm503720s.

(12) Tóthová, E.; Tarasenko, R.; Tkáč, V.; Orendáč, M.; Hegedüs, M.; Danková, Z.; Holub, M.; Baláž, M.; Matik, M. Microcrystalline Gd 2 MoO 6 Prepared by Combined Mechanochemical/Thermal Process and Its Magnetic Properties. *J. Mater. Sci.* **2019**, *54* (8), 6111–6121. https://doi.org/10.1007/s10853-019-03331-z.

(13) Brixner, L. H.; Sleight, A. W.; Licis, M. S. Ln2MoO6-Type Rare Earth Molybdates-Preparation and Lattice Parameters. *J. Solid State Chem.* **1972**, *5* (2), 186–190. https://doi.org/10.1016/0022-4596(72)90027-8.

(14) Gall, P.; Barrier, N.; Gautier, R.; Gougeon, P. Synthesis, Structural Trends, and Physical and Electronic Properties of the Reduced Molybdenum Oxides R4Mo4O11 (R = Nd-Tm and Y) Containing Infinite Chains of Trans-Edge-Shared Octahedral Clusters. *Inorg. Chem.* **2002**, *41* (11), 2879–2885. https://doi.org/10.1021/ic011000i.

(15) Gall, P.; Barrier, N.; Gautier, R.; Gougeon, P. Synthesis, Structural Trends, and Physical and Electronic Properties of the Reduced Molybdenum Oxides R4Mo4O11 (R = Nd-Tm and Y) Containing Infinite Chains of Trans-Edge-Shared Octahedral Clusters. *Inorg. Chem.* **2002**, *41* (11), 2879–2885. https://doi.org/10.1021/ic011000i.

(16) 13.1.13: The Shape of Absorption Bands - Chemistry LibreTexts https://chem.libretexts.org/Bookshelves/Organic_Chemistry/Map%3A_Organic_Chemistry_(Bruice)/13%3A_Mass_Spectrometry%2C_Infrared_Spectroscopy%2C_and_Ultraviolet/13.01%3A_Mass_Spectrometry%2C_Infrared_Spectroscopy%2C_and_Ultraviolet/Visible_Spectroscopy/13.1.13%3A_The_Shape_of_Absorption_Bands (accessed Jul 19, 2020).

(17) Lu, Z.; Karakoti, A.; Velarde, L.; Wang, W.; Yang, P.; Thevuthasan, S.; Wang, H. F. Dissociative Binding of Carboxylic Acid Ligand on Nanoceria Surface in Aqueous Solution: A Joint in Situ Spectroscopic Characterization and First-Principles Study. *J. Phys. Chem. C* **2013**, *117* (46), 24329–24338. https://doi.org/10.1021/jp4068747.

(18) Cass, L. C.; Malicki, M.; Weiss, E. A. The Chemical Environments of Oleate Species within Samples of Oleate-Coated PbS Quantum Dots. *Anal. Chem.* **2013**, *85* (14), 6974–6979. https://doi.org/10.1021/ac401623a.

(19) Zhang, J.; Ohara, S.; Umetsu, M.; Naka, T.; Hatakeyama, Y.; Adschiri, T. Colloidal Ceria Nanocrystals: A Tailor-Made Crystal Morphology in Supercritical Water. *Adv. Mater.* **2007**, *19* (2), 203–206. https://doi.org/10.1002/adma.200600964.

(20) Aronoff, Y. G.; Chen, B.; Lu, G.; Seto, C.; Schwartz, J.; Bernasek, S. L. Stabilization of Self-Assembled Monolayers of Carboxylic Acids on Native Oxides of Metals. *J. Am. Chem. Soc.* **1997**, *119* (2), 259–262. https://doi.org/10.1021/ja953848+.

(21) Zhang, J.; Naka, T.; Ohara, S.; Kaneko, K.; Trevethan, T.; Shluger, A.; Adschiri, T. Surface Ligand Assisted Valence Change in Ceria Nanocrystals. *Phys. Rev. B - Condens. Matter Mater. Phys.* **2011**, *84* (4), 1–9. https://doi.org/10.1103/PhysRevB.84.045411.

(22) Ogasawara, H.; Kotani, A.; Thole, B. T. Lifetime Effect on the Multiplet Structure of 4 d X-Ray-Photoemission Spectra in Heavy Rare-Earth Elements. *Phys. Rev. B* **1994**, *50* (17), 12332–12341. https://doi.org/10.1103/PhysRevB.50.12332.

(23) Lede, E. J.; Requejo, F. G.; Pawelec, B.; Fierro, J. L. G. XANES Mo L-Edges and XPS Study of Mo Loaded in HY Zeolite. *J. Phys. Chem. B* **2002**, *106* (32), 7824–7831. https://doi.org/10.1021/jp014648p.

(24) Scott, R. a. X-Ray Absorption Spectroscopy. *Compr. Coord. Chem. II* **2011**, 159–186. https://doi.org/10.1002/9781119951438.eibd0831.

(25) George, S. J.; Drury, O. B.; Fu, J.; Friedrich, S.; Doonan, C. J.; George, G. N.; White, J. M.; Young, C. G.; Cramer, S. P. Molybdenum X-Ray Absorption Edges from 200 to 20,000eV: The Benefits of Soft X-Ray Spectroscopy for Chemical Speciation. *J. Inorg. Biochem.* **2009**, *103* (2), 157–167. https://doi.org/10.1016/j.jinorgbio.2008.09.008.

(26) Henderson, G. S.; De Groot, F. M. F.; Moulton, B. J. A. X-Ray Absorption Near-Edge Structure (XANES) Spectroscopy. *Rev. Mineral. Geochemistry* **2014**, *78*, 75–138. https://doi.org/10.2138/rmg.2014.78.3.

(27) Schutte, W. J.; Disselborg, F.; De Boer, J. L. Determination of the Two-dimensional Incommensurately Modulated Structure of Mo2S3. *Acta Crystallogr. Sect. B* **1993**, *49* (5), 787–794. https://doi.org/10.1107/S0108768192006670.

(28) Shannon, R. D. Revised Effective Ionic Radii and Systematic Studies of Interatomic Distances in Halides and Chalcogenides. *Acta Crystallogr. Sect. A* **1976**, *32* (5), 751–767. https://doi.org/10.1107/S0567739476001551.

(29) Li, R.; Wei, Z.; Gou, X. Nitrogen and Phosphorus Dual-Doped Graphene/Carbon Nanosheets as Bifunctional Electrocatalysts for Oxygen Reduction and Evolution. *ACS Catal.* **2015**, *5* (7), 4133–4142. https://doi.org/10.1021/acscatal.5b00601.

(30) Wang, L.; Sofer, Z.; Pumera, M. Will Any Crap We Put into Graphene Increase Its Electrocatalytic Effect? *ACS Nano* **2020**, *14* (1), 21–25. https://doi.org/10.1021/acsnano.9b00184.

Chapter III

Synthesis and characterization of $Gd_{2(1-x)}Mo_{2x}O_2S$ by an one-step protocol

Tables of contents

1. Why synthesis via a one-step protocol for Mo-containing Gd_2O_2S-based nanoparticles?

In this project, we are interested in making molybdenum oxysulfide but for the moment there is no report on a precise synthesis giving a well-defined crystalline compound. Moreover, most of the existing methods are at high temperature or using physical methods. To the best of our knowledge, mostly no research is done on a colloidal synthesis of molybdenum-based oxysulfide nanoparticles in organic solvents, although it may provide better defined nanoparticles at lower energetic cost. In contrast, the colloidal synthesis of Gd_2O_2S nanoplatelets is well-known with the product structure well-described.[1,2] Starting from the synthesis method of Gd_2O_2S, the easiest way to introduce another metallic ions into the structure is to add another metallic precursor in the synthesis at the same time as Gd precursor. This method is identical to $Gd_{2(1-y)}Ce_{2y}O_2S$ ($0 \leq y \leq 1$) nanoparticles synthesis where two metallic precursors are added at the same time and the resulting phases contain a statistical number of Gd sites substituted by Ce.[2] In the structure of Gd_2O_2S, each Gd atom links to 4 O atoms and 3 S atoms (Figure 1B), if this site is substituted by a Mo, some Mo-S sites will be created. However, in Chapter I, we have seen already that such kind of substitution is impossible for the pair Gd – Mo cations. Hence, we might expect another kind of relation between two metals, e.g. a deposition of Mo cations on the surface of Gd_2O_2S nanoparticles as a shell by Mo-S bonds which may create also Mo-S sites. As it is known that the Mo-S edge sites in MoS_2 (Figure 1D) are the active site for reactions such as hydrodesulfurization (HDS),[3,4] and oxygen reduction reaction (ORR),[5] by this method, we may have an interesting catalyst for ORR.

In this chapter, a sample will be identified by the number of molar equivalent of Mo which is supposed to substitute Gd in Gd_2O_2S, i.e. $Gd_{2(1-x)}Mo_{2x}O_2S$, where x is the molar ratio between introduced Mo and the sum of both metals, which is constant at 0.5 mmol for all syntheses.

$$Gd_{2(1-x)}Mo_{2x}O_2S \qquad x = \frac{n_{Mo\ introduced}}{0.5}$$

0.5: total introduced metallic precursors in mole

x = molar ratio $\frac{Mo}{Gd+Mo}$

= name of sample

$2x$ = theoretical notation index

Example: for a sample 0.15 : $x = \frac{n_{Mo\ introduced}}{0.5}$ = 0.15 and notation $Gd_{1.7}Mo_{0.3}O_2S$.

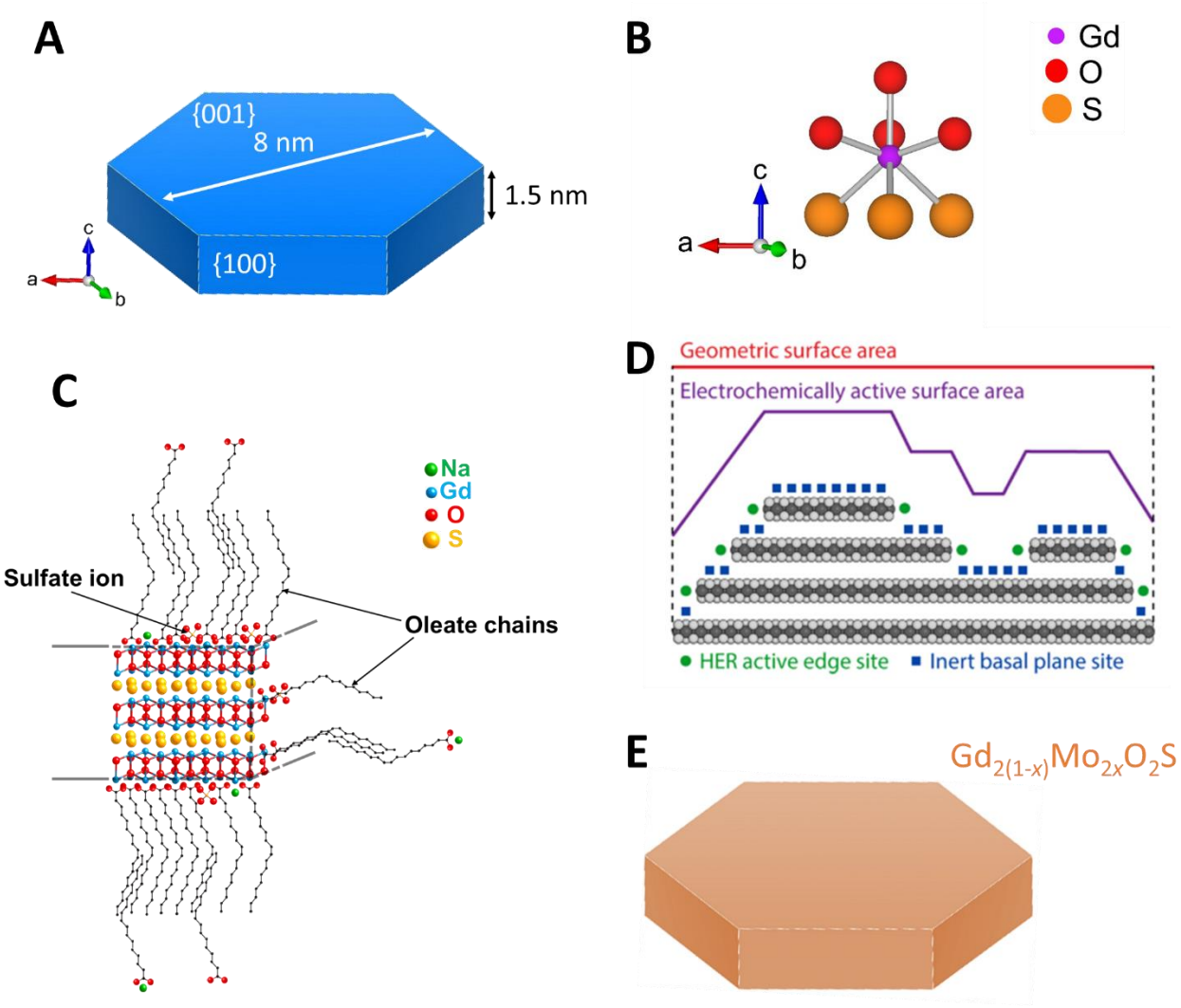

Figure 1 Schemes showing the structure of Gd_2O_2S nanoplatelets: (A) shape and average size of Gd_2O_2S nanoparticles; (B) local structure of a Gd site and (C) nanoplatelets with oleate ligands on their surface, figure from C. Larquet's thesis.[6] (D) Figure of active site in MoS_2: Mo-S edge sites, figure by J. D. Benck et al.[7] (E) Figure of nanoparticles $Gd_{2(1-x)}Mo_{2x}O_2S$ expected from this initiative.

The syntheses by the one-step protocol here were realized in parallel with those by the two-step protocol (see Chapter II). The structures of samples (crystalline and local), the morphologies and surface activities from the two series were compared to help understanding both series. The correspondence in notation between these two series is showed in Table 1. In practice, the introduced quantity of Mo precursor was always calculated based on its molar ratio to the molar sum of two metals ($\frac{Mo}{Gd+Mo}$). To facilitate the notation, different choices of *x*

were made for each series. Two samples in the same row are comparable as the introduced molar ratio of Mo precursor is practically the same and the difference between the two notations "2*x*" is negligible to the compositions of samples.

Table 1 Correspondence in notation between samples from two series: synthesis in one step and synthesis in two steps. Highlighted column: calculated molar quantity of Mo precursor to add in the synthesis. Crossed cells: inexistent samples.

Samples by one-step protocol $Gd_{2(1-x)}Mo_{2x}O_2S$			Samples by two-step protocol Gd_2O_2S/Mo_{2x}		
$x = \frac{Mo}{Gd+Mo}$	$\frac{Mo}{Gd}$	index Mo (2*x*)	$\frac{Mo}{Gd+Mo}$	$x = \frac{Mo}{Gd}$	index Mo (2*x*)
0	0	0	0	0	0
0.005	0.01	0.01			
0.01	0.01	0.02			
0.02	0.02	0.04	0.02	0.02	0.04
0.05	0.05	0.10	0.05	0.05	0.11
0.10	0.11	0.20	0.10	0.11	0.22
0.13	0.15	0.26			
0.15	0.18	0.30	0.15	0.18	0.36
			0.18	0.22	0.44
0.20	0.25	0.40	0.20	0.25	0.50
0.26	0.35	0.52	0.26	0.35	0.70
0.30	0.43	0.60	0.30	0.43	0.86
0.50	1.00	1.00	0.50	1.00	2.00
			0.67	2.03	4.06
0.70	2.33	1.40			

2. Synthesis protocol

Summary equation of the synthesis:

$$2(1\text{-}x)\ Gd(acac)_3 + 2x\ [Mo^{+X}] + \frac{1}{8}\ S_8 + 2\ Na(oleate) \xrightarrow[OM,\ OA,\ ODE]{310\ °C,\ 30\ min} Gd_{2(1-x)}Mo_{2x}O_2S,\ 0 < x < 2.33$$

For reference, all samples Gd_2O_2S classically synthesized in one-step protocol are taken into account. For Mo-containing samples, like in the Chapter II, there are three Mo molecular precursors used: $Cp_2Mo_2^{(+I)}(CO)_6$, $Mo^{(+III)}(acac)_3$ and $Mo^{(+VI)}O_2(acac)_2$.

Our research started with the Mo(+VI) precursor because it is the safest and the most inexpensive soluble compound. A complete series with *x* ranging from very low (0.005) to high (0.50) values was made with this precursor. The apparent yield of the synthesis was estimated, assuming the only phase has the formula $Gd_{2(1-x)}Mo_{2x}O_2S$, values between 50 % and 265 % were obtained (Table 2, values in orange). Most values were above 100 % (17 of 24 samples), which suggests that other phase(s) were formed, containing Mo. The color of obtained powder varies between dark brown to black.

Table 2 Yields of $Gd_{2(1-x)}Mo_{2x}O_2S$ syntheses with three Mo precursors: Mo(+I) (in white), Mo(+III) (in blue) and Mo(+VI) (in orange).

x	**0.005**	**0.01**	**0.02**	**0.05**	**0.10**		**0.13**
yield (%)	81	50	89	124	75	120	65
	79	82	89	120	192	88	
		90		111	128	81	
				68	215	176	
				100			
	0.15		**0.20**	**0.26**	**0.30**	**0.50**	**0.70**
	109	103	135	90	126	116	120
	129	82	115	94	72	140	
	265	84	67		63	145	
	101	91	80			50	
	125	64				113	
	74	91					

For the precursor $Cp_2Mo_2(CO)_6$, a complete series was also made, with *x* ranging from 0.005 to 0.70. The yields in this case varies between about 70 % to 180 % (Table 2, in white). There are less syntheses with yields superior to 100 % than those with Mo(+VI) precursor (5 of 21 samples). The color of samples varies from very light brown (mostly grayish for sample $x = 0.005$) to brown (sample $x = 0.70$): the colors are much lighter than for samples made with Mo(+VI) precursor.

In the case of $Mo(acac)_3$, this is an uncommon precursor which is not yet commercial, only few samples with *x* equals to 0.15 were done to compare with other precursors. For this precursor, the yield varies between about 60 % to about 90 % (Table 2, in blue). All these samples are black.

In order to see if it is possible to have such high yields in these syntheses, we assume that the final powders are mixtures of phases: Gd_2O_2S, Na_2MoO_4, free sulfate and about 30 wt% of organic ligands[6,8] to have as much weight of powder as possible. Table 3 shows the calculations for a sample with $x = 0.15$ (regardless the type of Mo precursor), for a comparison between a phases mixture we would find at 100 % yield and a mono-phase $Gd_{1.7}Mo_{0.3}O_2S_{0.4}$ at 100 % yield. From this assumption, the yield can be up to 200 %. Knowing that the powder is difficult to dry, there might be an amount of organic solvents and/or water which can make the yield even higher. Therefore, for the concerning syntheses, it is not illogical to have the yield frequently higher than 100 %.

Table 3 Yield calculation for a sample with x = 0.15, assuming that the final powder is a mixture of several phases: Gd_2O_2S, Na_2MoO_4, free sulfate and about 30 wt% of organic ligands.

Phase	n (mmol)	M (g.mol^{-1})	m (mg)	Yield compared to $Gd_{1.7}Mo_{0.3}O_2S_{0.4}$
$Gd_2O_2S_{0.4}$	0.2125	359	76.3	$\frac{132 + 132 \times 0.3}{85} = 200\ \%$
Na_2MoO_4	0.075	206	15.4	
Na_2SO_4	0.175	142	24.8	
SO_4^{2-}	0.26	96	25	
$Gd_{1.7}Mo_{0.3}O_2S_{0.4}$	0.25	340	85	100 %

Finally, for this synthesis in one step, no modification or optimization of the protocol was done. In all cases, the yields are at least 50 %, which suggests that most of the products are powders correctly separated from the solvent by centrifugation and washing.

3. Characterization

3.1. Trends observed in the series of samples

3.1.1. Trends in composition by EDS

As mentioned at the beginning of the chapter, three kinds of precursors were used for the synthesis of $Gd_{2(1-x)}Mo_{2x}O_2S$. Figure 2 shows the global results of analysis on their composition by EDS. For this analysis, the detector can only detect elements heavier than Fluorine. It means that the amount of oxygen in the powder is only a proposed value (based on the Gd_2O_2S structure without counting organic ligands) as we cannot quantify it. The other concerning elements (Gd, Mo, S and Na) are quantified by automatic calculation by the software INCA. For the same reason of the inseparable peaks Mo L-edge and S K-edge, all the discussion below is based on the assumption that the automatic calculation by INCA is correct.

Figure 2A and C show the relation between observed molar ratio Mo/Gd and S/Gd and introduced molar ratio Mo/Gd for each sample, calculated from EDS measurements. Each point on the graph is the average value of 3 to 5 zones of measurement and the error bar is its standard deviation. The samples made from **Mo(+I)** precursor are represented in black, the samples made from **Mo(+VI)** are in red and in green are the samples from **Mo(+III).** Figure 2A shows also the possible trends of observed ratio Mo/Gd when x increases: no Mo lost after each synthesis (the first bisector of the graph). It passes on most of points. Only two points corresponding to two samples made with Mo(+III) precursor, $x = 0.15$, and 2 points corresponding to 2 samples made with Mo(+I) precursor, $x = 0.43$ and 2.33, are slightly out of line. Figure 2C shows expected ratio S/Gd of 0.2 with a dash line: it is the observed value in the Gd_2O_2S reference, verified by our group and another group.[1,2] Compared to this value, the observed ratio S/Gd increases quickly from 0.2 to 1.0 with the increase of x (i.e. Mo/Gd from 0.005 to 0.43, Figure 2D).

In order to better visualize the evolution of ratios observed Mo/Gd and S/Gd in function of introduced Mo/Gd, the averages of observed ratios are calculated for each value of x and traced in function of introduced Mo/Gd (Figure 2B-D). Figure 2B shows two possible trend lines for two groups of samples: made with Mo(+I) precursor, in black, and made with Mo(+VI) precursor, in red. The slopes are 0.85 and 0.97 respectively, even with the black point at introduced Mo/Gd = 0.43 that falls farther from the trend. From the shown data, we can state that in all cases, very small amount of Mo was lost after the isolation of solid (assuming there is no loss of Gd).

Figure 2D shows two possible trend lines for two groups of samples with $x < 0.25$ (i.e. Mo/Gd up to 0.25): made with Mo(+I) precursor, in black, and made with Mo(+VI) precursor, in red. The values of S in both cases rise quickly with the increase of introduced Mo/Gd: the slopes are 1.38 and 2.46 respectively. Both regressions are quite accurate with R^2 of 0.91 and 0.94 respectively. Two dash lines show the ratio S/Gd in Gd_2O_2S reference (0.18, average value calculated from 6 samples) and possible saturation value (1.0, introduced ratio S/Gd) corresponding to a quantitative incorporation of sulfur in the powder. To reach observed S/Gd of 0.5 as in bulk Gd_2O_2S, only 0.18 equivalent of Mo(+I) or 0.15 equivalent of Mo(+VI) was needed (compared to the initial quantity of Gd). To reach the possible saturation value of 1.0, 0.43 equivalent of Mo(+I) or 1.0 equivalent of Mo(+VI) was needed. These results suggest that during the synthesis, as Mo has a high affinity to S, some other secondary phase(s) which contain both Mo and S were formed, which increase significantly the observed S/Gd of the powders.

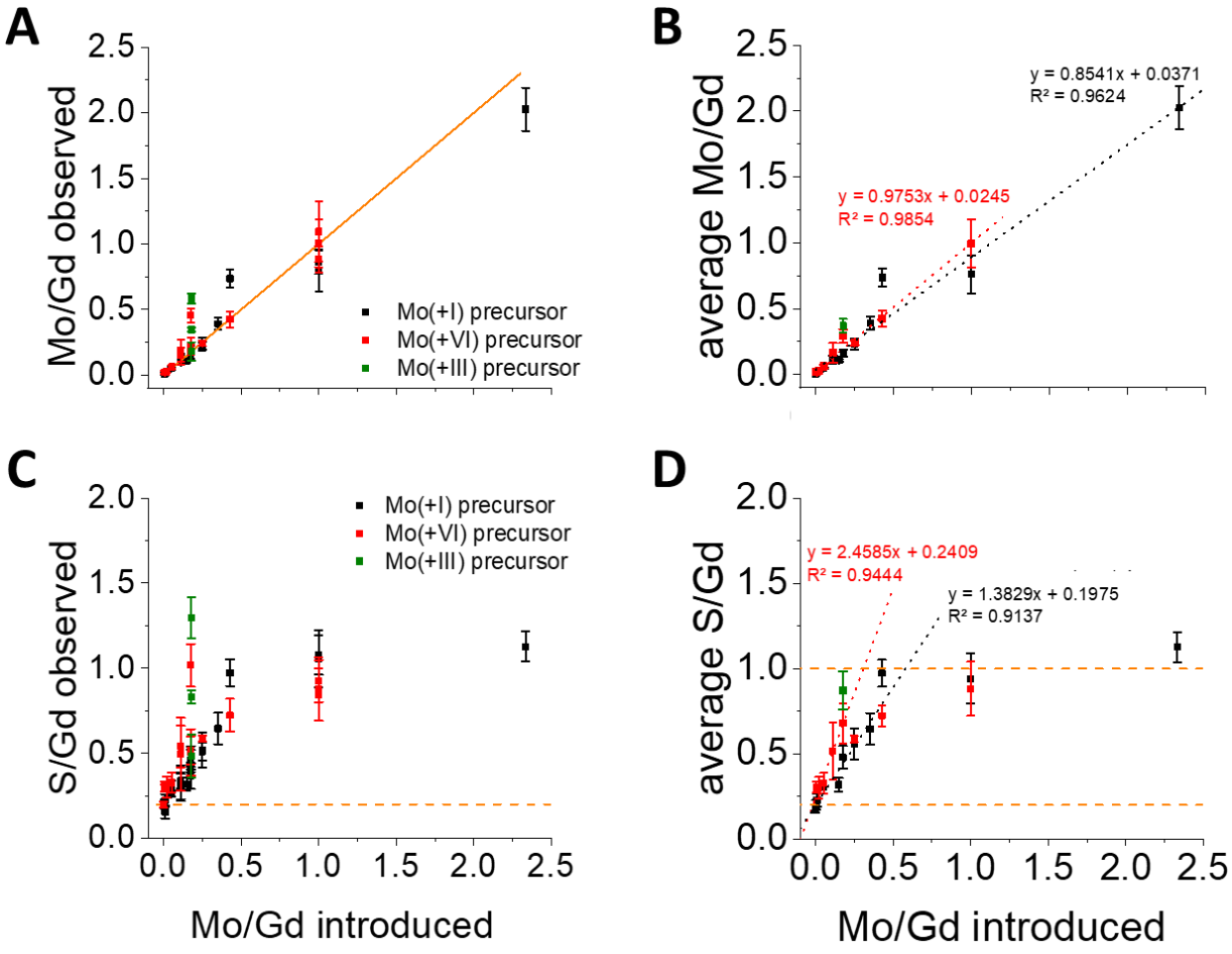

Figure 2 Composition analysis of all samples. (A) Observed molar ratio Mo/Gd vs. introduced molar ratio, raw data for each prepared sample: samples made with Mo(+I) precursor (black),

Mo(+VI) precursor (red) and Mo(+III) precursor (green). (B) Observed molar ratio Mo/Gd vs. introduced molar ratio, calculated average of all samples prepared with the same Mo/Gd ratio: samples made with Mo(+I) precursor (black), Mo(+VI) precursor (red) and Mo(+III) precursor (green). The dash line represents an estimation of possible trends for all samples made with Mo(+I) precursor (black) and for samples with $x \leq 0.5$ (Mo/Gd = 1.0), made with Mo(+VI) precursor (red). (C) Observed molar ratio S/Gd vs. introduced molar ratio Mo/Gd, raw data for each prepared sample: samples made with Mo(I) precursor (black), Mo(+VI) precursor (red) and Mo(+III) precursor (green). The dash line represents the average ratio S/Gd in Gd_2O_2S reference (= 0.2). (D) Observed molar ratio S/Gd vs. introduced molar ratio Mo/Gd, calculated average of all samples prepared with the same Mo/Gd ratio: samples made with Mo(+I) precursor (black), Mo(+VI) precursor (red) and Mo(+III) precursor (green). The dash line represents an estimation of possible trends for all samples made with Mo(+I) precursor (black) and for samples with $x \leq 0.5$, made with Mo(+VI) precursor (red). The dash line represents the average ratio S/Gd in Gd_2O_2S reference (0.18) and possible saturation value (1.0).

Considering the three samples with $x = 0.15$ made with the Mo(+III) precursor, the reaction was not repeatable. Figure 2A and C show 3 raw data points with significant difference in content of Mo and S: a factor of 2 between the highest and lowest contents and a factor of 2.5 between the highest and lowest contents of S. Each point has a small error bar, which might signify an even distribution of Mo and S in each sample. Figure 2B shows the average point of these samples situated slightly higher than the trend lines of the two other samples groups. Figure 2D shows that the average point reaches already S/Gd of 1.0. The effect of precursor in general and the repeatability of synthesis with Mo(+III) are not yet well understood, this investigation will need to be pursued in the future to enlighten these points.

3.1.2. Trends from structural analysis

In Figure 3, in some of the diffractograms, there is a large massive at small angles (marked with a star). It is probably due to the large quantity of surface ligands on the nanoparticles. In any case, the massive is present or not, there is no effect on the structure (crystalline or local) of the nanoparticles. From now, it is neglected.

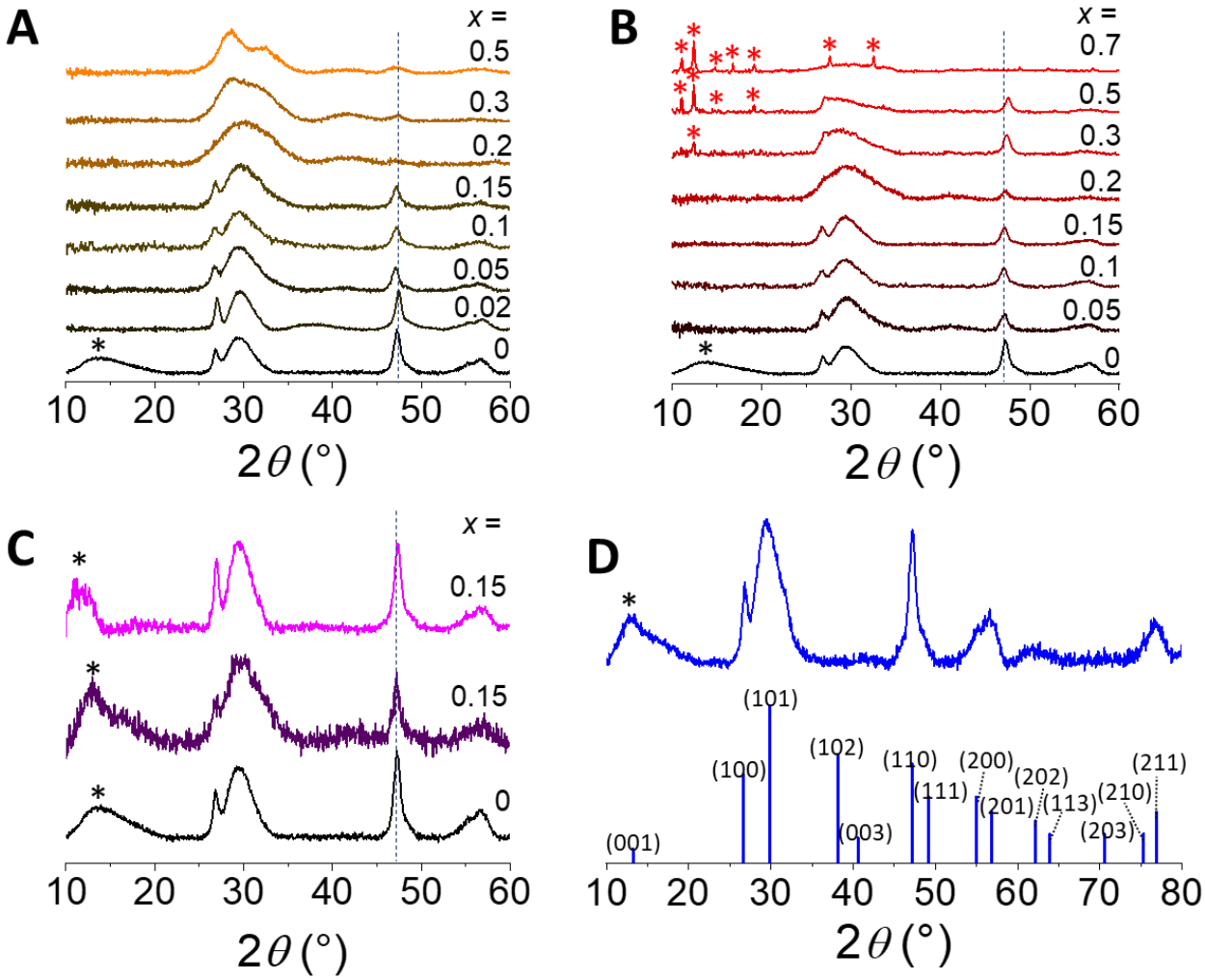

Figure 3 (A) XRD patterns of the samples made with the Mo(+VI) precursor with x from 0.02 to 0.5. (B) XRD patterns of the samples made with the Mo(+I) precursors with x from 0.05 to 0.7. The peaks marked with red stars are probably correspondent to a mixture of Na_2MoO_4 (JCPDS file 01-084-6509) and $Mo_{15}S_{20}$ (JCPDS file 04-018-5769). (C) XRD patterns of samples made with the Mo(+III) precursors with x = 0.15. (D) XRD pattern of Gd_2O_2S reference with peaks positions (JCPDS file 00-026-1422). Dash line: peak (110) of Gd_2O_2S used for structure analysis. Broad peaks marked with black star may link with impurities from organic ligands, not yet identified.

Figure 3A-C shows the diffractograms of three groups of samples made with the three precursors. For the samples made with Mo(+I) precursor, the value of *x* in the synthesis varies between 0.05 to 0.7. One of the diffractograms in Figure 3C has much more noise than all others. The cause has no relation with the structure of final product but with the shorter acquisition time, i.e. the structure of this sample is probably similar to the other sample with *x* = 0.15 in Figure 3C. For the samples made with Mo(+VI) precursor, the value of *x* in the

synthesis varies between 0.02 to 0.5. For the samples made with Mo(+III) precursor, only three samples with $x = 0.15$ were made, mostly as a comparison. Figure 3D represents the diffractogram of Gd_2O_2S reference with the theoretical position of bulk phase's Bragg peaks. From observation, we can initially divide these series into two subgroups: $x < 0.2$ (i.e. Mo/Gd up to 0.25, low quantity of Mo) where the main XRD peaks of Gd_2O_2S are recognizable and $x \geq 0.2$ (high quantity of Mo) where they are not anymore (Figure 3A and B). While the evolutions of crystalline structures in the two groups of sample made with low introduced quantity of Mo(+I) and Mo(+VI) precursors are similar, these for high introduced quantity of precursors are different. The powders made with Mo(+VI) tend to form amorphous phase(s) while the powders made with Mo(+I) precursor tend to form crystalline phase(s). The crystalline phases appearing in the case of Mo(+I) precursor are also found in the synthesis without Gd precursor and Na source: it is probably a mixture of peaks corresponding to Na_2MoO_4 and $Mo_{15}S_{20}$. These peaks will be discussed more in detail in the next chapter on the samples made without Gd precursor (Chapter IV).

In order to further analyze the patterns, only the (110) peak is taken into account. In particular, we were looking for a possible shift, as in the case of Ce-Gd substitution.[2] This will be discussed in another section below.

3.1.3. Analysis of morphology by TEM

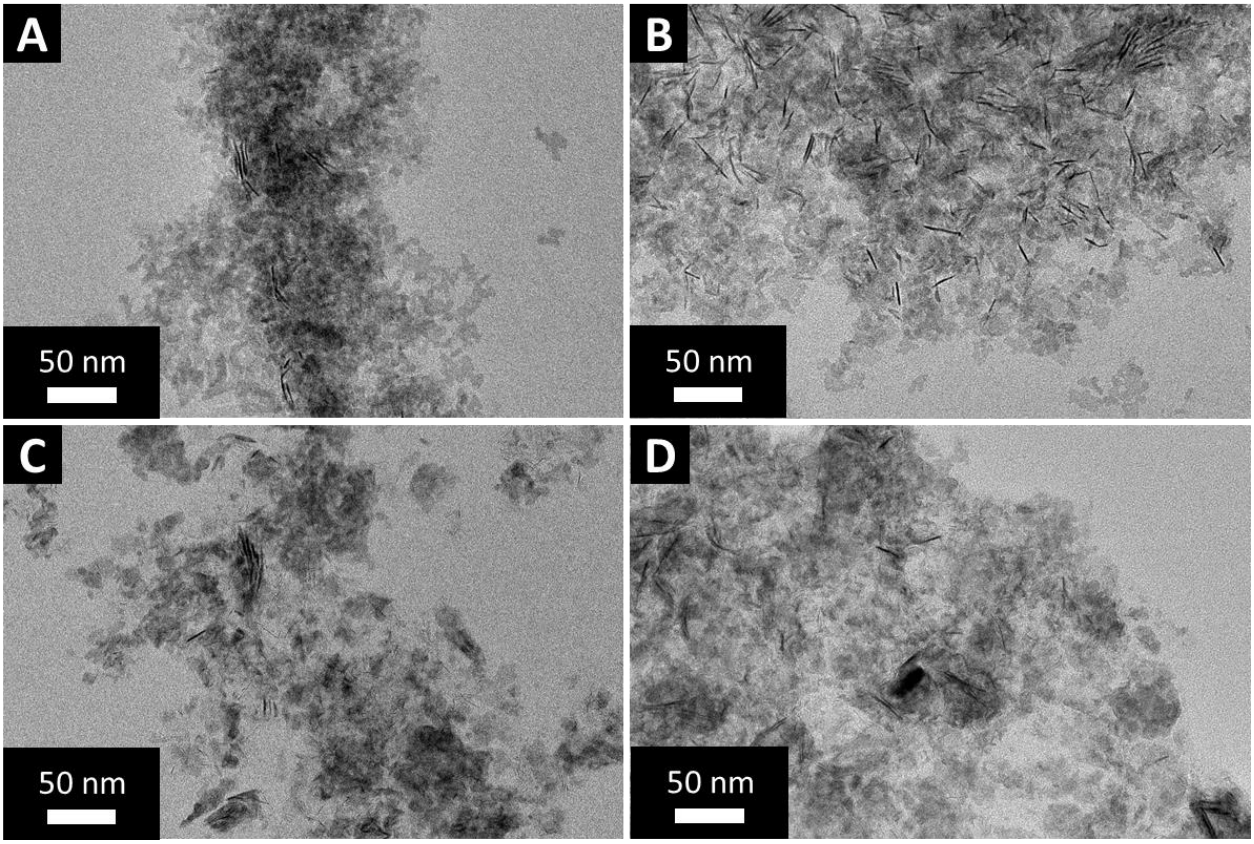

Figure 4 TEM images showing the morphology of (A) Gd_2O_2S reference, and $Gd_{1.7}Mo_{0.3}O_2S$ samples (x = 0.15) made with (B) Mo(+I) precursor, (C) Mo(+VI) precursor and (D) Mo(+III) precursor. Images are taken at ×42 000.

The morphology of nanoparticles in all samples was studied by Transmission Electron Microscopy (TEM). Figure 4 shows the representative images of Gd_2O_2S reference and three samples $Gd_{1.7}Mo_{0.3}O_2S$ (x = 0.15) made with the three precursors. Globally, all images show the morphology of nanoplates along (001) and (100) directions. No visible difference in shape or stacking is observed. This suggests that the addition of Mo precursors at the same time of Gd precursor in the synthesis does not change the overall aspect of the nanoparticles compared to the reference.

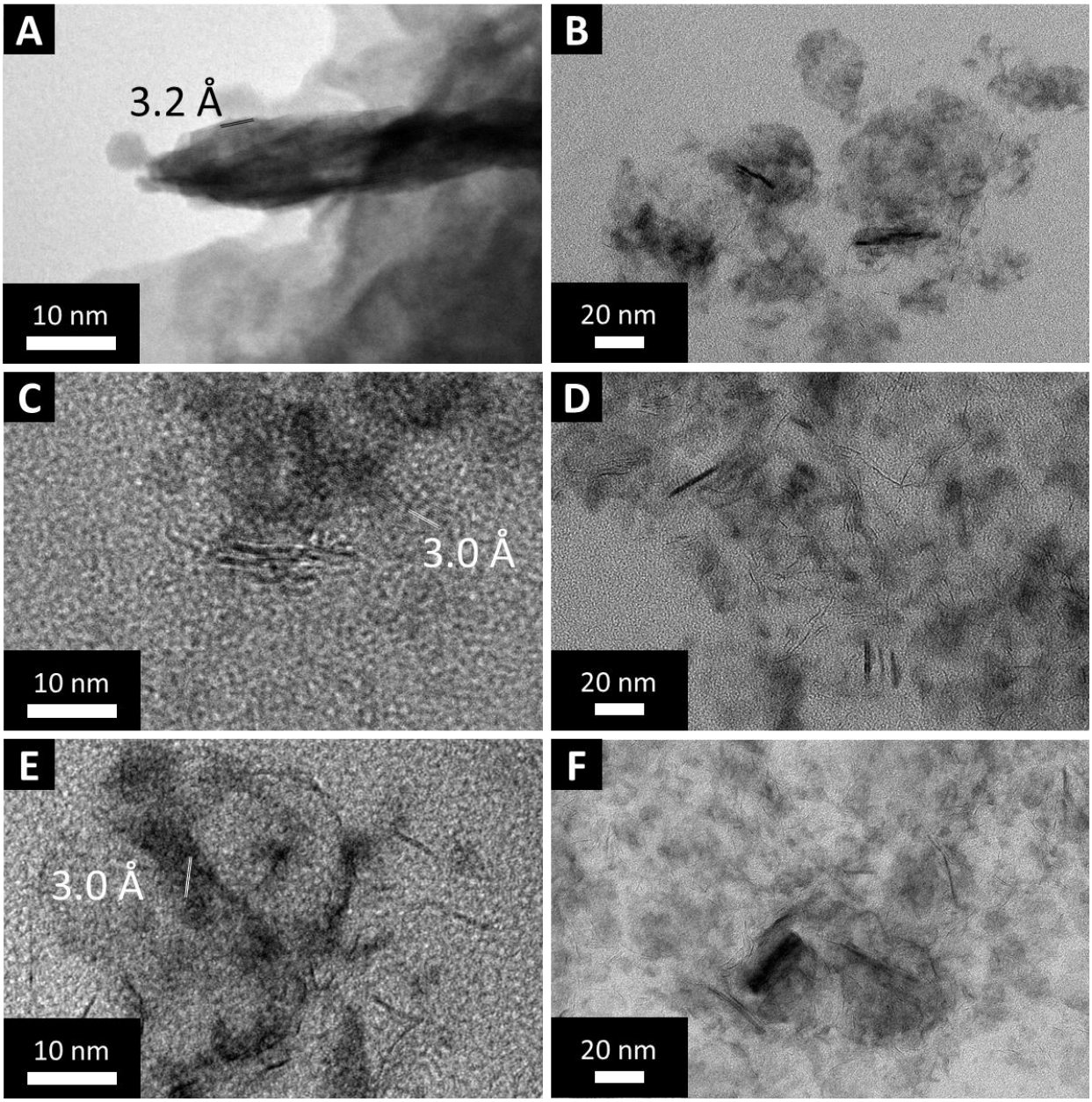

Figure 5 TEM images showing nanoparticles along {001} face and {100} side of samples $Gd_{1.7}Mo_{0.3}O_2S$ (x = 0.15), representative for each samples group, made with (A, B) Mo(+I) precursor, (C, D) Mo(+VI) precursor and (E, F) Mo(+III) precursor. (A, C, E) Images are taken at ×350 000. (B, D, F) Images are taken at ×110 000.

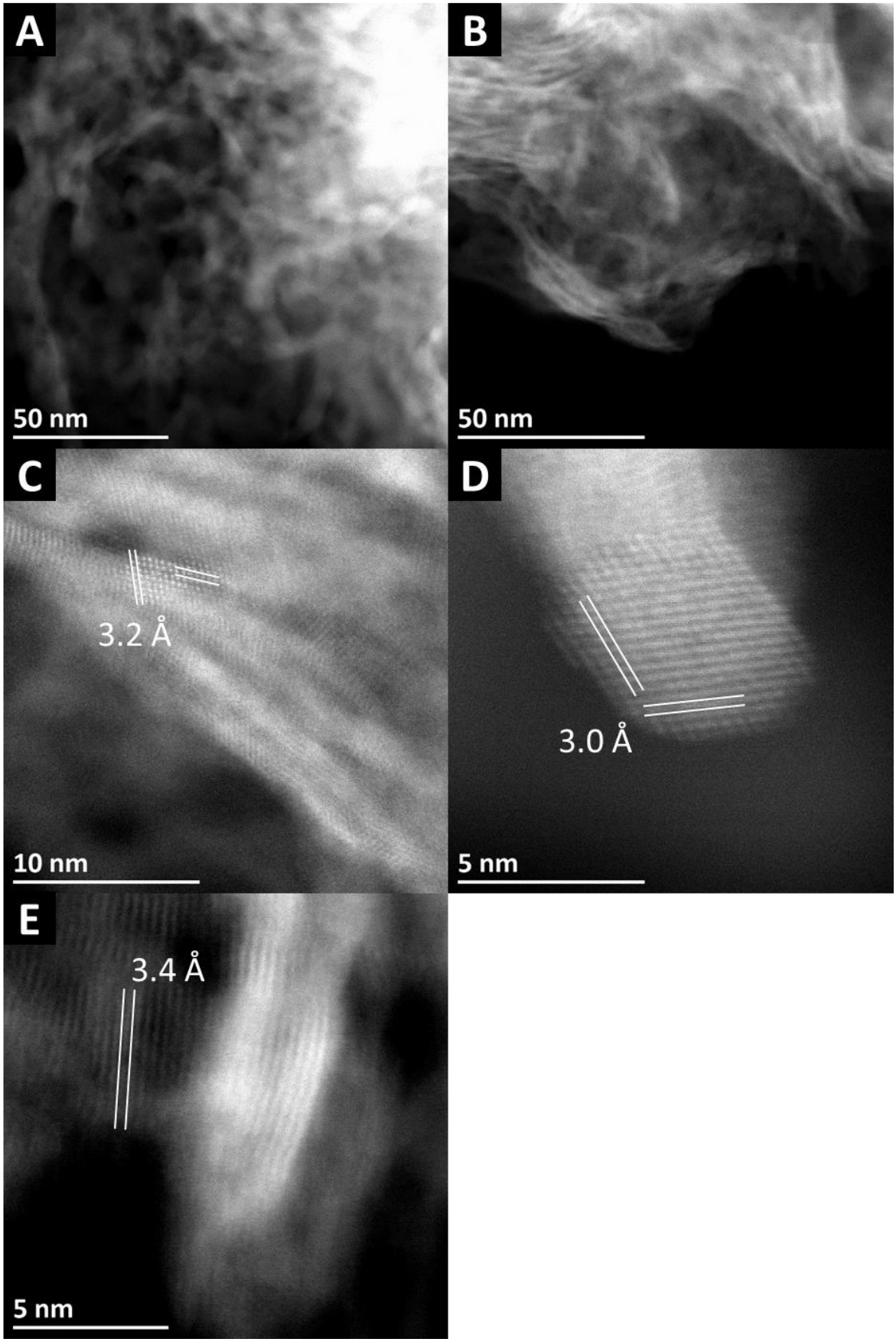
A
50 nm
B
50 nm
C
3.2 Å
10 nm
D
3.0 Å
5 nm
E
3.4 Å
5 nm

Figure 6 HRTEM images in dark field by Mounib Bahri and Ovidiu Ersen (Institut de Physique et Chimie des Matériaux de Strasbourg, IPCMS) of a sample $Gd_{1.7}Mo_{0.3}O_2S$ (x = 0.15) made with Mo(+I) precursor.

The nanoparticles in this case show only classical interplanar distances of about 3.0 Å, corresponding to the interplanar distances in (110) and (101) directions in Gd_2O_2S (Figure 5A, C, E), while all nanoparticles in the products made by the two-step protocol also show a typical distance of 8.0 Å under electron beam. Besides, for all kinds of Mo precursor, there are very thin nanoparticles formed in addition to Gd_2O_2S-like nanoplates (Figure 5B, D, F). It means that in a same sample, there are two kinds of nanoparticles morphologies coexisting: Gd_2O_2S-like nanoplates and filament-like nanoparticles. For the moment, it is not yet clear if the natures of these two morphologies are identical but the first analysis by High Resolution TEM (HRTEM) by Mounib Bahri and Ovidiu Ersen (Institut de Physique et Chimie des Matériaux de Strasbourg, IPCMS) did not show any remarkable point about the morphology (Figure 6). In these images, there are only Gd_2O_2S-like nanoplates were observed with the same visible interplanar distances, the very thin filaments were not seen.

3.1.4. Trends in local structures by XAS

To understand the local structure and local environment of Mo, the measurements of X-ray Absorption Spectroscopy were done at SOLEIL Synchrotron (SAMBA and LUCIA Beamlines). All spectra were obtained with samples diluted in pellet with graphite.

Figure 7A shows a comparison between a $Gd_{1.7}Mo_{0.3}O_2S$ ($x = 0.15$) sample and selected commercial references. The edge of the synthetic sample is similar to those of sulfide references ($Gd_{1.7}Mo_{0.3}O_2S$: 20 009.8 eV; MoS_2: 20 008.7 eV; MoS_3: 20 009.0 eV; MoS_4^{2-}: 20 009.7 eV) and different from those of MoO_3 and Na_2MoO_4 (20 018.3 eV and 20 018.9 eV, respectively), based on the first derivative (the pre-edges are not taken into consideration). This observation suggests that the oxidation state of Mo in the synthetic sample should be +IV as in the MoS_2 sulfide reference. In terms of the geometry of Mo, the clear absence of the pre-edge (compared to MoS_4^{2-} with the same oxidation state in tetrahedral geometry) indicates that Mo in the $Gd_{1.7}Mo_{0.3}O_2S$ sample is likely centrosymmetric (or close to a centrosymmetric geometry).

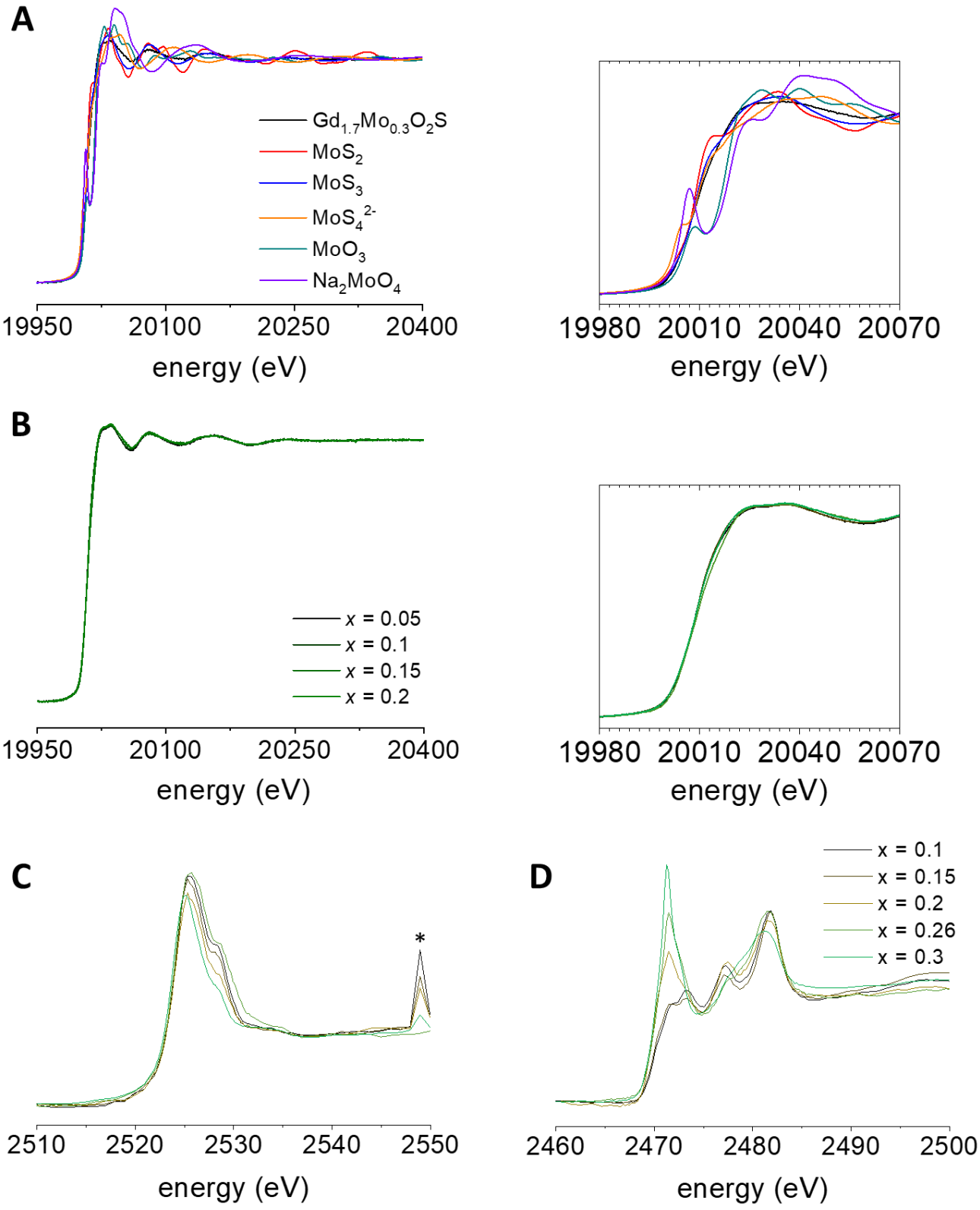

Figure 7 Comparison of XAS between: (A) a sample $Gd_{1.7}Mo_{0.3}O_2S$ (x = 0.15) and some commercial references, a zoom at XANES part is provided. XAS of samples made with Mo(+I) precursor at (B) Mo K-edge, $0.05 \leq x \leq 0.2$ with a zoom on the X-ray Absorption Near Edge

Structure (XANES) part; (C) Mo L_3-edge, $0.1 \leq x \leq 0.3$ and (D) S K-edge, $0.1 \leq x \leq 0.3$. The peak marked with a black star is an instrumental glitch. The legend in (D) is common for (C).

In Figure 7B, we observe that all samples ($0.05 \leq x \leq 0.2$) at Mo K-edge have the same edge position (20 009.8 eV), an absence of pre-edge, and the same shape of multiple-scattering zone. Similarly, at Mo L_3-edge and S K-edge, the edges of all the samples (with $0.1 \leq x \leq 0.3$) are situated at the same energy (2523 eV) (Figure 7C-D). Each spectrum at Mo L_3-edge has 2 peaks components with a splitting energy of about 3 eV. Each spectrum at Mo L_2-edge possess also 2 components similar to that at L_3-edge (data not shown). These observations confirm the similarity of the Mo's nature in all synthetic samples with different *x*.

In terms of S K-edge, based on the presence of the first peak at 2472.5 eV, corresponding to reduced S species (S^{2-}), the spectra can be divided into 2 subgroups: $x < 0.2$ (very low peak) and $x \geq 0.2$ (intense peak) (Figure 7D). While the spectra of samples with $x = 0.1$ and 0.15 are mostly the same, the first peak's intensity increases with the increase of *x* from 0.2 to 0.3, i.e. the increase of both S quantity and Mo quantity in the samples (Figure 2D). This may suggest that the main Mo-containing phases are formed with a significant amount of reduced S. Contrarily to this evolution of the first peak, the intensity of two others peaks around 2478.5 eV and 2483.0 eV, corresponding to oxidized S species does not change much between samples (Figure 7D).

From our first observation, we can state that the local structures of all samples in this series are globally similar, only the quantity of Mo-containing phases changes between samples. We will discuss further on the local structure of Mo atom in the next part in considering the results from others analysis methods to understand the structures of materials.

In terms of surface activity, only some tests on 2 samples made with Mo(+I) (x = 0.05) and Mo(+VI) (x = 0.15) precursors in ORR reaction were done to compare to the surface activity of the sample $Gd_2O_2S/Mo_{0.36}$ (x = 0.18) which was made by the two-step protocol. For the same reason that mentioned in Chapter II, there is no detailed analysis (Tafel plots) for these samples in this part. The measurement conditions are identical: electrolyte KOH 0.1 M (pH 13), rotation rate 1600 rpm, scan rate 10 mV/s. The inks are of type Cx1 for Gd_2O_2S sample and Cx2 for the two others.

3.2. Surface activity in ORR in basic medium

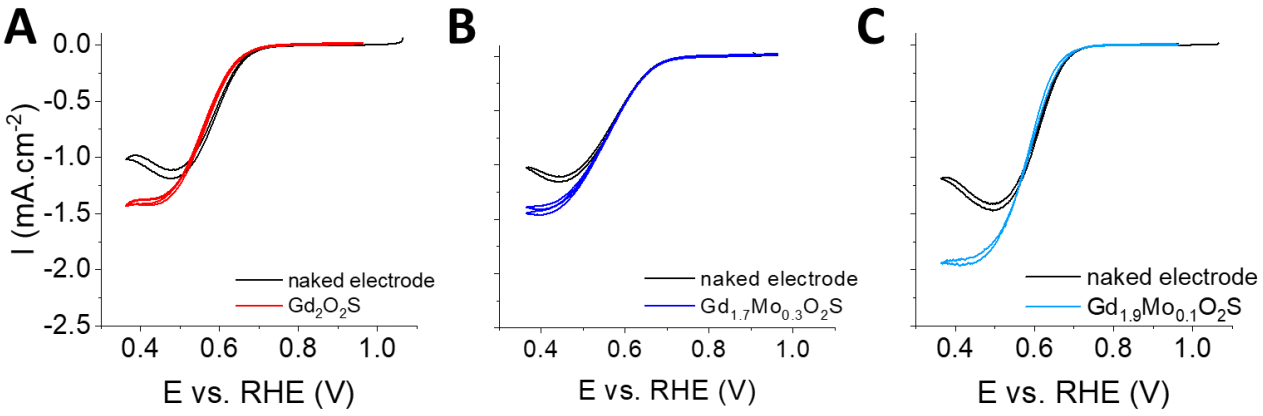

Figure 8 Electrochemical tests on: (A) Gd_2O_2S reference, (B) a sample $Gd_{1.7}Mo_{0.3}O_2S$ ($x = 0.15$) made with Mo(+VI) precursor and (C) a sample $Gd_{1.9}Mo_{0.1}O_2S$ ($x = 0.05$) made with Mo(+I) precursor.

The sample $Gd_{1.7}Mo_{0.3}O_2S$ ($x = 0.15$) has the same introduced ratio Mo/Gd as the $Gd_2O_2S/Mo_{0.36}$ sample but the real ratio Mo/Gd was found to be around 0.45 (Figure 2A) while it is only around 0.05 for the $Gd_2O_2S/Mo_{0.36}$ sample. The sample $Gd_{1.9}Mo_{0.1}O_2S$ ($x = 0.05$) was tested because it has the same observed ratio Mo/Gd as the $Gd_2O_2S/Mo_{0.36}$ sample despite the introduced ratio Mo/Gd was only 0.05 (see Chapter II). Figure 8 presents the results of the tests, compared to a Gd_2O_2S sample as reference. In all case, the cyclic voltammetry (CV) curves are perfectly superposed to the CV curves of naked electrode. The maximum currents in these case are slightly higher than the naked electrode due to the conductive C black in the ink. These null activities suggest that: firstly, the quantity of Mo in the sample does not have any relation with the activity, when the structure of Mo-containing phase(s) is not appropriate. Even if the Mo is more sulfide-like in the samples made by the one-step protocol than the others made by the two-step protocol, the Mo-S sites existence is not the necessary and sufficient condition for an ORR positive performance. Secondly, both products of syntheses with Mo(+I) and Mo(+VI) precursors in the one-step protocol are not active, it means that the active phase(s) is more likely to be formed during the second step of the two-step protocol.

4. Discussion

For practical reason, our project was focused on the use of Mo(+I) precursor for synthesis in two steps. The products from the synthesis in one step herein, for instance, were only prepared

for better understand those made by the two-step protocol. Hence, all the discussion in this part is also **principally on products made with Mo(+I) precursor**.

4.1. Elemental composition and crystalline structure

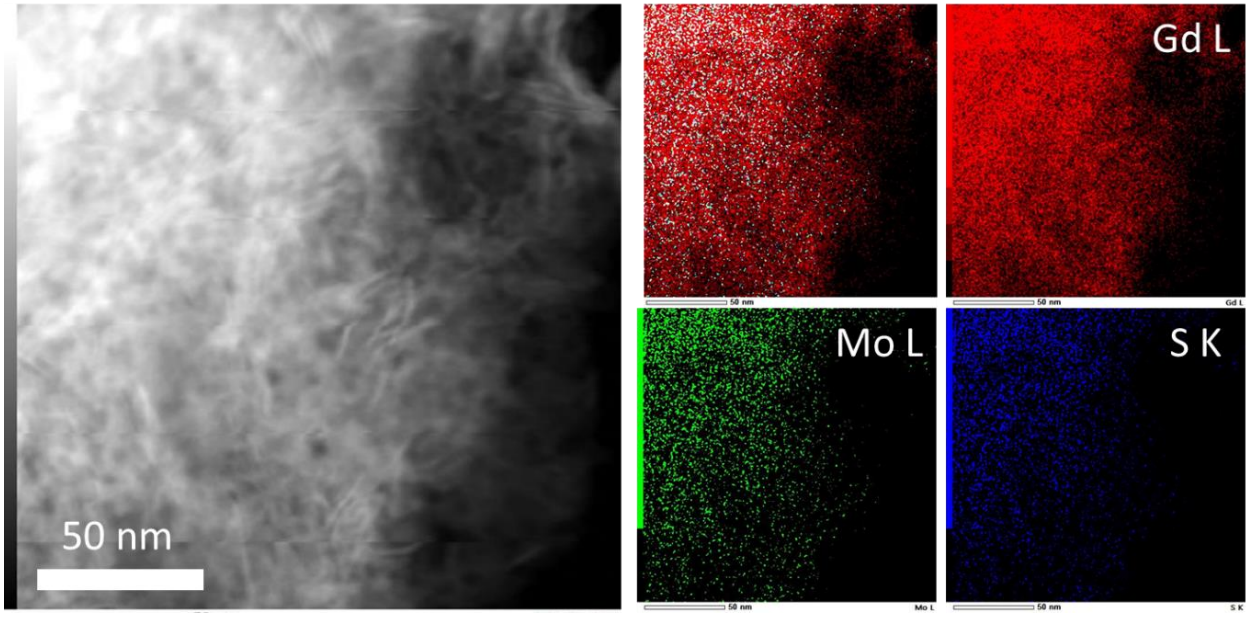

Figure 9 STEM-EDS cartography done one a $Gd_{1.7}Mo_{0.3}O_2S$ (x = 0.15) sample, made with Mo(+I) precursor. The measurements were performed by Mounib Bahri and Ovidiu Ersen (Institut de Physique et Chimie des Matériaux de Strasbourg, IPCMS). The scale bar is the same for all images.

Before going further into the detail on the structure of Mo-containing phases, the elemental distributions in final powders need to be investigated. Figure 9 shows images from an analysis by Scanning Transmission Electron Microscopy – Energy-dispersive X-ray spectroscopy (STEM-EDS) on a $Gd_{1.7}Mo_{0.3}O_2S$ (x = 0.15) sample. This analysis was performed by Mounib Bahri and Ovidiu Ersen (Institut de Physique et Chimie des Matériaux de Strasbourg, IPCMS). According to these results, all three relevant elements Gd, Mo and S are distributed homogenously in the sample at this scale. This suggests that at nanoscale, the material is *possibly* a homogenous mixture of different phases. The spectra of the sample at Mo K-edge can confirm this observation (discussion later with Figure 11C) as the multiple-scattering zone does not contain many oscillations following the white line, in contrast with the spectra of commercial crystalline products like MoS_2 or Na_2MoO_4. This spectrum form indicates amorphous and very dispersive phase(s) in the sample, which means that these phases do not form large, massive particles separately in the samples but rather to be well mixed together in

a homogenous manner. These results suggest that the Gd-containing phase and Mo-containing phase may either be homogeneously dispersed within one another or form a single phase.

Similar to the two-step protocol, there are three possibilities of product's nature made by this method:

- Formation of Mo-containing phase(s) disturbs completely Gd_2O_2S. Only other phase(s) are collected after the product isolation.
- Gd_2O_2S is formed normally, despite the addition of Mo precursor, and separated Mo-containing phase(s) is obtained.
- Gd_2O_2S is partially changed by an insertion of Mo in the structure:
    + $Mo^{\delta+}$ links to O terminated of double layers $[Gd_2O_2]^{2+}$ on the surface of nanoplates. Mo-O bonding is expected to observed by local structure analysis (EXAFS, PDF)
    + $Mo^{\delta+}$ links to S^{2-} terminated on the surface of nanoplates during the formation of Gd_2O_2S as it has a strong affinity to S. Mo-S bonding is expected to observed by local structure analysis (EXAFS, PDF)
    + $Mo^{\delta+}$ links to S^{2-} on the side of Gd_2O_2S nanoparticles.
    + $Mo^{\delta+}$ occupies some sites in the structure of Gd_2O_2S by insertion.
    + All of above

    In each case, a typical bonding, i.e. Mo-O, Mo-S or both of them, is expected to be observed by local structure analysis Extended X-ray Absorption Fine Structure (EXAFS).

In order to find out which possibility is the most likely, an analysis of high resolution diffractograms was done on the peak (110), the thinnest of the diffractogram, to see if there is any structural modification in the Gd_2O_2S structure. In general, a change in the crystalline structure, such as a defection, a substitution, an insertion etc. can be seen in a diffractogram via the position of peaks compared to a diffractogram reference. The reference can be the diffractogram of the bulk phase with well-defined thin peaks.

Considering the case of $Gd_{2(1-y)}Ce_{2y}O_2S$ where Ce substitutes a certain number of Gd sites in the structure of Gd_2O_2S, this substitution can be seen as a peak shift produced in the diffractogram.[2] The average size of nanoparticles is about 8 nm large and 1.5 to 2 nm thick, which broadens the Bragg peaks as predicted by the Scherrer's relation. The best peak of the diffractogram to study the shift value is then (110), which is the sharpest of all. The value of

this shift follows the Vegard's law, the shift should increase linearly with the increase of the inserted cation (here, Ce) in the structure of the initial compound (here, Gd_2O_2S).[2]

In the present case, as Mo is introduced in the synthesis of Gd_2O_2S before isolating the nanoparticles, we suppose that if Mo takes the place of some Gd sites or inserts in the Gd_2O_2S structure, this will cause the Bragg peak to shift. We apply the same analysis for these series of samples as in the case of $Gd_{2(1-y)}Ce_{2y}O_2S$. In order to analyze precisely the peak shift, firstly, the uncertainty of the method should be known. It is estimated directly on the system of Gd_2O_2S nanoparticles.

For this samples series, the peak (110) was also fitted to perform the best evaluation in the case of structural modification. The diffractograms were collected between 20 ° and 60 ° with the best conditions (cf. Experimental Section) to have the best fit possible. Then the fit was done with FULLPROF software. The error of all the process was estimated to be 0.003 Å (see Chapter II). Any shift superior than **0.005 Å** is considered as significant.

As mentioned previously in part 1, for samples with $x < 0.2$, it is clear that the characteristic peaks of Gd_2O_2S (peaks (100), (101), (110)) are still visible in all the diffractograms and no visible change in the position and the shape of peak (101) is seen (Figure 3). Figure 10 shows the fitting curves of the peak (110) of these samples (A), the quality of the fits (B) and the $d_{(110)}$ (Å) corresponding (C). Figure 10A shows that there is not much difference between the peak positions of one sample to the other and compared to Gd_2O_2S reference. The quality of the fits is good as there is no significant difference between the diffractogram (background subtracted) (Figure 10B, black) and the calculated curve (Figure 10B, blue). The peak positions are put on a graph in Figure 10C to better analyze the difference between them. The difference of $d_{(110)}$ between Mo-containing samples and Gd_2O_2S nanoparticles is ≤ 0.002 Å. Taking into account the error of 0.003 Å from the analysis method and the FULLPROF calculation, this difference becomes insignificant. Moreover, as mentioned above, the shift is significant only if it is higher than 0.005 Å. Here, we can state that there is no obvious shift for peak (110), for any Mo-containing sample compared to Gd_2O_2S reference. It signifies that there is no modification in the crystalline structure of Gd_2O_2S (by substitution and/or insertion of Mo cations). Hence, if there is any interaction between Mo atoms and Gd_2O_2S-like nanoplates in these samples, it should be only on the surface of the nanoplates which has to be low enough to not visibly change the crystalline structure.

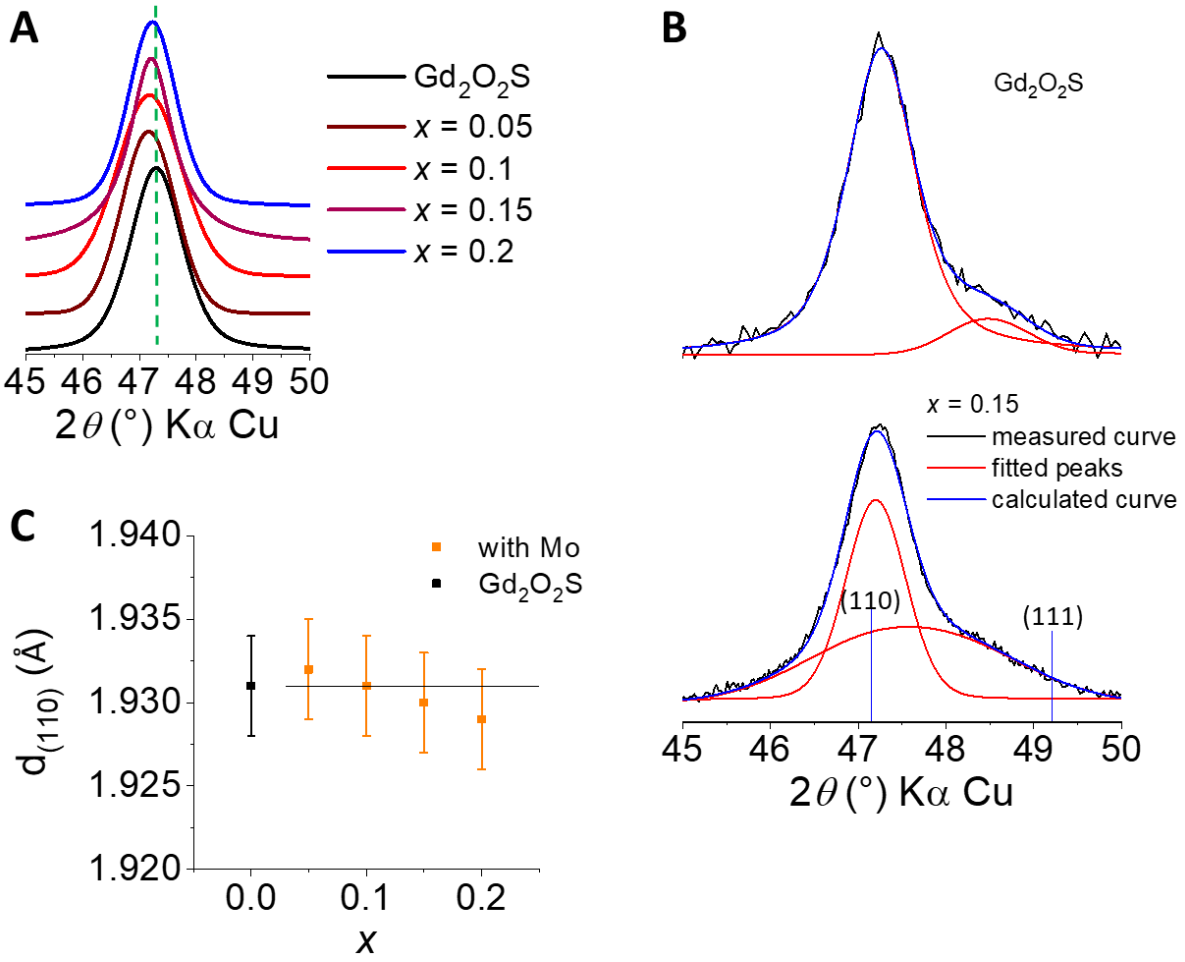

Figure 10 (A) Fitted curves of peak (110) from diffractograms of samples with x from 0 to 0.2. This peak is fitted separately to the rest of each pattern. (B) Peaks (110) and (111) after fitting, in comparison with the measured diffractogram and the calculated curve from the fits. Top: Fits for Gd_2O_2S nanoparticles. Down: fit for $Gd_{1.7}Mo_{0.3}O_2S$ (x = 0.15) sample, made with Mo(+I) precursor. The straight lines are from the reference Gd_2O_2S (JCPDS file 00-026-1422). (C) No peak shift between samples with Mo and Gd_2O_2S reference on the graph.

Another scenario is that at very low quantity of Mo ($x \leq 0.1$), there is substitution or insertion of Mo into Gd_2O_2S structure which cannot occur anymore with higher *x*. This may explain the tendency of the average value in Figure 10C (without counting the error bar) but it is not quite probable in practice since the radii difference between Gd^{+3} and Mo^{+3} shown in Chapter I is too much in all cases. The idea of interaction between Mo-containing phases and Gd_2O_2S nanoparticles occurs only on the surface (in case that there is any) which does not cause visible diffractogram changes is more legitimate. Or maybe these phases are simply independent.

From the arguments from the diffractograms analysis, we can state that: (1) the formation of Gd_2O_2S is not disturbed by the presence of Mo precursor in all tested cases and (2) the initial

crystalline structure of Gd_2O_2S is preserved after the synthesis with Mo precursor. However, the location of Mo in the final powders is not yet clear, whether Mo bonds to the surface of Gd_2O_2S nanoplates or completely in separated phases is still a question.

4.2. Local structure of Mo in $Gd_{1.7}Mo_{0.3}O_2S$

Compared to the case of samples made by the two-step protocol (see Chapter II), not only the tendency of Mo and S quantities in the final powders (EDS results) is different but so is the crystalline structure: no splitting of peak (101), no peak shift observed for (110). The morphologies of these two series are also found to be totally different: while the products made by the two-step protocol seem better defined with a typical interplanar distance of 8 Å, none of these was observed for the products made by the one-step protocol (Figure 5). These simple comparisons suggest that the reactions in two protocols are totally different which lead to globally different products series.

To understand what is likely to be the local environment of Mo in the products made by the one-step protocol, the PDF analysis and XAS (XANES and EXAFS) were done. The two methods PDF and EXAFS can be seen as complementary one to the other as the only difference is that EXAFS is selective for only one concerning element while PDF gives the information for all elements. The data treatment of XAS was done in collaboration with Alexy P. Freitas from our group and Asma Tougerti (Unité de Catalyse et Chimie du Solide, UCCS, Université de Lille I).

Figure 11 shows the spectra of a sample $Gd_{1.7}Mo_{0.3}O_2S$ (x = 0.15) at Mo $L_{3,2}$-edge and S K-edge, and a comparison at the same edges to a sample $Gd_2O_2S/Mo_{0.36}$ (x = 0.18) and selected commercial references. As we have seen earlier in this chapter, the peak corresponding to S^{2-} (as in MoS_2) of $Gd_{1.7}Mo_{0.3}O_2S$ is very small while other peaks corresponding to oxidized S are more intense. In the sample $Gd_2O_2S/Mo_{0.36}$ this peak is even mostly absent (Figure 11A). This may suggest an environment more similar to a sulfide for Mo in $Gd_{1.7}Mo_{0.3}O_2S$ than in $Gd_2O_2S/Mo_{0.36}$. At Mo L_2-edge, both samples have a splitting of spectrum into two components. The difference is that for $Gd_{1.7}Mo_{0.3}O_2S$, the first component is more intense than the second one while for the other sample, it is the opposite (Figure 11B). Concerning the edge position, it is located more to the left (lower energy) for $Gd_{1.7}Mo_{0.3}O_2S$ than for the other sample (which is identical to commercial Na_2MoO_4, at 2629 eV) and at the same position as commercial MoS_2 (both at 2627.4 eV). The same tendency is observed at Mo L_3-edge (Figure 11C): the edge positions of $Gd_{1.7}Mo_{0.3}O_2S$ and MoS_2 are identical at 2522.8 eV and to the left

of the edges of $Gd_2O_2S/Mo_{0.36}$ and Na_2MoO_4 (2524.5 eV and 2523.6 eV, respectively). However, at both Mo $L_{3,2}$-edges, commercial MoS_2 has only one component while $Gd_{1.7}Mo_{0.3}O_2S$ has two. It means that the oxidation state of Mo in $Gd_{1.7}Mo_{0.3}O_2S$ sample is likely +IV (as in MoS_2) but the local environment is not exactly the same (perhaps certain S atoms are substituted by O atoms as in oxysulfide) which causes the splitting of the spectrum. At this point, a comparison of the sample's spectrum and a simple linear combination of two reference compounds MoS_2 and Na_2MoO_4 can confirm the presence of both Mo(+IV) and Mo(+VI) as a mixture in the synthetic sample or this is another kind of Mo species. By doing this comparison, we may understand the difference between spectra at Mo K-edge (perfectly similar to amorphous MoS_2 by calculation, data not shown) and $L_{3,2}$-edges (contain two maxima instead of only one as MoS_2). Unfortunately, the quality of spectrum for the references (at least for Na_2MoO_4, Figure 11B-C) is not enough to do this linear combination (as Mo(+VI), Na_2MoO_4 should give a higher intensity than Mo(+IV) in MoS_2, here it is not the case). All the differences in local and crystalline structures between $Gd_{2(1-x)}Mo_{2x}O_2S$ samples and Gd_2O_2S/Mo_{2x} have to be the reason of the difference in surface activity in ORR which was explained in section 3.2.

The comparison of spectra at Mo K-edge confirms the oxidation state similarity between commercial MoS_2 and $Gd_{1.7}Mo_{0.3}O_2S$ (Figure 11D). These two solids have the same edge at 20 009 eV and situated more to the left (low energy) than Na_2MoO_4. Figure 11E shows the three spectra plotted by radial distance (in Å), corrected by +0.5 Å because of the phase shift of the photo-electron wave, caused when it passes through the potential of the absorbing and scattering atoms.[9] This graph gives the idea that maybe there are both components corresponding to Mo-O (as in Na_2MoO_4) and Mo-S (as in MoS_2) in the synthetic sample. For the reason that there is too much noise in the oscillation of the synthetic sample, we do not consider yet the FT of its spectrum. It means that the presence of the two components needs to be confirmed in the future work before considering fitting the EXAFS with proper oxysulfide reference(s). This would be an excellent achievement if we can prove that both components belong to the same phase, i.e. oxysulfide, in the future work as it means that we are the first who succeed making molybdenum oxysulfide in colloidal solution.

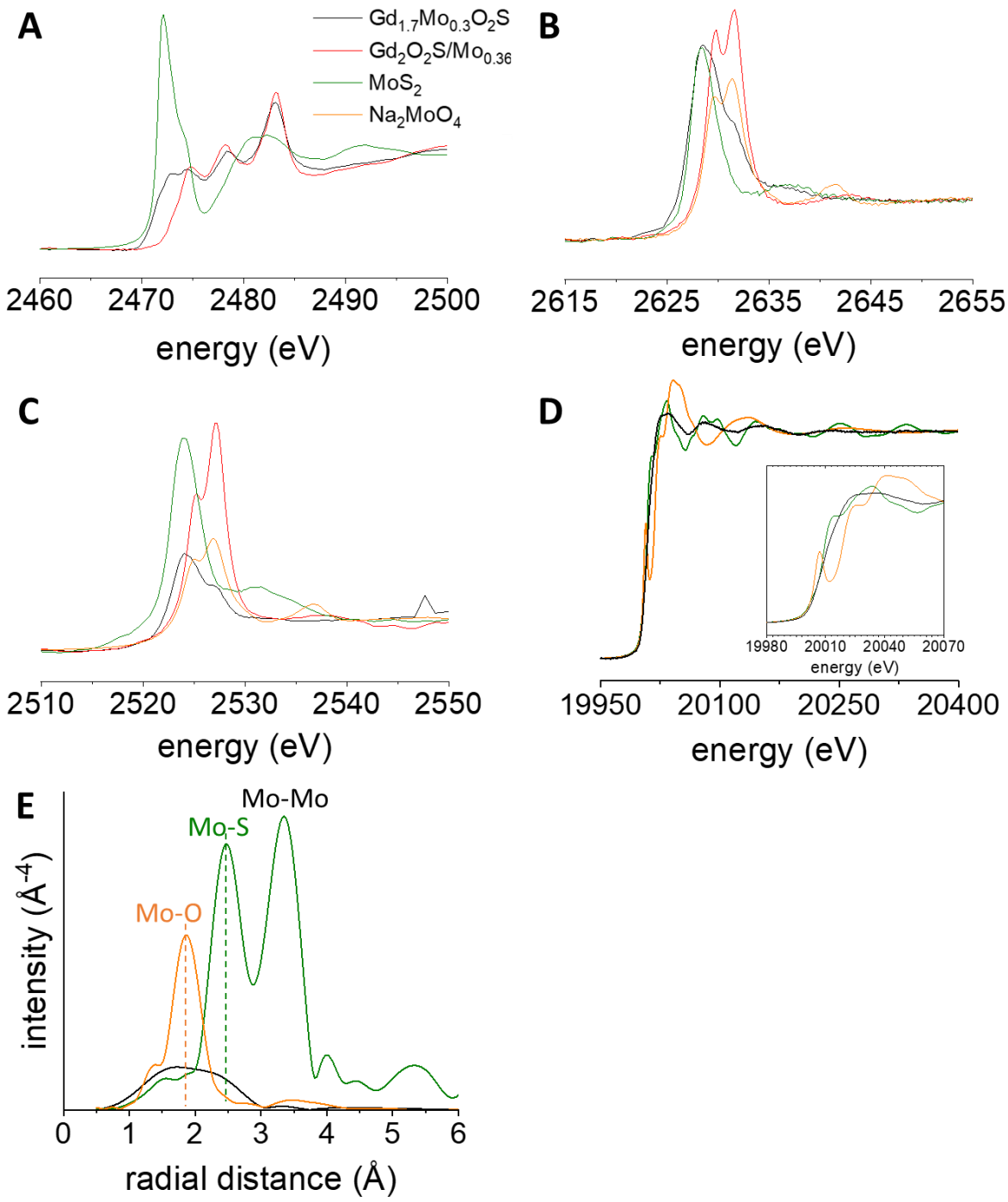

Figure 11 Comparison of XAS between samples $Gd_{1.7}Mo_{0.3}O_2S$ (x = 0.15), a sample $Gd_2O_2S/MoS_{0.36}$ (x = 0.18), both made with Mo(+I) precursor, and commercial references MoS_2 and Na_2MoO_4 at (A) S K-edge; (B) Mo L_2-edge; (C) Mo L_3-edge and (D) Mo K-edge with a zoom on XANES part. (E) Distribution of radial distance (Å), calculated from spectra at Mo K-edge in (D) and corrected by +0.5 Å to visualize the real bond lengths. Dash lines represent typical distances in molybdenum oxide (orange) and molybdenum sulfide (green). The legend in (A) is common for all figure.

5. Conclusion

In this chapter, we treated the study on the synthesis in one step, with the same concept as the synthesis of $Gd_{2(1-y)}Ce_{2y}O_2S$ nanoparticles, and the characterization of Mo-containing samples resulting from these syntheses. For instance, we understand that the products from these syntheses are totally different from others made by the two-step protocol in Chapter II. Hence, the reactions during the synthesis have to be also different. Unlike the materials in Chapter II, these products do not have any visible differences in crystalline structure and morphology compared to Gd_2O_2S nanoparticles. The analyses on local environment of Mo suggest that Mo is likely to have the oxidation state of +IV in all powders with low Mo quantity ($x \leq 0.2$), mainly close to a centrosymmetric geometry and can probably have bonds both with O and S.

For the samples with low Mo quantity ($x \leq 0.2$), the Mo-containing phases are not yet identified for the moment. The reason is firstly that they are probably (nearly) amorphous which cannot be seen by XRD. At high Mo quantity ($x \geq 0.5$), some crystalline phases were observed and briefly identified as some molybdenum-sulfide-like and Na_2MoO_4-like phases. The PDF measurements have been done on the samples with $x \leq 0.2$. The data treatment is in progress in order to better understand the Mo-containing phases and also to see if there is any relation between them and Gd_2O_2S nanoplates in the powders. Another idea is to anneal some of these materials to see which phases we could obtain at the end, which is either by the growth of the (nearly) amorphous phases or by the reaction of the amorphous precursor to form new phases. In any case, it provides the information on the Mo-containing phases at low Mo quantity.

In terms of the ORR catalytic activity, for the moment, two samples made with Mo(+I) and Mo(+VI) precursors with different quantity were tested. None of them showed a positive activity. Compared to the tests with the samples made by the two-step protocol, we learnt that a high quantity of Mo does not mean a higher activity. The catalytic activity relates directly to the structure of the Mo-containing phases, hence the reactions of their formation. Although for the quest of ORR catalytic activity, the samples made by the one-step protocol do not show any hope but pursuing the study on their structures (crystalline and local) and reactivity is still very helpful to understand the other series which is a better candidate as a new ORR catalyst that we have been searching for.

6. Bibliographies

(1) Ding, Y.; Gu, J.; Ke, J.; Zhang, Y. W.; Yan, C. H. Sodium Doping Controlled Synthesis of Monodisperse Lanthanide Oxysulfide Ultrathin Nanoplates Guided by Density Functional Calculations. *Angew. Chemie - Int. Ed.* **2011**, *50* (51), 12330–12334. https://doi.org/10.1002/anie.201105025.

(2) Larquet, C.; Nguyen, A.-M.; Ávila-Gutiérrez, M.; Tinat, L.; Lassalle-Kaiser, B.; Gallet, J.-J.; Bournel, F.; Gauzzi, A.; Sanchez, C.; Carenco, S. Synthesis of Ce 2 O 2 S and Gd 2(1– y) Ce 2 y O 2 S Nanoparticles and Reactivity from in Situ X-Ray Absorption Spectroscopy and X-Ray Photoelectron Spectroscopy. *Inorg. Chem.* **2017**, *56* (22), 14227–14236. https://doi.org/10.1021/acs.inorgchem.7b02336.

(3) Sebenik, R. F.; Burkin, A. R.; Dorfler, R. R.; Laferty, J. M.; Leichtfried, G.; Meyer-Grünow, H.; Mitchell, P. C. H.; Vukasovich, M. S.; Church, D. A.; Van Riper, G. G.; et al. Molybdenum and Molybdenum Compounds. In *Ullmann's Encyclopedia of Industrial Chemistry*; Wiley-VCH Verlag GmbH & Co. KGaA: Weinheim, Germany, 2000; pp 413–454. https://doi.org/10.1002/14356007.a16_655.

(4) Kumar, N.; Seminario, J. M. Computational Chemistry Analysis of Hydrodesulfurization Reactions Catalyzed by Molybdenum Disulfide Nanoparticles. *J. Phys. Chem. C* **2015**, *119* (52), 29157–29170. https://doi.org/10.1021/acs.jpcc.5b09712.

(5) Wang, T.; Gao, D.; Zhuo, J.; Zhu, Z.; Papakonstantinou, P.; Li, Y.; Li, M. Size-Dependent Enhancement of Electrocatalytic Oxygen-Reduction and Hydrogen-Evolution Performance of MoS2 Particles. *Chem. - A Eur. J.* **2013**, *19* (36), 11939–11948. https://doi.org/10.1002/chem.201301406.

(6) Larquet, C. Nanoparticles of Lanthanide and Transition Metal Oxysulfides: From Colloidal Synthesis to Structure, Surface, Optical and Magnetic Properties, 2018.

(7) Benck, J. D.; Hellstern, T. R.; Kibsgaard, J.; Chakthranont, P.; Jaramillo, T. F. Catalyzing the Hydrogen Evolution Reaction (HER) with Molybdenum Sulfide Nanomaterials. *ACS Catal.* **2014**, *4* (11), 3957–3971. https://doi.org/10.1021/cs500923c.

(8) Larquet, C.; Hourlier, D.; Nguyen, A.; Torres-Pardo, A.; Gauzzi, A.; Sanchez, C.; Carenco, S. Thermal Stability of Oleate-Stabilized Gd 2 O 2 S Nanoplates in Inert and Oxidizing Atmospheres. *ChemNanoMat* **2019**, *5* (4), 539–546. https://doi.org/10.1002/cnma.201800578.

(9) Scott, R. a. X-Ray Absorption Spectroscopy. *Compr. Coord. Chem. II* **2011**, 159–186. https://doi.org/10.1002/9781119951438.eibd0831.

Chapter IV

Explorative work on colloidal syntheses with molybdenum molecular precursors

Table of contents

1. Synthesis approaches

In Chapters II and III, I have discussed the work on Mo-containing Gd_2O_2S-based nanoparticles. As mentioned, this synthesis protocol is well described and well-known for lanthanide oxysulfide.[1,2] For d-block metals, as the electronic configuration is different (valence orbitals of (n - 1)d instead of (n - 2)f), the chemical properties are also very different. It is the reason why applying the same synthesis method for d-block metals can give unpredictable results. In this chapter, we attempted the synthesis of nanoparticles without lanthanide. The modified syntheses were applied with molybdenum as the sole metal precursor in purely explorative purpose. The temperature and heating duration were maintained as in the original synthesis of Gd_2O_2S nanoparticles.

$$[Mo^{+X}] + \frac{1}{16} S_8 + a\,[Na^+] \xrightarrow[310\ °C,\ 30\ min]{OM + OA + ODE} \text{“}MoO_{(2.5+0.5a)}S_{0.5}/Na_a\text{”} \qquad (1)$$

$$[Mo^{+X}] + \frac{1}{4} S_8 \xrightarrow[310\ °C,\ 30\ min]{ODE} \text{“}MoS_2\text{”} \qquad (2)$$

The reaction (1) gives the information about the ratio of reagents, solvents and reaction conditions. The notation of product is only symbolic, i.e. it signifies only the expecting ratio of concerning elements without any information about the exact structure: this is why we note them between quotes. The indexation of O is calculated with the assumption that the oxidation state of Mo in the final powders is +VI. This is a very *simple assumption* from the fact that we started this synthesis with Mo(+VI) precursor and the diffractograms of final powders displayed a crystallized content isostructural to sodium molybdate, in which Mo has also the oxidation state of +VI (it will be discussed more in detail in the next part of this chapter).

At first, the sodium cations were maintained in the protocol as we now understand that it plays a big role in the formation of Gd_2O_2S nanoparticles.[3] In the next part of the work, the sodium was taken out and the reagent ratio was modified to aim for a MoS_2-like phase. In this case, no sodium oleate and no acid oleic were added to simplify the system. Oleylamine could be also removed to simplify the system even more (reaction 2). In both synthesis methods (with or without Na), the first tests were done with the precursor $MoO_2(acac)_2$, we were expecting that the products could be oxysulfides as the Mo-O double bonds are already present in the precursor and the strong affinity of Mo towards S could lead to the formation of Mo-S bonds in the products. In the other syntheses using Mo(+I) and Mo(+III) precursors, which do not contain Mo-O (excluding the Mo-O_{ligand} bonds) as Mo(+VI) precursor, oxygen from air and/or

water in solvents during the washing process might be oxygen source for final products which probably contains both Mo and S after the reactions.

As this is an explorative work, there are many possibilities of parameter changes, only some of them were tested (Table 1). In the table, the yields are shown in the precursor columns. In order to estimate these values, the mass of organic ligands is not taken into account. The final products are named as "$MoO_{3.5}S_{0.5}/Na_2$" (MW = 214 g.mol^{-1}) and "$MoO_3S_{0.5}/Na$" (MW = 183 g.mol^{-1}). As mentioned above, both formulas are assumptions.

Table 1 Reagents and solvents/capping agents tested for "$MoO_{(2.5+0.5a)}S_{0.5}/Na_a$" with a = 1 or 2 and "$MoS_2$" with introduced S/Mo ratio = 2. The numbers in the precursor columns are estimated yields in percent, calculated by assuming formulas in the first column.

Assumed formulas	Reagents						Solvents/capping agents		
	Mo precursors			Na^+ sources			OM	OA	ODE
	Mo (+VI)	Mo (+I)	Mo (+III)	Na oleate	Na acac	Na citrate			
"$MoO_3S_{0.5}/Na_1$"	107			x			x	x	x
	102				x				
	127					x			
		67		x					
		58			x				
"$MoO_{3.5}S_{0.5}/Na_2$"	103 99 271 101 91 95			x					
	66				x				
	100					x			
		80			x				
"MoS_2"	107						(x)		x
		99 89 88							
			N/A (pasty)						

In this table, we see that the yields of all syntheses with Mo(+VI) and sodium oleate (original protocol) are from 90 % while the syntheses with Mo(+I) have the yield only between 60 and

80 %. For sure, this evaluation is not exact as the nature of the powders (composition, how many phases and which ones) are not yet clear but it is likely that little material was lost during the washing step, meaning that a significant amount of products is solid collected by centrifugation.

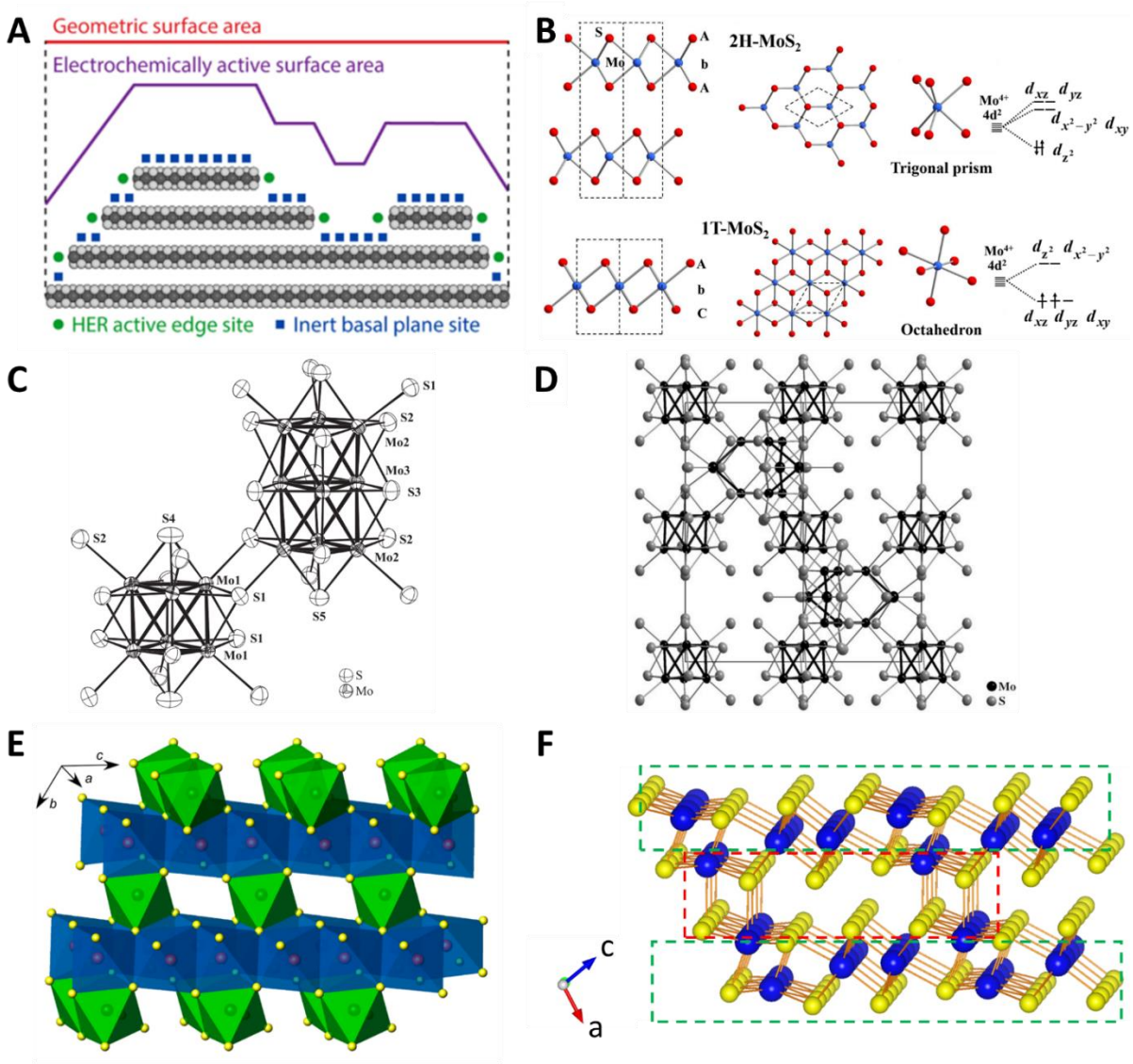

Figure 1 Some structures of molybdenum sulfides in the literature: (A) Figure of active site in MoS_2: Mo-S edge sites, figure by J. D. Benck et al.[4] *(B) Two different geometries of Mo centers in MoS_2 (centrosymmetric and none centrosymmetric), figure by Y. Fang et al.*[5] *(C) $Mo_6S_8S_6$ and $Mo_9S_{11}S_6$ units in $Mo_{15}S_{19}$ (Chevrel-like structure), figure by D. Salloum et al.*[6] *Thin lines denote the Mo-S bonds, thick lines denote the Mo-Mo bonds. (D) Mo_9S_{27} and $Mo_6S_8S_6$ units in $Mo_{15}S_{20}$ (Chevrel-like structure), figure by D. Salloum et al.*[7] *Thin lines denote the Mo-S bonds, thick lines denote the Mo-Mo bonds. (E) Polymorph Mo_3S_4 (Chevrel-like structure) depicted in a polyhedral model, figure by H. Fukuoka et al.*[8] *Yellow spheres show S atoms. Green*

polyhedra represent Mo1 octahedra, and blue ones represent Mo2 and Mo3 octahedra. (F) Monoclinic Mo_2S_3 with distorted zig-zag chains of Mo atoms (two kind of Mo atoms), figure constructed from .cif file on ICSD, Coll. Code 73453, referenced from the article of W. Schutte et al.[9] Blue spheres show Mo atoms. Yellow spheres show S atoms. In the green cadres are 1T-MoS_2 units, in the red cadre are vertical zig-zag chains. b axis points inwards.

For the reason that the molybdenum's chemistry is different from that of gadolinium, it would be surprising to obtain a similar structure to that of gadolinium oxysulfide. However, we were still expecting that the capping agents might stabilize the surface of particles and keep them at nanoscale in the medium of organic solvent. Also, the obtained solids could possess Mo-S edges which are considered as ORR active sites in the same manner as in MoS_2 (Figure 1A).[4] The Mo centers in MoS_2 can be centrosymmetric (octahedron, 1T-MoS_2) or not (trigonal prism, 2H-MoS_2) (Figure 1B).[5]

$Mo_{15}S_{19}$ and $Mo_{15}S_{20}$ are both of the Chevrel-like structure which contains Mo_6 cluster units (Figure 1C-E).[6–8] $Mo_{15}S_{19}$ is resulting from the oxidation by HCl gas of $In_{3.4}Mo_{15}S_{19}$ (a Chevrel phase which is made from H_2 reduced MoS_2, In and sulfur in a two-step solid-state synthesis with the temperature up to 1060 °C during several days) at 550 °C during 24 h to remove completely In.[10] According to D. Salloum *et al.*, in order to obtain $Mo_{15}S_{20}$, starting material $Mo_{15}S_{19}$ needs to be annealed at 700 °C during 45 days.[7] These Chevrel-like phases all contain Mo_6 and Mo_9 units. They form the cavities surrounded by only S which can accommodate other ternary metal ions by electrochemistry (or low temperature solid-state reactions).[10] Hence, they are interesting materials for electrode in Li, Na batteries.

Another interesting molybdenum sulfide is $Mo_2^{(+III)}S_3$ (monoclinic, $P2_1/m$) which has a linear-chain-structure with two inequivalent types of zig-zag Mo chains parallel along *b* axis.[9,11] This quasi-one-dimensional material can be made by vapor transport of Mo and S powders in double-sealed quartz tubes at 1300 °C (duration not mentioned),[12] or at 400 °C during 2 days then at 950 °C during 10 days,[13] or in molten NaCl at 1173 °C during 20h.[14] It is found that this material can undergo low-temperature phase transitions to exist in a metastable highly conducting state (along the direction of Mo chains).[11,15] It was also tested as cathode material for thin-layer rechargeable Li-ion power source[16] and claimed to be more active and more stable for HER in acidic medium than MoS_2.[14]

2. Synthesis protocol with Na^+

We recall here the reaction performed in this section:

$$[Mo^{+X}] + \frac{1}{16} S_8 + a\,[Na^+] \xrightarrow[310\ °C,\ 30\ min]{OM + OA + ODE} \text{“}MoO_{(2.5+0.5a)}S_{0.5}/Na_a\text{”} \qquad (1)$$

2.1. Choice of precursors of Mo and Na and structural characterization

2.1.1. Study on the synthesis with Mo(+VI) precursor

2.1.1.1. With Na^+ source of oleate

The syntheses following the same method as Gd_2O_2S were firstly done with the Mo(+VI) precursor with sodium oleate and $a = 1$. The product's diffractogram (Figure 2B-1, black) shows a phase isostructural to $Na_2MoO_4{\cdot}2H_2O$ (reference Figure 2A) with good yield compared to the assumed formulae "$MoO_3S_{0.5}/Na_1$" (Table 1). First of all, it is sure that there is a large difference between the obtained solid and $Na_2MoO_4{\cdot}2H_2O$ as the synthetic powder is totally black while the commercial $Na_2MoO_4{\cdot}2H_2O$ is made of white crystals. A closer look on the peaks did not reveal any shift, which could have been a signature of structural modification.

In the hypothesis that $Na_2MoO_4{\cdot}2H_2O$-like particles are indeed the major product of the reaction, the stoichiometry of Na (2 equiv. introduced instead of 1 equiv.) would allow a theoretical maximum yield of 100 % *vs.* Mo. Hence, we attempted reactions with $a = 2$ ("$MoO_{3.5}S_{0.5}/Na_2$"). The final products are all isostructural to Na_2MoO_4 (hydrated or dehydrated) according to their diffractograms (Figure 2B). In both cases, hydrated or dehydrated Na_2MoO_4, Mo(+VI) centers are tetrahedral but for Na_2MoO_4 hydrated, the crystal structure is cubic and for the other, it is orthorhombic as there are water molecules in the structure. No peak shift was observed in any case (Figure 2B-2 and Figure 2B-3 compared to the references (B-a) and (B-b), only intensity differences. The most visible difference is that for the curve (B-2), qualitatively, the intensity ratio between the first peak and the others is lower than in the reference hydrated molybdate (B-a). This may be due to the uneven growth of nanoparticles in the medium during the reaction/washing. It can be linked to the unusual morphology of the nanoparticles which will be discussed further in the next part.

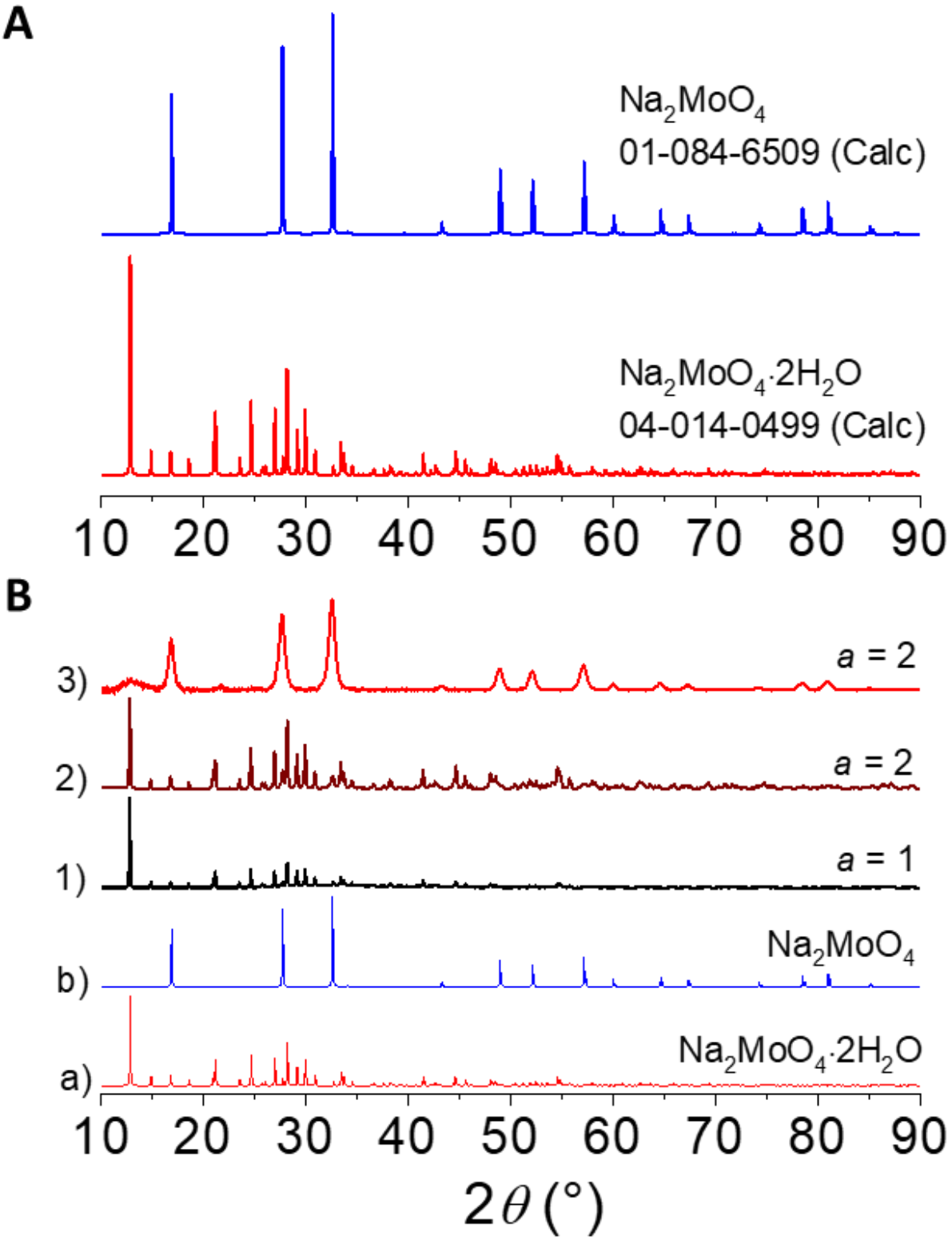

Figure 2 (A) Calculated diffractograms of two references sodium molybdate (hydrated and dehydrated) from ICDD with JCPDS file numbers indicated on the figure. (B) Diffractograms of samples made with Mo(+VI) precursors and sodium oleate with a = 1 and 2. (a, b) Calculated reference shown in (A). (2) and (3) are 2 kinds of diffractograms which can be obtained from the same synthesis protocol with a = 2.

In Figure 2B, it is clear that the major phase shown in (B-2) is isostructural to hydrated sodium molybdate and in (B-3) is to dehydrated sodium molybdate. However, the protocol for both syntheses is identical. One hypothesis is that the difference comes from the reactions between the raw medium and solvents/air during the washing steps. Figure 3 shows comparison between the calculated reference diffractograms and diffractograms corresponding to different moments of a sample (made with Mo(+VI) precursor, a = 1) in the glovebox or in free air. The pattern (1a) was obtained with a so-called "raw material" (only centrifuged twice at low speed in the glovebox, first time without any solvent, 2nd time with 10 mL of THF coming from a water-free bottle in the glovebox): it is not a powder but rather a paste (powder mixed with a significant amount of oily organic compounds). The diffraction was done for this paste in a closed sample holder to avoid as much as possible the contact with air. In this pattern and also in the pattern (1b) which corresponds to the same paste after two weeks staying in the glovebox, there are only very small peaks corresponding to three first peaks of Na_2MoO_4 reference (blue curve). This paste, after two more weeks staying in free air (tube lid open), gave a diffraction pattern (1c) much more similar to the product in Figure 2B-3. Firstly, it suggests that a product isostructural to Na_2MoO_4 or $Na_2MoO_4{\cdot}2H_2O$ may be formed only during the washings as the medium is in contact with air (oxygen) instead of directly during the heating. The appearance of the Bragg peaks corresponding to Na_2MoO_4 of a reaction medium left in contact with air during two weeks may confirm this observation (Figure 3-1). The fact the pattern (1a) (fresh reaction medium) already shows very small amount of the phase isostructural to Na_2MoO_4 may be due to the quality of the treatment (transport the medium into the glovebox, the sample holder was not well closed). This point needs to be confirmed in the future as this was only a one-time test. Secondly, the water in the final structure should be from the washing solvents because for the treatment in glovebox, the medium was totally sheltered from water during the first washings (when the compounds should be the most reactive). Any change of the medium is not visible after 2 weeks in the glovebox (Figure 3-1b). The same medium in contact with air during 2 weeks turns into a product isostructural to the dehydrated molybdate (Figure 3-1c). The supernatant from these washings, a suspension, was centrifuged at higher speed and rewashed outside of the glovebox and led to a product isostructural to the hydrated molybdate (Figure 3-2). The water source here should be from technical ethanol 96 % (washing solvents).

The crystalline domain size calculated via Scherrer's relation from the diffractograms in Figure 2B-3 is around 15 nm.

In order to control the structure of the products (based on their diffractograms), the most dried solvents were used in the syntheses after (n-hexane or cyclohexane and absolute ethanol). In both cases, treatments inside and outside of the glovebox, the raw diffractograms show that the backgrounds are high, which suggests that there are some (mostly) amorphous phase(s) in the samples. After the background extraction of the diffractograms, these phases are not visible anymore, only crystalized phases are observed (Figure 2, Figure 4). We keep in mind the existence of some amorphous phases in all samples for the discussion in the next part.

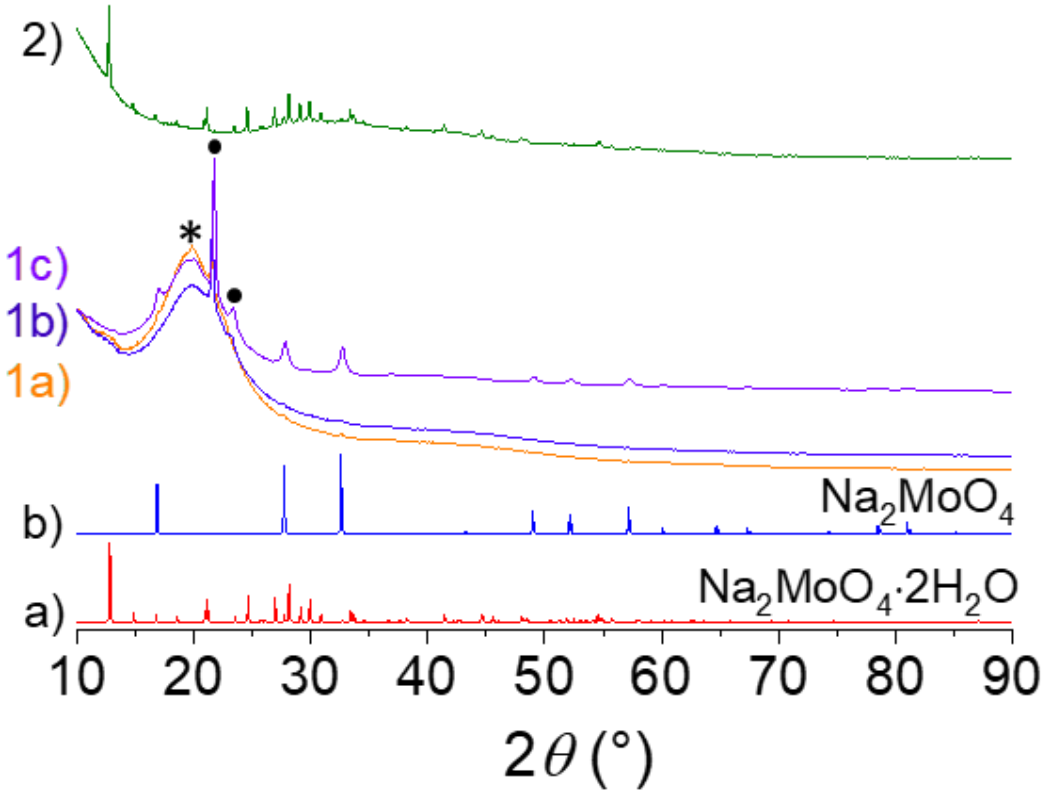

Figure 3 Comparison between (a, b) calculated diffractograms of two molybdate references from ICDD (Figure 2A) and raw diffractograms of a sample made with Mo(+VI) precursor, sodium oleate and a = 1: (1a) fresh paste after treatment in the glovebox, (1b) after 2 weeks in the glovebox, (1c) after 2 more weeks in free air; (2) fresh solid after the treatment of the first supernatant from (1a). The broad peak noted by a star is the signal of the sample holder's cap. The thin peaks noted by black dots may correspond to some structure of excess sulfur, not yet identified.

2.1.1.2. With other Na^+ sources: acac and citrate

Two other kinds of sodium sources were tested for comparison: sodium acac (Figure 4A-1) and monosodium citrate (Figure 4A-2). For each of them, a pair of samples were made with a = 1 and 2 to understand the influence of sodium amount and sources. In the case of a = 1,

with sodium acac, the diffractograms show a bump to the left of each peak (Figure 4A-1a, highlighted with red arrows) while with monosodium citrate, the products present a clear mixture of two phases: hydrated and dehydrated sodium molybdate-like (Figure 4A-2a). With a double quantity of sodium source (a = 2), the diffractogram appears to be cleaner than with a = 1 for sodium acac but still displays bumps at the bottom of peaks (Figure 4A-1b) and there still is a mixture of at least two phases for monosodium citrate (Figure 4A-2b). It is not sure yet if the mixture of phases is the consequence of the washings protocol or it is caused by the sodium source because the syntheses were not yet reproduced. However, for the syntheses with Mo(+VI) precursor, it is quite clear that the diffractograms of products made with sodium oleate and are now the best controlled.

2.1.2. Study on the synthesis with Mo(+I) precursor

Regarding the influence of the Mo precursor, some tests with Mo(+I) precursor were done to compare with samples made with Mo(+VI) precursor (Figure 4B). All samples shown in this figure were made with a = 1. Considering the same Na source as oleate, in the case of Mo(+I) precursor, compared to the powder obtained with Mo(+VI) precursor, there are additional peaks (marked with red dots) to the others corresponding to Na_2MoO_4 and $Na_2MoO_4{\cdot}2H_2O$ (Figure 4B-1 *vs.* Figure 4B-2a). The sample made with Mo(+I) precursor contains a mixture of phases isostructural to both Na_2MoO_4 and $Na_2MoO_4{\cdot}2H_2O$ (Figure 4B-2a) while there is only one visible phase for the sample made with Mo(+VI) precursor (Figure 4B-1). When it comes to the powder made with Mo(+I) precursor and sodium acac (Figure 4B-2b), the diffractogram becomes more complicated: the additional peaks (red dots) are different than ones in Figure 4B-2a and much more intense. The peaks corresponding to Na_2MoO_4 are still visible and intense but not largely major anymore. These phases, for instance, are not yet identified. All starred (i.e. reliable information) molybdenum sulfides and oxides phases in the database PLU2019 do not match. The only oxide sulfide phase Mo_3S_3O (JCPDS file 04-006-1208) does not match either.

In all cases, the major phases are isostructural to Na_2MoO_4 or $Na_2MoO_4{\cdot}2H_2O$ and the powders made with Mo(+VI) precursor do not exhibit a crystalline secondary phase. This gives the idea that the Mo(+VI) precursor may be the best choice to obtain a well-defined phase.

The open questions here are the structure of obtained powders, their composition and if there is any clue that they would contain an oxysulfide.

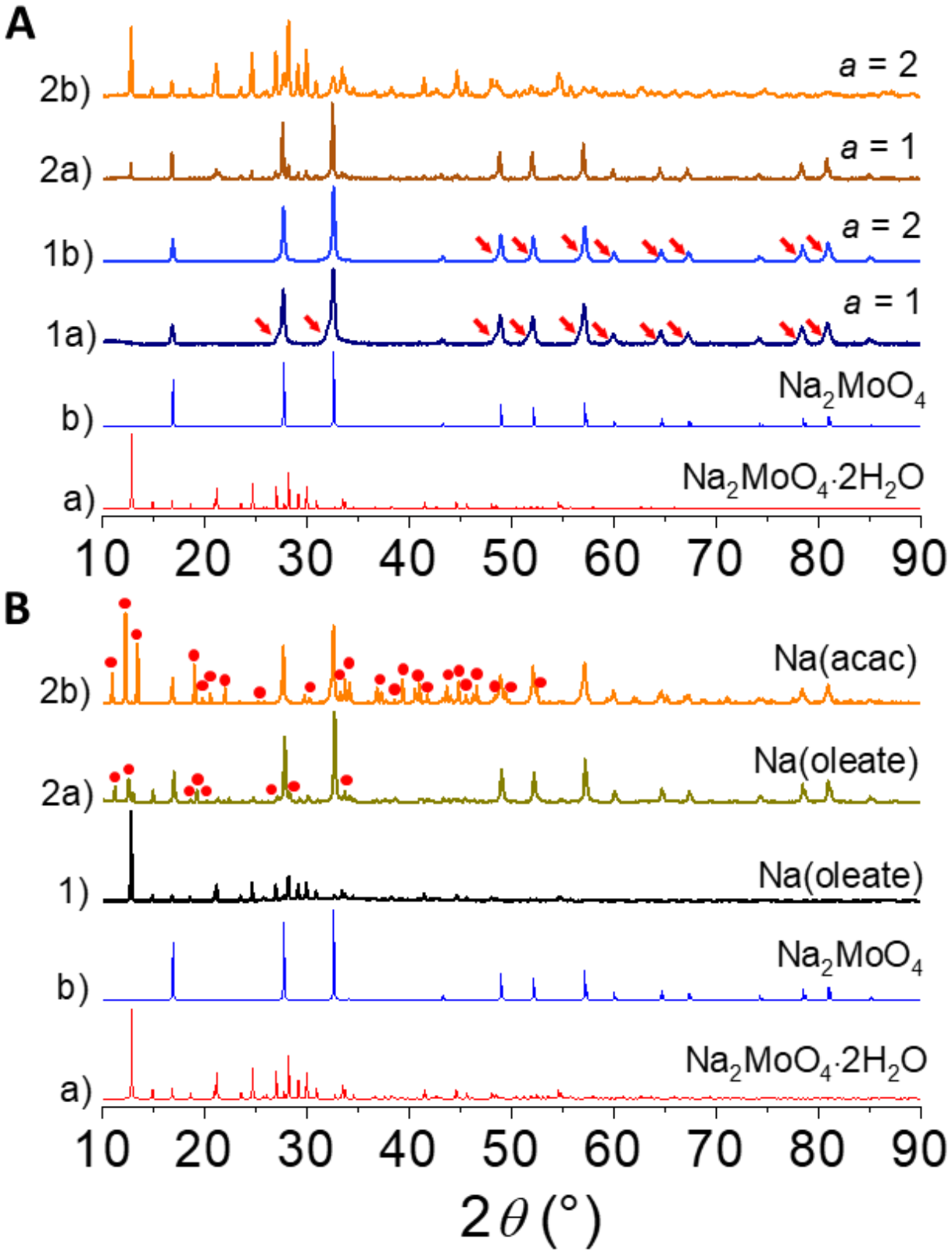

Figure 4 (A) Diffractograms of samples made with Mo(+VI) precursors and two other sodium sources: (1a, 1b) sodium acac and (2a, 2b) monosodium citrate. The values of a are indicated on the graph. The bumps are noted with red arrows. (a, b) Calculated reference shown in Figure 2A. (B) Diffractograms of samples with a = 1, made with (1) Mo(+VI) precursor and

(2a, 2b) Mo(+I) precursor. The sodium sources are indicated on the graph. The peaks noted with red dots do not belong to neither Na_2MoO_4 nor $Na_2MoO_4{\cdot}2H_2O$. (a, b) Calculated reference shown in Figure 2A.

2.2. Characterization of composition, morphology and local structure

Until now, the analysis by XRD shows that the most proper powders are made with Mo(+VI) precursor and sodium oleate. In this part, only these samples will be considered. They are classified into 3 groups by their XRD patterns and *a*:

(1) *a* = 1, patterns type "$Na_2MoO_4{\cdot}2H_2O$" (Figure 2B-1);

(2) *a* = 2, patterns type "$Na_2MoO_4{\cdot}2H_2O$" (Figure 2B-2);

(3) *a* = 2, patterns type "Na_2MoO_4" (Figure 2B-3).

From here, the samples will be named by their group number, i.e. type (1), type (2) and type (3), corresponding to the criteria above.

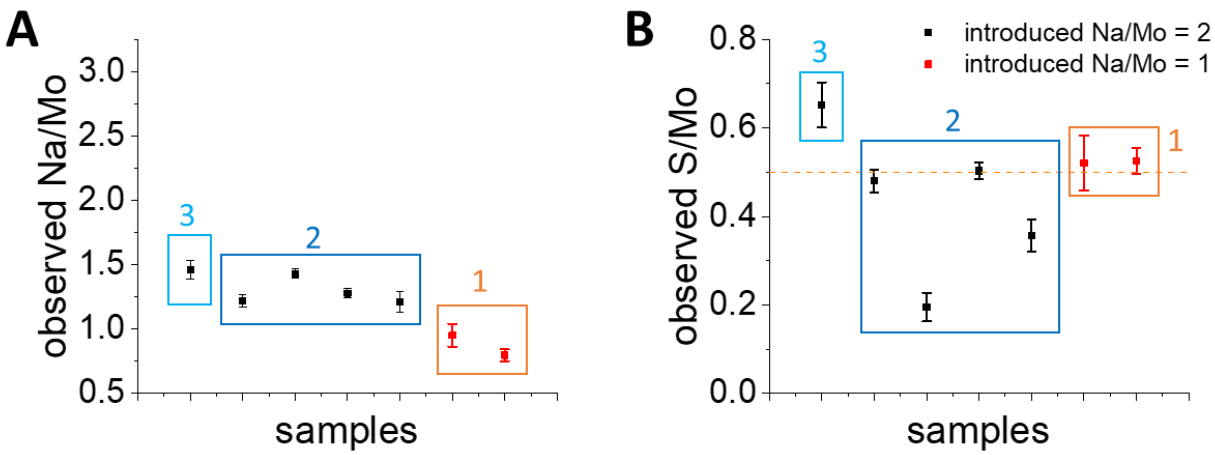

Figure 5 Composition analysis of all samples. (A) Observed molar ratio Na/Mo of each sample. (B) Observed molar ratio S/Mo of each sample. All samples were made with Mo(+VI) precursor and sodium oleate. In red: samples with a = 1, in black: samples with a = 2. Data is divided into 3 groups as mentioned at above.

The elemental analysis shows that the observed ratio Na/Mo in each powder is always lower than 2 (it varies around 1.3) for all sample groups, i.e. not high enough to form only one stoichiometric Na_2MoO_4 phase in the sample (Figure 5A). The quantity of sulfur is mostly around 0.5 which is the initial introduced ratio (Figure 5B, 5/7 samples in all groups). Taking the average observed ratio Na/Mo of 1.3 in the samples, if all this Na exist in a Na_2MoO_4-like stoichiometric phase without vacancies, the excess of Mo is about 0.3 equiv. The presence of

0.5 equiv. S in the powders, possibly trapped the 0.3 equiv. of Mo in an amorphous phase. Alternatively, this sulfur is in substitution of the oxygen. Both could be the cause of the color difference between the black samples and the white commercial Na_2MoO_4. Also, from the precedent section, we saw that the visible Na_2MoO_4-like phase in the diffractograms and some other (nearly) amorphous phase(s) may coexist in each sample. It means that they can be MoS_x phases (or even MoO_yS_x) in the samples.

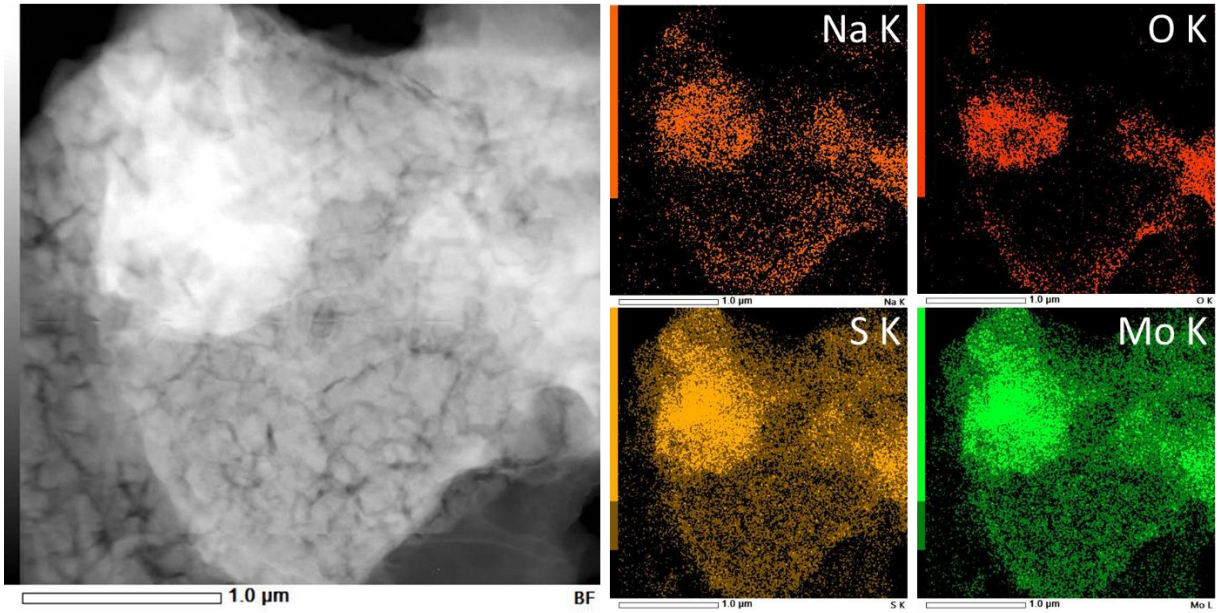

Figure 6 Images of STEM-EDS cartography done one a sample type (2) (a = 2, sodium oleate, XRD pattern type "$Na_2MoO_4 \cdot 2H_2O$"). Large image is in dark field (STEM-HAADF). The small images from left to right, top to bottom represent the cartography at Na K-edge (orange), O K-edge (red), S K-edge (yellow) and Mo L-edge (green). The measurements are realized by Mounib Bahri and Ovidiu Ersen (Institut de Physique et Chimie des Matériaux de Strasbourg, IPCMS). The scale bars are 1 µm.

The cartography by STEM-EDS was provided by Mounib Bahri and Ovidiu Ersen (Institut de Physique et Chimie des Matériaux de Strasbourg, IPCMS) on a sample type (2) (Figure 6). According to this analysis, at large scale, the distribution of all concerning elements (Mo, O, S, Na) seems to be homogeneous. The sample is probably a mixture of phases; we may say the mixture is also homogeneous. However, for the same problem mentioned in Chapter II on the inseparable peaks at S K-edge and Mo L-edge, this observation needs to be confirmed in the future.

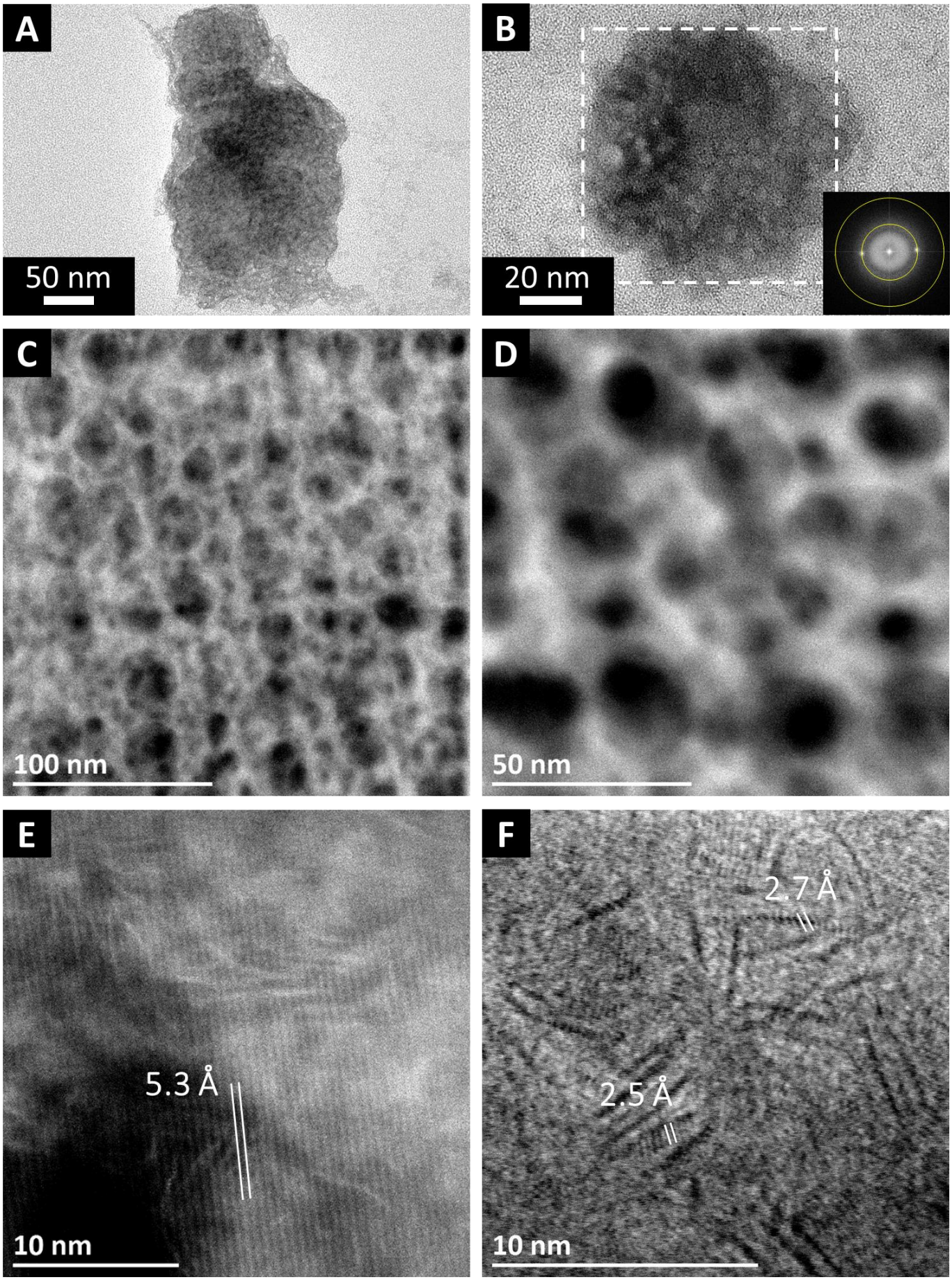
A
50 nm
B
20 nm
C
100 nm
D
50 nm
E
5.3 Å
10 nm
F
2.7 Å
2.5 Å
10 nm

Figure 7 (A) TEM image showing the global morphology of nanoparticles from a sample type (3). (B) TEM image of one single nanoparticle in a sample type (3) at higher zoom. A large crystalline domain of a with corresponding FFT, two visible distances at 5.1 Å and 2.6 Å. (C, D) The porous structure typically observed for a sample type (2). (E, F) Close-up images for the porous structure and other coexisting filaments of the same sample as in (C, D). Images from (C) to (F) were provided by Mounib Bahri and Ovidiu Ersen (Institut de Physique et Chimie des Matériaux de Strasbourg, IPCMS).

The morphology analysis by TEM and STEM shows that the nanoparticles tend to form big aggregates (Figure 7A) with very clear "holes" on/in them (Figure 7B). There is no analysis on the nanoparticles size yet for the reason of time but from the TEM observation, the nanoparticles are often in the sphere-like form with the diameter around 40 – 60 nm (observation on single nanoparticles). The calculated FFT in Figure 7B indicates that the concerning nanoparticle seems to have only one crystalline domain because there are only 1 direction of diffraction fringes in the TEM image and only 2 distances observed by FFT in the same direction. The diameter of this single nanoparticle is about 60 nm. This observation is not quite coherent with the corresponding diffractogram: Scherer's relation indicates that the average crystalline domain size is only around 15 nm large. There might be an epitaxy between the domains of the same nanoparticle which makes it looking like single-domained. Moreover, the "holes" in these images are difficult to understand as we observe also the diffraction fringes through them and their sizes are different to the size of pores observed by STEM in Figure 7C-D. Besides the unclear porous structure, the powders contain also some MoS_2-like filaments (Figure 7F), which can be found among the porous structure (Figure 7E). The image analysis by ImageJ shows an interplanar distance of 5.3 Å for the large crystalline domain (coherent with the distance of 5.1 Å from the FFT in Figure 7B) and 2.5 to 2.7 Å for the filaments. Taking the hypothesis that the porous structure is made of $Na_2MoO_4 \cdot 2H_2O$ or Na_2MoO_4-base, i.e. the structure is made of orthorhombic/cubic crystals with many defects ("holes"), and the filaments are made of MoS_2-base, 5.3 Å can be the distance along (111) axis of Na_2MoO_4 and 2.5 to 2.7 Å can be the distances along (101) and (100) of MoS_2, respectively.

The local structure analysis of the samples was done by XAS on SAMBA and LUCIA Beamlines. The data treatment and interpretation were done in collaboration with Alexy P. Freitas from our group and Asma Tougerti (Unité de Catalyse et Chimie du Solide, UCCS, Université de Lille). For all measurements, the pellets were prepared in air and stocked in a normal box (in contact with air the whole time).

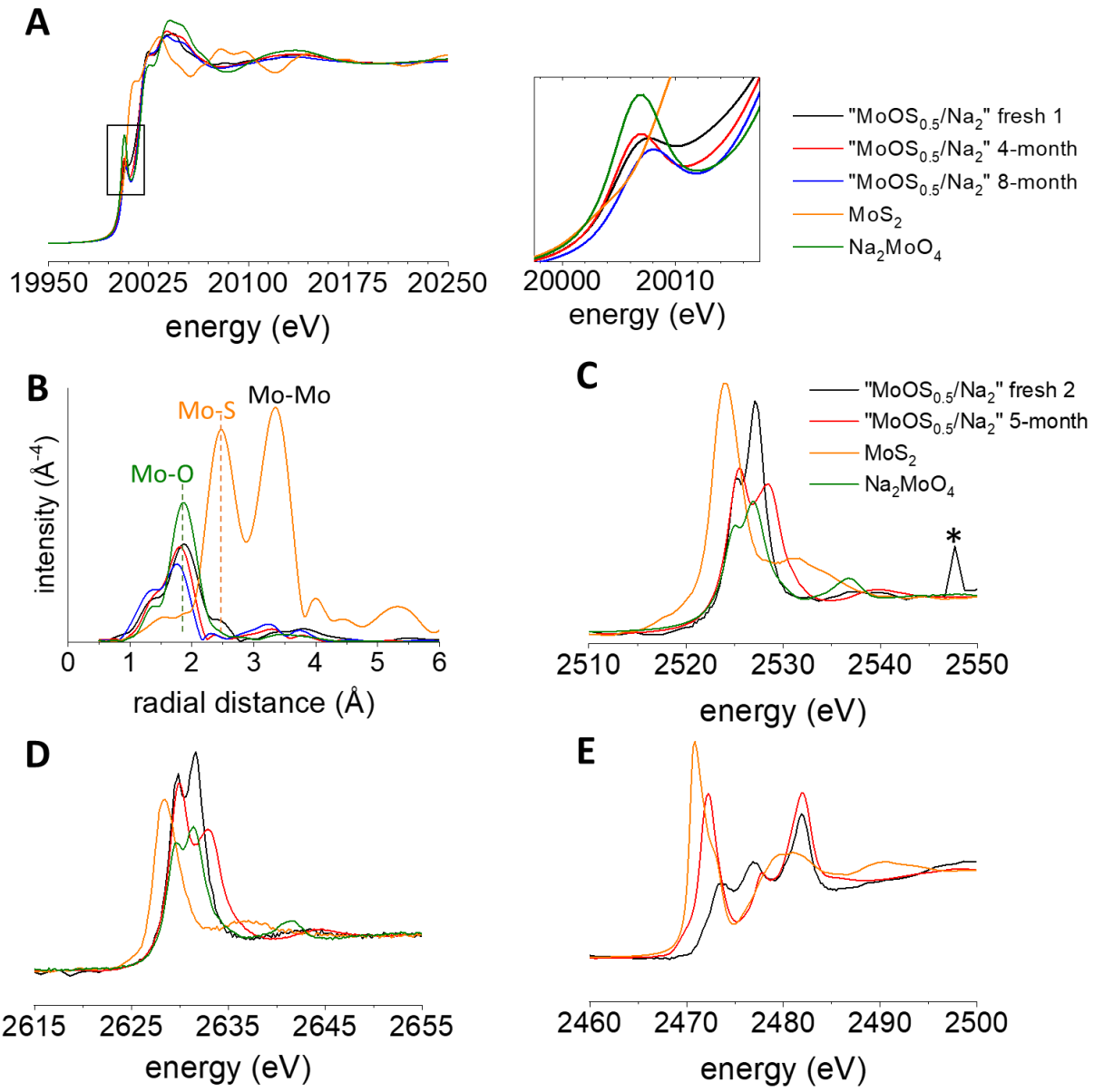

Figure 8 X-ray Absorption Spectroscopy (XAS) at different edges, the color code of the spectra is common for all graphs: black for fresh samples, red and blue for old sample, orange for MoS_2 and green for Na_2MoO_4. The sodium molybdate reference is dehydrated. (A) Spectra at Mo K-edge with an inset for pre-edges. The legend is common for (A) and (B). Sample "fresh 1" is ***type (3)****, sample "4-month" and "8-month" are identical,* ***type (2)****. (B) Distribution of radial distance (Å), calculated from spectra at Mo K-edge in (A), adjusted by +0.5 Å to visualize the real bond lengths. The intensities of three "$MoO_{(2.5+0.5a)}S_{0.5}/Na_2$" curves are multiplied by 10. Dash line in green indicates the oxide component zone, dashed line in orange indicates the sulfide component zone. The second intense peak of MoS_2 corresponds to Mo-Mo distance. (C) Spectra at Mo L_3-edge. The sample "fresh 2" is* ***type (3)****. The sample "5-month"*

is identical to the old sample in (A, B). The legend is common for (C-E). (D) spectra at Mo L_2-edge and (E) spectra at S K-edge. The peak marked with a black star is an instrumental glitch.

In Figure 8, the two samples named as "fresh 1" and "fresh 2" are of **type (3)** (only about one week between the synthesis and the analysis); while the sample considered as "old" (with the number of months between the synthesis and the analysis) is of **type (2)** and unique for all figure. The color code is common for all figures: black for fresh samples, red and blue for the old one, orange for MoS_2 and green for Na_2MoO_4. This difference does not change the geometry of Mo atoms very much as in both cases, Mo centers are tetrahedral, hence, similar XAS signature are expected. At the beginning of data treatment, our idea is that the difference is only that in the hydrated phase, Mo centers are slightly deformed from the perfect tetrahedral,[17] which may cause a less intense pre-edge than the dehydrated phase where Mo centers are perfectly tetrahedral. Based on this idea, we analyzed the results as below.

From the spectra at Mo K-edge and $L_{2,3}$-edges (Figure 8A, C-D), we observe that in each case, the edges of the fresh and old samples are situated *mostly* at the same position as commercial sodium molybdate (20 018.9 eV): +0.4 eV for the fresh sample, -0.8 eV for the 4-month old sample and -0.4 eV for the 8-month sample (a transition of valence corresponds to about 2 eV shift for the edge or 0.6 eV for the pre-edge at K-edge[18]). The edges are taken at the position of the 2nd maximum of the signal's first derivative (the first maximum corresponds to the pre-edge). This suggests that globally the Mo in all synthetic samples have the oxidation state of +VI as in Na_2MoO_4 with probably a modified local environment which cause the small differences of edge positions. A possible mixture of phases in these samples with slightly different oxidation states can also be the cause of the edge difference but this point is not yet clarified for the Mo K-edge. The pre-edges of synthetic samples are clear. Assuming that the oxidation state of Mo in the sample is only +VI, the intensity change of the pre-edge can signify a change from more deformed non-centrosymmetric to less deformed non-centrosymmetric geometries (we do not have enough proof at this point to conclude a perfect tetrahedral geometry). **Or**, it may signify an oxidation from a more reduced Mo to Mo(+VI) from the fresh sample to the 8-month old sample. A mixture of oxidation states in the fresh sample can also be the cause of the smaller pre-edge. The latter hypothesis seems to be more likely as the pre-edges of the fresh sample and the 4-month old sample are situated at the same position (20 004.6 eV) as the pre-edge of commercial Na_2MoO_4 while the pre-edge of the 8-month old sample is not, it is shifted by +0.8 eV (at 20 005.4 eV) which is significant as a transition of valence.[18]

The pseudo-radial distance distribution calculated from the spectra at Mo K-edge shows that each sample contains Mo centers linking mainly to O (Figure 8B). These shown curves are only resulted from the pre-treatment of spectra at Mo K-edge (normalization) in Figure 8A, no fitting is done yet for any sample, hence, the observation on the peak positions here is only qualitative for instance. In this figure, the intensities of the synthetic samples (black, red and blue) are multiplied by 10 to better visualize and compare to the references. Comparing the black and red curves, the peak corresponding to oxide zone is higher for the 4-month old sample (red) than for the fresh one (black). The difference in intensity between the references and the synthetic samples is probably due to the material concentrations in the pellets. The evolution of peak intensity from the fresh sample to the old sample may be due to the difference in crystalline structure: the distance Mo-O in dehydrated molybdate is longer than in hydrated molybdate (e.g. 1.74 Å for $Na_2MoO_4 \cdot 2H_2O$ and 1.78 Å for K_2MoO_4[17]). From the red curve to the blue curve (same sample), the intensity of Mo-O peak is not only lower for the blue one but its position is also located slightly to the shorter length. However, these observations need to be confirmed later by optimizing the EXAFS extraction because in changing some parameters, the peak positions may change slightly.

The spectra at Mo $L_{3,2}$-edges confirm the similarity of the edge's position between the synthetic samples and Na_2MoO_4 (Figure 8C, D). However, the ratio between the two peaks (2629.8 eV and 2631.6 eV, splitting energy 1.8 eV) of the black spectrum at Mo L_2-edge is much more similar to those of Na_2MoO_4 than the corresponding two peaks of the red one (2629.9 eV and 2633.0 eV, splitting energy 3.1 eV) (Figure 8D). As mentioned previously on the Mo K-edge, the fresh sample may have a mixture of Mo's oxidation states, this makes the analysis based on the splitting energy and the area ratio harder: instead of conclude directly from the splitting energy and/or peak ratio, we now have to fit the spectra with references of different Mo's oxidation states to understand it exactly.

At S K-edge, both samples fresh and old contain sulfur more oxidized (peaks at 2476.9 eV, 2477.7 eV and 2482.0 eV) than S^{2-} in MoS_2 (edge at 2469.8 eV) (Figure 8E). Both samples contain oxidized sulfur as sulfate (peak at 2482.0 eV). The sulfur in the fresh sample appears to be more oxidized than in the old sample. It is difficult to conclude on this point as not every phase in the mixture is identified.

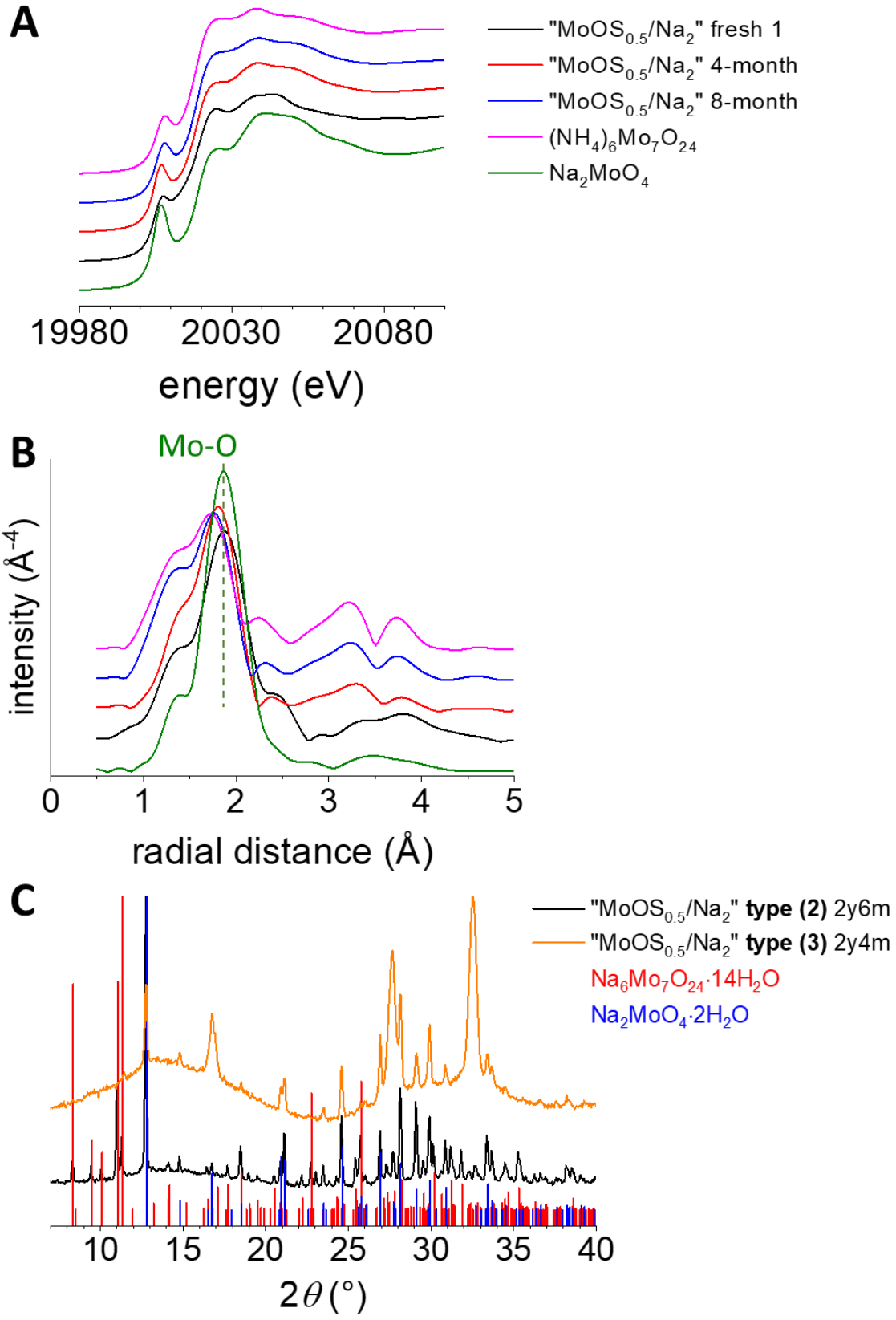

Figure 9 (A) Spectra at Mo K-edge with an vertical offset. The legend is common for (A) and (B). Sample "fresh 1" is ***type (3)****, sample "4-month" and "8-month" are identical,* ***type (2)****. (B) Distribution of radial distance (Å), calculated from spectra at Mo K-edge in (A), adjusted*

by +0.5 Å to visualize the real bond lengths. The intensities of three "$MoO_{(2.5+0.5a)}S_{0.5}/Na_2$" curves and of $Na_6Mo_7O_{24}{\cdot}14H_2O$ are multiplied by 10. Dash line in green indicates the oxide component zone. (C) Comparison of diffractograms between an aged sample ***type (2)*** *(identical to the aged sample in (A) and (B)), an aged sample* ***type (3)****, $Na_2MoO_4{\cdot}2H_2O$ and $Na_6Mo_7O_{24}{\cdot}14H_2O$.*

In collaboration with Asma Tougerti, an expert on XAS, we found out a similarity between the aged synthetic samples' spectra at Mo K-edge and heptamolybdate ($Mo_7O_{24}^{6-}$). Figure 9A shows the similarity of spectra at Mo K-edge between aged samples **type (2)** and $(NH_4)_6Mo_7O_{24}$ (red, blue and magenta curves). A fresh sample **type (3)** (black) seems to be a transition between the two spectra of molybdate (green) and heptamolybdate (magenta). The pseudo-radial distance distribution calculated from the spectra at Mo K-edge (Figure 9B) between 2 and 4 Å shows also the same trend as the spectra above. The presence of heptamolybdate phase was verified by realizing XRD on the same sample **type (2)** concerning after a very long time (2 years and 6 months). Without changing any physical aspects, the sample gave a diffractogram which signifies a mixture of at least two phases isostructural to heptamolybdate and molybdate (Figure 9C, black curve). Meanwhile, after mostly the same time, the fresh sample **type (3)** concerning seems to change from **type (3)** to a mixture of **types (2) and (3)** with a presence of amorphous phase(s) (Figure 9C, orange curve). No Bragg peaks corresponding to sodium heptamolybdate were observed for this sample as in the previous one.

Combining the observations on XAS and XRD, we hypothesize that the local environment of Mo atoms in synthetic samples slowly changes from isostructural to molybdate to isostructural to heptamolybdate. The presence of water molecules in the crystalline structure may accelerate this process: the sample **type (3)** may need to be transformed to **type (2)** before becoming heptamolybdate. The fact that no heptamolybdate crystals were seen by XRD while seen by XAS is probably because heptamolybdate can be formed easily in solid state and can even be amorphous. This is coherent with the first results we obtained. Further analysis will be done in the future to understand more this ageing process. This may also give the idea on the activity of molybdate tetrahedrons in samples made by the two-step protocol.

2.3. Discussion on the products' structure

The work on this synthesis was started with Mo(+VI) precursor. Meanwhile, some tests with Mo(+I) precursor were done and showed a mixture of phases (Figure 4B-2). Hence, the next work was continued only with Mo(+VI) precursor as the products in this case are already

difficult to understand. Even if only one crystalline phase was observed by XRD, in XANES it seems to be a mixture of oxidation states. As the consequence, the discussion in this part is only about the products made with Mo(+VI) precursor.

Assuming that it is an ideal case where the product is a single phase isostructural to Na_2MoO_4, there are two questions to answer: can it be an oxysulfide by substitution of certain O by S? and what makes the pores in the nanoparticles?

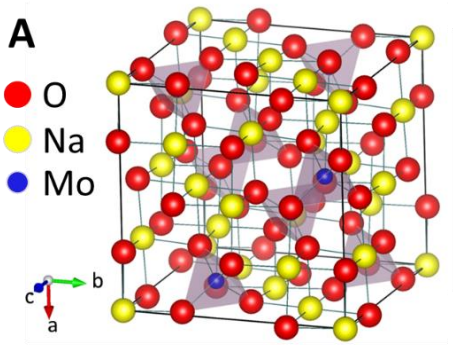

C

Ions	Coordination	Crystal radius (Å)
Mo(+VI)	4	0.8
Na(+I)	6	1.2
O(-II)	**4**	**1.2**
S(-II)	**6**	**1.7**
S(+VI)	**4**	**0.3**

Figure 10 (A) Unit cell of the cubic Na_2MoO_4. Structure drawn from JCPDS file 04-01-8839. (B) Structure around the O atom, angles and bond lengths measured on the model (A). (C) Crystal radii of all involved atoms with their coordinations in the structure, S(-II) and S(+VI) with their possible coordinations.[19]

For the first question on the substitution O by S in the structure of Na_2MoO_4, a theoretical approach is considered. Figure 10 shows the model structure of spinel Na_2MoO_4 from ICDD database (JCPDS file 04-010-8839) and the information on the coordinations and crystal radii of Na, Mo, O and S according to Shannon.[19] In this structure, O^{2-} has a coordination of 4 and a crystal radius of 1.2 Å. Considering the same coordination 4, only S(+VI) can present it but its crystal radius is way too small (1/4 the size of initial O(-II), Figure 10C) and it is charged positive. Such substitution is not possible. Considering the same oxidation state (-II), the anion S^{2-} is 1.5 times larger than O^{2-} in a crystal and the only possible coordination is 6. This very important difference in size makes the substitution of O by S in the structure of Na_2MoO_4 impossible. Assuming that it still happens, only some O on the surface are substituted because the number of Mo-S bonds needs to be low enough to maintain the position of all Bragg peaks. There might be some O of molybdate ions on the surface are replaced by O_{ligand} and/or some defections of these O that create the pores observed on TEM images in Figure 7. This assumption would be a good explanation if there is no lack of sodium (Na/Mo found from around 1.2 to 1.5 instead of 2.0, Figure 5A) and at the same time, there is not that much sulfur in the powder (S/Mo $\geq$ 0.2 and most samples present a ratio $\geq$ 0.4, Figure 5B). Again, a

substitution O by S appears to be impossible. Another simpler hypothesis is that the sample is truly a mixture of phases, corresponding to the mixture of Mo's oxidation states. In this case, in plus of veritable Na_2MoO_4 there are other amorphous phase(s) which are in the form of very thin filaments as seen by TEM and STEM. The pores on the polycrystalline nanoparticles may be issued from the quick crystal growth during the washing, which leaves some holes in/on the nanoparticles.

In fact, the hypothesis of a mixture of phases is supported by all results already shown in the previous section (results of XRD, EDS, TEM, STEM and preliminary results of XAS). This mixture includes a Na_2MoO_4-like phase and other (nearly) amorphous phase(s), which contains at least Mo and S. In the STEM images, the large porous structure seems to be formed by Na_2MoO_4-like phase with very small and thin filaments/sheets evenly distributed in/on it (Figure 6, Figure 7). This can explain the diffractograms where only the large structures are visible, the thin filaments are nearly amorphous and hidden under the Bragg peaks of Na_2MoO_4 (Figure 3). The first analysis on the images suggests that the filaments are very thin, similar to MoS_2 sheets. Also, the presence of two phases explains the oxide and sulfide components in the distribution of pseudo-radial distances (Figure 8B) of the samples.

Most of the questions on these series are not yet answered as we are only at the beginning of the study. No electrochemical test was done on these products yet. So, we do not know the activity of the material. If this is molybdenum sulfide supported on a very porous and stable structure, it may be active for ORR and/or HER. Moreover, the presence of Na_2MoO_4-like phase with some nanoparticles with the same kind of morphology in the sample with $x = 2.03$ made by the two-step protocol suggests that maybe the reaction we are considering in this part is the same which led to the active isolated molybdate tetrahedrons in Chapter II.

Then, it would be worthy a further study to understand more on both the structure and the activity of these beautiful nanoparticles.

3. Synthesis protocol without Na^+

3.1. Synthesis protocol and the choice of Mo precursor

We recall here the reaction performed in this section:

$$[Mo^{+X}] + \frac{1}{4} S_8 \xrightarrow[310\ °C,\ 30\ min]{ODE + OM} \text{“}MoS_2\text{”} \qquad (2)$$

The second explorative synthesis pathway is without any sodium cation. It was performed in order to avoid the formation of Na_2MoO_4-related phases. Only a Mo precursor and S_8 are mixed together in the mixture of ODE and OM for the reaction. Only five tests were done with the use of three Mo precursors in this part (Table 1). Figure 11 shows the results of all XRD and EDS analyses. First of all, the diffractograms show a similarity between products coming from Mo(+VI) (Figure 11B-c, blue) and Mo(+III) precursors (Figure 11B-d, green), and between products coming from Mo(+I) precursor (Figure 11B-e, magenta) and a sample $Gd_{0.6}Mo_{1.4}O_2S$ (x = 0.7) made by the one-step protocol with Mo(+I) precursor (Figure 11B-b, red). All three diffractograms of samples made with Mo(+I) precursor has the same peaks and their positions, there are only some differences in the intensity.

Both samples made with Mo(+VI) (blue) and Mo(+III) (green) precursors are mostly amorphous but the one made with Mo(+VI) precursor (blue) seems to be less crystalline: it does not have neither other bumps at 18 °, 62 ° and 80 ° nor the thin peaks around 20 ° (the dotted peaks for the sample made with Mo(+III) precursor might be attributed to excess S in the final powder). For the other pair of products (samples “MoS_2” and $Gd_{0.6}Mo_{1.4}O_2S$ both with Mo(+I) precursor), the similarity stays for the second crystalline phases with peaks lower than 15 ° (11 °, 12.5 ° and 14.8 °). The first crystalline phase observed in the $Gd_{0.6}Mo_{1.4}O_2S$ sample and marked with black stars corresponds to a phase isostructural to Na_2MoO_4, similar to the synthesis in section 2 of this chapter. The similarity is possible because in both syntheses ($Gd_{0.6}Mo_{1.4}O_2S$ and “$MoO_{3.5}S_{0.5}/Na_2$”), Mo(+VI) precursor is in contact with S_8 and Na oleate in the same conditions of reaction. However, all the other phases in Figure 11A, crystalline or amorphous, are not yet identified in an exact manner: no simple oxides or oxysulfide available in ICDD database match with the thin peaks. In terms of sulfides, there is only one phase that can match partially with the diffractograms: $Mo_{15}S_{20}$ (JCPDS file 04-018-5769).[7] The similarity between this reference and the synthetic samples $Gd_{0.6}Mo_{1.4}O_2S$ and “MoS_2” both with Mo(+I) precursor is shown by blue dash lines in Figure 11. This $Mo_{15}S_{20}$ phase appears to be a possibility for the dotted unidentified phase in Figure 4B-2 (samples also made with Mo(+I) precursor). Only the peaks lower than 35 ° can be distributed and an intense peak of the reference at around 47 ° is missing but for now, this is the best matching and it does not seem impossible.

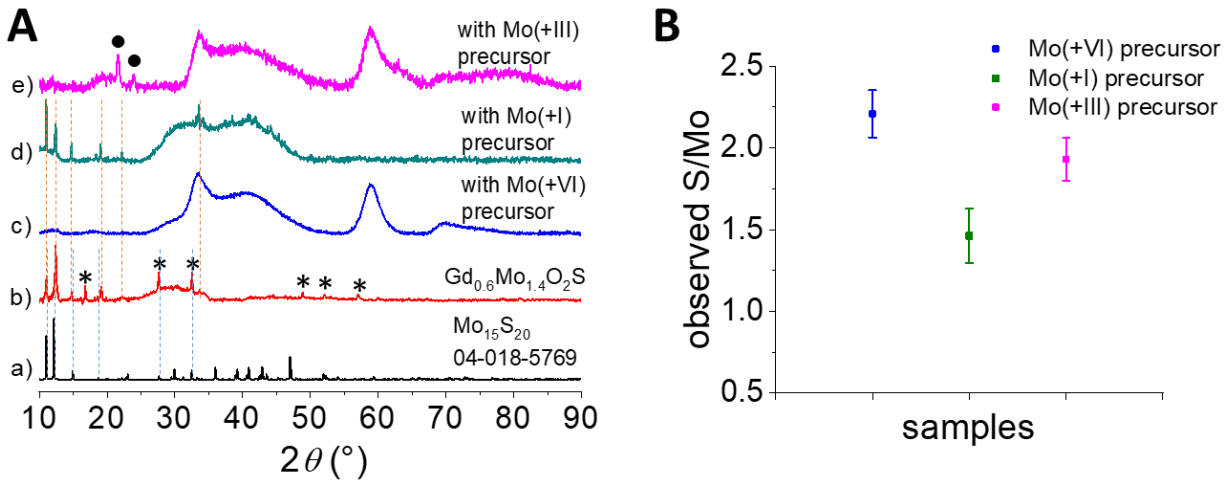

Figure 11 (A) Diffractograms of samples without Gd made with three Mo precursors, in comparison to a $Gd_{0.6}Mo_{1.4}O_2S$ (x = 0.7) sample and a molybdenum sulfide $Mo_{15}S_{20}$ with it JCPDS file number.[7] The peaks marked with black stars belong to Na_2MoO_4 phase. Orange dash lines signify the similarity between (b) and (d). Blue dash lines signify the similarity between (b) and (a). (B) Observed molar ratio S/Mo in all samples without Gd. In red: with Mo(+VI) precursor, in green: sample made with Mo(+I) precursor, average value from 3 syntheses, and in magenta: with Mo(+III) precursor. Dotted peaks: probably excess S.

In order to better understand these results, it is useful to have a closer look at the literature about molybdenum sulfides. In terms of the formation temperature of molybdenum sulfides, as mentioned at the beginning of this Chapter, by solid-state synthesis, the required temperature is very high (higher than 1000 °C). Taking a simpler molybdenum sulfide MoS_2, by solid-state synthesis, the first step is the formation of MoS_3 by thermal decomposition of $(NH_4)_2MoS_4$ at 250 °C, then it is treated by H_2/H_2S ranging from 350 to 900 °C, depending on the crystal size wanted.[20,21] The synthesis in solution can reduce the required temperature highly compared to solid-state synthesis. A colloidal synthesis in water does not seem to help reducing the required temperature very much, even if the nanoparticles size is very small: K. Chang *et al.* made ultra-small freestanding amorphous molybdenum sulfide colloidal nanodots from a solution of $(NH_4)_2MoS_4$ in water in presence of $LiCO_3$ at 800 °C during 8 h.[22] Besides, by changing the solvent to methanol and an atmosphere of 42 psi of H_2/CO, B. Moreno *et al.* synthesized a colloidal dispersion of molybdenum sulfide at only 100 °C during 1h, resulting the nanoparticles of molybdenum sulfide of medium size about 5 nm.[23] A synthesis from molecular precursors as Mo and S sources can occur at low temperature too: C. Meerback *et al.* heated a mixture of $MoCl_5$ and CS_2 or $(NH_4)_2S$ in formamide under Ar atmosphere at only 170 °C

during 1h to form MoS_2 nanosheets mostly amorphous. To make oleylamine-capped MoS_2 nanosheets, the reaction mixture was composed with oleylamine and oleic acid (and another long-chained organic agent), similar to our method, and heated at 320 °C during about 1 h 15 min.[24]

Going back to our case, we heated at 310 °C, a bit lower than the mentioned colloidal synthesis of C. Meerback *et al.*, it would be quite surprising to obtain some clearly crystalline sulfides as in Figure 11A. Although, it is not impossible as the precursor we used is Mo(+I) which is easier to react than $MoCl_5$. Our syntheses using Mo(+III) or Mo(+VI) precursors result amorphous phases too. Even better: the diffractogram of "MoS_2" made with Mo(+III) precursor (Figure 11A-e) is similar to that of molybdenum sulfide made with $MoCl_5$ and $(NH_4)_2S$ by C. Meerback *et al.*; and the diffractogram of "MoS_2" made with Mo(+III) precursor (Figure 11A-c) is similar to that of molybdenum sulfide made with $MoCl_5$ and CS_2 by the same author. Along with the fact that the ratio S/Mo observed in these two samples is close to 2.0 (Figure 11B), it suggests that the products "MoS_2" we made with Mo(+VI) and Mo(+III) precursor are perhaps actually molybdenum sulfides. Hence, it is meaningful to analyze the crystalline phases in the powders made with Mo(+I) precursor with sulfides references. Another interesting point is that in the previous part on "$MoO_{(2.5+0.5a)}S_{0.5}/Na_2$" samples, in the STEM images (Figure 7F), we observed some very thin filaments. Taking into account the possibility of making molybdenum sulfide with the setup conditions, these filaments might be MoS_2 nanosheets too. It would mean that the reaction occurring in this part *without* Na^+ can also take place in the synthesis *with* Na^+. This can explain the lack of Na^+ in the final powders (Figure 5A).

The EDS results showing the observed molar ratio S/Mo is represented in Figure 11B. We see that it can be spread from 1.3 to nearly 2.5, depending on the used Mo precursor. For the syntheses with Mo(+I) precursor (Figure 11B, green point), the S/Mo ratios can be considered as identical in all 3 samples (1.46 ± 0.16) and lower than in the other two syntheses with other precursors (2.21 ± 0.14 and 1.93 ± 0.13). However, this point needs to be confirmed later as there was only one synthesis done for each of Mo(+VI) and Mo(+III) precursors.

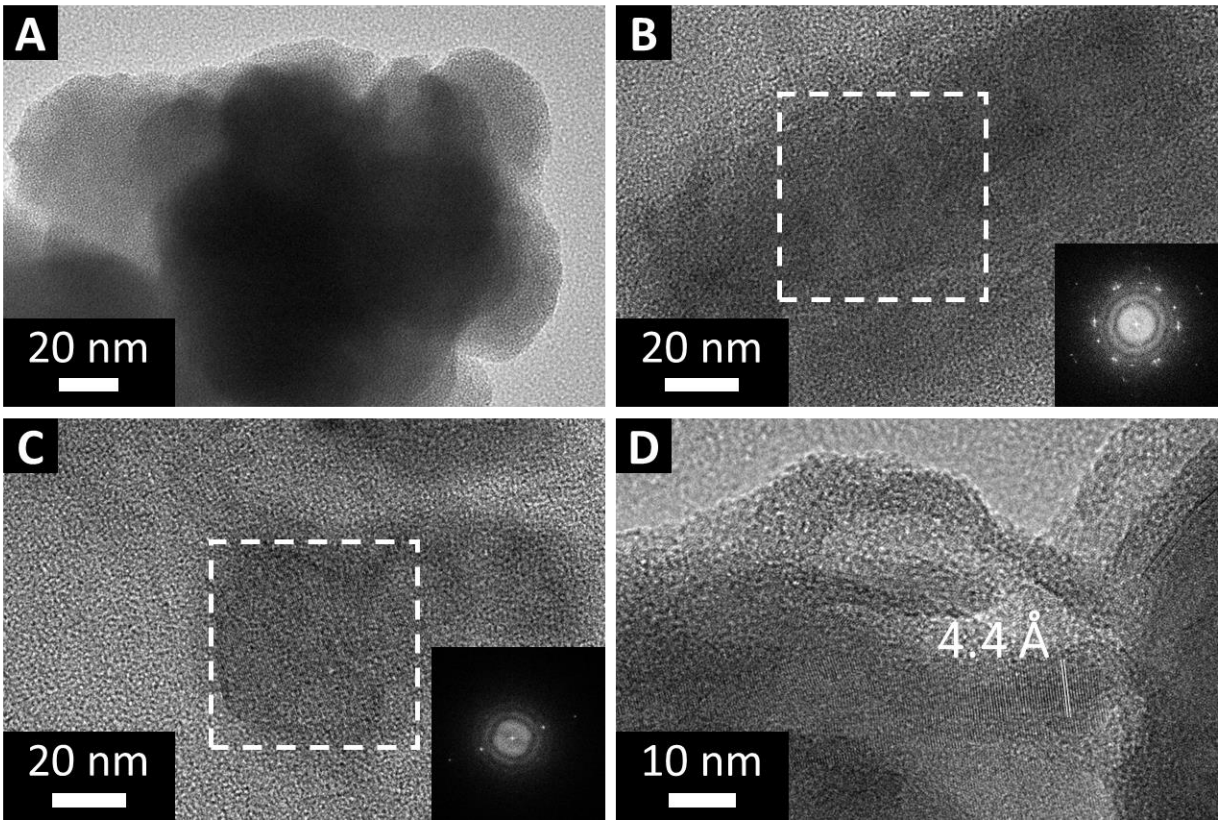

Figure 12 Morphologies of samples made without Gd and with Mo(+I) precursor: (A) amorphous component, (B) large crystalline particle with corresponding electronic diffraction, four visible distances at 9.0 Å, 4.5 Å, 3.2 Å and 2.6 Å; (C) smaller crystalline nanoparticle with corresponding electronic diffraction, two visible distances at 6.0 Å and 3.0 Å; (D) a mixture of crystalline and amorphous components. (A-B) are from sample KL042 and (C-D) are from sample KL116.

The morphology analysis by TEM was done on the two samples made with Mo(+I) precursor (Figure 12). In these powders, some very large amorphous (Figure 12A) or crystalline particles (Figure 12B) are observed at the same time as some much smaller crystalline nanoparticles (Figure 12C) and a mixture of them (Figure 12D). A brief analysis by ImageJ on these images shows some visible interplanar distances: 9.0 Å, 4.5 Å, 3.2 Å, 2.6 Å (Figure 12B), 6.0 Å, 3.0 Å (Figure 12C), and 4.4 Å (Figure 12D). The distance 4.5 Å in Figure 12B may represent the same crystal's facet as the distance 4.4 Å in Figure 12D.

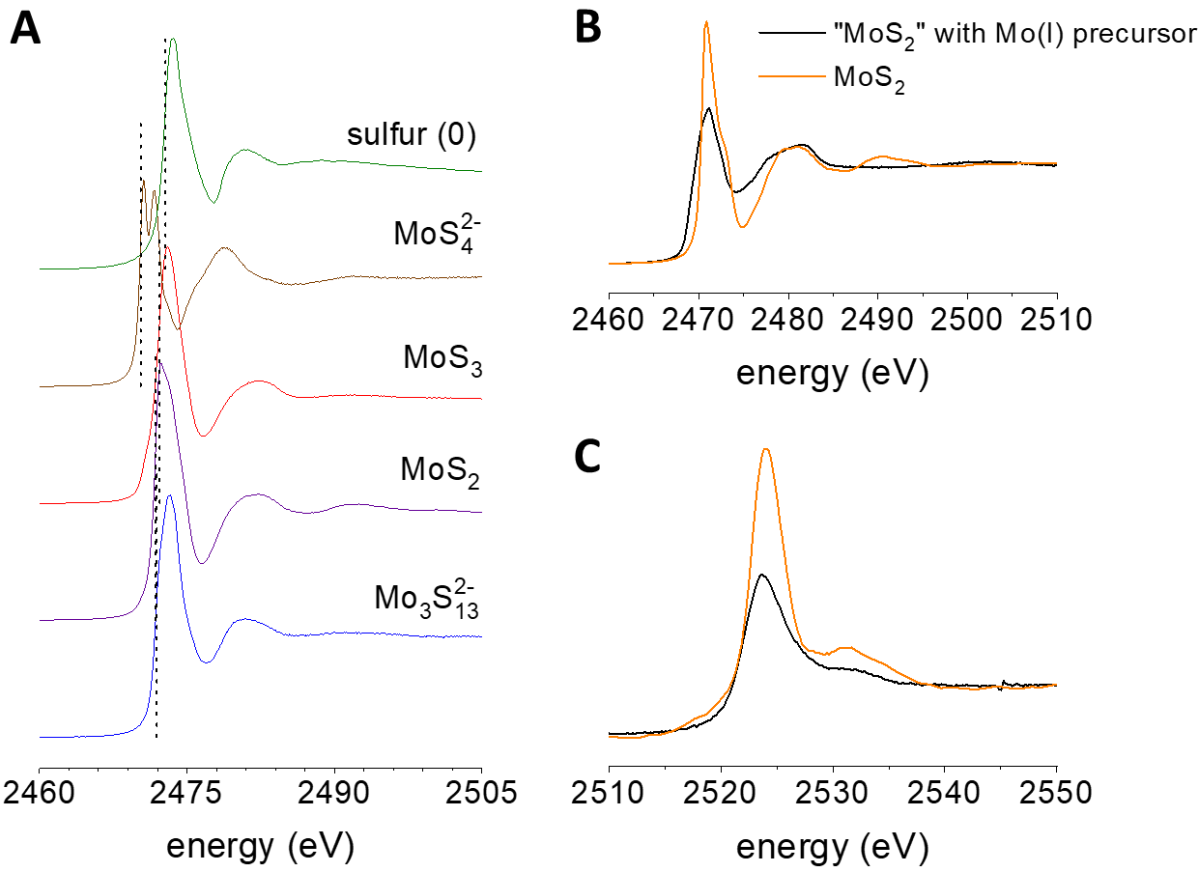

Figure 13 (A) XAS at S K-edge of some references containing Mo-S bonds, provided by Benedikt Lassalle-Kaiser (LUCIA Beamline, Synchrotron SOLEIL). The edge positions are marked by dotted lines. (B) XAS of a sample "MoS_2" made with Mo(+I) precursor in comparison with spectrum of commercial MoS_2 (90 nm) at S K-edge. The legend is common for (B) and (C). (C) XAS of a sample "MoS_2" made with Mo(+I) precursor in comparison with spectrum of commercial MoS_2 (90 nm) at Mo L_3-edge.

Analysis by XAS was done on a sample made with Mo(+I) precursor at Synchrotron SOLEIL, on LUCIA Beamline (Figure 13). At S K-edge, a similarity is observed between the sample and commercial MoS_2. The edge appears even at a slightly lower position (2468.8 eV) than S^{2-} in MoS_2 (2470.3 eV), suggesting a slightly more reduced sulfur (Figure 13B). This can be totally possible as the edge position depends not only on the oxidation state of the concerning element but also the local environment, the oxidation state of metallic ion and also the characteristics of the bond.[25] More visually, in Figure 13A, considering some references provided by Benedikt Lassalle-Kaiser (LUCIA Beamline, Synchrotron SOLEIL), in these sulfide structures, S atoms link principally to Mo only, the spectra at S K-edge are different from one to the other, not only the edge position (marked with dotted lines in the figure) but also the white-lines and multiple-scattering regions. At Mo L_3-edge, there is also a similarity

between the sample and the reference (edges at 2522.0 eV and 2521.9 eV, respectively). This suggests that the oxidation state of Mo in the sample is +IV similar to MoS_2.

For instance, for the reason of the work planning, the analysis on this material family is still brief. Further work will be pursued in the future.

3.2. Discussion on the identification of the crystalline product

The first question to answer is to identify the phases in the products for each Mo precursor. The easiest is to identify the crystalline phases in the samples made with Mo(+I) precursor, represented by thin Bragg peaks in Figure 11A.

For these samples, compared to the MoS_2 from the PLU2019 ICDD database, only two distances 6.0 Å and 3.0 Å in Figure 12C can be indexed as interplanar distances via (001) and (002) axes. On the other hand, if we consider $Mo_{15}S_{20}$ (JCPDS file 04-018-5769, a prototype material by D. Salloum *et al.*[7]) from the same database, a brief comparison of diffractograms in Figure 11A shows already some certain coherence between it and the thin peaks in synthetics samples. The analysis of TEM images by ImageJ shows that more distances can be attributed for $Mo_{15}S_{20}$ than MoS_2 as reference. The ratio S/Mo in this case is also more accurate, to 1.3 in $Mo_{15}S_{20}$ *vs.* 2.0 in MoS_2 to the observed one. According to the information from the database, this phase is hexagonal and has the symmetry group $P6_3/m$ (176) and contain Mo_6 and Mo_9 clusters.[6,7]

Table 2 shows only some of interplanar distances of $Mo_{15}S_{20}$ which are coherent with those in TEM images and calculated from XRD patterns. In this table, the coherence is accepted with a quite large difference between three values. For example, the distance 5.92 Å at 14.9 ° of $Mo_{15}S_{20}$ is considered as found in TEM image as 6.0 Å and in diffractogram at 14.8 °, despite the relative intensity of this peak is not the same as in the reference (Figure 11A, curve (a) *vs.* (d)). Or the distance 7.29 Å at 12.1 ° of $Mo_{15}S_{20}$ is considered as found in the diffractogram at 12.5 °, despite the fact that 0.4 ° of difference cause surely a modification of the structure. We propose three reasons for this approximation. Firstly, there are not yet enough of TEM images to make an average value. Secondly, the calculation of interplanar distance from diffractograms was done by peak picking, this method is not very precise. Moreover, $Mo_{15}S_{20}$ is a prototype from one scientific article, there is not yet enough information about the phases (defections, deformations) which may occur in our case as the synthesis method is totally different (by solid-state synthesis for the reference, mentioned in part 1). Combining with the first spectroscopy analysis, we can state that the phases mixture made with Mo(+I) precursor

contains molybdenum sulfide with the structure close to $Mo_{15}S_{20}$. As the same Bragg peaks are found in the diffractograms of $Gd_{2(1-x)}Mo_{2x}O_2S$ ($x \geq 1$) (Figure 11A-b), one of the secondary reaction in the one-step protocol with Mo(+I) precursor should be identical to the one that occurs in this synthesis.

What if the slight difference between the product and $Mo_{15}S_{20}$ (that we tolerate recently) is because it contains oxygen atoms somehow in its structure? For instance, we do not know it yet because of the lack of information in the database on molybdenum oxysulfides. The two phases $MoS_{0.12}O_{1.88}$ (JCPDS file 04-007-8381) and $Mo_4S_{0.42}O_{10.56}$ (JCPDS file 04-007-8380) are mentioned in Chapter I that no scientific article reference found. Another phase, so-called "Mo_3S_3O" (JCPDS file 04-006-1208) is found in the database but the article reference claimed the opposite: this phase was supposed to obtain when some S in the Chevrel structure Mo_6S_8 are substituted by O but they found out that was not the case.[26] The diffractogram of this "$Mo_6S_6O_2$" is identical to M_6S_8's while we discussed earlier in this chapter that it would be totally impossible if the substitution S-O takes place. Further work should be pursued not only to understand the product from this synthesis but also to understand the products from the one-step protocol.

Table 2 Comparison between the phase $Mo_{15}S_{20}$ (JCPDS file 04-018-5769) from PLU2019 ICDD database, the distances observed in TEM images and the distances calculated from the diffractograms of the sample "MoS_2" made with Mo(+I) precursor. Cells in the same color represent the coherence between the two analysis results and the theoretical numbers from database. Texts in the same color signify a coherence between the results of only one data analysis method and the theoretical numbers.

$Mo_{15}S_{20}$				Analysis TEM by FFT in ImageJ, d(Å)	Analysis XRD	
d(Å)	I	2θ (°)	(hkl)		Bragg calculation, d(Å)	peak picking, 2θ (°)
8.01	387	11.0	(100)	9.0	8.03	11.0
7.29	627	12.1	(101)		7.07	12.5
5.92	107	14.9	(102)	6.0	5.98	14.8
4.73	31	18.7	(103)		4.82	18.4
					4.67	19.0
4.47	12	19.8	(111)	4.5		
4.40	21	20.2	(004)	4.4		
3.31	5	26.9	(203)	3.2		
3.22	84	27.7	(105)			
3.19	6	28.0	(114)			
3.03	72	29.5	(120)	3.0		
2.98	293	29.9	(121)			
2.96	41	30.1	(204)			
2.93	24	30.4	(006)			
2.69	62	33.3	(213)	2.6	2.67	33.5
2.67	12	33.5	(300)		2.61	34.3
2.64	26	33.9	(205) (301)			
2.55	4	35.1	(302)			

For the two samples made with Mo(+VI) and Mo(+III) precursors, as mentioned at the beginning of this part that they could be nanoparticles of MoS_2 based on the diffractogram similarity between our samples and the samples by C. Meerback *et al.*,[24] here we will consider a simple comparison between them. Figure 14A-B show a comparison between the diffractograms extracted from the reference publication's supporting information and those of

our samples, comparing to the bulk MoS_2 (JCPDS 00-037-1492). It is clear that the samples' diffractograms do not match perfectly to the bulk's pattern. They explained it by the size and the thickness of the nanosheets which contains only one or some layers only. Also, the relatively low temperature (320 °C in their synthesis and 310 °C in our case) results a portion of amorphous MoS_2 which is the cause of poorly defined XRD patterns. In order identify the phase, C. Meerback *et al.* used XPS and Raman spectroscopy (Figure 14C, D). For both their samples, they found two intensive peaks in Raman spectra (Figure 14C) which correspond to the vibrations $E_{2g}{}^1$ (in the basal planes, at 372 and 373 cm^{-1}) and A_{1g} (in *z*-direction, at 400 and 401 cm^{-1}) of hexagonal MoS_2. In XPS spectra, they observed two main signals at binding energies of 230 and 233 eV, which were assigned to the $3d_{5/2}$ and $3d_{3/2}$ peaks of Mo(+IV), while a small shoulder at 235 eV might be assigned to Mo(+VI) (Figure 14D). Furthermore, the small signal at 226 eV corresponds to the 2s peak of S due to the interaction between Mo and S. Finally, in the S 2p spectrum, two closely situated peaks at 162 and 163 eV correspond to the $2p_{3/2}$ and $2p_{1/2}$ of S^{2-} orbitals and confirm the -II oxidation state of S. The morphology of their nanosheets shown in Figure 14E is similar to what we observed in our samples $Gd_{2(1-x)}Mo_{2x}O_2S$ with $x \leq 0.2$, presented in Chapter III.

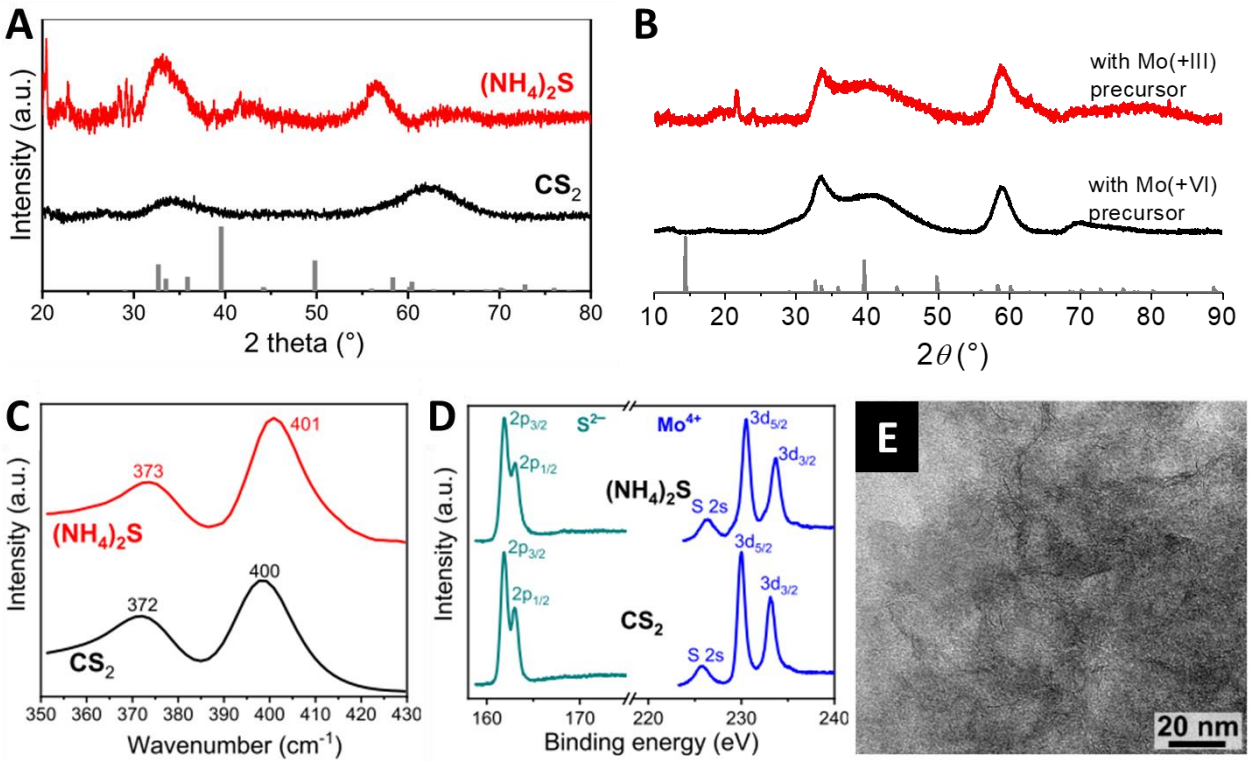

Figure 14 (A) Diffractograms of nanosheets MoS_2 made with $MoCl_5$ and two different S sources as indicated, compared to the pattern of the bulk MoS_2 (JPCDS 00-037-1492) in gray. (B) Diffractograms of our samples "MoS_2" made with S_8 and two different Mo precursors as

indicated, compared to the pattern of the bulk MoS_2 (JPCDS 00-037-1492) in gray. (C) Raman spectra of two samples having the corresponding diffractograms in (A). (D) XPS spectra of two samples having the corresponding diffractograms in (A). (E) Morphology by TEM of the sample made with $(NH_4)_2S$. The figures (A), (C-D) are extracted from the publication of C. Meerback et al.[24]

We can be sure for now that the products by three Mo precursors are different from one to the other. The phases mixture from Mo(+I) precursor displays a crystalline content possibly close to $Mo_{15}S_{20}$ while the products from two other precursors are briefly identified as nanosheets of MoS_2 for instance. Even if the similarity between our samples and the reference article is now only on the diffractograms, the fact of finding some preceded work can give us some ideas how to analyze our samples and how to continue the research.

The question of the O atoms' presence in the samples "MoS_2" as oxysulfides remains to be answered.

4. Conclusion on explorative syntheses without Gd precursor

In this chapter, a brief explorative work was presented on the modified Gd_2O_2S nanoparticles synthesis, applied on molybdenum. As predicted, the products in these syntheses have their structures hardly similar to Gd_2O_2S. Even if they are not yet well described, we already have some idea about their possible structures. This is absolutely a good start to pursue this work.

Although the total identification of the products with or without sodium cation in this part is not finished yet, the similarity of their XRD patterns to the secondary crystalline phases in the products by the one-step protocol ($x \geq 1$) is undeniable. There is also peaks corresponding to Na_2MoO_4 phase in a sample made by the two-step protocol at very high Mo doping. It means that continuing on these two syntheses may clarify the Mo-containing products made by both the one-step and two-step protocols. Also, we might understand if the Mo-containing phase(s) in products made by one-step protocol with $x < 1$ are the same with smaller size or totally different from the crystalline phases.

The samples from the syntheses *with* Na^+ are likely to be a mixture of phases with different Mo's oxidation states. The porous structure is not yet confirmed as purely Na_2MoO_4 or S-containing. This structure is worth a further work on both the structure and the stability as it could be a good support for a certain catalyst in the suitable conditions. In the near future, an

evaluation of specific surface (by BET method) for these samples needs to be done as the surface it provides is probably interesting for a catalyst or a support of catalyst. Also, annealing these samples or trying to heat the synthesis at a much higher temperature to favor the formations of sulfides will possibly give some more ideas about the amorphous phases. The surface activity of these samples should be considered also as the analyses suggest a mixture of porous structures and molybdenum sulfides in/on them. If this observation and the hypothesis are confirmed, it means that by this synthesis method, we are able to make a supported ORR catalyst as molybdenum sulfides are known as ORR active.

The samples from the syntheses *without* Na^+ are partially identified, for instance, as molybdenum sulfides based on the XRD patterns. The structures of these samples are barely studied for now but the similarity between the diffractograms of our products and a former work of another group encourages a lot and even gives us the idea of how to analyze our samples. The presence of very thin filaments in the samples made with Na^+ even gives the idea that the formation of such molybdenum sulfide could occur at the same time as the formation of Na_2MoO_4 and well dispersed into each other. By pursuing this direction, we might propose a new method to synthesize molybdenum sulfide at much lower temperature or during a shorter time compared to using synthesis methods of MoS_2 today.[27] And we may hope for a supported catalyst based on molybdenum sulfide made by an one-pot synthesis in the future.

Amazing!

5. Bibliographies

(1) Ding, Y.; Gu, J.; Ke, J.; Zhang, Y. W.; Yan, C. H. Sodium Doping Controlled Synthesis of Monodisperse Lanthanide Oxysulfide Ultrathin Nanoplates Guided by Density Functional Calculations. *Angew. Chemie - Int. Ed.* **2011**, *50* (51), 12330–12334. https://doi.org/10.1002/anie.201105025.

(2) Larquet, C.; Nguyen, A.-M.; Ávila-Gutiérrez, M.; Tinat, L.; Lassalle-Kaiser, B.; Gallet, J.-J.; Bournel, F.; Gauzzi, A.; Sanchez, C.; Carenco, S. Synthesis of Ce 2 O 2 S and Gd 2(1– y) Ce 2 y O 2 S Nanoparticles and Reactivity from in Situ X-Ray Absorption Spectroscopy and X-Ray Photoelectron Spectroscopy. *Inorg. Chem.* **2017**, *56* (22), 14227–14236. https://doi.org/10.1021/acs.inorgchem.7b02336.

(3) Larquet, C.; Carriere, D.; Nguyen, A.-M.; Le, T. K.-C.; Frogneux-Plé, X.; Génois, I.; Le Griel, P.; Gauzzi, A.; Sanchez, C.; Carenco, S. Unraveling the Role of Alkali Cations in the Growth Mechanism of Gd 2 O 2 S Nanoparticles. *Chem. Mater.* **2020**, *32* (3), 1131–1139. https://doi.org/10.1021/acs.chemmater.9b04059.

(4) Benck, J. D.; Hellstern, T. R.; Kibsgaard, J.; Chakthranont, P.; Jaramillo, T. F. Catalyzing the Hydrogen

Evolution Reaction (HER) with Molybdenum Sulfide Nanomaterials. *ACS Catal.* **2014**, *4* (11), 3957–3971. https://doi.org/10.1021/cs500923c.

(5) Fang, Y.; Pan, J.; He, J.; Luo, R.; Wang, D.; Che, X.; Bu, K.; Zhao, W.; Liu, P.; Mu, G.; et al. Structure Re-Determination and Superconductivity Observation of Bulk 1T MoS2. *Angew. Chemie - Int. Ed.* **2018**, *57* (5), 1232–1235. https://doi.org/10.1002/anie.201710512.

(6) Salloum, D.; Gautier, R.; Gougeon, P.; Potel, M. Syntheses and Structural Trends of the InxMo15S 19 (0≤x≤3.7) Compounds Containing Mo6 and Mo 9 Clusters. *J. Solid State Chem.* **2004**, *177* (4–5), 1672–1680. https://doi.org/10.1016/j.jssc.2003.12.023.

(7) Salloum, D.; Gautier, R.; Potel, M.; Gougeon, P. Mo15S20: First Evidence of a New Molybdenum Cluster Type in a Metastable Solid-State Compound. *Chem. - A Eur. J.* **2006**, *12* (33), 8513–8517. https://doi.org/10.1002/chem.200601256.

(8) Fukuoka, H.; Masuoka, K.; Hanaoka, T.; Inumaru, K. New Polymorph of Mo3S4 Prepared Using a High-Pressure Synthesis Technique: Crystal Structure, Electronic Property, and Band Calculation. *Inorg. Chem.* **2013**, *52* (14), 7918–7922. https://doi.org/10.1021/ic400423n.

(9) Schutte, W. J.; Disselborg, F.; De Boer, J. L. Determination of the Two-dimensional Incommensurately Modulated Structure of Mo2S3. *Acta Crystallogr. Sect. B* **1993**, *49* (5), 787–794. https://doi.org/10.1107/S0108768192006670.

(10) Tarascon, J. M.; Hull, G. W. On Several New Ternary Molybdenum Sulfide Phases M3.4Mo15S19 (M = Vacancy, Li, Na, K, Zn, Cd, Sn and Tl). *Mater. Res. Bull.* **1986**, *21* (7), 859–869. https://doi.org/10.1016/0025-5408(86)90172-8.

(11) Fagerquist, R. L.; Kirby, R. D. Metastable Conduction States in Mo2S3: Pulse Conductivity and Thermoelectric Power. *Phys. Rev. B* **1988**, *38* (6), 3973–3985. https://doi.org/10.1103/PhysRevB.38.3973.

(12) Rastogi, A. K. Non-Equilibrium Effects on the Electric and Magnetic Properties of the Mo-Chain Compound Mo2S3. *Philos. Mag. B Phys. Condens. Matter; Stat. Mech. Electron. Opt. Magn. Prop.* **1985**, *52* (4), 909–919. https://doi.org/10.1080/13642818508238936.

(13) Shigegaki, Y.; Basu, S. K.; Wakihara, M.; Taniguchi, M. Thermal Analysis and Kinetics of Oxidation of Molybdenum Sulfides. *J. Therm. Anal.* **1988**, *34* (5–6), 1427–1440. https://doi.org/10.1007/BF01914367.

(14) Zhou, X.; Zhao, W.; Pan, J.; Fang, Y.; Wang, F.; Huang, F. Urchin-like Mo2S3 Prepared via a Molten Salt Assisted Method for Efficient Hydrogen Evolution. *Chem. Commun.* **2018**, *54* (90), 12714–12717. https://doi.org/10.1039/c8cc06714g.

(15) Deblieck, R.; Van Dyck, D.; Van Tendeloo, G.; Van Landuyt, J.; Amelinckx, S.; Wiegers, G. A.; Bronsema, K. D. Clustering and "Phase Ordering" Transitions in Molybdenum (III) Sulfide, Mo2.065S3. *Phys. Status Solidi* **1983**, *77* (1), 249–261. https://doi.org/10.1002/pssa.2210770130.

(16) Shembel, E.; Apostolova, R.; Kirsanova, I.; Tysyachny, V. Electrolytic Molybdenum Sulfides for Thin-Layer Lithium Power Sources. *J. Solid State Electrochem.* **2008**, *12* (9), 1151–1157.

https://doi.org/10.1007/s10008-007-0463-5.

(17) Matsumoto, K.; Kobayashi, A.; Sasaki, Y. The Crystal Structure of Sodium Molybdate Dihydrate, Na2Mo04.2H20. *Bull. Chem. Soc. Jpn.* **1975**, *48* (3), 1009–1013.

(18) Henderson, G. S.; De Groot, F. M. F.; Moulton, B. J. A. X-Ray Absorption Near-Edge Structure (XANES) Spectroscopy. *Rev. Mineral. Geochemistry* **2014**, *78*, 75–138. https://doi.org/10.2138/rmg.2014.78.3.

(19) Shannon, R. D. Revised Effective Ionic Radii and Systematic Studies of Interatomic Distances in Halides and Chalcogenides. *Acta Crystallogr. Sect. A* **1976**, *32* (5), 751–767. https://doi.org/10.1107/S0567739476001551.

(20) Daage, M.; Chianelli, R. R. Structure-Function Relations in Molybdenum Sulfide Catalysts: The "Rim-Edge" Model. *Journal of Catalysis*. 1994, pp 414–427. https://doi.org/10.1006/jcat.1994.1308.

(21) Tauster, S. J.; Pecoraro, T. A.; Chianelli, R. R. Structure and Properties of Molybdenum Sulfide: Correlation of O2 Chemisorption with Hydrodesulfurization Activity. *J. Catal.* **1980**, *63* (2), 515–519. https://doi.org/10.1016/0021-9517(80)90109-8.

(22) Chang, K.; Pang, H.; Hai, X.; Zhao, G.; Zhang, H.; Shi, L.; Ichihara, F.; Ye, J. Ultra-Small Freestanding Amorphous Molybdenum Sulfide Colloidal Nanodots for Highly Efficient Photocatalytic Hydrogen Evolution Reaction. *Appl. Catal. B Environ.* **2018**, *232* (2010), 446–453. https://doi.org/10.1016/j.apcatb.2018.03.087.

(23) Moreno, B.; Vidoni, O.; Ovalles, C.; Chaudret, B.; Urbina, C.; Krentzein, H. Synthesis and Characterization of Molybdenum Based Colloidal Particles. *J. Colloid Interface Sci.* **1998**, *207* (2), 251–257. https://doi.org/10.1006/jcis.1998.5631.

(24) Meerbach, C.; Klemmed, B.; Spittel, D.; Bauer, C.; Park, Y. J.; Hübner, R.; Jeong, H. Y.; Erb, D.; Shin, H. S.; Lesnyak, V.; et al. General Colloidal Synthesis of Transition-Metal Disulfide Nanomaterials as Electrocatalysts for Hydrogen Evolution Reaction. *ACS Appl. Mater. Interfaces* **2020**, *12* (11), 13148–13155. https://doi.org/10.1021/acsami.9b21607.

(25) Fleet, M. E.; Liu, X.; Harmer, S. L.; King, P. L. Sulfur K-Edge XANES Spectroscopy: Chemical State and Content of Sulfur in Silicate Glasses. *Can. Mineral.* **2005**, *43* (5), 1605–1618. https://doi.org/10.2113/gscanmin.43.5.1605.

(26) Selwyn, L. S.; McKinnon, W. R.; Dahn, J. R. Lack of Oxygen Substitution in the Chevrel Compound Mo6S8. *Solid State Commun.* **1987**, *64* (7), 1025–1028. https://doi.org/10.1016/0038-1098(87)91023-4.

(27) Krishnan, U.; Kaur, M.; Singh, K.; Kumar, M.; Kumar, A. A Synoptic Review of MoS 2 : Synthesis to Applications. *Superlattices Microstruct.* **2019**, *128* (December 2018), 274–297. https://doi.org/10.1016/j.spmi.2019.02.005.

To the MoO_xS_y star and beyond…

Synthesis of Mo-containing Gd_2O_2S-like nanoparticles by one-pot synthesis

On this subject, we really have gone a long way from the idea of the material four years ago to the idea of the structure now. Achieving the well-known synthesis of lanthanide oxysulfides with an addition of d-block metals (molybdenum in our case) is clearly explorative and not an easy task at all. By both protocols presented in this thesis, all products made are at nanoscale and the Mo-containing phases are dispersive amongst/onto the Gd_2O_2S nanoparticles, which we may see as a support, and do not form any kind of massive phase. Those are very first positive points as we are aiming to find a new *nanoscaled* ORR catalyst.

On the practical work, despite many difficulties in analyzing the final products, we have found much important information on the structure and the morphology. Only by comparing the products from the two series, it is found that the Mo-containing phases in the two cases have totally different structures, which signifies also the different reactions taking place in each kind of synthesis. By going further on the data treatment over all used techniques, we now can conclude on the oxidation state of Mo (+VI for samples made by the two-step protocol and +IV for samples made by the one-step protocol) that we could not do two years ago. Not only the oxidation state, the local and crystalline structures of the two series are totally different: the samples made by the two-step protocol is identified having isolated tetrahedron of molybdate while the other series seem to have a more sulfide-like environment of Mo.

By analyzing the samples made by the one-step protocol, we learnt that the reaction between the Mo precursor and sulfur under the set-up conditions is totally independent to the formation of Gd_2O_2S, resulting in a sulfide-like final products. By preliminary EXAFS treatment, we found that Mo in these samples have bonds with both O and S but we do not know yet if there is any O-Mo-S as an oxysulfide. Based on the diffractograms, at low Mo doping the Mo-containing phases are not visible while at high Mo doping they become visible as crystalline phases. These phases appear to be similar to molybdenum sulfide $Mo_{15}S_{20}$'s diffractogram. Since this material is a prototype, for instance, the authors provided only crystallographic information. Also, no information on XAS of $Mo_{15}S_{20}$ was found, along with its complicated structure, the prediction of $Mo_{15}S_{20}$'s XAS to compare to our samples is very difficult. Another thing that we do not know yet about these crystalline phases is that if they are already formed

at low Mo doping as (mostly) amorphous or they are only created when the Mo quantity is high enough to obstruct the formation of Gd_2O_2S.

By simply comparing the samples made by the two-step protocol to the annealed Gd_2O_2S sample, we conceived that the change in XRD patterns and the morphology are not linked to the addition of Mo in the synthesis but probably to the evolution of Gd_2O_2S during the 2nd heating and to the rearrangement of organic ligands on the surface of nanoparticles. Taking into account all the conditions of local structure and the insights from the latest PDF measurements, we succeeded in proposing the very first structural model for samples made by the two-step protocol as a molybdate-doped modified Gd_2O_2S which does not contradict any other analysis results. The single molybdate tetrahedrons link to the surface of Gd_2O_2S by weak interaction Gd-O which can explain the big loss of Mo at low doping (in the case that the EDS results are all reliable) while at very high doping, sodium molybdate is formed.

In terms of the ORR catalytic activity we want to achieve, the sample series made by the two-step protocol has shown some first positive results. By comparing with the results of electrochemical tests between samples from two series, we perceived that the ORR activity links directly to the structure of Mo atoms in the materials, hence, the reactions during the synthesis, and not at all to the quantity of Mo in the powder. The relation between the structure and the ORR reactivity of samples made by the two-step protocol is still under study but we proposed already three hypotheses where the quick reduction of Mo by ethanol during the ink preparation can be seen as an activation process. The veritable active sites and the formation's mechanism in this case are still under investigation. In the first chapter, we have seen that some researches showed that oxysulfide is an active intermediate in some organic reactions, it would be very exciting if it is the case here too! For instance, the activity remains quite low but we are working to figure out the relation between the structure of Mo centers and the activity they provide as well as the way to make a better catalyst.

In short, at the point where we are for the moment, we can say surely that besides the gracious results we achieved, there are numerous researching paths towards a supported catalyst in the future.

Explorative colloidal synthesis of Mo-containing nanoparticles without Gd precursor

The first kind of synthesis was done exactly in the same way as the formation of Gd_2O_2S with the Gd precursor replaced by Mo precursor. The final products made with Mo(+VI) precursor turned out isostructural to sodium molybdate (hydrated or dehydrated) with a strange morphology with holes on/in the nanoparticles. The similarity between the synthetic powders and commercial sodium heptamolybdate was observed also by XANES: the same edge position at all K-edge and $L_{3,2}$-edges and the similar spectrum shape. However, the synthetic powders seem to be likely a mixture of phases with different Mo's oxidation states. Some tests were done to briefly exploring the effects of Mo precursors and sodium sources to the final structure. Based on the XRD patterns, Mo(+VI) precursor and sodium oleate appear to be the best matching for this synthesis in order to get the most "proper" diffractograms.

The second kind of synthesis was done with only Mo precursor (tested for three types) and S_8 without oleic acid. Only the synthesis with Mo(+I) precursor gave crystalline phase(s), visible in the diffractograms as thin peaks, the two other ones gave amorphous phases. These phases contain a significant amount of S (observed S/Mo varies between 1.3 and 2.2 depending on the Mo precursor). The oxidation state of Mo is close to +IV as in MoS_2 with a similar local environment, which was observed by XANES at Mo L_3-edge and S K-edge. The brief research in the literature showed already a good sign about this synthesis: the amorphous phases in our case could be actually nanoparticles/nanosheets of MoS_2 since their diffractograms are quite similar. Also, the presence of some thin filaments in the samples made with Na gives the idea that the reaction in this synthesis can actually occur in the first one. The presence of O in these phases is still under the investigation.

When these two explorative syntheses were started, we thought they were totally irrelevant to the synthesis with Gd and Mo precursors. Interestingly, by combining the analysis results, it turned out that probably everything is connected. Our hypothesis is that the formation of molybdenum sulfides in the synthesis *without* Na^+ can possibly occur in the synthesis *with* Na^+ *and without Gd*; together with the formation of sodium molybdate in the synthesis *with* Na^+ *and without Gd*, it can occur in the synthesis *with Gd* in one step (XRD results), possibly with different ratio. And, the formation of molybdate occurs in the synthesis *with Gd* in two steps. It means that by understanding these two explorative syntheses, we will understand the

mechanism of the synthesis with both metals as the reactions are easier to analyze when they are separated from each other.

And beyond…

The end of this PhD project is not the end of the whole project as the destination of molybdenum oxysulfide as ORR catalyst is still ahead.

For the materials made with both Gd and Mo precursor, the final structures which contain both metals are now being clarified. The first model for samples made by the two-step protocol is released, a proposition of the crystalline phases at high Mo doping for samples made by the one-step protocol is made. The relation between the products' structures and the ORR activity they performed is also hypothesized. The next step will be indeed the confirmation of these hypotheses by PDF calculation and finishing the data treatments for other methods to complete the structural modelling. Once the structure is totally unveiled and the mechanism is better learnt, the ORR catalytic activity of these materials will be hopefully enhanced.

For the samples without any Gd, at the moment, no electrochemical tests were done. We do not know yet if they will be active as the samples made by the two-step protocol or inactive as the other ones. Nevertheless, continuing the study on these powders will reveal not only their structures but also will lead to more profound understanding not only on the structures of molybdate-doped Gd_2O_2S nanoparticles made by the two-step protocol and the mechanism of its electrocatalytic reaction, but also the structure of Mo-containing phase in powders made by the one-step protocol and its formation. From there, a new optimized protocol might be developed in order to get better defined catalyst.

We are aware that the applicable final catalyst is still far away from where we are at the moment and reaching it is surely very challenging. The good point is that we have achieved very interesting results and we have many ideas and paths to continue the research.

We have gone a long way and still keep following it. At the end of the road, there will be rainbows celebrating our success!

Experimental section

Table of contents

1. Synthesis protocol

1.1. Information regarding all the colloidal syntheses of nanoparticles

For all syntheses, the reaction is always done in inert atmosphere (N_2) in a three-neck round-bottom flask of 100 mL. The heater is equipped with a temperature controller (PID). The temperature is controlled with a probe immersed in the reaction medium via a glass immersion sleeve.

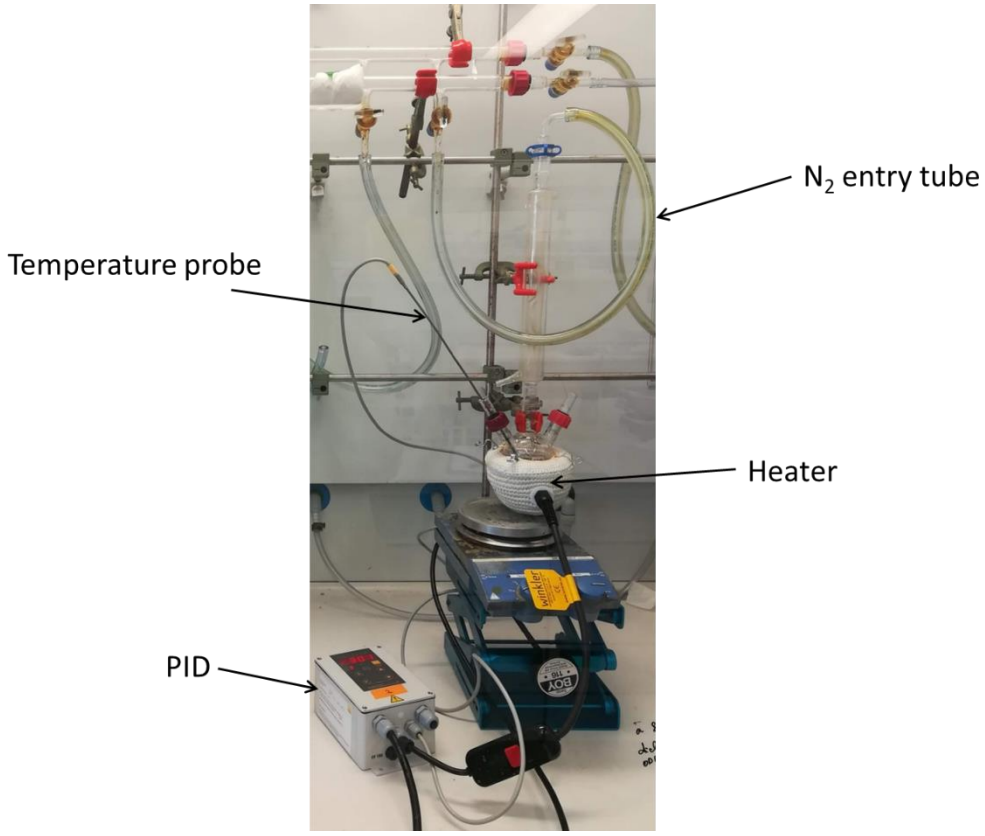

Figure 1 Synthesis setup.

All the synthesis protocols, in one step or two steps, are considered as one-pot because there is no product isolation or treatment after each step. The product treatment is only done at the very end of the protocol.

For all synthesis, oleylamine (OM; technical grade, 70 %), oleic acid (OA; technical grade, 90 %), sulfur (S_8; ≥ 99.5 %), 1-octadecene (ODE; technical grade, 90 %), sodium oleate (Na(oleate); ≥ 99 %), sodium citrate monobasic (Na(citrate); anhydrous; ≥ 99.5 %), cyclopentadienylmolybdenum(I)tricarbonyl, dimer ($[CpMo(CO)_3]_2$, 98 %) and bis(acetylacetonato)dioxomolybdenum(VI) ($MoO_2(acac)_2$, 95 %) were purchased from Sigma-Aldrich. Gadolinium acetylacetonate hydrate ($Gd(acac)_3 \cdot xH_2O$; 99.9 %) and sodium

acetylacetonate (Na(acac), 98 %) were purchased from Strem Chemicals. Molybdenum(III) acetylacetonate ($Mo(acac)_3$) was provided by V. Mougel and colleagues from Collège de France. All products were used as received without further purification.

The initial reaction medium is firstly degassed 3 times, about 3 min each, at ambient temperature. Its composition changes in function of the synthesis. It is a mixture of OM, OA, ODE, Gd precursor, S_8 and Na(oleate) for the synthesis of Gd_2O_2S nanoparticles (identical for the first step of the two-step protocol). For the synthesis of Mo-containing samples via the one-step protocol or for syntheses without Gd precursor, the Mo(+VI) precursor was added before the degassing, while the two other Mo precursors needed to be added after. Agitation is maintained during all the process. After finishing heating, the heater is taken out to cool down the reaction medium under a N_2 flux. For product isolation at the end of synthesis, in general, the centrifugation is done four times for 10 min each, at 7000 rpm (5259 ×G) at 20 °C in 50 mL plastic tubes with conical bottoms and screw caps: either VWR® SuperClear® or FALCON™. All differences in washing process for specific cases will be detailed in the next part. The obtained solid is dried under N_2 flux then ground to make a fine powder before being analyzed.

All samples are stored in the glovebox to decrease as much as possible the effect of air on the nanoparticles.

1.2. Molybdenum-free synthesis protocol

There are two approaches for synthesis of Mo-containing Gd_2O_2S nanoparticles: in one step protocol or in two-step protocol. In the one-step protocol, we expected to have the products with a substitution Gd-Mo, similarly to the case of the $Gd_{2(1-y)}Ce_{2y}O_2S$ synthesis where certain Gd sites are substituted by Ce. This synthesis was performed by C. Larquet from our research group[1] and also by Y. Ding *et al.*[2] For the products from the one-step protocol, classical Gd_2O_2S nanoparticles are taken as initial point for comparison.

A two-step protocol may lead to core-shell nanoparticles. In this case, we expected a deposition of Mo on the surface of freshly formed Gd_2O_2S nanoparticles during the 2nd step. For the samples made by this protocol, an initial point of classical Gd_2O_2S nanoparticles made by the one-step protocol is not legitimate anymore. Instead, freshly formed Gd_2O_2S nanoparticles were annealed directly in its reaction medium to give a material which serves as the initial point for the Mo-containing samples made by the two-step protocol. This annealed sample helps understanding the structures of the materials from the two-step protocol.

The samples made by the one-step protocol and by the two-step protocol are noted as **$Gd_{2(1-x)}Mo_{2x}O_2S$** and **Gd_2O_2S/Mo_{2x}**, respectively. The corresponding references samples for comparison are the cases of $x = 0$. The signification of x will be clarified for each protocol in the following parts.

1.2.1. Classical Gd_2O_2S nanoparticles synthesis[1,2]

The mixture of solvents and stabilizers is made with OM (4.54 g, 17 mmol, 34 equiv.), oleic acid (0.72 g, 2.5 mmol, 5 equiv.) and 1-octadecene (8.2 g, 32.5 mmol, 65 equiv.) in a glass three-neck round-bottom flask of 100 mL. The number of equiv. is calculated as the ratio of their molar quantity divided by the molar quantity of $Gd(acac)_3$ precursor. In this mixture, the molecular precursor $Gd(acac)_3$ (227 mg, 0.5 mmol, 1 equiv.) is added with sulfur S_8 (8 mg, 0.03 mmol, 0.5 equiv. of S) and sodium oleate (152 mg, 0.5 mmol, 1 equiv.). The mixture is then agitated and put under N_2 atmosphere at room temperature by three cycles N_2/vacuum for 3 minutes each. At this point, the solids are not yet soluble in the liquid mixture. This is then degassed at 120 °C during at least 20 min under primary vacuum. The solids are more and more soluble with the temperature increase. When it reaches 120 °C, the reaction medium becomes a transparent orange solution which is the color of soluble sulfur. A light reflux can be observed by the condensation on the flask wall, up to about 2 cm above the liquid surface. Then, the medium is heated to 310 °C during 30 min under a N_2 flux. This process lasts for about 20 min. The solution color becomes lighter to yellow as the temperature increases. From about 280 °C, the transparent solution becomes visibly turbid with white solid. The reflux is a bit stronger by this moment: some drops are formed at the bottom of the refrigerant column and fall in the solution from time to time. It may cause some white smoke inside the flask but it disappears very quickly (after about 1 min). After cooling down during about 25 min to around 30 °C, the reaction medium seems to be a little less turbid than when it was at 310 °C. It is collected with THF (less than 5 mL) and then mixed with ethanol (10 mL) and centrifuged at 20 °C, 7000 rpm for 10 min. The supernatant here is yellow and transparent as it contains the excess sulfur. The obtained solid (off-white) is washed three times with THF (about 4 mL) and ethanol (to make 25 mL of solvent mixture). Finally, the solid is dried under a N_2 flux during 1 h and ground with a mortar to obtain a powder for analysis.

1.2.2. One-pot annealing of Gd_2O_2S nanoparticles in solution at 310 °C, as a second step: Gd_2O_2S/Mo_0

The mixture of solvents and stabilizers is made with OM (4.54 g, 17 mmol, 34 equiv.), oleic acid (0.72 g, 2.5 mmol, 5 equiv.) and 1-octadecene (8.2 g, 32.5 mmol, 65 equiv.) in a glass three-neck round-bottom flask of 100 mL. The number of equiv. is calculated as the ratio of their molar quantity divided by the molar quantity of $Gd(acac)_3$ precursor. Then, in this mixture, the molecular precursor $Gd(acac)_3$ (227 mg, 0.5 mmol, 1 equiv.) is added with sulfur S_8 (8 mg, 0.03 mmol, 0.5 equiv. of S) and sodium oleate (152 mg, 0.5 mmol, 1 equiv.). The mixture is then agitated and put under N_2 atmosphere at room temperature by three cycles N_2/vacuum for 3 minutes each. At this point, the solids are not yet soluble in the liquid mixture. This is then degassed at 120 °C during at least 20 min under primary vacuum. The solids are more and more soluble with the temperature increase. When it reaches 120 °C, the reaction medium becomes a transparent orange solution which is the color of soluble sulfur. A light reflux can be observed by the condensation on the flask wall, up to about 2 cm above the liquid surface. Then, the medium is heated to 310 °C during 30 min under a N_2 flux. This process lasts for about 20 min. The solution color becomes lighter to yellow as the temperature increases. From about 280 °C, the transparent solution becomes visibly turbid with white solid. The reflux is a bit stronger by this moment: some drops are formed at the low of the refrigerant column and fall in the solution from time to time. It may cause some white smoke inside the flask but it disappears very quickly (after about 1 min). After cooling down during about 25 min to around 30 °C, the reaction medium seems to be a little less turbid than when it was at 310 °C.

After cooling down the reaction medium to about between 30 and 40 °C by N_2 flux (during about 25 min), it is reheated to 310 °C during 30 min under the same N_2 flux. No visible change was observed during this process. After cooling down the reaction medium a second time during about 25 min to about 30 °C, it is recuperated with THF (less than 5 mL) and then mixed with ethanol (10 mL) and centrifuged at 20 °C, 7000 rpm for 10 min. The supernatant here is yellow and transparent as it contains the excess sulfur. The obtained solid (off-white) is washed three times with THF (about 4 mL) and ethanol (to make 25 mL of solvent mixture). Finally, the solid is dried under a N_2 flux during 1 h and ground with a mortar to obtain a powder for analysis.

1.3. Molybdenum-containing synthesis protocol

1.3.1. Synthesis of Mo-containing Gd_2O_2S-like nanoparticles in two steps: Gd_2O_2S/Mo_{2x}

The products from this method are all based on preformed Gd_2O_2S nanoparticles. These are formed during the first step in the same way as described in 4.1. In the second step, a Mo molecular precursor is added and the mixture is heated one more time at 310 °C during 30 min as in the first step. We expected to obtain Mo-containing Gd_2O_2S nanoparticles at the end by deposition of Mo on the surface of Gd_2O_2S nanoparticles. The obtained solids were expected to be core-shell nanoparticles.

The molar quantity of Gd precursor is maintained at 0.5 mmol and considered as the unit for equivalent (equiv.) calculation in each synthesis. The calculation of *x* is as below:

Gd_2O_2S/Mo_{2x} $\quad x = \frac{n_{Mo\ introduced}}{0.5}$

0.5 = introduced molar quantity of Gd precursor

x = molar ratio $\frac{Mo}{Gd}$

= name of sample

$2x$ = theoretical notation index

All three described protocols below are for samples with ***x* = 0.18**, i.e. the molar ratio Mo/Gd is 0.18. The generic formula for all these samples is then: **$Gd_2O_2S/Mo_{0.36}$.**

1.3.1.1. Synthesis with Mo(+VI) precursor

The mixture of solvents and stabilizers is made with OM (4.54 g, 17 mmol, 34 equiv.), oleic acid (0.72 g, 2.5 mmol, 5 equiv.) and 1-octadecene (8.2 g, 32.5 mmol, 65 equiv.) in a glass three-neck round-bottom flask of 100 mL. The number of equiv. is calculated as the ratio of their molar quantity divided by the molar quantity of $Gd(acac)_3$ precursor. Then, in this mixture, the molecular precursor $Gd(acac)_3$ (227 mg, 0.5 mmol, 1 equiv.) is added with sulfur S_8 (8 mg, 0.03 mmol, 0.5 equiv. of S) and sodium oleate (152 mg, 0.5 mmol, 1 equiv.). The mixture is then agitated and put under N_2 atmosphere at room temperature by three cycles N_2/vacuum for 3 minutes each. At this point, the solids are not yet soluble in the liquid mixture. This is then degassed at 120 °C during at least 20 min under primary vacuum. The solids are more and more soluble with the temperature increase. When it reaches 120 °C, the reaction medium becomes a transparent orange solution which is the color of soluble sulfur. A light reflux can be observed by the condensation on the flask wall, up to about 2 cm above the liquid

surface. Then, the medium is heated to 310 °C during 30 min under a N_2 flux. This process lasts for about 20 min. The solution color becomes lighter to yellow as the temperature increases. From about 280 °C, the transparent solution becomes visibly turbid with white solid. The reflux is a bit stronger by this moment: some drops are formed at the low of the refrigerant column and fall in the solution from time to time. It may cause some white smoke inside the flask but it disappears very quickly (after about 1 min). After cooling down during about 25 min to around 30 °C, the reaction medium seems to be a little less turbid than when it was at 310 °C.

After cooling down the reaction medium to about between 30 and 40 °C by N_2 flux (during about 25 min), the molecular precursor $MoO_2(acac)_2$ (28.8 mg, 0.09 mmol, 0.18 equiv.) is added under N_2 atmosphere. The solid is not soluble in the reaction medium. The mixture is heated to 310 °C and maintained during 30 min under a N_2 flux. With the increase of temperature, the solid is more and more soluble to give a homogenous orange mixture. The reaction medium at 120 °C is orange and turbid, all the solid is soluble. As the temperature increases more, the color becomes darker and darker, from about 250 °C, it is totally black. The reflux and white smoke are also observed from 280 °C. After cooling down to room temperature, the reactional medium is recuperated with THF (less than 5 mL) and then mixed with ethanol (10 mL) and centrifuged at 20 °C, 7000 rpm for 10 min. The supernatant here is yellow-orange and see-through. The obtained solid (dark gray) is washed three times with THF (about 4 mL) and ethanol (to make 25 mL of solvent mixture). These three supernatants are colorless. Finally, the solid is dried under a N_2 flux during 1 h and ground with a mortar to obtain a powder for analysis.

1.3.1.2. Synthesis with Mo(+I) precursor

The mixture of solvents and stabilizers is made with OM (4.54 g, 17 mmol, 34 equiv.), oleic acid (0.72 g, 2.5 mmol, 5 equiv.) and 1-octadecene (8.2 g, 32.5 mmol, 65 equiv.) in a glass three-neck round-bottom flask of 100 mL. The number of equiv. is calculated as the ratio of their molar quantity divided by the molar quantity of $Gd(acac)_3$ precursor. Then, in this mixture, the molecular precursor $Gd(acac)_3$ (227 mg, 0.5 mmol, 1 equiv.) is added with sulfur S_8 (8 mg, 0.03 mmol, 0.5 equiv. of S) and sodium oleate (152 mg, 0.5 mmol, 1 equiv.). The mixture is then agitated and put under N_2 atmosphere at room temperature by three cycles N_2/vacuum for 3 minutes each. At this point, the solids are not yet soluble in the liquid mixture. This is then degassed at 120 °C during at least 20 min under primary vacuum. The solids are more and more soluble with the temperature increase. When it reaches 120 °C, the reaction

medium becomes a transparent orange solution which is the color of soluble sulfur. A light reflux can be observed by the condensation on the flask wall, up to about 2 cm above the liquid surface. Then, the medium is heated to 310 °C during 30 min under a N_2 flux. This process lasts for about 20 min. The solution color becomes lighter to yellow as the temperature increases. From about 280 °C, the transparent solution becomes visibly turbid with white solid. The reflux is a bit stronger by this moment: some drops are formed at the low of the refrigerant column and fall in the solution from time to time. It may cause some white smoke inside the flask but it disappears very quickly (after about 1 min). After cooling down during about 25 min to around 30 °C, the reaction medium seems to be a little less turbid than when it was at 310 °C.

After cooling down the reaction medium to about between 30 and 40 °C by N_2 flux (during about 25 min), the molecular precursor $Cp_2Mo_2(CO)_6$ (22 mg, 0.045 mmol, 0.09 equiv.) is added under N_2 atmosphere. The solid isn't soluble in the reaction medium. The mixture is heated at 310 °C during 30 min under a N_2 flux. With the increase of temperature, the solid is more and more soluble. The color change from red of Mo precursor to black quickly: at 120 °C it's already changed to dark orange-red. As the temperature increases more, the color becomes darker and darker, from about 250 °C, it is totally black. The reflux and white smoke are also observed from 280 °C. After cooling down to room temperature, the reactional medium is recuperated with THF (less than 5 mL) and then mixed with ethanol (10 mL) and centrifuged at 20 °C, 7000 rpm for 10 min. The supernatant here is black, the intensity of the color increases with the increase of *x*. In this case $x = 0.18$, the supernatant in the tube is still see-through. The obtained solid (gray) is washed three times with THF (about 4 mL) and ethanol (to make 25 mL of solvent mixture). These three supernatants are colorless. Finally, the solid is dried under a N_2 flux during 1 h and ground with a mortar to obtain a powder for analysis.

1.3.1.3. Synthesis with Mo(+III) precursor

The mixture of solvents and stabilizers is made with OM (4.54 g, 17 mmol, 34 equiv.), oleic acid (0.72 g, 2.5 mmol, 5 equiv.) and 1-octadecene (8.2 g, 32.5 mmol, 65 equiv.) in a glass three-neck round-bottom flask of 100 mL. The number of equiv. is calculated as the ratio of their molar quantity divided by the molar quantity of $Gd(acac)_3$ precursor. Then, in this mixture, the molecular precursor $Gd(acac)_3$ (227 mg, 0.5 mmol, 1 equiv.) is added with sulfur S_8 (8 mg, 0.03 mmol, 0.5 equiv. of S) and sodium oleate (152 mg, 0.5 mmol, 1 equiv.). The mixture is then agitated and put under N_2 atmosphere at room temperature by three cycles N_2/vacuum for 3 minutes each. At this point, the solids are not yet soluble in the liquid mixture.

This is then degassed at 120 °C during at least 20 min under primary vacuum. The solids are more and more soluble with the temperature increase. When it reaches 120 °C, the reaction medium becomes a transparent orange solution which is the color of soluble sulfur. A light reflux can be observed by the condensation on the flask wall, up to about 2 cm above the liquid surface. Then, the medium is heated to 310 °C during 30 min under a N_2 flux. This process lasts for about 20 min. The solution color becomes lighter to yellow as the temperature increases. From about 280 °C, the transparent solution becomes visibly turbid with white solid. The reflux is a bit stronger by this moment: some drops are formed at the low of the refrigerant column and fall in the solution from time to time. It may cause some white smoke inside the flask but it disappears very quickly (after about 1 min). After cooling down during about 25 min to around 30 °C, the reaction medium seems to be a little less turbid than when it was at 310 °C.

After cooling down the reaction medium to about between 30 and 40 °C by N_2 flux (during about 25 min), the molecular precursor $Mo(acac)_3$ (35 mg, 0.09 mmol, 0.18 equiv.) is added under N_2 atmosphere. The solid isn't soluble in the reaction medium. The mixture is heated at 310 °C during 30 min under a N_2 flux. With the increase of temperature, the solid is more and more soluble. The color change from brown-red of Mo precursor to black: at 120 °C the solid is totally soluble to make a brown-red solution. As the temperature increases more, the color becomes darker, from about 295 °C, it is totally black. The reflux and white smoke are also observed from 280 °C. During this part, black solid can be seen on the flask wall. After cooling down to room temperature, the reactional medium is recuperated with THF (less than 5 mL) and then mixed with ethanol (10 mL) and centrifuged at 20 °C, 7000 rpm for 10 min. The supernatant here is lightly dark and see-through. The obtained solid (black) is washed three times with THF (about 4 mL) and ethanol (to make 25 mL of solvent mixture). These three supernatants are colorless. Finally, the solid is dried under a N_2 flux during 1 h and ground with a mortar to obtain a powder for analysis.

1.3.2. Synthesis of Mo-containing Gd_2O_2S nanoparticles in one step: $Gd_{2(1-x)}Mo_{2x}O_2S$

In this method, all the precursors are added at the same time at the beginning of the process. We expected to obtain Mo-containing Gd_2O_2S nanoparticles where Mo substitutes some Gd sites in the structure.

The overall amount of metallic precursors (Gd and Mo) is adjusted to 1 equiv. *vs.* Na(oleate), to keep an overall molarity of heavy metals similar to these of the Gd_2O_2S synthesis. **In other**

words, for every mole of Gd removed, one mole of Mo is introduced and the total molarity of both metallic precursors is constant at 0.5 mmol. The calculation of *x* is as below:

$Gd_{2(1-x)}Mo_{2x}O_2S$ $\quad x = \frac{n_{Mo\ introduced}}{0.5}$

0.5: total introduced metallic precursors in mole

x = molar ratio $\frac{Mo}{Gd+Mo}$

= name of sample

$2x$ = theoretical notation index

All the three described protocols below are for samples with ***x* = 0.15**, i.e. the molar ratio Mo/Gd is 0.18. The different choice of *x*'s calculation between this section and 1.3.1 is for an easier notation. The generic formula for all these samples is then **$Gd_{1.7}Mo_{0.3}O_2S$**.

1.3.2.1. Synthesis with Mo(+I) precursor

The mixture of solvents and stabilizers is made with OM (4.54 g, 17 mmol, 34 equiv.), oleic acid (0.72 g, 2.5 mmol, 5 equiv.) and 1-octadecene (8.2 g, 32.5 mmol, 65 equiv.) in a glass three-neck round-bottom flask of 100 mL. Then, in this mixture, the molecular precursor $Gd(acac)_3$ (193.2 mg, 0.425 mmol, 0.85 equiv.) is added with sulfur S_8 (8 mg, 0.03 mmol, 0.5 equiv. in S) and sodium oleate (152 mg, 0.5 mmol, 1 equiv.). The mixture is then agitated and put under N_2 atmosphere at room temperature by three cycles N_2/vacuum for 3 minutes each. The molecular precursor $Cp_2Mo_2(CO)_6$ (18.4 mg, 0.038 mmol, 0.075 equiv.) is then added under N_2 atmosphere. This mixture is degassed at 120 °C during at least 20 min under primary vacuum. The mixture's color change from orange-red to dark orange-red at 120 °C. Then, the medium is heated to 310 °C during 30 min under a N_2 flux. The color changes gradually to black when the temperature increases. Some drops are formed at the low of the refrigerant column and fall in the solution from time to time. It may cause some white smoke inside the flask but it disappears very quickly (after about 1 min). After cooling down the reaction medium, it is recuperated with THF (less than 5 mL) and then mixed with ethanol (10 mL) and centrifuged at 20 °C, 7000 rpm for 10 min. The obtained solid (black) is washed three times with THF (about 4 mL) and ethanol (to make 25 mL of solvent mixture). All the supernatants are dark and get lighter with the washings. The color intensity of the first supernatant increase with the value of *x*. In the case of $x = 0.18$, it's still see-through. Finally, the solid is dried under a N_2 flux during 1 h and ground with a mortar to obtain a powder for analysis.

1.3.2.2. Synthesis with Mo(+VI) precursor

The mixture of solvents and stabilizers is made with OM (4.54 g, 17 mmol, 34 equiv.), oleic acid (0.72 g, 2.5 mmol, 5 equiv.) and 1-octadecene (8.2 g, 32.5 mmol, 65 equiv.) in a glass three-neck round-bottom flask of 100 mL. Then, in this mixture, the molecular precursor $Gd(acac)_3$ (193.2 mg, 0.425 mmol, 0.85 equiv.) and the precursor $MoO_2(acac)_2$ (24.5 mg, 0.075 mmol, 0.15 equiv.) are added with sulfur S_8 (8 mg, 0.03 mmol, 0.5 equiv. in S) and sodium oleate (152 mg, 0.5 mmol, 1 équiv.). The mixture is then agitated and put under N_2 atmosphere at room temperature by three cycles N_2/vacuum for 3 minutes each. Next, it is degassed at 120 °C during at least 20 min under primary vacuum. The mixture's color change in function of the temperature increase: from orange at ambient temperature to dark orange-red at 120 °C. Then, the medium is heated to 310 °C during 30 min under a N_2 flux. From 170 °C, the medium is black. The reflux starts around 200 °C and from 305 °C, black solid can be seen on flask wall. Some drops can be formed at the low of the refrigerant column and fall in the solution from time to time. It may cause some white smoke inside the flask but it disappears very quickly (after about 1 min). After cooling down the reactional medium, it is recuperated with THF (less than 5 mL) and then mixed with ethanol (10 mL) and centrifuged at 20 °C, 7000 rpm for 10 min. The supernatant at this stage is yellow and transparent. The obtained solid (black) is washed three times with THF (about 4 mL) and ethanol (to make 25 mL of solvent mixture). These three supernatants are colorless. Finally, the solid is dried under a N_2 flux during 1 h and ground with a mortar to obtain a powder for analysis.

1.3.2.3. Synthesis with Mo(+III) precursor

The mixture of solvents and stabilizers is made with OM (4.54 g, 17 mmol, 34 equiv.), oleic acid (0.72 g, 2.5 mmol, 5 equiv.) and 1-octadecene (8.2 g, 32.5 mmol, 65 equiv.) in a glass three-neck round-bottom flask of 100 mL. Then, in this mixture, the molecular precursor $Gd(acac)_3$ (193.2 mg, 0.425 mmol, 0.85 equiv.) is added with sulfur S_8 (8 mg, 0.03 mmol, 0.5 equiv. in S) and sodium oleate (152 mg, 0.5 mmol, 1 equiv.). The mixture is then agitated and put under N_2 atmosphere at room temperature by three cycles N_2/vacuum for 3 minutes each. The molecular precursor $Mo(acac)_3$ (29.5 mg, 0.075 mmol, 0.15 equiv.) is then added under N_2 atmosphere. This mixture is degassed at 120 °C during at least 20 min under primary vacuum. The initial color of the mixture is brown-red, and doesn't changes when the temperature reaches 120 °C. Then, the medium is heated to 310 °C during 30 min under a N_2 flux. The color is changed to black. Some drops are formed at the low of the refrigerant column and fall in the solution from time to time. It may cause some white smoke inside the flask but

it disappears very quickly (after about 1 min). After cooling down the reactional medium, it is recuperated with THF (less than 5 mL) and then mixed with ethanol (10 mL) and centrifuged at 20 °C, 7000 rpm for 10 min. The supernatant at this stage is black. The obtained solid (black) is washed three times with THF (about 4 mL) and ethanol (to make 25 mL of solvent mixture). These three supernatants are colorless. Finally, the solid is dried under a N_2 flux during 1 h and ground with a mortar to obtain a powder for analysis.

1.3.3. Synthesis without Gd precursor

1.3.3.1. Synthesis of $MoOS_{0.5}/Na_a$ with Na(oleate)

1.3.3.1.1. Synthesis with Mo(+VI) precursor and a = 2

The mixture of solvents/stabilizers is made with OM (4.54 g, 17 mmol, 34 equiv.), oleic acid (0.72 g, 2.5 mmol, 5 equiv.), 1-octadecene (8.2 g, 32.5 mmol, 65 equiv.) in a glass three-neck round-bottom flask of 100 mL. Then, in this mixture, the molecular precursor $MoO_2(acac)_2$ (163 mg, 0.5 mmol, 1 equiv.) is added with sulfur S_8 (8 mg, 0.03 mmol, 0.5 equiv.) and sodium oleate (304 mg, 1.0 mmol, 2 equiv.). The orange-brown mixture is then agitated and put under N_2 atmosphere at room temperature by three cycles N_2/vacuum for 3 minutes each. Then it is degassed at 120 °C during at least 20 min under primary vacuum. At this temperature, all solids are soluble to make an orange solution. A reflux is observed. Then, the medium is heated to 310 °C during 30 min under a nitrogen flux. The color is changed totally to black at 160 °C. From 200 °C, a reflux is observed again. After cooling down to room temperature, the reaction medium is viscous, it is recuperated with n-hexane or cyclohexane (less than 5 mL) and then mixed with ethanol (10 mL) and centrifuged at 20 °C, 7000 rpm for 10 min. The supernatant here can be monophasic yellow or biphasic dark colored-colorless, and see-through in all cases. The obtained solid (mostly black) is washed three times with n-hexane or cyclohexane (about 4 mL) and absolute ethanol (to make 25 mL of solvent mix). These three supernatants are colorless. Finally, the solid is dried under a nitrogen flux during 1 h and ground with a mortar to obtain a powder for analysis.

The same protocol was also done for $a = 1$.

Two testing synthesis ($a = 1$ and 2) with Na(acac) (e.g. $a = 2$, 122 mg, 1.0 mmol, 2 equiv.) and two other with Na(citrate) (e.g. for $a = 2$, 214 mg, 1.0 mmol, 2 equiv.) were done for comparison.

1.3.3.1.2. Synthesis with Mo(+I) precursor and a = 1

Only one test was done with this protocol.

The mixture of solvents/stabilizers is made with OM (4.54 g, 17 mmol, 34 equiv.), oleic acid (0.72 g, 2.5 mmol, 5 equiv.), 1-octadecene (8.2 g, 32.5 mmol, 65 equiv.) in a glass three-neck round-bottom flask of 100 mL. Then, in this mixture, sulfur S_8 (8 mg, 0.03 mmol, 0.5 equiv.) and sodium oleate (304 mg, 1.0 mmol, 2 equiv.) are added. The mixture is then agitated and put under N_2 atmosphere at room temperature by three cycles N_2/vacuum for 3 minutes each. This mixture is degassed at 120 °C during at least 20 min under primary vacuum. The mixture's color changes from red to intense orange as the temperature rises. At 80 °C, all solids are soluble to make an orange solution. From 100 °C, a strong reflux is observed. After degassing, the mixture is cooled down to ambient temperature. Then, the molecular precursor $Cp_2Mo_2(CO)_6$ (245 mg, 0.5 mmol, 1 equiv.) is added under N_2 atmosphere. The red mixture is heated to 310 °C during 30 min under a nitrogen flux. The color changes quickly to nearly black at 90 °C. From 150 °C, the medium is totally black. The bubbles are observed from 90 °C to around 240 °C. The reflux is observed from 270 °C. After cooling down to room temperature, the reaction medium is recuperated with THF (less than 5 mL) and then mixed with ethanol (10 mL) and centrifuged at 20 °C, 6000 rpm for 10 min then left still during the night as no solid is seen in the tube. After that, 12.5 mL of methanol is added, centrifuged at 15 °C, 7000 rpm for 20 min. Half of the supernatant is collected by pipette to have the rest of 15 mL. 15 mL of acetone is added to the rest to centrifuge in the same conditions. The supernatant is again collected by pipette to have the rest of 10 mL. 5mL of THF and 15 mL of acetone are added and then centrifuged in the same conditions. This time, as the solid are formed in the tube, all supernatant is collected by pipette. The last washing was with about 2 mL of THF and 15 mL of acetone. Finally, the solid is dried under a nitrogen flux during 1 h. The final solid is black, hard but knead-able.

1.3.3.2. Synthesis of "MoS_2"

1.3.3.2.1. With Mo(+VI) precursor

Only one test was done for this protocol.

The molecular precursor $MoO_2(acac)_2$ (163 mg, 0.5 mmol, 1 equiv.) is added in a glass three-neck round-bottom flask of 100 mL with sulfur S_8 (32 mg, 0.12 mmol, 2 equiv.) with OM (4.54 g, 17 mmol, 34 equiv.) and 1-octadecene (8.2 g, 32.5 mmol, 65 equiv.) as solvents. The mixture is then agitated and put under N_2 atmosphere at room temperature by three cycles N_2/vacuum for 3 minutes each. This mixture is degassed at 120 °C during at least 20 min under primary vacuum. The mixture's color changes from brown and opaque at the beginning to mostly black after 20 min at 120 °C. Then, the medium is heated to 310 °C during 30 min under

a nitrogen flux. From 160 °C, the medium is totally black. The reflux starts at around 230 °C. From 280 °C, grains of solid can be seen in the flask. After cooling down to room temperature, the reaction medium is viscous, it is recuperated with n-hexane (about 10 mL) and then mixed with ethanol (10 mL) and centrifuged at 20 °C, 7000 rpm for 10 min. The supernatant here is lightly yellow, the solid doesn't stick well on the tube wall. Hence, the supernatant is collected by pipette to have a rest of 22 mL. 10 mL of n-hexane is added and the whole is divided into 2 tubes. 5 mL of methanol is added to each tube and then centrifuged for 20 min. A maximum of supernatant is collected by pipette. 15 mL of n-hexane and 5 mL ethanol are added to each tube and centrifuged for 45 min at 15 °C. A maximum of biphasic supernatant is collected by pipette. 18 mL of n-hexane and 5 mL ethanol are added to each tube then the whole is divided into 4 tubes. About 5 mL of THF is added into each tubes and left still during the night. After that, the mixture in 4 tubes is decanted to concentrate into 8 mL of all. 10 mL of THF and 5 mL of methanol are added, the whole is divided into two tubes and left still during 2 days to have the solid falling down to the bottom of the tubes. The supernatant in each tube is then collected at maximum, leaves about 3mL of mixture. 15mL of acetone and 5 mL of ethanol are added then centrifuged for 10 min at 20 °C. The supernatant is collected by pipette and the rest is dried under N_2 flux to obtain the final black solid. All supernatants are transparent. At first the color was yellow but after some washing, it becomes colorless at the end.

1.3.3.2.2. With Mo(+I) precursor

Two tests were done with this precursor. The difference in protocol is only for one synthesis, the solvent mixture is OM and ODE and for the other, only ODE was used.

Sulfur S_8 (32 mg, 0.12 mmol, 2 equiv.) is added in a glass three-neck round-bottom flask of 100 mL with 1-octadecene (9.3 mg, 37 mmol, 74 equiv.) as solvent. The mixture is then agitated and put under N_2 atmosphere at room temperature by three cycles N_2/vacuum for 3 minutes each. S_8 is totally soluble to make a colorless solution. The molecular precursor $Cp_2Mo_2(CO)_6$ (122.5 mg, 0.25 mmol, 1 equiv.) is added under N_2 atmosphere. This mixture is degassed at 120 °C during at least 20 min under primary vacuum. At 100 °C, white smoke is observed in the flask. Then, the medium is heated to 310 °C during 30 min under a nitrogen flux. At 230 °C, more smoke is observed and the mixture is black. At 260 °C, big aggregates are observed in the flask. After cooling down to room temperature, the reaction medium is recuperated with THF (less than 5 mL) and then mixed with ethanol (10 mL) and centrifuged at 20 °C, 7000 rpm for 10 min. The supernatant at this point is biphasic, dark but see-through. The obtained solid (black) is washed one more time with THF (about 4 mL) and ethanol (to

make 25 mL of solvent mix) and centrifuged at 15 °C. After taking out the colorless supernatant, the solid is dried under a nitrogen flux during 1 h and ground with a mortar to obtain a powder for analysis.

The same synthesis was also done with a mixture of solvents: OM (4.54 g, 17 mmol, 34 equiv.) and 1-octadecene (8.2 g, 32.5 mmol, 65 equiv.). The washing process was easier. After cooling down to room temperature, the reaction medium is recuperated with THF (less than 5 mL) and then mixed with ethanol (10 mL) and centrifuged at 20 °C, 7000 rpm for 10 min. The supernatant here is yellow and see-through. The black solid is washed three more times with THF (about 4 mL) and ethanol (to make 25 mL of solvent mix). These supernatant are colorless. Finally, the solid is dried under a nitrogen flux during 1 h and ground with a mortar to obtain a powder for analysis.

1.3.3.2.3. With Mo(+III) precursor

Only one test was done with this protocol.

Sulfur S_8 (16 mg, 0.06 mmol, 2 equiv.) is added in a glass three-neck round-bottom flask of 100 mL with OM (4.54 g, 17 mmol, 34 equiv.) and 1-octadecene (8.2 g, 32.5 mmol, 65 equiv.) as solvents. The mixture is then agitated and put under N_2 atmosphere at room temperature by three cycles N_2/vacuum for 3 minutes each. S_8 is totally soluble to make a colorless solution. The molecular precursor $Mo(acac)_3$ (98.6 mg, 0.25 mmol, 1 equiv.) is added. The mixture is then agitated and put under N_2 atmosphere at room temperature by three cycles N_2/vacuum for 3 minutes each. This mixture is degassed at 120 °C during at least 20 min under primary vacuum. At this temperature, the medium is already black. Then, the medium is heated to 310 °C during 30 min under a nitrogen flux. At 310 °C, many big aggregates are formed on the flask wall. After cooling down to room temperature, the reaction medium is recuperated with THF (less than 5 mL) and then mixed with ethanol (10 mL) and centrifuged at 20 °C, 7000 rpm for 10 min. The supernatant is yellow and see-through; the black solid doesn't stick well on the tube wall. The supernatant is collected by pipette to have a rest of 5 mL. Ethanol is added to have a total of 25 mL. After the centrifugation, the solid still doesn't stick well on the tube, the colorless supernatant is taken out carefully. The solid is washed two more times with THF (about 4 mL) and ethanol (to make 25 mL of solvent mix). Finally, the solid is dried under a nitrogen flux during 1 h to have a final pasty product.

2. Analysis methods

2.1. Energy-dispersive X-ray Spectroscopy (EDS)

EDS analyses were performed on a SEM HITACHI S-3400N at 10 kV. Cobalt was chosen as reference for quantitative calibration of the machine. For each sample, three or five different zones were analyzed. About 2 mg of sample is fixed on the plot by carbon tape. A carbon layer of about 20 nm is then deposed on the surface of the sample for conduction by an evaporator from the laboratory. All the preparation process is in free air. For samples isolated in the glovebox, the preparation of plot is done inside the glovebox but then it is kept in free air for the deposition of carbon because by this method, we only quantify the elements but not their oxidation state.

2.2. X-ray Diffraction (XRD)

The X-ray diffraction patterns of dry powders were measured on a Bruker D8 diffractometer using Cu Kα radiation ($\lambda_1 = 1.5406$ Å, $\lambda_2 = 1.5444$ Å) on reflexing mode. Typical diffractograms were collected between 10 ° and 90 ° (2θ) with steps of 0.05 ° and a scanning speed of 1 s/point. For further analysis on peak shift, the diffractograms are collected between 20 ° and 60 ° (2θ) with steps of 0.025 ° and a scanning speed of 10 s/point to increase significantly the signal/noise ratio. The backgrounds of the patterns were subtracted using the EVA software. In the case where the powder quantity is small, loading it on a normal sample holder can cause a destruction of sample surface which then causes a peak shift in diffractograms. To prevent this problem, we used an adapted kind of sample holder (Figure 2C).

2.3. Pair Distribution Function analysis (PDF)

The PDF measurements of dry powders were measured on a Bruker D8 diffractometer using Mo Kα radiation ($\lambda_1 = 0.7093$ Å, $\lambda_2 = 0.7136$ Å) in transmission mode with a focusing Göbel mirror and a LYNXEYE detector (Figure 2A). The samples were loaded in thin-walled (0.01 mm) capillaries of borosilicate glass with the size adapted to the sample's quantity (Figure 2B). The

most frequent size is 1 mm of diameter. For some samples of too low quantity, the capillaries of 0.5 mm of diameter were used. The blank capillaries of both sizes are measured frequently to increase the accuracy of background subtraction.

Measurements were performed from Q_{min} = 0.12 Å^{-1} to Q_{max} = 17.0 Å^{-1} ($Q = 4\pi \sin\frac{\theta}{\lambda}$) with sample rotation around its elongation axis while the detector turns around it (from $2\theta_i$ = 0.8 ° to 150 °). The counting parameters evolves in function of Q-range during the analysis to optimize the counting rate at high Q. The final pattern was thus obtained from the combination of 7 component patterns, converted in counts per second, with the following parameters $2\theta_i$ (°) – $2\theta_f$ (°) – step size (°) – step time (s): 0.8 – 31 – 0.02 – 2, 29 – 61 – 0.04 – 6, 59 – 91 – 0.06 – 15, 89 – 121 – 0.1 – 40 (twice) and 119 – 150 – 0.1 – 100 (twice). The total duration is 34 hours. The empty capillaries were measured in the same conditions.

Raw data were treated using the PDFgetX3 program.[3] Standard corrections were applied to the total scattering data. After a normalization step, they were reduced into the structure function. The experimental PDF G(r) is finally obtained by a Fourier Transform (FT).

PDF calculations are from structural models by Capucine Sassoye, Alex Lemarchand and Mohamed Selmane from laboratory. The simulated profiles were calculated using the PDFgui software with periodic boundary conditions.[4]

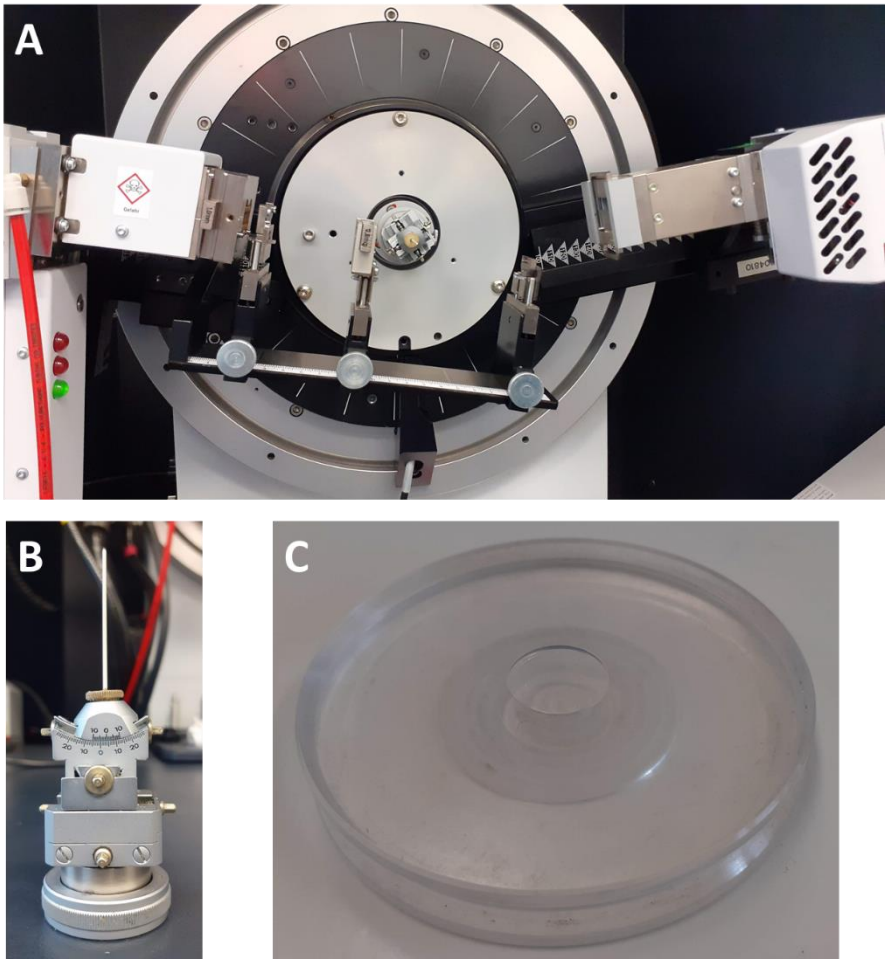

Figure 2 (A) Diffractometer Bruker D8 used for PDF measurements in transmission mode in capillary. (B) A capillary filled with sample fine powder in its support. (C) A sample holder for XRD measurement for small quantity samples.

2.4. Transmission Electronic Microscopy (TEM)

The Tecnai Spirit 2, a 20-120 kV / LaB_6 Transmission Electronic Microscope, is a general-purpose, high-resolution instrument. It was used to investigate the morphology of nanoparticles at 120 kV. The sample was deposed on an amorphous carbon-coated copper grid by drop-casting method. The suspension of nanoparticles was made from about 1 mg of sample in about 0.5 mL of THF sonicated during 15 to 20 minutes. After the suspension deposition, the grid was allowed to dry in free air during about 20 min.

ImageJ was used to analyze the TEM images, in order to find the periodic distances representing the crystalline structure.

3. Synchrotron-based techniques

At the SOLEIL synchrotron facility, the analyses were conducted using an electron energy of 2.7 GeV and an average ring current of 450 mA.

We had access to SAMBA and LUCIA Beamlines for X-ray Absorption (XAS) analysis and to TEMPO-B Beamline for Near Ambient Pressure-X-ray Photoelectron Spectroscopy (NAP-XPS). XAS is combined by X-ray Absorption Near Edge Structure (XANES) and Extended X-ray Absorption Fine Structure (EXAFS). On LUCIA Beamline, XANES spectra of Mo at $L_{2,3}$-edge and S at K-edge are done at the same time. On SAMBA Beamline, both XANES and EXAFS spectra of Mo are registered. All of them provide complementary information on local environment of Mo, S and also their oxidation states in different samples.

3.1. PDF on CRISTAL Beamline

CRISTAL is an undulator-based multi-technique diffraction beamline, dedicated to studies of the structural properties of condensed matter, on different length and time scales, possibly in non-ambient conditions. In our case, the PDF analysis on powders was done in capillaries at $\lambda = 0.5129$ Å during a much shorter time of 2 h (instead of 34 h as in LCMCP).

The preparation of samples is strictly similar to the PDF analysis in LCMCP as described above. Since the Q_{max} provided by the grand instrument at SOLEIL is higher than that of the LCMCP equipment, the signal quality obtained at SOLEIL is higher than at LCMCP: higher peak intensity with less oscillations. For a comparison of experimental curves, see Annex 2.

Both the analysis and the data treatment are done by Capucine Sassoye and Alex Lemarchand from laboratory.

3.2. XANES analysis on LUCIA Beamline[5]

LUCIA (Line for Ultimate Characterization by Imaging and Absorption) Beamline has a "tender" X-ray source (0.8-8 keV). The energy range offered by the beamline corresponds to the best performances of SLS and SOLEIL in terms of brilliance. It allows XAS experiments at the K edge of elements from Na to Fe, L edges from Ni to Gd, and M edges of rare earths and actinides. In our case, this technique is chosen due to its possibility of measurements at Mo $L_{3,2}$-edge and S K-edge not only in pellet but also in an in situ electrochemical cell where the membrane size is only 1×1 mm.

The size of X-ray source is 2 × 2 mm, it can be adjusted by 2 movable slits to adapt to the size of samples (pellet or membrane). The spectra are registered in fluorescence mode from

2420 eV (just before the absorption of Mo L_3-edge) to 2660 eV (just after the XANES part of S K-edge).

The pellets (size 6 mm) are made from a mixture of 4 mg of nanoparticles diluted in 40 mg of graphite, compressed under 2 tons' pressure. They are then fixed on a copper plate by carbon tape, maximum 9 pellets on the same plate (Figure 3). As the source is not energetic: the working range is from 2420 eV to 2660 eV, it cannot penetrate an electrode in glassy carbon. Hence, the electrode used in electrochemical cell is made from Si_3N_4 of only 200 nm thick. This facilitates the penetration of X-ray to hit the sample then going back to hit the detector (detailed description in the next part).

During the measurement, the inner pressure is maintained around 10^{-2} mbar (primary vacuum). The entering electrons are chosen with a Si(111) monochromator and the outgoing ones are collected with a Bruker Si fluorescence detector. Before all data treatments, all the spectra are calibrated to the first peak at S K-edge of thiosulfate (2470.8 eV).[5]

All preparations were done in free air.

Figure 3 Pellets on holder for measurements on LUCIA Beamline.

3.3. XAS analysis on SAMBA Beamline[6]

SAMBA (**S**pectroscopy **A**pplied to **M**aterial **B**ased on **A**bsorption) Beamline has a "hard" X-ray source. The optics design is optimized in order to be very versatile and to cover the 4.5-43 keV energy range with a high flux of photons and stability and optimum energy resolution. A 35 pixels HPG fluorescence detector is available since 2012 for measurements on highly diluted specimens. The spectra are registered from 19.850 keV to 21 keV to have both XANES and EXAFS parts at Mo K-edge.

On this beamline, we can measure the samples not only in pellet but also in an adapted electrochemical cell with a very small deposed amount of ink, i.e. very small amount of material available. The pellets were made in the same method as being used on LUCIA Beamline but with 2 mg of nanoparticles instead of 4 mg for LUCIA Beamline. The X-ray source here is highly energetic, it can penetrate easily a glassy carbon plates of 500 μm, hence, there is not much difference from electrochemical setup here and in LCMCP (detailed description in the next part).

All samples were measured in free air and there is no calibration needed before data treatment of spectra.

Figure 4 Pellets on holder for measurements on SAMBA Beamline.

3.4. NAP-XPS on TEMPO-B Beamline

The NAP-XPS spectra were done on TEMPO-B (**T**ime resolved **E**xperiments on **M**aterials with **P**hot**O**electron spectroscopy-B) Beamline. It covers the photon energy range between 50 eV and 1500 eV which is particularly well suited for magnetic materials studies and for chemistry applications. The whole range of K edges (C, O, N, F 1s) of organic molecules, the 4th period transition metal L (2p) edges of transition metals (with applications to metal-organic molecules and metal surfaces), and M edges of rare earths is covered. Moreover, on this Beamline, we are able to pump gases in the chamber during the measurements to study the

material surface's activity towards these gases.

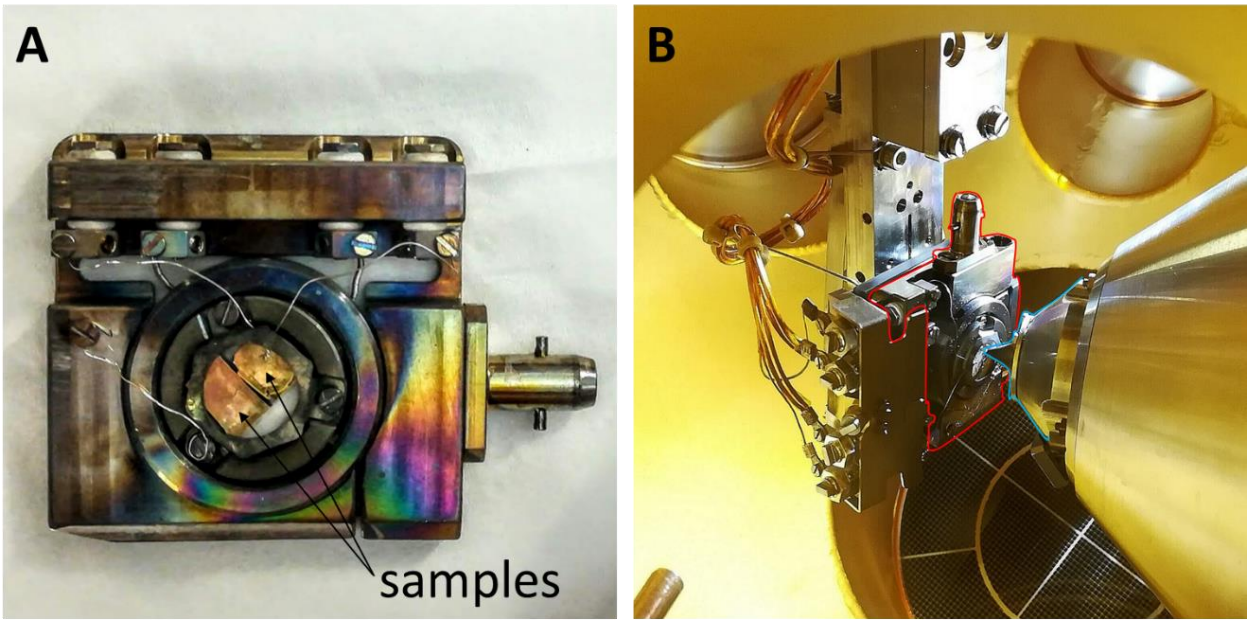

Figure 5 (A) Sample holder with 2 samples loaded. (B) Samples loaded in the sample holder (contoured in red) in the vacuum chamber with the point (contoured in blue) on its surface just before a run.

In our case, on this Beamline, we collected spectra of some chosen samples and their surface state change under 2 mbar of $O_2/H_2/CO_2/H_2O$ with or without heating. The samples were deposed on a 50-nm-gold-coated Si wafer by drop casting: deposition of 100 µL from a suspension of 0.5 mg of nanoparticles in 0.5 mL of THF (Figure 5A). For samples treated in glovebox, their initial state is pasty, a small amount of paste was taken with a spatula, diluted with some drop of THF and deposed on the support. In order to mitigate beam damage, measurements were performed on several spots on the sample surface.

The data treatment was performed by Alexy P. Freitas from our research group.

4. Oxygen Reduction Reaction electrochemical tests

The materials were studied in Oxygen Reduction Reaction (ORR) in basic media:

$$O_2 + 4e + 2\,H_2O \xrightarrow{\text{electrocat.}} 4OH^-$$

Three-electrode setup system, which contains a working electrode, a counter-electrode and a reference electrode, was employed. The electrolyte used was KOH 0.1 M solution freshly prepared every day from solid KOH (> 85 %, Sigma Aldrich).

For ink preparation, Nafion 117 solution 5 wt% in alcohols and water (Sigma Aldrich), absolute ethanol (VWR) and hydrophilized acetylene black (C black, Alfa Aesar, 99.9 %, 75 m^2/g) were employed. For the hydrophilization (performed by Madeleine Han), 0.5 g of C black was treated in 50 mL of HNO_3 20 % at 80 ºC under stirring overnight, followed by centrifugation, washing with water and vacuum drying.[7] Molybdenum disulfide powder (90 nm) (MoS_2, 99 %, Sigma-Aldrich) was used as reference.

4.1. Activity evaluation tests done in LCMCP on rotating disk electrode (RDE)

4.1.1. Experiment setup

The electrochemical tests performed by this methodology represent *ex situ* experiments. They were performed in a three-electrode setup using a rotating disk electrode (RDE) made of glassy carbon (GC), Ag/AgCl in saturated KCl and a Pt wire as working, counter and reference electrodes, respectively (Figure 6B). The rotating speed of the working electrode was 1600 rpm (Figure 6A). Before the tests, the electrolyte was saturated with O_2 by bubbling during at least 30 min. During the reaction, O_2 was blown on the surface of electrolyte in order to maintain the concentration of O_2 in the solution.

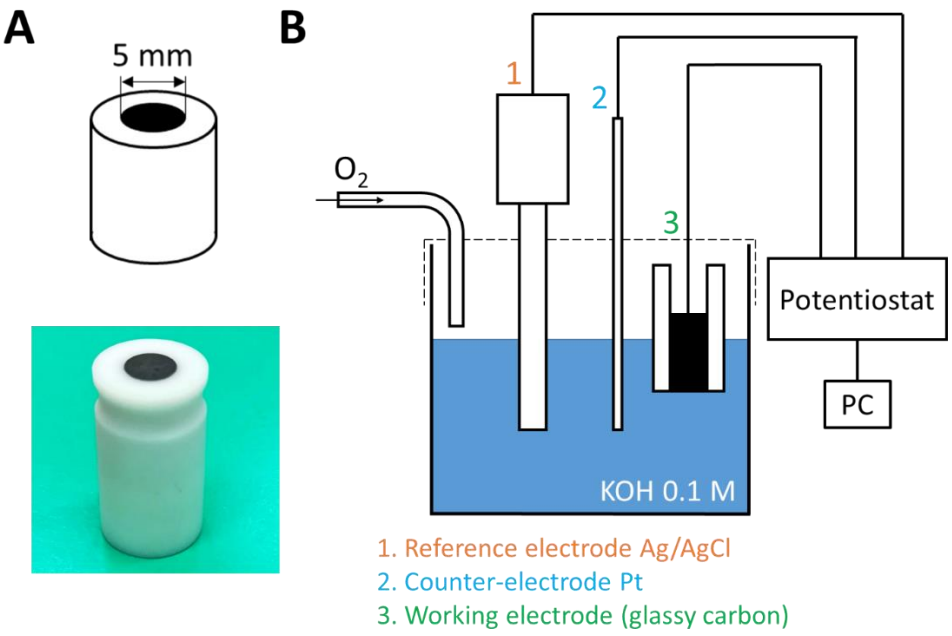

Figure 6 (A) RDE and (B) three-electrode system used for electrochemical tests in LCMCP.

4.1.1.1. Ink preparation

4 types of inks were prepared for different objectives. All of them have the same ratio between the Nafion solution and C black (43.5 µL of Nafion solution is added for each 1 mg of nanoparticles).

1) Classical ink (noted "*Cx1*"): 10 mg of sample and 10 mg of C black were dispersed in 10 mL of absolute ethanol during 2 hours by sonication. Then, 435 µL of Nafion 5 wt% solution was added and the mixture was sonicated during 30 min.
    - Nanoparticles concentration: 1 mg/mL
    - C black concentration: **1** mg/mL
2) Ink with C black doubled (noted "*Cx2*"): 10 mg of sample and 20 mg of C black were dispersed in 10 mL of absolute ethanol during 2 hours by sonication. Then, 870 µL of Nafion 5 wt% solution was added and the mixture was sonicated again, during 30 min.
    - Nanoparticles concentration: 1 mg/mL
    - C black concentration: **2** mg/mL
3) Ink with C black tripled (noted "*Cx3*"): 10 mg of sample and 30 mg of C black were dispersed in 10 mL of absolute ethanol during 2 hours by sonication. Then, 1.305 mL of Nafion 5 wt% solution was added and the mixture was sonicated during 30 min more.
    - Nanoparticles concentration: 1 mg/mL
    - C black concentration: **3** mg/mL
4) Inks from nanoparticles suspensions with double amount of C black (noted "*NPS*"): 10 mg of sample were dispersed in 10 mL of absolute ethanol and 870 µL of Nafion 5 wt% solution during 1 hour. The suspension was either used fresh or left ageing during 2 weeks. Then, 20 mg of C black were added and the mixture was sonicated during 2 hours more.
    - Nanoparticles concentration: 1 mg/mL
    - C black concentration: **2** mg/mL

More than one deposition can be made with the same ink. To lower the aggregates of C black and/or nanoparticles in the ink, before the deposition, it was sonicated during about 30 min.

The inks *Cx1* were made first to evaluate the materials' activity. The inks *Cx2* and *Cx3* were made later to investigate the effect of higher amount of C black on the conductivity and the behavior of the materials during the reaction. The *NPS* inks were prepared to understand the origin of activity loss of the materials after aging in free air. The comparison of activity between these two inks will reveal if the origin of the activity loss is from the ageing of nanoparticles in free air or from the aggregation of C black.

4.1.1.2. Working electrode preparation

The working electrode preparation procedure contains 3 parts: polishing, washing by sonication and drying. Firstly, it was polished during 8 min with a diamond suspension (1 µm, BAS Inc.) followed by 8 min polishing with a 50 nm diamond suspension (BAS Inc.). Next, it was sonicated during about 5 min to clean the electrode. Finally, it was clean with a Kimtech paper and dried under a small beaker to protect it from dust during 30 min before the naked electrode test. The procedure will be repeated until the CV of naked electrode fulfills the conditions: half-wave potential $E_{1/2}$ is -0.38 ± 0.01 V and maximum current I_{max} is -0.21 ± 0.02 V. Once the naked electrode was validated, the electrode is rinsed thoroughly with water and absolute ethanol before deposing 5 µL of ink and drying.

After that, the film was wetted with some drops of the electrolyte to prevent the adherence of air bubbles in the electrolyte.

4.1.2. Measuring protocol

After saturating the electrolyte with O_2 by bubbling during 30 min and wetting the film for 5 min, the electrode is connected at the electrocatalytic setup (Figure 6B) and left spinning in the electrolyte during 2 to 3 min to assure good wetting and to remove the bubbles on the surface.

During all the measurements, the O_2 flux was maintained on the surface of the electrolyte to assure the maximum O_2 concentration in electrolyte. After finishing a program of 10 to 15 min long, a waiting time of about 10 min of free O_2 bubbling can be added to remit the concentration in the electrolyte.

The working range for cyclic voltammetry (CV) and linear sweep voltammetry (LSV) is from 0 V to -0.6 V *vs.* Ag/AgCl in saturated KCl at the scan rate of 10 mV/s. The raw data collected was normalized to the geometrical surface of GC disk (0.196 cm^2) before tracing curves with Origin for comparisons. Other normalizing methods are discussed more in detail in Chapter II.

For representation of the potential in figures, the electrode reference is converted to Reversible Hydrogen Electrode (RHE) by adjusting +0.964 V to all electrochemical curves.

After finishing all the measurements, the raw data is exported to .txt files for data treatments with Origin software. The deposition is wiped down carefully with a Kimtech paper and ethanol before starting the preparation procedure as above.

4.2. Electrochemical tests at Synchrotron SOLEIL in adapted setups

The idea of *in situ* tests done at Synchrotron SOLEIL on two Beamlines, SAMBA and LUCIA, is to understand the nature of Mo before, during and after electrochemical reaction. On SAMBA Beamline, we studied Mo at K-edge and on LUCIA Beamline, we studied both Mo at $L_{3,2}$-edge and S at K-edge. All the setups were designed and adapted for each Beamline by Benedikt LASSALLE-KAISER.[8,9] As these tests are very delicate, our work was considered as the first phase of method developing and optimization.

4.2.1. Electrochemical tests on SAMBA Beamline with GCE

4.2.1.1. Setup and electrode preparation

Glassy carbon plate was used as a working electrode because the X-ray source on this Beamline can go through the GCE without any problem (90 % of transmission for a 500 µm thick GCE). The setup was close to the setup in LCMCP (Figure 7) in which the cell was bottle-like with a hole for fixing the working electrode near the bottom. Its cap had 3 holes to fix 2 other electrodes in the system and O_2 entry.

Pt wire and Ag/AgCl in saturated KCl were used as counter and reference electrodes, respectively. The working electrode consisted in a glassy carbon plate (2.5 cm × 1 cm × 500 µm) affixed to the cell with an epoxy glue (LOCTITE DOUBLE BUBBLE) and changed after each deposition. Once the glue was dried, the ink was deposed on the electrode and left to dry during 30 min in free air.

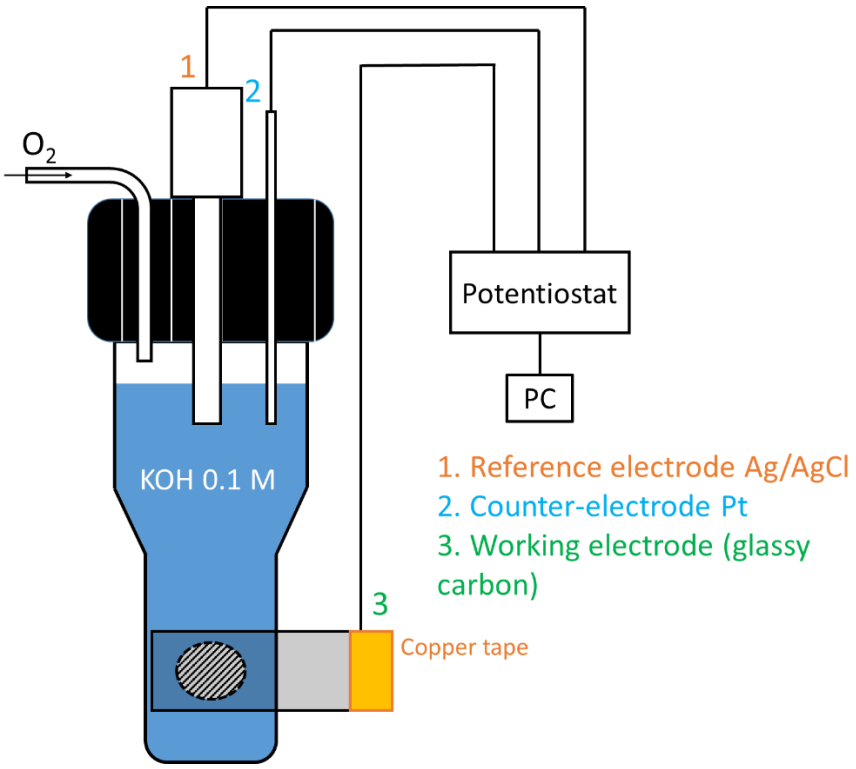

Figure 7 Three-electrode system used on SAMBA Beamline, designed by Benedikt Lassalle-Kaiser.

4.2.1.2. Ink preparation

The ink ingredients were the same as the inks made in LCMCP but with different compositions for optimization of signal/noise ratio.

INK1: for a $Gd_2O_2S/Mo_{0.36}$ sample, a "$MoO_{3.5}S_{0.5}/Na_2$" sample and commercial MoS_2 90 nm reference: prepared as inks *Cx1*.

INK2: for a "$MoO_{3.5}S_{0.5}/Na_2$"sample: having the same nanoparticles concentration as inks *Cx1* but without Nafion added.

INK3: for a $Gd_2O_2S/Mo_{0.36}$ sample, a "$MoO_{3.5}S_{0.5}/Na_2$" sample and commercial MoS_2 (90 nm) reference: prepared in 1 mL of absolute ethanol, with 1 mg of C black and 10 times less Nafion (4.8 µL) than inks made in LCMCP. The quantity of sample for each ink was:

$Gd_2O_2S/Mo_{0.36}$ 10 times more concentrated: 10 mg product. In this ink, the product is not well dispersed, there are still some aggregates.

"$MoO_{3.5}S_{0.5}/Na_2$" and MoS_2 5 times more concentrated: 5 mg product.

INK4: for a $Gd_{1.7}Mo_{0.3}O_2S$ sample: 4 times more concentrated and Nafion 10 times diluted: 4 mg product, 1 mg black C and 4.8 µL Nafion in 1 mL EtOH absolute. In this ink, the product is not very well dispersed, the deposition is not homogenous.

4.2.2. Electrochemical tests on LUCIA Beamline with a gold-coated Si_3N_4 membrane as electrode

4.2.2.1. Setup and electrode preparation

The X-ray source on LUCIA Beamline is considered as "tender" which means that it can be easily absorbed by GCE and a primary vacuum chamber is needed. The setup needs to be modified to adapt to measure conditions.

The electrochemical cell (Figure 8A-B) has both counter and reference electrode which consist in Pt wires, the working electrode was a gold-coated Si_3N_4 membrane supported on Si. The size of Si frame is 1.0 cm × 1.0 cm × 525 µm (thickness) while the size of the membrane is 2 mm × 2 mm × 200 nm (thickness) (Figure 8C). The very limited thickness of the membrane provokes the setup's high fragility and the delicacy of the experiments. The gold-coating was done in LCMCP with a metallator Q150T ES from Quorum Technologies. The Si_3N_4 membranes were firstly coated with 5 nm of titanium for adherence and then 10 nm of gold for electrical conduction. The current needed for Ti and Au coatings are 100 mA and 25 mA respectively. The coatings' thicknesses were controlled by a probe integrated inside the vacuum chamber of the machine.

Because of the membrane's fragility, the electrolyte was saturated with O_2 before being pumped into the cell. During the spectroscopy measurement, the pumping was stopped to avoid the noise due to dynamical effect of liquid flux and too high pressure on the fragile membrane. After each measurement, the inner electrolyte was renewed to recuperate the O_2 saturation in the cell.

The real volume of the cell is only 2.5 µL approximately. The tiny volume in addition with the membrane's fragility caused an additional problem of electrolyte pumping speed: it had to be high enough to fill up the cell without leaving an air bubble while being low enough to not to break the membrane. We also tried to pre-fill the cell up before assembling all the parts. Unfortunately, this method caused a damage of electrical contact in the cell.

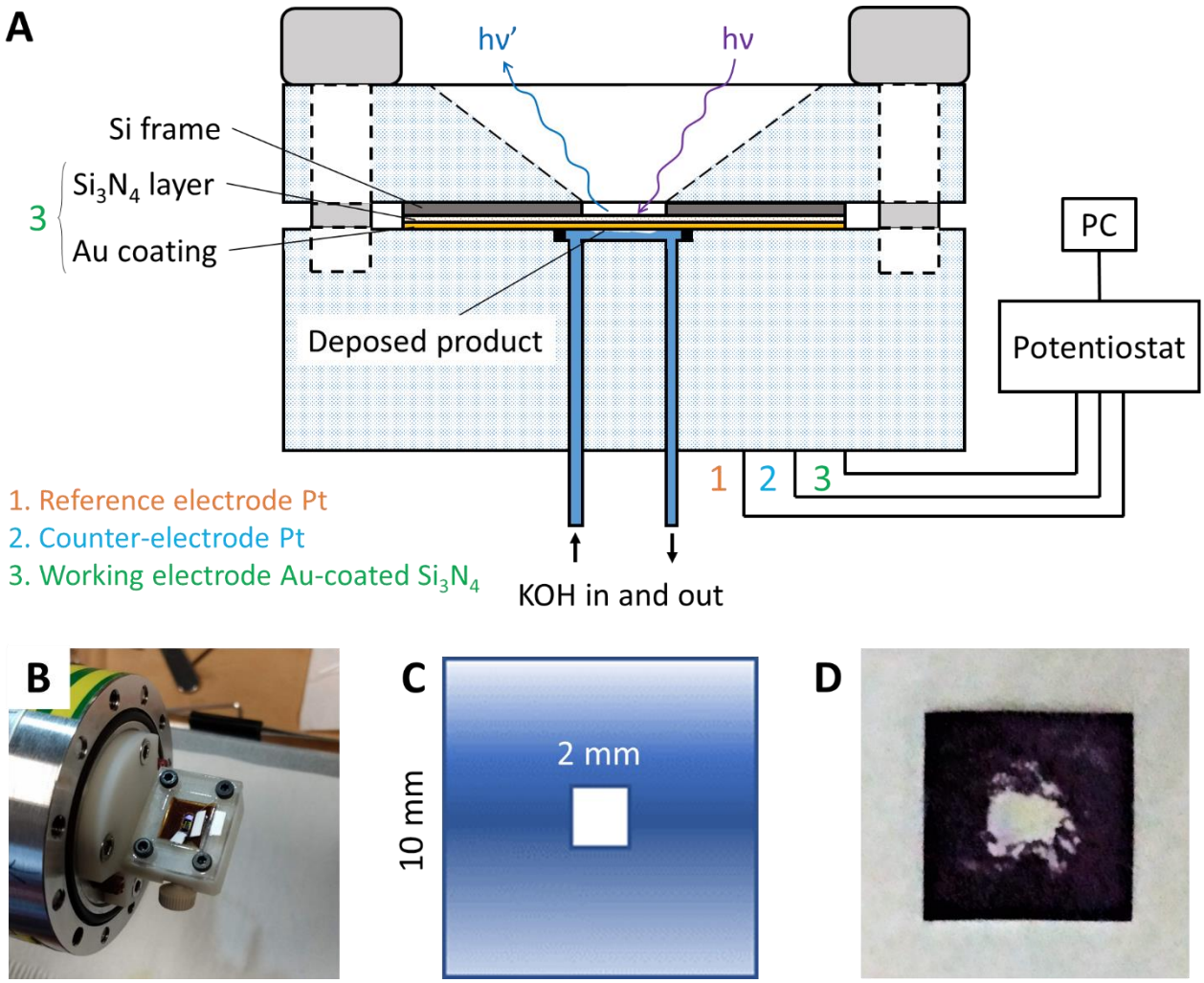

Figure 8 (A) Three-electrode system used on LUCIA Beamline, designed by Benedikt LASSALLE-KAISER. (B) Photo of the cell already assembled, ready to be installed in vacuum chamber. (C) Illustration of working electrode. (D) Photo of a working electrode with a deposition.

4.2.2.2. Ink preparation

Because of the low penetration of X-ray source, the ink made for this electrode was simplified to prevent the signal loss by the absorption of other materials and to increase the signal/noise ratio. The nanoparticles were deposed directly on the membrane (Figure 8D). Around 2 mg of sample were wetted in a dozen of drops of absolute ethanol and then divided into 2 depositions.

5. References

(1) Larquet, C.; Klein, Y.; Hrabovsky, D.; Gauzzi, A.; Sanchez, C.; Carenco, S. Tunable Magnetic Properties of (Gd,Ce) 2 O 2 S Oxysulfide Nanoparticles. *Eur. J. Inorg. Chem.* **2019**, *2019* (6), 762–765. https://doi.org/10.1002/ejic.201801466.

(2) Ding, Y.; Gu, J.; Ke, J.; Zhang, Y.-W.; Yan, C.-H. Sodium Doping Controlled Synthesis of Monodisperse Lanthanide Oxysulfide Ultrathin Nanoplates Guided by Density Functional Calculations. *Angew. Chemie Int. Ed.* **2011**, *50* (51), 12330–12334. https://doi.org/10.1002/anie.201105025.

(3) Juhás, P.; Davis, T.; Farrow, C. L.; Billinge, S. J. L. PDFgetX3: A Rapid and Highly Automatable Program for Processing Powder Diffraction Data into Total Scattering Pair Distribution Functions. *J. Appl. Crystallogr.* **2013**, *46* (2), 560–566. https://doi.org/10.1107/S0021889813005190.

(4) Farrow, C. L.; Juhas, P.; Liu, J. W.; Bryndin, D.; Boin, E. S.; Bloch, J.; Proffen, T.; Billinge, S. J. L. PDFfit2 and PDFgui: Computer Programs for Studying Nanostructure in Crystals. *J. Phys. Condens. Matter* **2007**, *19* (33). https://doi.org/10.1088/0953-8984/19/33/335219.

(5) Vantelon, D.; Trcera, N.; Roy, D.; Moreno, T.; Mailly, D.; Guilet, S.; Metchalkov, E.; Delmotte, F.; Lassalle, B.; Lagarde, P.; et al. The LUCIA Beamline at SOLEIL. *J. Synchrotron Radiat.* **2016**, *23* (2), 635–640. https://doi.org/10.1107/S1600577516000746.

(6) Belin, S.; Briois, V.; Traverse, A.; Idir, M.; Moreno, T.; Ribbens, M. SAMBA a New Beamline at SOLEIL for X-Ray Absorption Spectroscopy in the 4-40 KeV Energy Range. *Phys. Scr. T* **2005**, *T115*, 980–983. https://doi.org/10.1238/Physica.Topical.115a00980.

(7) Gonell, F.; Sanchez-Sanchez, C. M.; Vivier, V.; Méthivier, C.; Laberty-Robert, C.; Portehault, D. Structure-Activity Relationship in Manganese Perovskite Oxide Nanocrystals from Molten Salts for Efficient Oxygen Reduction Reaction Electrocatalysis. *Chem. Mater.* **2020**, acs.chemmater.0c00681. https://doi.org/10.1021/acs.chemmater.0c00681.

(8) Cheaib, K.; Maurice, B.; Mateo, T.; Halime, Z.; Lassalle-Kaiser, B. Time-Resolved X-Ray Absorption Spectroelectrochemistry of Redox Active Species in Solution. *J. Synchrotron Radiat.* **2019**, *26*, 1980–1985. https://doi.org/10.1107/S1600577519013614.

(9) Gorlin, Y.; Lassalle-Kaiser, B.; Benck, J. D.; Gul, S.; Webb, S. M.; Yachandra, V. K.; Yano, J.; Jaramillo, T. F. In Situ X-Ray Absorption Spectroscopy Investigation of a Bifunctional Manganese Oxide Catalyst with High Activity for Electrochemical Water Oxidation and Oxygen Reduction. *J. Am. Chem. Soc.* **2013**, *135* (23), 8525–8534. https://doi.org/10.1021/ja3104632.

Annexes

Table of contents

1. XRD at small angles of Gd_2O_2S/Mo_0

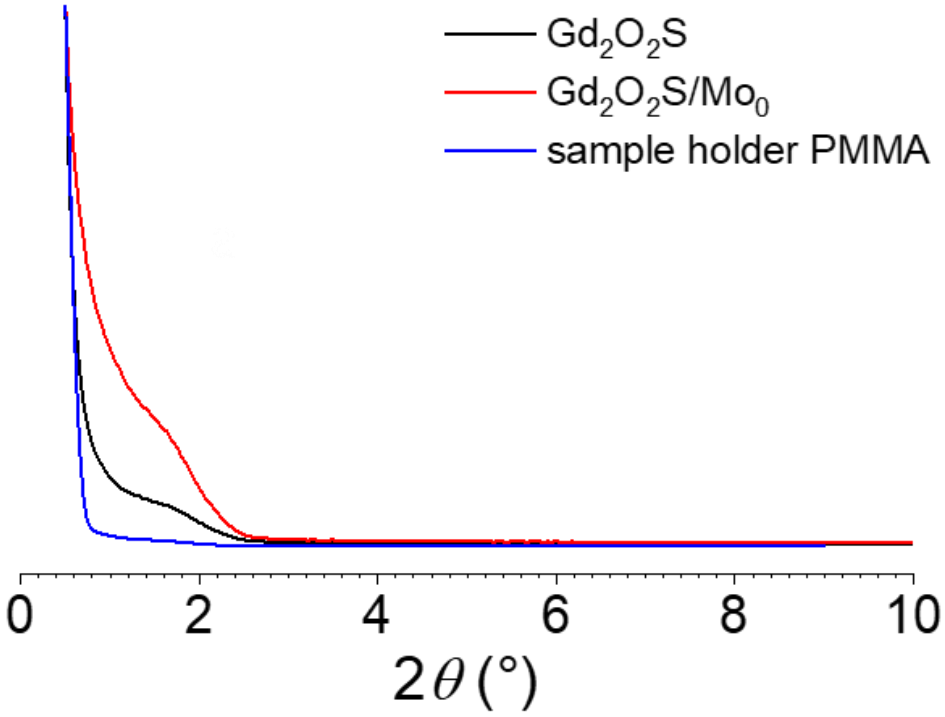

Figure 1 XRD patterns at small angles of (A) Gd_2O_2S nanoparticles, (B) Gd_2O_2S/Mo_0 nanoparticles and (C) sample holder PMMA.

No macro-structure is observed for any synthetic samples. Also, the inter-planar distance of 8.0 Å is not observed. This confirms that this is not an inter-reticular distance.

2. Comparison of PDF patterns by laboratory equipment and by large instrument at SOLEIL Synchrotron

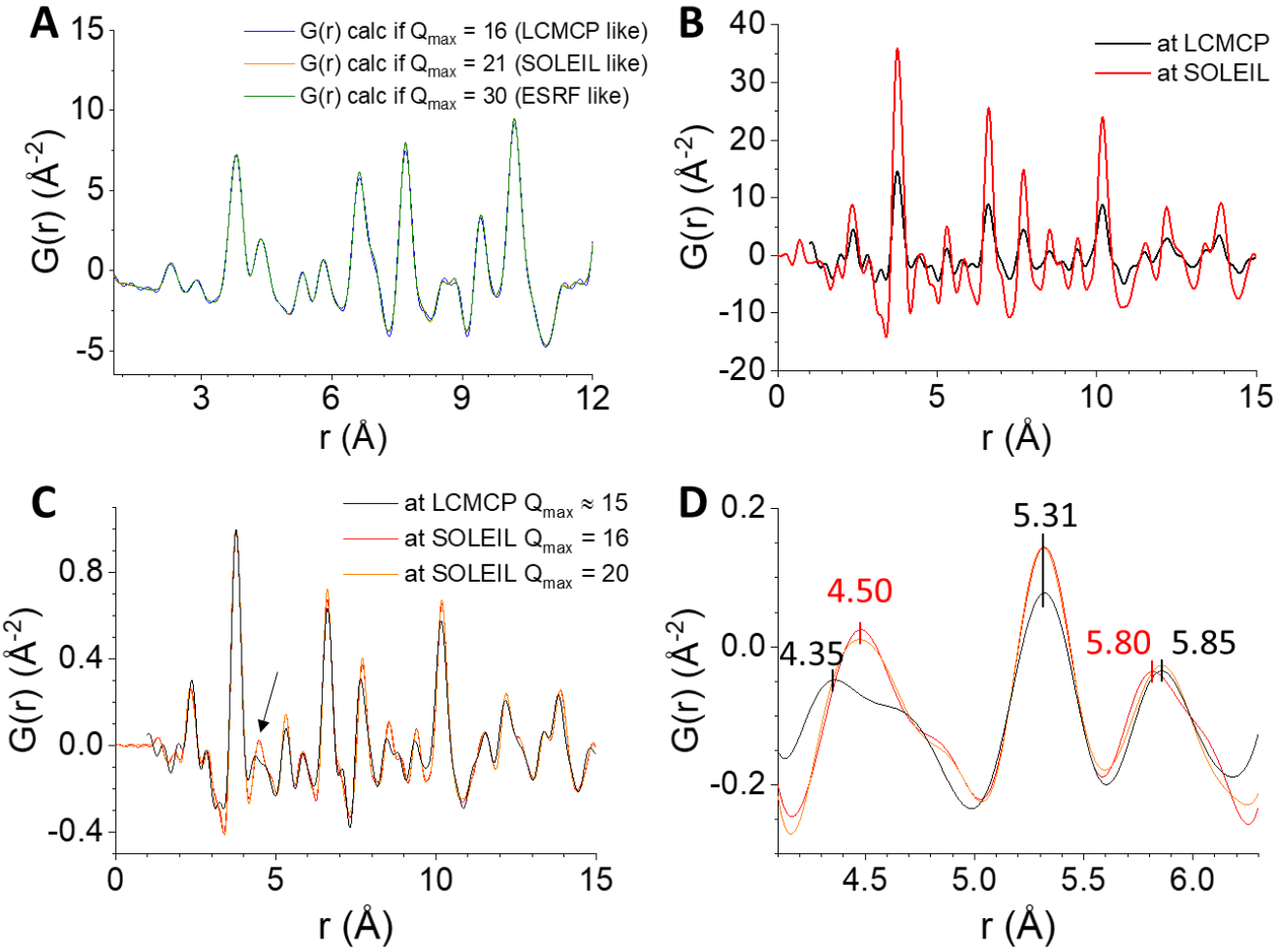

Figure 2 (A) Comparison between calculated G(r) of bulk $Gd_2O_2S_{0.5}$ with different Q_{max} corresponding to the capacity of LCMCP, SOLEIL and ESRF. Comparison of experimental G(r) of the same Gd_2O_2S sample (not annealed) measured at LCMCP and at SOLEIL Synchrotron between: (B) raw data; (C) normalized data with 2 values of Q_{max} for SOLEIL pattern and (D) a zoom of (C) between 4.1 Å and 6.3 Å. The legend is common for (C, D).

A comparison between calculated G(r) of bulk $Gd_2O_2S_{0.5}$ with different Q_{max} corresponding to the capacity of LCMCP, SOLEIL and ESRF shows very small differences between the LCMCP-like curve and the two others, although the higher Q_{max} usually gives thinner peaks associated with less oscillations (Figure 2A). This confirms that theoretically, the signal quality performed by LCMCP equipment is good enough for further analysis.

In terms of the signal quality, the curve G(r) measured at SOLEIL Synchrotron has higher peak intensity compared to the measurement done at LCMCP (Figure 2B). After normalizing the data, there is a high level of coherence between the two measurements (peaks contributions, peaks positions with low difference in normalized peaks intensities). Although, in the region around 4.5 Å, there is a clear difference between them (Figure 2C, zone marked with an arrow). The use of different Q_{max} for SOLEIL pattern does not affect the signal: there is no difference between these two curves (red and orange). The difference between the pattern SOLEIL and the pattern LCMCP is shown more clearly in Figure 2D with some distances labeled. Globally, the results from both instruments are comparable but when we need to analyze peak by peak to go further in the detailed local structure, the data treatment needs to be done for each dataset separately. It is quite unfortunate not to be sure about certain peaks in the patterns acquired at SOLEIL since their signal quality is much better than in our laboratory.

In general, there should be no difference between the results from the two instruments for the reason shown in Figure 2A. The cause of the observed differences is not yet clear. For now, the G(r) extraction of SOLEIL pattern is slightly better with Q_{max} = 16. Hence, this will be used for the future data treatment.

Experimental PDFGETX3: $G_{(r)}$ extraction:

SOLEIL: 0.3 mm capillary	IMPC: 0.5 mm capillary
Background coefficient = 0.85	Background coefficient = 0.7
Q range: 0.5 → 16	Q range: 0.5 → 15
R poly: 1.6	R poly: 1.6

3. Effect of Mo quantity on the signal quality of PDF patterns acquired at CRYSTAL Beamline

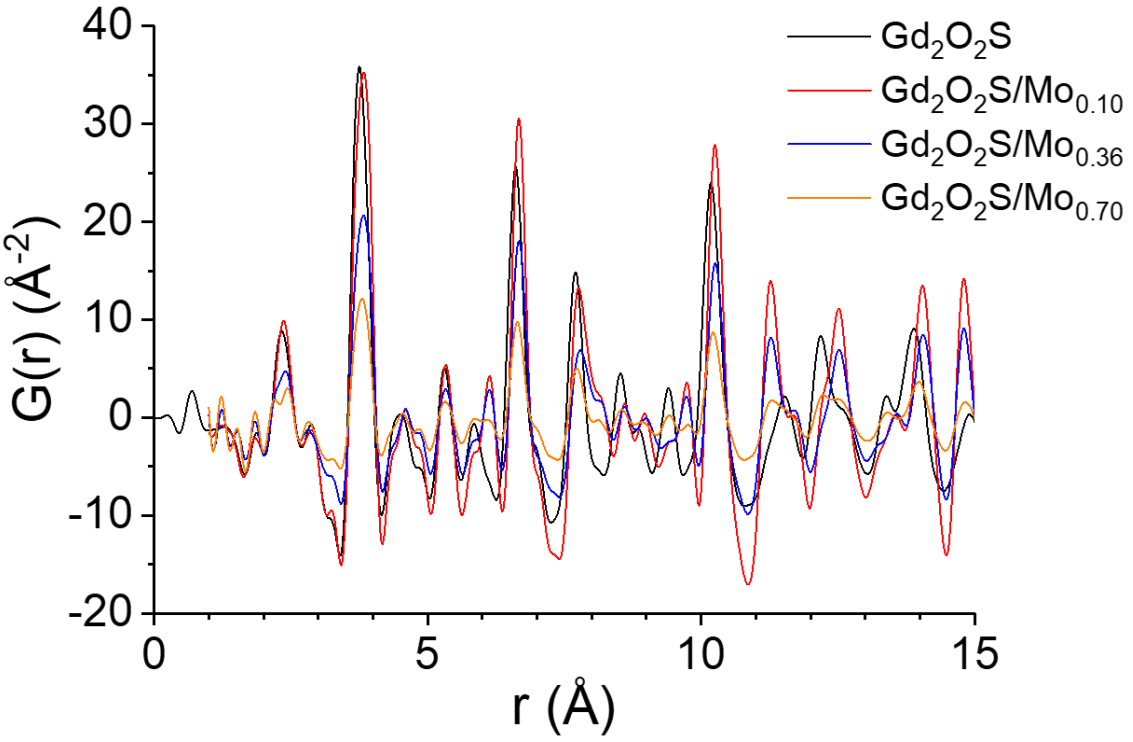

Figure 3 Comparison of raw data of $G_{(r)}$ extracted from the measurements done at CRYSTAL Beamline between Mo-containing samples with different x values and a sample Gd_2O_2S not annealed.

Looking strictly only on the peak intensities of the patterns, we observe that the intensities of the peaks decrease with the increase of Mo theoretically in the samples (the exact values for the moment are still under evaluation). Knowing that the wavelength used at CRYSTAL Beamline is 0.5 Å, i.e. environ 24.1 keV, while the Mo K-edge is about 20.0 keV, there might be some fluorescence parasite problems for Mo-containing samples. Meanwhile, at LCMCP, the wavelength used is 0.7 Å, i.e. about 17.4 keV, which does not cause this problem.

For this reason, the curves can only be compared within the same dataset. It is quite unfortunate not to be sure about certain peaks in the patterns acquired at SOLEIL since their signal quality is much better than in our laboratory.

The measuring conditions at Synchrotron should be optimized in the future.

Abstract:

Today, in personal vehicles, fuel cells are competing with the Li-ion batteries to provide the next technological leap. Hence, replacing noble metal by non-noble metal catalysts is essential to make them affordable. Molybdenum can be a good candidate as some compounds (e.g. MoS_2, MoO_2) are showing activity for the Oxygen Reduction Reaction (ORR). Uncommon molybdenum oxysulfides could be used as electrodes for Li-ion batteries or catalysts thanks to their porous structure in amorphous forms (thin films and bulk powders). Their colloidal synthesis at low temperature, favoring the nanoscaled materials and bypassing the simple energy-consuming synthesis, is barely reported. The same goes for their ORR catalytic reactivity, which was almost never studied.

Here, the well-known colloidal synthesis of lanthanide oxysulfides at low temperature (around 300 °C), producing nanoparticles such as Gd_2O_2S, is extended to the use of Mo molecular precursors. We studied two pathways: by a two-step protocol (adding the Mo precursor to freshly formed, unwashed Gd_2O_2S nanoplates) or a one-step protocol (adding simultaneously both metallic precursors). The structural analysis showed that the first method possibly leads to a deposition of isolated molybdate tetrahedrons on Gd_2O_2S nanoplates without changing their shape and size, while the latter one leads to a more sulfide-like environment of Mo. As observed, only molybdate-doped samples (at low dose) showed positive results in terms of electrochemical activity, which is found related directly to the Mo's presence. Other explorative work on the syntheses without Gd is being pursued to complement the study on the structure and the formation mechanism of the interested materials. Overall, this is the first attempt to synthesize molybdenum oxysulfide by applying the synthesis method of lanthanide oxysulfide.

Résumé :

Aujourd'hui, dans les véhicules individuels, les piles à combustible concurrencent les batteries Li-ion par de nombreux avantages. Donc, remplacer les métaux nobles par des métaux plus abondants dans des catalyseurs est essentiel pour les rendre abordables. Le molybdène peut être un bon candidat puisque certains composés (ex. MoS_2, MoO_2) ont une activité pour la réduction de l'oxygène (ORR). Les oxysulfures de molybdène, relativement méconnus, pourraient être utilisés comme électrodes pour les batteries Li-ion ou les catalyseurs grâce à leur structure poreuse sous formes amorphes (couches minces et poudres massives). Leur synthèse colloïdale à basse température, favorisant les matériaux nanométriques et évitant des synthèses énergivores, est très peu étudiée. Il en va de même pour leur réactivité catalytique en ORR.

Ici, la synthèse colloïdale bien connue d'oxysulfures de lanthanides à basse température (environ 300 °C), produisant par exemple Gd_2O_2S, est étendue à l'usage de précurseurs de molybdène. Nous avons étudié deux voies de synthèse basées sur celle des nanoplaquettes de Gd_2O_2S : par un protocole en deux étapes (ajout d'un précurseur de Mo à des nanoplaquettes de Gd_2O_2S fraîchement formées et non lavées) ou un autre en une étape (ajout simultané des deux précurseurs métalliques). L'analyse structurale a montré que la première méthode conduit possiblement à un dépôt de tétraèdres isolés de molybdate sur des nanoplaquettes de Gd_2O_2S sans changer leur forme et leur taille, tandis que la deuxième conduit plutôt à un environnement local de Mo plus sulfuré. En ORR, seuls les échantillons dopés au molybdate (à faible dose) ont montré des résultats positifs, qui sont directement liés à la présence de Mo. D'autres travaux exploratoires sur les synthèses sans Gd sont en cours pour compléter l'étude sur la structure et le mécanisme de formation des matériaux concernés. Dans l'ensemble, il s'agit de la première tentative d'application de la synthèse de l'oxysulfure de lanthanide pour synthétiser des oxysulfures de molybdène.